MACROPOROUS CRYOGEL COMPOSITES FOR REMOVAL OF HEAVY METALS FROM AQUEOUS AND BIOLOGICAL MEDIA

Alzhan Baimenov

A thesis is submitted in partial fulfillment of the requirements for the degree of

Ph.D. in Science, Engineering, and Technology

June 2020

ABSTRACT

The deficiency of clean water is intensely associated with poor health, poverty and a general decline in living standards. Water is important not only for life but it is also the main resource for food and crops production and is used in most industrial processes. In spite of the natural source of water contamination, a continuous rise of heavy metals discharges to aquatic bodies caused by fast industrial development over the last century has been observed. Heavy metals such Cd^{2+} and Hg^{2+} are of the most toxic and, as all heavy metals, have a tendency to accumulate in the food chain potentially causing serious health disorders. Another source of water contamination is the nuclear power plants. Among the harmful radionuclides discharged are the radioisotopes of I^{-}, Cs^{+} and Sr^{2+}. To improve the availability of clean water, low-cost and effective treatment methods must be developed to remove toxic metal ions. Several water treatment technologies are available with adsorption/ion-exchange combined to chelation/complexation are the most effective.

In this work, highly effective adsorbents based on polymeric cryogels were developed for the removal of Cd^{2+} Hg^{2+}, Sr^{2+}, Cs^{+} and silver-modified forms for targeted removal of I^{-}. Two types of macroporous cryogels were synthesized by free-radical co-polymerization of acrylate-based precursors with allylamine under sub-zero temperature conditions. The adsorption/ion exchange capacity of cryogels is due to the presence of key monomers, methacrylic acid and 2-acrylamido-2-methyl-1-propansulfonic acid. The cryogels were comprehensively characterized and used for the removal of the above mentioned ions from model solutions. Kinetics and equilibrium studies were conducted, models were applied and in combination to post-sorption characterizations potential removal mechanisms were proposed. Finally, the cryogels were tested under environmentally relevant conditions (tap water, river water and sea water) and compared to commercial adsorbents (zeolite Y, ion exchange resin and activated carbon) for the removal of Hg^{2+} showing excellent behavior. After successful experiments on water, cryogels were used as enterosorbents in animal experiments by using rats. The rats were poisoned with LD_{50} dose of metals and were treated by cryogels. The results showed high survival rate and an overall decline of concentration of metals in animal tissues. The discoveries of this work demonstrate that cryogelic sorbents have possible implementation in water treatment and as poisoning antidotes.

CO-AUTHORSHIP STATEMENT

This PhD thesis is a combination of 4 published and 2 prepared papers: five journal articles and one conference proceeding.

Chapter 2 was reproduced from the published review article in Advances in Colloid and Interface Science journal, entitled “A review of cryogels synthesis, characterization and applications on the removal of heavy metals from aqueous solutions” co-authored with D. Berillo, S. Poulopoulos and V. Inglezakis [1].

Chapter 4 was produced based on a published paper in the Journal of Hazardous Materials. The title of the manuscript is “Efficient removal of mercury (II) from water by use of cryogels and comparison to commercial adsorbents under environmentally relevant conditions” co-authored with D.A. Berillo, K. Moustakas and V.J. Inglezakis [2].

Chapters 5-7 were produced based on the ready for publication manuscript entitled “Kinetics and equilibrium studies on the removal of Cd^{2+}, Sr^{2+} and Cs^{+} from water from single- and multi-component solutions by use of cryogels” in collaboration with D. Berillo and V. Inglezakis. Also, Chapter 5 has some results of the conference paper entitled “Novel Amphoteric cryogels for Cd^{2+} ions removal from aqueous solutions” co-authored with D. Berillo, L. Abylgazina, S. Poulopoulos and V. Inglezakis published in Key Engineering Materials.

Chapter 8 was based on the results of published paper in Journal of Molecular Liquids entitled “Cryogel-based $Ag°/Ag_2O$ nanocomposites for iodide removal from water” together with D. Berillo and V. Inglezakis [3].

Chapter 9 will be written on the results of conducted in the Kazakh National Medical University *in vivo* animal experiments. The research article with the proposed title “Macroporous polymer antidotes for treatment of rats intoxicated by LD_{50} dose of heavy metal ions” in collaboration with I. Fakhradiyev, D. Berillo, T. Saliyev, V. Inglezakis and T. Nurgozhin is under preparation.

The contributions of the author of the thesis in all journal articles, conference proceedings and presentations, as the first author, include literature search, carrying out the experiment, data collection and analysis, and provision of the first draft of articles. The co-authors contributed to critical review and modification of the final manuscripts.

ACKNOWLEDGEMENTS

During my 4 year PhD journey, I met a lot of people and would like to thank all of them for their help and advice.

I would like to express my special gratitude to Dr. Vasileios Inglezakis with whom it was a great honor and pleasure to work for over the past years. It should be noted that his strong supervision skills and ability to achieve goals, the ability to motivate and provide unlimited support were invaluable experiences and were an example for me what a real scientist and mentor should be.

Many thanks to my external supervisor Dr. Dmitriy Berillo, whose knowledge of chemistry and polymer science is really impressive, and his enthusiasm and support have been invaluable for me.

My co-supervisor Dr. Stavros Poulopoulos was also supportive throughout the Ph.D. by advising and providing critical reviews of manuscripts.

Also, I would like to express my thanks to my external supervisor Prof. Talgat Nurgozhin, who organized and fully supported experiments on animals.

Special thanks to Director of PhD Studies, prof. Luis Rojas-Solorzano, who significantly improved doctoral studies program and does everything possible to make every PhD student feel comfortable.

I would like to thank my colleagues – Zhandos, Aliya, Almira, Aknur and Seitkhan, the Core Facilities fellows and colleagues from the medical university, without whom it would be very hard to achieve any results.

Finally, I would like to express never-ending appreciation and love to my fascinating wife Zhuldyz, my little princess Aida, and my lovely parents, who fully supported and motivated me throughout this Ph.D. adventure.

DECLARATION

I declare that the research contained in this thesis, unless otherwise formally indicated within the text, is the original work of the author. The thesis has not been previously submitted to this or any other university for a degree and does not incorporate any material already submitted for a degree.

Signed

Date

TABLE OF CONTENTS

LIST OF TABLES

LIST OF FIGURES

LIST OF ABBREVIATIONS

4-VP - 4-vinylpyridine

AA - allylamine

AAc - acrylic acid

AdeM – adeninemethacrylate

AgNP – silver nanoparticles

AMPS - 2-acrylamido-2-methyl-1-propansulfonic acid

APS - ammonium persulfate

AIBN - azoisobutyronitrile

AAm - acrylamide

AN - acrylonitrile

APTACl - (3-acrylamidopropyl)-trimethylammonium chloride

BisAAm - N,N-methylenebis(acrylamide)

CMC – carboxymethyl cellulose

C_e - concentration of adsorbate at equilibrium (mg/L)

CHI – chitosan

C_o - initial concentration of adsorbate (mg/L)

D_3AAm – D_3-acrylamide

DAH- diamino hexane

DEAE - diethylaminoethyl

DMAAm - N,N-Dimethylacrylamide

DMAEMA- dimethylaminoethyl methacrylate

DMSO - Dimethyl sulfoxide

EDC - 1-Ethyl-3-(3-dimethylaminopropyl) carbodiimide

EGDMA - ethylene glycol dimethacrylate

HA - hydroxyapatite

HEMA - 2-Hydroxyethyl methacrylate

His - histidine

FTIR - Fourier-transform infrared spectroscopy

GA – glutaraldehyde

Gel - gelatin

KPS - potassium persulphate

MAAc - methacrylic acid

MAC - N-methacryloyl-L-cysteine

MAH - N-methacryloyl-l-histidine

MALA - maleamic acid

MAPA - N-methacryloyl-(L)-phenylalanine

MIP – molecular imprinted polymer

MMCs - metal-polymer coordinated complex

MCL - maximum contaminant level

n - Freundlich constant

Na_2(EDTA) - Ethylenedinitrilotetraacetic acid disodium salt

NHS - N-hydroxysuccinimide

NIPA - N-isopropylacrylamide

NPs - nanoparticles

OxD – oxidized dextran

P2 - pseudo 2nd-order kinetic rate constant (g/mg min)

PEI - polyethylenimine

PEGDA- polyethylene (glycol) Diacrylate

PEGMA - poly(ethylene glycol) methyl ether methacrylate

pH-PZC - point of zero charge

PVA – polyvinyl alcohol

PSI - polysuccinimide

q_e - amount adsorbed at equilibrium (mg/g)

R^2 - correlation coefficient

SA - sodium acrylate

SEM – scanning electron microscopy

T - temperature (◦C)

t - time (min)

TEMED - N,N,N,N-tetramethylethylenediamine

ThU - thiourea

GMA- glycidyl methacrylate

Jeff 600– jeffamine ED600 (O,O′-Bis(2-aminopropyl) polypropylene glycol-block-polyethylene glycol-block-polypropylene glycol)

MIM - 5-methyl-4-imidazolylmethanol hydrochloride

IEP – isoelectric point

MIP – ion imprinted polymer

K_F - Freundlich adsorption constant (mg/g)(L/mg)

K_L - Langmuir adsorption constant (L/mg)

TMP - 1,1,3,3-tetramethylpropane

VAm - vinyl amine

VIM - N-vinyl imidazole

VBTACl - (Vinylbenzyl)trimethylammonium chloride

Q-NFC - quaternized nanofibrillated cellulose

LIST OF APPENDICES

D. Appendices for Chapter 8.

Fig D1. EDS mapping images of AAC-Ag sample

Fig D2. EDS mapping images of SAC-Ag sample

Fig D3. EDS mapping images of AAC-AgI sample

Fig S4. EDS mapping images of SAC-AgI sample

Table D1. Silver and iodide content in Ag-modified and iodide-loaded cryogels (wt %).

Table D2. Conductivity and pH of solutions after I^- removal by Ag-cryogels

CHAPTER 1

INTRODUCTION

1.1. Background

Over the last century as a result of industrialization, a continuous increase of heavy metal contamination of water bodies has been observed. Among the several harmful water contaminants, heavy metals such as arsenic, cadmium, copper, zinc and mercury are most prevalent. At high concentrations, heavy metals are toxic and have a tendency to accumulate in the nutrition chain and can cause various health disorders [4,5]. Accumulation is enhanced by the affinity of heavy metals to form complexes with biological matter [6–8]. Consumption of cadmium, arsenic, mercury and lead above the tolerance levels lead to kidney failure [9–11], DNA damage [12,13], cancer [7,8,14], brain damage [7,15], initiate the development of cardiovascular diseases by blocking of proteins and oxidation of lipids [10,16,17]. The ratified by US Environmental Protection Agency (US EPA) [18] maximum contaminant level (MCL) standards of heavy metals concentrations in drinking water and their toxic effect on human organism is presented in **Table 1.1**.

Table 1.1. The toxic effect and MCL standards for the highly poisonous metals.

Heavy metal	**Toxicity**	**US EPA MCL (mg/L)**
Arsenic	Skin and vascular disease; visceral tumors	0.01
Cadmium	Kidney and liver dysfunction; carcinogen	0.005
Chromium	Headache; diarrhoea; nausea; vomiting; carcinogenic	0.1
Copper	Liver damage; Wilson disease; insomnia	1.3
Lead	Damage the fetal brain; failure of the kidneys, circulatory and nervous system	0.015
Mercury	Rheumatoid arthritis; failure of the kidneys, circulatory and nervous system disease	0.002

However, the abovementioned metalloids are dangerous in high concentrations and/or with prolonged intoxication, while their or other radioisotopes deadly even at low doses. Unsafety

use of nuclear energy actuate many dangers to society and the environment, including the leakage of radioactive waste from tanks and the unregulated release of colossal quantities of radionuclides triggered by nuclear accidents, like it was in Chernobyl and Fukushima nuclear power plants (NPP) [19]. Amidst the dangerous radionuclides leaked from NPP accidents, cesium (^{137}Cs) and strontium (^{90}Sr) have the most substantial toxic effects of emitting beta-particles and gamma rays. Both radioactive Cs and Sr isotopes have half-life around 30 years; therefore, it is vital to remove such elements from the environment and water for sustainable environmental preservation [20]. Moreover, due to the chemical similarity of ^{137}Cs and ^{90}Sr to potassium and calcium, respectively, the released isotopes can be easily anchored into terrain and aquatic organisms. One more radioactive ion which usually arises with ^{137}Cs is radioactive iodide. During the recent catastrophe in Chernobyl in 1986 of 1.76×10^{18} Bq of ^{131}I was discharged, while after the NPP accident in Fukushima in 2011, which produced the discharge of 1.5×10^{17} Bq of ^{131}I, the concentration for radioactive iodide was drastically grow in the environment [21] and rose global interest of scientist for the development of appropriate ways of removal of radioactive iodide.

The effective removal of any of metal ions is a challenging task because of complicacy and high-priced treatment methods, which are exceedingly reliant on the composition of the solutions. For this purpose, numerous techniques like membrane separations, ion exchange and adsorption [22,23], coagulation [24], chemical precipitation [25,26] and bioremediation have been used [27–29].

Of all above methods, adsorption/ion-exchange is a beneficial method in terms of operating uncomplicatedness and cost-effectiveness. Most of natural materials (zeolites, activated carbons), industrial inorganic substances (coals, resins, silica) and by-products (fly-ash), are widely used for heavy metal elimination. Per contra, all of these commercial adsorbents have restrictions such as low kinetics and small adsorption capacity. The new type of synthetic polymers, such as cryogels, may overcome these problems and potentially can replace commonly used adsorbents.

Cryogels are several low temperature-structured polymeric materials that have attracted interest in various fields, such as medicine and biology, tissue engineering, food production, environmental remediation, construction in long-lasting frost regions and others [30–38]. Cryogels are synthesized by a freeze-thawing technique forming three-dimensional flexible polymeric structures [39–41]. The main advantages of cryogels include a macroporous cross-linked matrix, a variety of functional groups, chemical and structural stability [38,41–

46]. Moreover, by applying hydrophilic functional groups, a large liquid holding capacity could be reached [43]. These sorbents are comparable with ion-exchange resins in numerous sights: they are polymer-based sorbents and engage electrostatic interactions for the adsorption of ionic pollutants from aqueous media. On the other hand, resins' structures are sturdy, while the cryogels matrix are elastic and able to preserve expressively more water [47,48]. The availability of definite functional groups such as -COOH, -$CONH_2$, -OH, -NH_2 and -SO_3H in cryogels are improving the adsorption of water contaminants [49–51]. The impurities can be adsorbed onto the external surface and as well into the swollen 3D structure of cryogels. Additionally, due to the bio- and hemocompatible properties of most types of cryogels [52–55], they can be used for purification of blood plasma from Fe(III) ions [52].

Cryogel properties can be developed by adjusting the synthesis conditions, such as the nature of monomers, temperature, ratio of precursors [56–59] and reaction time [60–62]. Cryogels with precise features can be prepared by co-polymerization of more than one kind of monomer or by post-modification of the polymerized materials via graft polymerization and other methods [46,48,63]. Along with high removal capability and comprehensive modifiability, such polymers can be renewed by desorbing the contaminants and recovering the sorption capacity in repeated removal series [49,64,65]. However, there are quite a few issues that prevent the scaling from the lab-scale to pilot and practical commercial applications. Selectivity and competitive adsorption in complex water matrices [66–68] and stability issues, causing structural failure and inhibit their reuse [55,65] are the most prevalent limitations.

The leading amount of research papers and reviews on the application of cryogels are proposed for use in medicine [37,41,69–72] as tissue engineering scaffolds [73] and drug delivery systems [74] or protein purification agents [75], environmental engineering for cleaning of soil and water from dyes [76], organic and inorganic contaminants, in supercapacitors applications [77,78] and sensors [79]. Nevertheless, despite the fact that cryogels have numerous advantages over other sorbents, the research on the use of cryogels for the elimination of heavy metals from water is minimal.

The main motivation to do this research was to optimize the synthetic conditions of the two types of novel compositions of cryogels for removal of various cations such as Cd^{2+}, Hg^{2+}, Sr^{2+} and Cs^{+}. For the targeted removal of iodide from model and real seawater solutions, the synthesized cryogels were modified by silver nanoparticles (AgNPs). We consider that

highly macroporous cryogel could be produced and effectively applied to wastewater treatment and use as oral sorbents for poisoned by heavy metal ions living organisms. In this work, we present two types of cryogels with different functional groups and test them for cadmium(II), mercury(II), cesium(I) and strontium(II) removal under simulated adsorption conditions. For targeted elimination of iodide, Ag-modified cryogels were tested in simulated and natural seawater experiments. To evaluate the effectiveness of produced cryogels as antidotes for cations treatment, the polymers were tested for biocompatible properties and used in the experiments on animals (rats) intoxicated by LD50 dose of the selected metal ion.

1.2. Thesis hypothesis and statements

Based on the literature review on the synthesis and use of various types of cryogels and their use in water treatment the following thesis hypothesis and statements were defined.

Thesis hypothesis:

- The highly macroporous cryogels could be expertly produced by a selecting and varying the ratio of monomers, reaction time and temperature conditions.
- Having the functional groups and their concentration defined capacity, removal mechanisms and selectivity of the synthesized cryogels toward targeted ions could be predicted and experimentally verified by cutting-edge characterizations tools and methods.
- Taking into account that silver nanoparticles have been used with several other materials for targeted removal of iodide from water, the synthesized cryogels can be modified by silver nanoparticles and used for efficient iodide removal.
- Given the behavior in water solutions, the produced cryogels could be used as antidotes for the elimination of toxic metals from experimental animals

Thesis statements:

- To conduct a comprehensive literature review on the synthesis and use of cryogels and their composites for ions removal from water and treatment of intoxicated animals;

- Varying reagents ratio, temperature and freezing time identify the optimum synthesis conditions for two types of cryogels;
- Fully characterize the surface morphology and properties, pore structure, swelling degree and availability of functional groups by advanced characterization methods;
- To effectively use a novel cryogels for the removal of Cd^{2+}, Sr^{2+}, Hg^{2+} and Cs^{+} under different concentrations and conditions;
- To modify the surface of cryogel with silver nanoparticles for targeted and efficient removal of I^{-} from water;
- To study and propose the removal mechanisms by use of kinetics and equilibrium modeling and cutting-edge characterization methods (XRD, XPS, FT-IR, SEM/EDS, TEM/EDS);
- To study the removal efficiency in environmentally relevant conditions and compare with commercial adsorbents
- To test the synthesized cryogels in animal studies for mitigation of metals poisoning and compare them to commercial products

1.3. The novelty of the research

To the best of the author's knowledge the novelty of this research is:

- The synthesis of novel cryogels and their silver nanocomposites;
- Use of novel cryogel for various cations and targeted removal of iodide;
- Investigation of the detailed mechanism of removal of cations and iodide ions from water using removal experiments, aqueous phase speciation, equilibrium and kinetics modeling and advanced characterization methods;
- Testing the cryogels under environmentally relevant conditions and compare them to commercial adsorbents
- Testing of cryogel effectiveness toward various cations in *in vivo* animal studies

1.4. Research contributions

2 published research and 1 review papers,, 2 prepared research articles:

1) A.Zh. Baimenov, D.A. Berillo, V.J. Inglezakis. Cryogel-based Ag°/Ag2O nanocomposites for iodide removal from water. Journal of Molecular Liquids,

Volume 299, 1 February 2020, Article 112134. Impact factor 4.56, Quartile 1. https://doi.org/10.1016/j.molliq.2019.112134.

2) A.Zh. Baimenov, D.A. Berillo, S.G. Poulopoulos and V.J. Inglezakis. A review of cryogels synthesis, characterization and applications on the removal of heavy metals from aqueous solutions. Advances in Colloid and Interface Science, Volume 276, February 2020, Article 102088. Impact factor 8.24, Quartile 1. https://doi.org/10.1016/j.cis.2019.102088.
3) A.Zh. Baimenov, D.A. Berillo, K. Moustakas and V.J. Inglezakis. Efficient removal of mercury (II) from water by use of cryogels and comparison to commercial adsorbents under environmentally relevant conditions. Journal of Hazardous Materials. Available online 27 May 2020, Article 123056, Impact factor 7.65, Quartile 1. https://doi.org/10.1016/j.jhazmat.2020.123056
4) A.Zh. Baimenov, D.A. Berillo, and V.J. Inglezakis. Kinetics and equilibrium studies on the removal of Cd^{2+}, Sr^{2+} and Cs^{+} from water from single- and multi-component solutions by use of cryogels. To be submitted to Elsevier journal.
5) A. Baimenov, I. Fakhradiyev, D. Berillo, T. Saliyev, V. Inglezakis and T. Nurgozhin. Macroporous polymer antidotes for treatment of rats intoxicated by LD_{50} dose of heavy metal ions. To be submitted to Elsevier journal.

1 published conference proceedings:

1) A. Baimenov, D. Berillo, L. Abylgazina, S. Poulopoulos and V. Inglezakis. Novel Amphoteric cryogels for Cd^{2+} ions removal from aqueous solutions. Key Engineering Materials. 2018 (775), 376-382, https://doi.org/10.4028/www.scientific.net/KEM.775.376

3 presentations on international conferences and seminars:

1) A. Baimenov, V. Inglezakis and D. Berillo "Nanostructured cryogel composites for removal of heavy metals from aqueous solutions". Postgraduate Research Week, 15-19 May 2017, University of Brighton, Brighton, UK (under Erasmus+ student exchange program).
2) A. Baimenov, D. Berillo, L. Abylgazina, S. Poulopoulos and V. Inglezakis. “Novel Amphoteric cryogels for Cd^{2+} ions removal from aqueous solutions”. The 8th

International Conference on Key Engineering Materials, March 16-18, 2018, Osaka, Japan (oral presentation).

3) A. Baimenov, D. Berillo and V. Inglezakis "Macroporous cryogel composites for removal of heavy metals from aqueous and biological media". Annual NANOMED project meeting, December 2-5, 2018, Budapest, Hungary (oral presentation).

CHAPTER 2
LITERATURE REVIEW

2.1. Cryogels synthesis

A class of gels with a macroporous spongy-like 3D structure prepared via freeze-thawing technique is named as cryogels. Cryogels may be categorized into cationic, anionic and amphoteric, due to the existence of the monomers used. Examples of most common monomers, their structure and main functional groups used for the synthesis of cryogels are presented in **Table 2.1**.

Table 2.1. List of monomers used in the cryogels synthesis (acronym in parenthesis)

Monomer	**Structure**	**Functional group(s)**	**Ref.**
2-Hydroxyethyl methacrylate (HEMA)	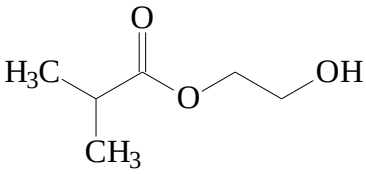	Hydroxyl and vinyl ester groups	[52,66, 80]
Poly(ethylene glycol) methyl ether methacrylate (PEGMA)	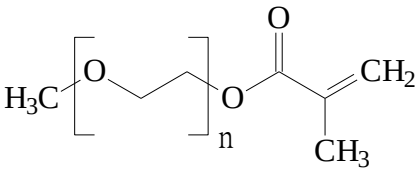	Ether and vinyl groups	[81,82]
Polyvinyl alcohol (PVA)	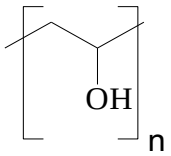	Hydroxyl group	[39,83]
Oxidized dextran (OxD)	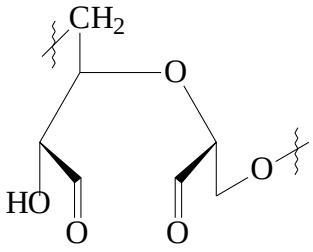	Carbonyl, hydroxyl and ether groups	[42,84, 85]

Methacrylic acid (MAAc)	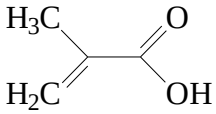	Carboxyl and vinyl groups	[82,86]
Chitosan (CHI)	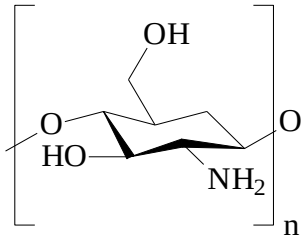	Primary amino, amide, ether and hydroxyl groups	[55,85, 87]
Ethylenglycol dimethacrylate (EGDMA)	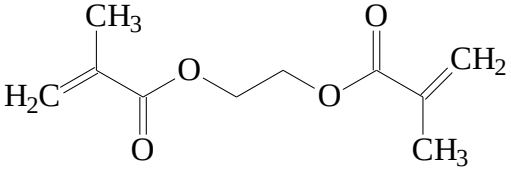	Ester and vinyl groups	[50,88 –94]
N,N′-Methylenebis-(acrylamide) (BisAAm)	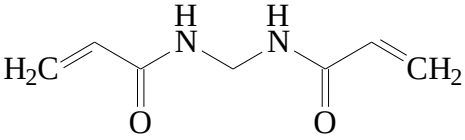	amide and vinyl groups	[49,95]
2-Acrylamido-2-methyl-1-propan sulfonic acid (AMPS)	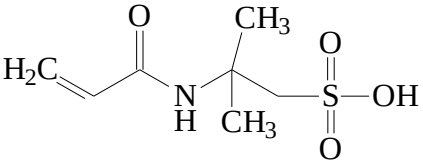	Sulfogroup, amide and vinyl groups	[94,96]
Allylamine (AA)	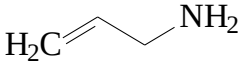	Primary amino group, vinyl group	[97,98]
2-(Dimethylamino) ethyl methacrylate (DMAEMA)	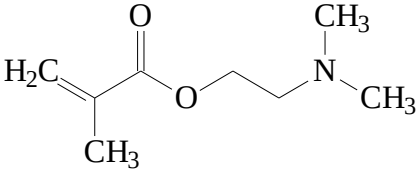	Tertiary aminogroup and vinyl group	[97,98]
N,N-dimethyl acrylamide (DMAAm)	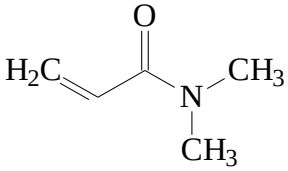	Carboxyl, amide, vinyl groups	[51]

Glycidylmethacrylate (GMA)	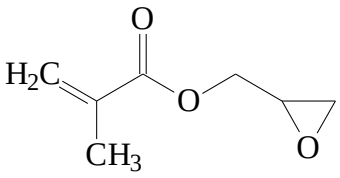	Vinyl, ester and epoxy groups	[95,99]
(3-acrylamidopropyl)-trimethylammonium chloride (APTACl)	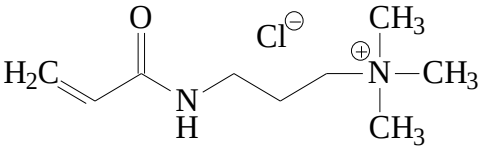	Amide, quaternary amino and vinyl groups	[100]
4-vinylpyridine (4-VP)	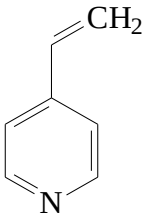	Vinyl group, pyridine	[90]
1-vilylimidazole (VIM)	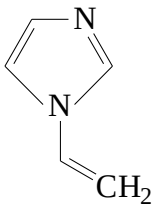	Vinyl and imidazole group	[46]
Glutaraldehyde (GA)	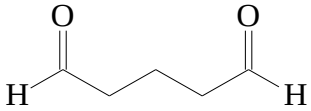	carbonyl groups	[42,84, 85]
N-(2-methacryloyl)-L-histidine (MAH)	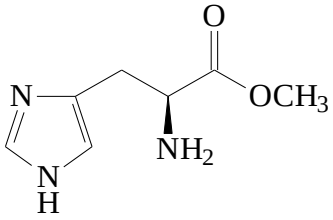	Amino, imidazole, ester groups	[49]
Acrylonitrile (AN)	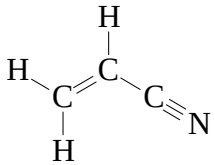	Nitrile and Vinyl groups	[101]
Acrylamide (AAm)	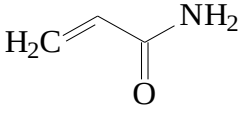	Carboxyl, amine and vinyl groups	[90]

Polyethylenimine (PEI)	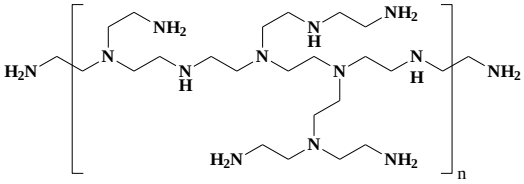	Primary, Secondary and tertiary amino groups	[102]
Diamino hexane (DAH)	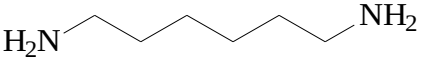	Primary amino group	[103]
Vinylamine (VAm)	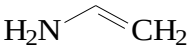	Vinyl and primary amine groups	[104]

The polymers cryogelation procedure involves co-polymerization of monomer(s) and cross-linker(s) dissolved in the various solvents such as water, dioxane and dimethyl sulfoxide (DMSO), which is used as pore developer [105–108]. The preparation of the cryogel must be attentively regulated to assure that the freezing of the solvent and the formation of ice crystals did not occur before the co-polymerization reaction and the development of the 3D polymer structure (**Fig. 2.1**). Depending on the temperature of the synthesis of cryogels, the type of solvent is selected. For example, in the case when a cryogel should be prepared at a temperature of +12 °C, then 1,4-dioxane or DMSO can be used instead of water. After completion of the polymerization, the solvent is thawed from the polymer matrix, leaving a macroporous structure inside the crosslinked cryogel network.

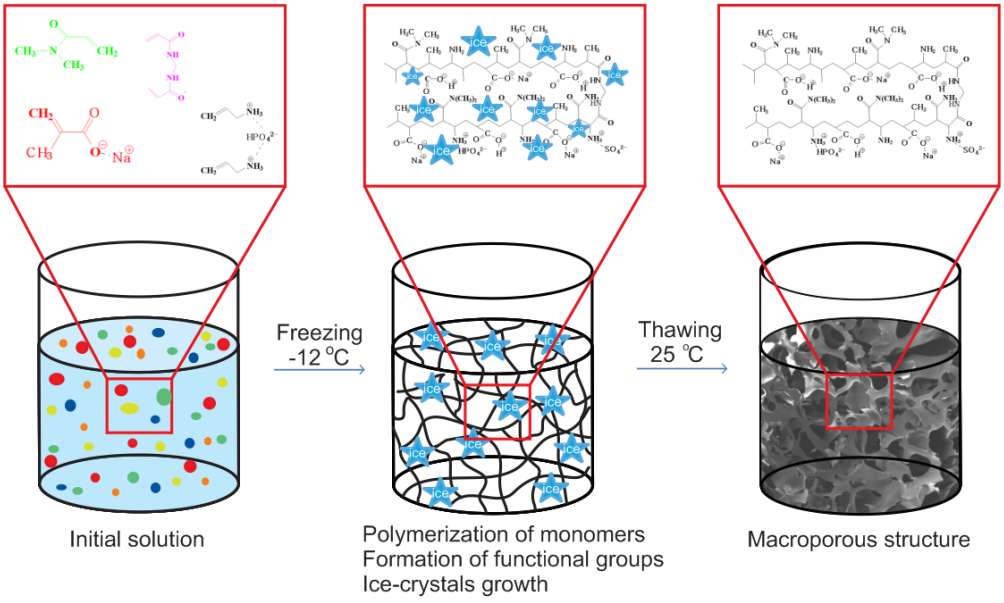

Fig. 2.1. Schematic illustration of the development of cryogels

The widely used methods of cryogels synthesis include free-radical polymerization [109–112], gamma-rays, electron beam, UV irradiation [113,114], self-assembly based gel formation [115], polycondensation reaction under cryo-conditions [42,84,85], enzymatic catalysis [116], metal-polymer coordinated bonds or ionic interactions [85,117] techniques.

Crosslinking plays an important role in the development of cryogels structure, since it influences the morphological properties of polymers, elasticity and degree of swelling. The crosslinking of cryogels networks takes place either physically or covalently [118–120]. Physical crosslinking follows via non-covalent interactions (Van der Waals and electrostatic interactions, hydrogen bonding, metal coordination, p-p interactions) [42,45,85,98], while chemical interactions complete covalent crosslinking by a cross-linking agent or zero-valent bond using enzymatic cross-linking or carbodiimide/succinimide strategy [116].

Since the polymerization process finishes, cryogels are defrosted and thoroughly rinsed with solvent to exclude non-reacted components. The produced cryogel replicates the form of the vessel where the synthesis happened. The pores size and shape are generally controlled by the ratio of monomers to cross-linker, freezing time and temperature [121–124]. The illustration of the macroporous structure formation at different time points is shown in **Fig. 2.2**.

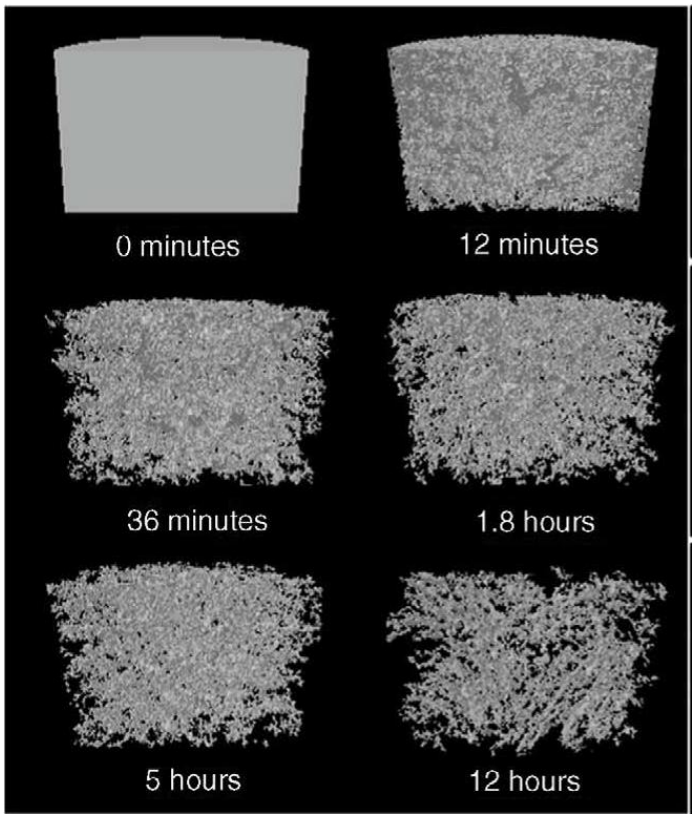

Fig. 2.2. The effect of time on the development of polyacrylamide cryogel porosity [44]

Also, apart from using synthetic chemicals for the synthesis of cryogels, researchers make an attempt to apply low-cost and non-toxic natural materials. Elbarbary et al. produced a p(CHI-HEMA) cryogel, where one of the ingredient - chitosan is used as a natural product having a large number of functional groups [66]. Chitosan is a linear polysaccharide which is widely known for its high adsorption properties toward cations and anions [85,87].

Cryogels can be used as a scaffold for the embedding of nanoparticles (NPs), i.e. forming nanocomposites [90,125,126]. Cryogel nanocomposites with precise properties can be synthesized both by direct polymerization of a purposeful monomer with NPs or by adapting a prepared polymer by secondary reactions and addition of various metal NPs [50,64,67,85,92,127].

An alternative method of synthesis of cryogel based composites is a metal ion-imprinting (MIP) technique, used for targeted adsorption of metal ions. Typically, metal ions interact with the purposeful monomer(s) before the polymerization reaction occurs, after which they are detached from the cryogel structure. The resulting holes in the polymer matrix have specific binding sites with metal ions used for imprinting, which makes them a highly

selective adsorbent. However, the MIP technique usually consists of the multistage synthesis procedure that may cause some complexity. For example, Jällilzadeh and Ṣenel prepared p(HEMA-MAH)/MIP-Cu composite using two-step synthesis method [49]. In the first step, $Cu(NO_3)_2$ was mixed with water-dissolved MAH monomer to appear MAH-Cu(II) pre-polymerization compound. Then, HEMA monomer was added to MAH-Cu^{2+} solution and cryogel template was prepared. Afterwards the polymerized p(HEMA-MAH)/MIP-Cu composite was washed by Na_2(EDTA) solution to separate the imprinted Cu^{2+} ions from the composite structure [49].

2.2. Cryogels characterization techniques

2.2.1 Porosimetry and surface area

The low-temperature nitrogen adsorption/desorption technique is commonly used for the determination of micro- and mesoporosity of materials. For determination of the surface area, pore volume and pore size distribution from the nitrogen adsorption/desorption isotherms the Brunauer-Emmett-Teller (BET), Density Functional Theory (DFT), and Barrett, Joyner, and Halenda (BJH) equations are usually used [128]. Since polymer cryogels are super-macroporous in nature, of the above models, only the BET equation is used to measure specific surface area (S_{BET}) due to the presence of micropores in the polymer walls [46,129–132]. For the correct evaluation of the S_{BET}, the sorbents must be thoroughly dried and degassed. Due to the polymeric nature of cryogels, moderate degassing temperatures, typically less than 100^{o}C are used [49,102], but the temperatures up to 150^{o}C were also observed in the literature [46,88]. The S_{BET} values of some cryogels are presented in **Table 2.2**.

Table 2.2. Specific surface area of cryogel materials

Cryogel	S_{BET} (m^2/g)	Reference
P(HEMA-VIM)	39.7	[46]
P(HEMA-VIM)/p(HEMA)	78.6	[46]
p(HEMA-MAH)	18.6	[49]
p(HEMA-MAH)/MIP-Cu	43.4	[49]
p(HEMA-MAH)/MIP-Cu-Fe_20_3	106	[49]
p(AA-MA-AAc)	21.9	[129]
p(AA-MA-AAc)-ThU	17.2	[129]
P(HEMA)	27.2	[88]

P(HEMA-DEAE)	9.3	[102]
P(HEMA-PEI)	8.9	[102]
P(HEMA)/p(GMA-EDMA)	18.4	[102]
P(HEMA)	8.7	[102]
P(NIPA-MAH)	16.9	[133]
P(HEMA-MAGA)/p(HEMA)	29.2	[130]
P(HEMA- co-AdeM)	6.7	[131]
P(CHI-QNFC)	49.5	[134]
p(HEMA-GMA)	4.9	[135]
p(HEMA-GMA)-PEI-MIP-Cu	8.4	[136]
P(HEMA-MAPA)	42	[132]

Another method of determination of the porosity of macroporous cryogels is the mercury porosimetry technique [137,138]. As for a nitrogen porosimeter, a dried sample must be used for analysis on a mercury porosimeter. However, when drying cryogels for analysis on a mercury porosimeter, significant structural changes and even complete destruction of the entire pore network can occur [41,71,139]. Also, since cryogenic polymers are soft and elastic during the intrusion/extrusion of mercury under high pressures, the shirking of the cryogels takes place, which will also affect the quality of the results. For such reasons, the mercury porosimetry technique is rarely used because it does not guarantee precise results.

2.2.2 FT-IR characterization

Fourier-transform infrared spectroscopy (FT-IR) technique is one of the informative and easy-to-conduct methods of functional group evaluation [43,51,54,103,127]. The most wide-spread functional groups of cryogels and their typical wavelength ranges are presented in **Table 2.3**.

Table 2.3. Functional groups and frequencies

Functional group	Functional group name	Type of vibration	Wavelength range, cm^{-1}	Ref
OH	Hydroxyl group	Stretching, intra-molecular hydrogen bonds	3600-3200	[46,140]
$-NH_2$	Primary amine	Stretching	1690-1640	[103]

-NH	Secondary amine	Bending	1650-1580	[49]
-C=O	Amide(I)	Stretching	1690-1650	[141]
-C-N	Amine	Stretching	1250-1000	[141]
-COOH	Carboxylic acid group	Stretching	3400-2500	[141,142]
$-CONH_2$	Amide(II)	Stretching	3500-3400, 1560-1510, 1650-1620	[90]
-CONHR	Amide(III)	Stretching	1550-1530	[94]
$-C=CH_2$	Alkene	Stretching	3080, 2950	[51]
-C-O	Ether	Stretching	1150-1050	[94]
-C=O	Carbonyl	Stretching	1750-1715	[140]
-C-O-C	Ether	Stretching	1100	[143]
-C-H	Alkyl	Stretching	3000-2850	[93]
-C-H	Alkane	Bending	1390-1370, 1470-1450, 1070-1060	[46]
$-SO_3H$	Sulfur	Stretching	1070-1030,1245-1130	[144,145]

Tekin with co-workers had evaluated the functional groups of the parent and VIM monomer modified p(HEMA-VIM)/p(HEMA) cryogel. The FT-IR spectra of p(HEMA) has a peak at 3525 cm^{-1} that matches to the vibration band of a hydroxyl group, while after the adding the VIM the hydroxyl group band became broader. The non-modified p(HEMA) polymer also has an ester band at 1262 cm^{-1}, the peak of the carbonyl group at 1728 cm^{-1}, and aliphatic C-H group at 2955 cm^{-1}. However, with addition of VIM, a new peaks of imidazole ring and C-H bending group was detected [46].

2.2.3 Zeta potential

The pH at which the negatively and positively charges of the surface are equal is called the point of zero charge (pH-PZC) [41,67,146]. If the surface of the material charged positively then the pH<pH-PZC, while when pH>pH-PZC, the material acts as a negatively charged surface [41]. Therefore, when the pH of the solution is lower than the pH-PZC, the material

will better absorb anionic adsorbate, and *vice versa*. [127]. Also, the electrokinetic phenomena could be described by the determination of the isoelectric point (IEP). In case of the absence of specific adsorption on the material's surface, the IEP is equivalent to pH-PZC [147]. Generally, the IEP is evaluated by titration (potentiometric and/or conductometric) by using acidic and basic solutions [97,104] or using equipment for zeta potential measurement [51]. As example, in the work of Tatykhanova et al. [97] was found that using potentiometric titration the IEP of p(AA-MAAc-AAm) was in the range between 4.0 and 4.3. The determined IEP indicates that the cryogel contains predominantly acidic groups, because the acid/base ratio it directly affects the IEP value [148].

Dragan with colleagues determined the pH-PZC of initial and modified with (vinylbenzyl diethyl 2-hydroxyethyl) ammonium chloride p(CHI-VAm) cryogels. It was determined that at pH ~ 5.5, the surface of parent cryogel had zero charge, whereas, after addition of VBTACl monomer, pH-PZC was shifted by 0.6 units to pH around 4.9 (**Fig. 2.3**) [104]. Akilbekova et al. found that by varying the ratio of monomers, different charge of the surface can be obtained. The gelatin-oxidized dextran cryogel with ratio (1:1), (2:1), and (3:1) had IEPs at pH 4.59, 6.11, and 4.05, respectively, while pure gelatin at around pH 7.0 [85].

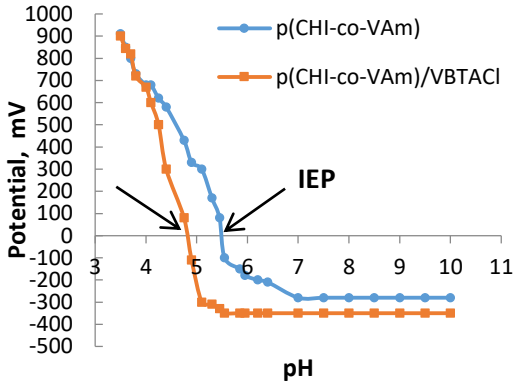

Fig. 2.3. Determination of IEP of parent and modified p(CHI-VAm) cryogels.

[Reprinted with permission from Ref. [149]. Copyright 2020, Elsevier]

2.2.4 Interaction of cryogels with water

2.2.4.1 Water permeability

The high permeability and flow rate of solutions through adsorbents are extremely important properties of separation processes. Cryogels in the form of monolith are promising wastewater filters with a high liquid flow rate due to their interlinked macropores, allowing unrestricted diffusion of water matrix and mass transfer of substances [52,53,141,143,150,151]. Permeability is highly dependent on the nature of monomer, the proportion of the crosslinking agent, and the dimensions of the cryogel monolith. Andrabi et al. studied the flow rate of the aqueous solutions spiked with As^{3+} and Cr^{6+} through the at lab scale filter of p(CHI-DMAEMA)/ Fe_3O_4 (2,5 cm in height and 1 cm in diameter) and fabricated pilot filter with 6,5 cm height and 7 cm in diameter. The lab scale sample has 8 mL/min flow rate, while pilot model has 85 mL/min [143]. In another paper [52] was found that the adsorption capacity of the p(HEMA-MAH) cryogel decreases by four times with the increase of the flow rate of Fe^{3+}-containing solutions from 0.5 to 4 mL/min (**Fig.2.4 left**). An increase in the liquid flow rate decreases the contact time of the ions with the polymer surface, which leads to a fall in the adsorption efficiency. [143]. Lastly, the similar results were found by Asir et al. during the treatment of blood plasma from Cd^{2+} ions by p(HEMA-MAC)-MIP-Cd cryogels. With an increase in the flow rate from 1 to 4 mL/min, the removal efficiency sharply decreased from 2.6 to 0.34 mg/g (**Fig. 2.4 right**) [151].

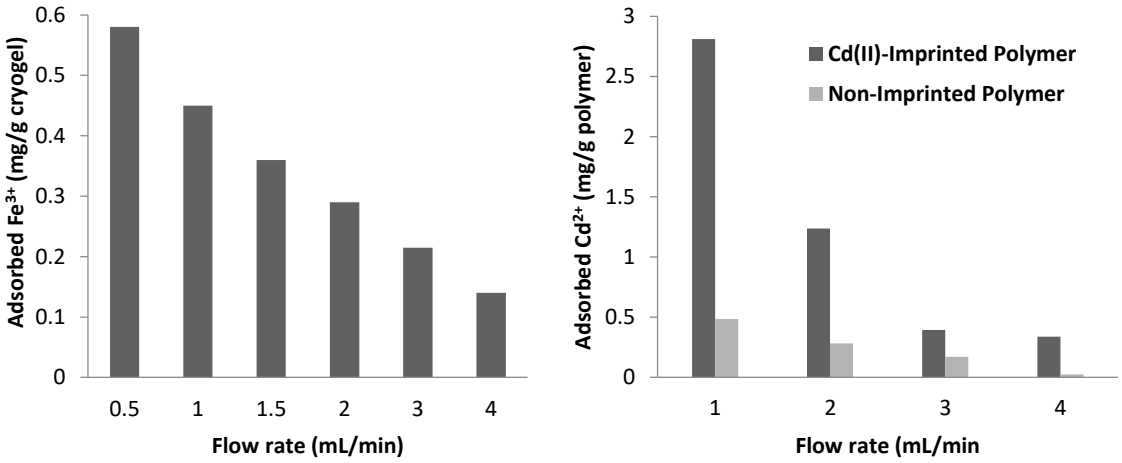

Fig. 2.4. Dependence of the flow rate on the removal of Fe^{3+} (left) [52] and Cd^{2+} (right) [151] ions by different cryogels [Reprinted with permission from Ref. [149].

2.2.4.2 Swelling

Due to the monomers chemical nature and the degree of crosslinking of the cryogels the water swelling time and amount may differ. Commonly, the higher the crosslinking degree, the lower the swelling and adsorption capacity of polymers [152–154]. In their study, Erdem et al. [103] validated that the ratio of cross-linking and chain-extending agents contributes significantly in the removal of metal ions (**Fig. 2.5**).

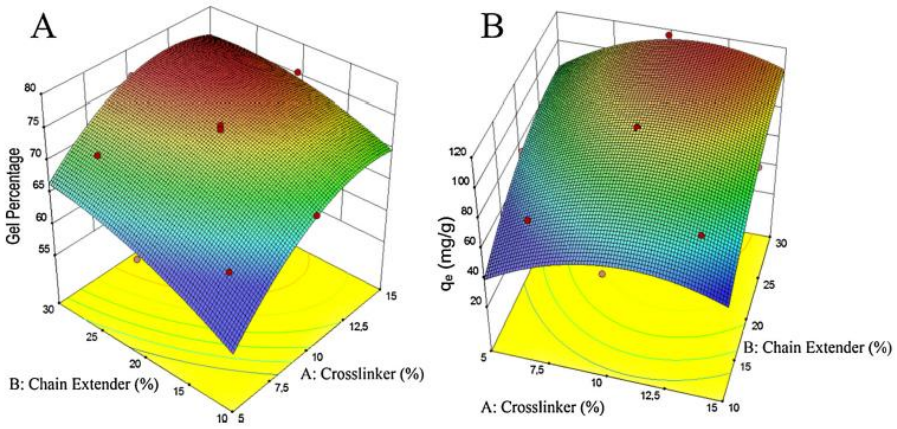

Fig. 2.5. Effect of crosslinker and chain extender ratios to gel percentage (A) and Cd^{2+} removal capacity (B) [Reprinted with permission from Ref. [103]. Copyright 2017, Elsevier]

In the work of the Sahiner and Seven [91], the swelling behaviour of the hydrogel and hydrogel based on AMPS monomer and crosslinked by 0.1 and 10 % of the cross-linking agent, respectively, is clearly presented (**Fig. 2.6**). It follows from the picture that cryogel requires 10 seconds for complete swelling, while the hydrogel reaches maximal swelling in 8 hours. Even taking into account that the ratio of the crosslinking agent is 100 times higher in the hydrogel than in the cryogel, the macroporous cryogel swells 3600 times faster than hydrogel. Fast swelling behavior delivers many benefits in water treatment procedure.

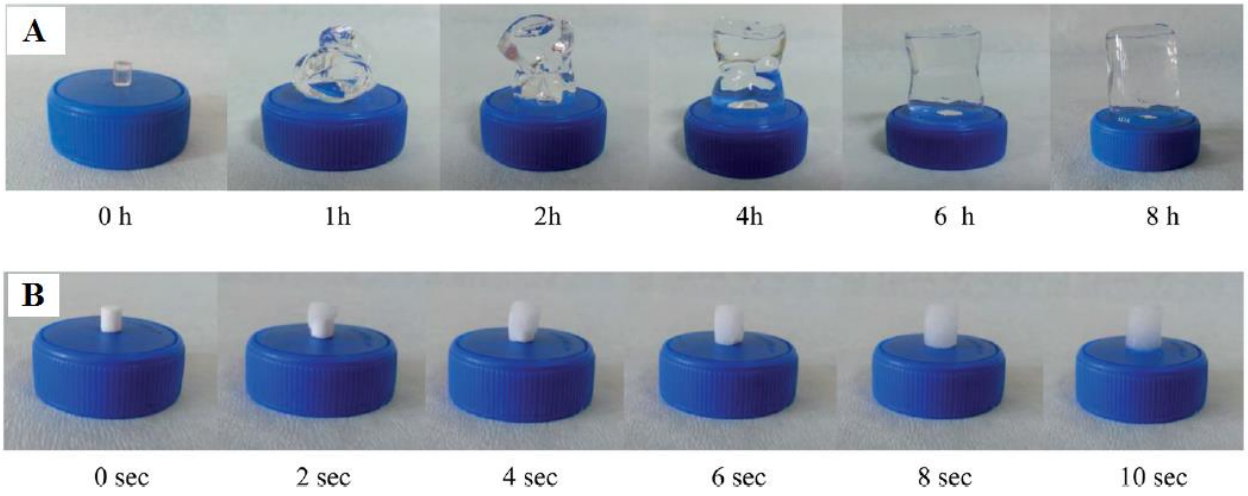

Fig. 2.6. Water swelling of p(AMPS) hydrogel (a) and cryogel (b) during the time [Reprinted with permission from Ref. [91]. Copyright 2014, The Royal Society of Chemistry]

2.2.5 Optical and SEM/TEM microscopy

One of the most straightforward methods of investigation of the porosity of polymers is optical microscopy technique. The cryogel photography's shown in **Fig. 2.7 (e,f)** obtained by an optical microscope clearly show the developed structure of p(AMPS) cryogel with macro-sized pores [91].

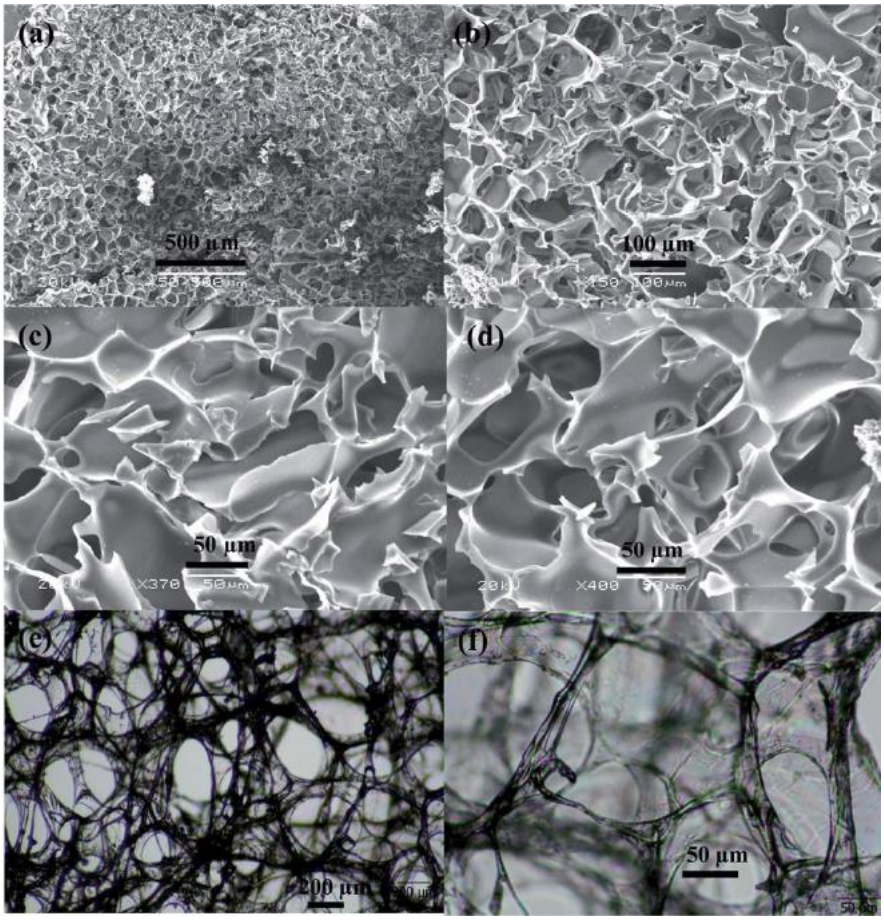

Fig. 2.7. SEM microphotographs (a-d) and optical microscope images (e,f) of p(AMPS) cryogels under different magnifications. [Reprinted with permission from Ref. [91]. Copyright 2014, The Royal Society of Chemistry]

Obtained by Sahiner and Seven the SEM images (**Fig. 2.7(A-D**)) of p(AMPS) cryogel represent the developed macroporous structure. The pore size distribution varies in the range of 30–120 µm. The SEM imaging is often used for the evaluation of the porous structure of the sorbents; however, if materials were modified by different metallic nanoparticles, the best technique is transmission electron microscopy (TEM). For example, using the TEM technique Onnby et al. demonstrated the existence and size variations of Al-NPs on the surface of the cryogel nanocomposite (**Fig. 2.8**) [64].

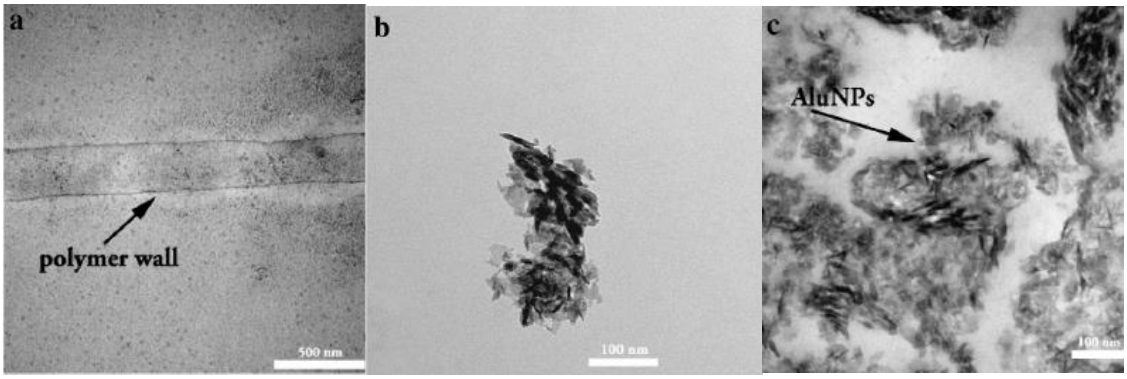

Fig. 2.8. TEM images of parent p(AAm) (a) and Al-modified p(AAm)/Fe-Al_2O_3 (b, c) cryogels at different magnifications [Reprinted with permission from Ref. [64]. Copyright 2014, Elsevier]

2.3. Adsorption of heavy metals by cryogels

2.3.1. Overview

Table 2.4 represents the review of the cryogels and some commercial adsorbents used for adsorption of heavy metals.

Table 2.4. The list of cryogels used for heavy metals removal from aqueous media with main adsorption parameters

Metal	Cryogel	Main functional groups	Predominant mechanism(s)	C_0 (mg/L)	q_e (mg/g)	pH	Ref.
Al^{3+}	p(HEMA)-P. chrysosporium	biosorption	Coordination	27	3.0	6.0	[155]
	Amberlite IR 120H (resin)	R-SO_3H	Ion exchange	100	118	5.0	[156]
Cu^{2+}	p(Jeff600-GA-DAH)	-NH_2 R-COOH	Chemisorption Physisorption	100	119	5.5	[103]
	p(Jeff600-GA)	-NH_2 R-COOH	Physisorption	80	55	5.5	[140]
	p(Jeff900-GA)	-NH_2 R-COOH	Physisorption	80	47	5.5	[140]
	p(Jeff2003-GA)	-NH_2	Physisorption	80	34	5.5	[140]

		R-COOH					
	p(GMA-His)	-OH -C=O	Coordinate-covalent bonding	600	5.6	5.5	[95]
	p(HEMA-VIM)/p(HEMA)	-OH -CH=CH_2	Chelation	20	2.5	5.5	[46]
	p(CHI-HEMA)	-NH_2 -OH -C=O	Chelation	100	66.3	6.0	[66]
	p(HEMA-MAH)/MIP-Cu	-NH_2 -C=O -NH	Chemisorption	60	77.2	6.0	[49]
	p(HEMA-MAH)/MIP-Cu-Fe_2O_3	-NH_2 -C=O -NH	Chemisorption	60	182.7	6.0	[49]
	p(HEMA-GMA)-PEI-MIP-Cu	R-COOR -OH	Electrostatic interaction	120	1.21	5.5	[99]
	p(AA-MAAc-AAm)	-COOH -NH_2 -C=O	Metal complexation	64	630	4.0	[97]
	p(HEMA)-P. chrysosporium	biosorption	Coordination	63.5	24.1	6.0	[155]
	p(PVA-CMC)	-OH -COOH	Ion exchange	100	5.5	-	[68]
	Scolecite	-	Ion exchange	30	4.1	6.0	[157]
	Clinoptilolite	-	Ion exchange	200	5.9	5.0	[158]
	Clinoptilolite	-	Ion exchange	310	11.7	4.0	[159]
	Clinoptilolite	-	Ion exchange	-	0.7-8.9	-	[160]
	Clinoptilolite	-	Ion exchange	800	12.9	6.2	[161]
	Activated carbon	-	Adsorption	20	22.7	5.0	[162]
Fe^{2+}	p(HEMA)-P. chrysosporium	biosorption	Coordination	55.8	5.6	6.0	[155]
	Lewatit TP 207 (resin)	-NH -OH	Ion exchange	5.34	17.1	6.0	[163]
	Amberlite IR 120H (resin)	R-SO_3H	Ion exchange	100	18.5	5.0	[156]
	Activated carbon	-	Adsorption	20	62.5	5.0	[162]
Fe^{3+}	Clinoptilolite	-	Ion exchange	182	5.6	2.0	[159]
UO_2^{2+}	p(AN)	-C≡N -CH=CH_2	Chelation	6.8	1.8	7.8	[141]

Pb^{2+}	p(GMA-His)	-OH -C=O	Coordinate-covalent bonding	600	6.9	5.0	[95]
	p(HEMA-VIM)/p(HEMA)	-OH $-CH=CH_2$	Chelation	20	7.6	5.5	[46]
	p(AAm)/TiO_2	$-NH_2$ -C=O	Ion exchange	100	23.3	5.5	[164]
	p(AA-DMAAm-AAc)-ThU	-COOH $-NH_2$ -C=O	Ion exchange Metal complexation	400	164.3	7.0	[129]
	Scolecite	-	Ion exchange	30	5.8	6.0	[157]
	Amberlite IR 120 (resin)	$R-SO_3H$	Ion exchange	20	3.9	5.0	[165]
	Clinoptilolite	-	Ion exchange	1000	101.5	4.0	[159]
	Clinoptilolite	-	Ion exchange	-	23-124	-	[160]
	Clinoptilolite	-	Ion exchange	800	13.9	6.2	[161]
	Activated carbon	-	Adsorption	20	23.5	5.0	[162]
Zn^{2+}	p(GMA-His)	-OH -C=O	Coordinate-covalent bonding	600	4.2	5.0	[95]
	p(CHI-HEMA)	$-NH_2$ -OH -C=O	Chelation	100	57.6	6.0	[66]
	p(HEMA-VIM)/p(HEMA)	-OH $-CH=CH_2$	Chelation	4.3	7.6	5.5	[46]
	p(PVA-CMC)	-OH -COOH	Ion exchange	100	5.3	-	[68]
	p(HEMA)-P. chrysosporium	biosorption	Coordination	65.4	7.9	6.0	[155]
	Lewatit TP 207 (ion exchange resin)	-NH -OH	Ion exchange	17.1	32.7	6.0	[163]
	Scolecite	-	Ion exchange	15	2.1	6.0	[157]
	Clinoptilolite	-	Ion exchange	200	3.4	6.0	[158]
	Clinoptilolite	-	Ion exchange	-	3.2-24	-	[160]
	Activated carbon	-	Complexation Ion exchange	20	11.7	5.0	[162]
Cd^{2+}	p(GMA-His)	-OH -C=O	Coordinate-covalent bonding	600	6.4	5.0	[95]
	p(HEMA-MAC)	-NH -COOH -SH	Metal complexation	100	0.5	-	[151]

		-C=O					
	p(HEMA-MAC)	-NH -COOH -SH -C=O	Chemisorption	20	0.01	6.0	[94]
	p(HEMA-MAC)/MIP-Cd	-NH -COOH -SH -C=O	Chemisorption	20	0.03	6.0	[94]
	p(HEMA-MAC)/MIP-Cd	-NH -COOH -SH -C=O	Metal complexation	100	3.0	-	[151]
	p(PVA-HA)	-OH PO_4	Metal complexation	100	53.2	6.0	[65]
	p(HEMA-VIM)/p(HEMA)	-OH $-CH=CH_2$	Chelation	20	5.8	5.5	[46]
	p(AAm)/TiO_2	$-NH_2$ -C=O	-	10	11	4.0	[67]
	p(HEMA)-P. chrysosporium	biosorption	Coordination	112.4	16.8	6.0	[155]
	Scolecite	-	Ion exchange	15	0.4	6.0	[157]
	Amberlite IR 120 (resin)	$R-SO_3H$	Ion exchange	20	3.9	5.0	[165]
	Clinoptilolite	-	Ion exchange	200	4.6	6.0	[158]
	Clinoptilolite	-	Ion exchange	-	0.3-10.7	-	[160]
	Clinoptilolite	-	Ion exchange	80	2.1	6.2	[161]
	Activated carbon	-	Complexation Ion exchange	20	15.1	5.0	[162]
Co^{2+}	p(AMPS)	SO_3H-	Ion exchange	500	91.7	4.0	[91]
	p(AA-MAAc-AAm)	-COOH $-NH_2$ -C=O	Metal complexation	59	590	4.0	[97]
	p(HEMA)-P. chrysosporium	biosorption	Coordination	58.9	5.3	6.0	[155]
	Scolecite	-	Ion exchange	15	0.9	6.0	[157]
	IRN 77 (resin)	$R-SO_3H$	Ion exchange	150	75	5.3	[166]
	Clinoptilolite	-	Ion exchange	-	13.2	-	[160]
Ni^{2+}	p(AMPS)	SO_3H-	Ion exchange	500	84.3	4.0	[91]

	p(PVA-CMC)	-OH -COOH	Ion exchange	100	6.0	-	[68]
	p(AA-MAAc-AAm)	-COOH -NH_2 -C=O	-	58	580	4.0	[97]
	p(IM-AA)	-NH_2 =CH_2	Metal complexation	410	3.5	5.3	[167]
	p(HEMA)-P. chrysosporium	biosorption	Coordination	58.7	12.9	6.0	[155]
	Lewatit TP 207 (resin)	-NH -OH	Ion exchange	0.395	1.2	6.0	[163]
	IRN 77 (resin)	R-SO_3H	Ion exchange	150	50	4.8	[166]
	Scolecite	-	Ion exchange	30	0.9	6.0	[157]
	Clinoptilolite	-	Ion exchange	200	2.0	6.0	[158]
	Clinoptilolite	-	Ion exchange	-	0.5-5	-	[160]
	Clinoptilolite	-	Ion exchange	800	6.5	6.2	[161]
	Activated carbon	-	Adsorption	20	12.0	5.0	[162]
Ca^{2+}	p(CHI-HEMA)	-NH_2 -OH -C=O	Metal complexation	100	48.7	6.0	[65]
	Lewatit TP 207 (resin)	-NH -OH	Ion exchange	6.7	12.4	6.0	[163]
Cr^{6+}	p(CHI-DMAEMA)/ Fe_3O_4	-N-R2 -NH_2 -OH	-	0.25	14.2	-	[143]
	p(CHI-VAm)/VBTACl	-NH_2 -OH =CH_2	Chemisorption	1000	317	5.5	[104]
	p(CHI-VAm)	-NH_2 -OH =CH_2	Chemisorption	1000	225	5.5	[104]
Cr^{3+}	p(HEMA)-P. chrysosporium	biosorption	Coordination	52	7.3	6.0	[155]
	IRN 77 (resin)	R-SO_3H	Ion exchange	150	75	3.5	[166]
	Clinoptilolite	-	Ion exchange	200	4.1	4.0	[158]
	Clinoptilolite	-	Ion exchange	170	6.8	3.0	[159]
As^{3+}	p(CHI-DMAEMA)/ Fe_3O_4	-N-R2 -NH_2	-	0.2	11.5	-	[143]

		-OH					
	p(HEMA-PEGDA)/Fe_2O_3	-COOH R-COOR -OH	Metal complexation	2	2.7	7.0	[125]
	p(HEMA-PEGDA)/Fe_3O_4	-COOH R-COOR -OH	Metal complexation	4	3.1	7.0	[125]
	p(APTMACl)/Fe	-NH -C=O	Ionic interaction Ion exchange	100	140	-	[93]
	p(AAm)/$Fe(OH)_3$-$Al(OH)_3$	-NH_2 -C=O	Chemisorption	100	24.6	4-11	[168]
	p(AAm)/$Fe(OH)_3$-$Al(OH)_3$	-NH_2 -C=O	Chemisorption	1	82.3	7.0	[169]
As^{5+}	p(AAm)/Fe	-NH_2 -C=O	Electrostatic interaction	100	50	7.0	[50]
	p(AAm)/$Fe(OH)_3$-$Al(OH)_3$	-NH_2 -C=O	Chemisorption	1	49.6	7.0	[169]
	p(AAm-D_3AAm)/ Al_2O_3	-NH_2 -C=O	Metal complexation	5	6.0	7.0	[64]
	p(AAm-AA)-SH	-NH_2 -C=O	Chelation/ coordination	60	2.0	7.0	[90]
	p(AAm-AA)-MIP	-NH_2 -C=O	Chelation/ coordination	60	20.6	7.0	[90]
	p(AAm-AA)-Al-NP	-NH_2 -C=O	Chelation/ coordination	60	20.3	7.0	[90]
	p(APTMACl)/Fe	-NH -C=O	Ionic interaction Ion exchange	400	118	9.3	[100]
Ag^{+}	p(HEMA-MAC)MIP-Ag	-NH -COOH -SH -C=O	Ionic interaction	20	49.3	4.0	[170]
Hg^{2+}	PEI	-NH	Ionic interaction	100	1280	7.0	[171]
	p(HEMA)-chrysosporium	P. biosorption	Coordination	200	75.2	6.0	[155]
	p(CHI-PVA)	-NH_2 -OH -C=O	Ionic interaction Ion exchange	2069	585.9	5.5	[172]

Purolite S-920 (resin)	$-NH_2$ -S	Chelation/ coordination	-	361.0	4.0	[173]
Rohm & Haas GT-73 (resin)	-SH	Ion exchange	-	722.1	6.0	[173]

C_0 - Initial aqueous phase concentration

q_e - Adsorption capacity

The presented in the **Table 2.3** results show that adsorption capacities of major cryogels are no less than commercial adsorbents. As an example, sorption capacities of some cryogels and commercial zeolites, ion-exchange resins and activated carbons will be compared below. Elbarbary et al. synthesized p(CHI-HEMA) cryogel and tested for the removal of Ca^{2+}, Cu^{2+} and Zn^{2+} from aqueous solutions. The p(CHI-HEMA) sample reached the maximum capacity of 48.7 mg/g for Ca^{2+}, 66.3 mg/g for Cu^{2+} and 57.6 mg/g for Zn^{2+} by chelation mechanism [66]. In another study, Cimen et al. used the synthesized poly-L-histidine modified p(GMA) cryogenic polymer to remove a number of cationic heavy metals. The adsorption results showed that p(His-GMA) cryogel was able to remove up to 7 mg/g for Pb^{2+} and Cd^{2+}, about 6 and 5 mg/g for Cu^{2+} and Zn^{2+}, respectively [95]. For comparison, the Kocaoba [165] tested the Amberlite IR 120H ion exchange resin (manufactured by Rohm and Haas) with respect to the removal of Pb^{2+} and Cd^{2+} from water. The investigated resin showed only 4 mg/g removal of both metal ions. The another ion-exchange resin TP 207 (Lanxess Lewatit Resins) was tested by Silva et al [163], where authors the maximum adsorption of Fe^{2+}, Zn^{2+}, Ni^{2+} and Ca^{2+} reached 17.1, 32.7,1.2 and 12.4 mg/g, respectively. Other commercial adsorbents widely used in the treatment of wastewater contaminated with heavy metals are natural zeolites [160]. Sprynskyy et al. tested a zeolite from Ukraine which has a maximum capacity of 13.9 mg/g of Pb^{2+} [161], whereas a Greek clinoptilolite exhibited significantly higher efficiency for an ion of the same metal - 101.5 mg/g [159]. The high effectiveness of Hg^{2+} removal was publicized by Lloyd-Jones et al. [173], where Purolite S-920 and Rohm & Haas GT-73 ion-exchange resins reached 722 mg/g, while Purolite S-920 capacity was twice lower. However, comparing these data with cryogels, PEI and p(CHI-co-PVA) have a sorption capacity of 1280 and 585.9 mg/g, respectively [171,172].

To increase the adsorption of heavy metals, cryogels can be modified by various nanoparticles. Suresh Kumar et al. [169] embedded iron and aluminum oxides to the p(AAm) cryogels to improve sorption of As^{3+} and As^{5+} ions from water. The results of the extended

X-ray absorption fine structure of (EXAFS) showed that As^{3+} forms a mononuclear complex with iron ions, while As^{5+} binds to aluminum ions in a dual-core complex or to single-core iron ions.

To improve the selectivity and adsorption capacity, metal-imprinted polymer (MIP) modification can be applied. Tabakli et al. produced Cd-MIP and non-ion imprinted cryogels (NIP) by free-radical polymerization of HEMA and MAC monomers. The obtained results indicated that the ion-imprinted p(HEMA-MAC)/MIP-Cd composite was capable to adsorb 32.2 μg/g of Cd^{2+} while the non-modified one removed two times less [94]. Jallilzadeh et al. fabricated p(HEMA-MAH)/Cu^{2+}-MIP cryogels and modified them with Fe_2O_3 for effective elimination of Cu^{2+} from water media [49]. It was found that magnetic nanoparticles additionally improve the removal capacity of MIP cryogels. The quantity of adsorbed Cu^{2+} ions by non-magnetic-MIP cryogels was 77.2 mg/g while the magnetic-MIP cryogel reached 182.7 mg/g. The p(CHI-HEMA) cryogel achieved a capacity of 48.7 mg/g for Ca^{2+}, 66.3 mg/g for Cu^{2+} and 57.6 mg/g for Zn^{2+} mainly by chemical chelation with functional groups of the cryogel.

2.3.2. Heavy metals removal mechanism on cryogels

Understanding the mechanism of removal is necessary for further research on the process of removing heavy metals on various sorbents. However, the elucidation of removal mechanisms of heavy metals on cryogels is a stimulating chore and literature is usually overtaking the subject perfunctorily. Different adsorption mechanisms such as physisorption, including electrostatic interaction and attraction by van der Waals forces, chemical sorption as chelation, metal coordination and complexation (**Fig. 2.9**) and ion-exchange (**Fig. 2.10**) or a combination of several of these mechanisms have been discussed in the literature [97,174–176].

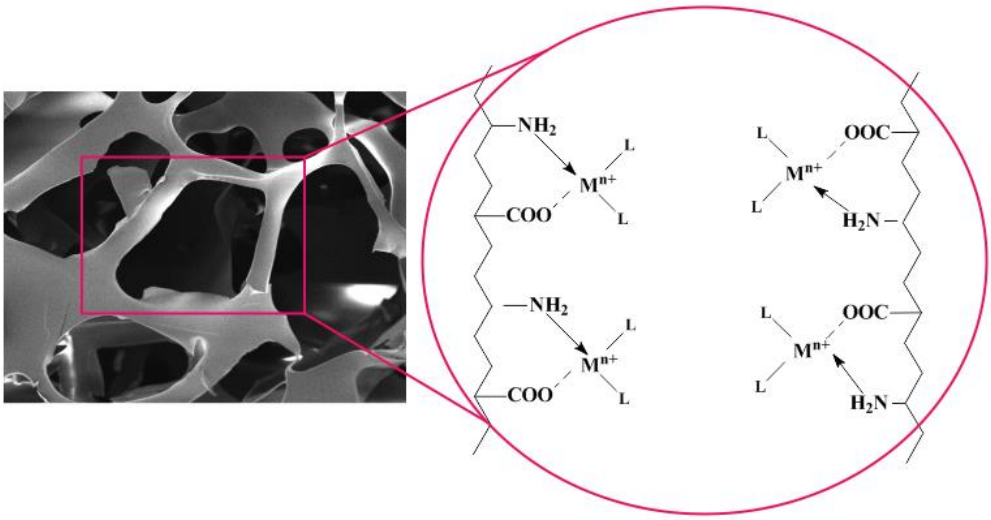

Fig.2.9. Schematically representation of metal-polymer complexes in cryogel pores [Reprinted with permission from Ref. [149]. Copyright 2020, Elsevier]

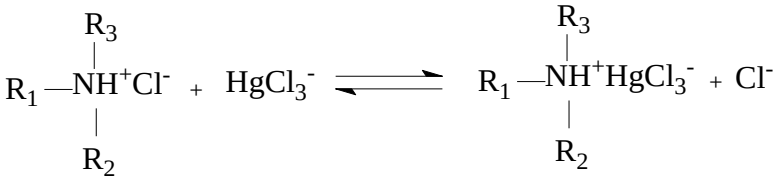

Fig. 2.10. Reaction of Hg(II) ions with amino group [Reprinted with permission from Ref. [149]. Copyright 2020, Elsevier]

The adsorption mechanism of heavy metals by the macroporous cryogels depends on the chemical composition of the adsorbents and classically comprises more than one mechanism [177]. The selective sorption on polymers toward heavy metals ions is influenced by several factors relevant to the physicochemical properties of the surfaces, including the functional groups, chelating agents, surface charge and active components as nanoparticles. Surface functional groups reactions are the dominant factor when it comes to selectivity and capacity [52,54,63]. For instance, amino-functionalized materials are sufficient for the removal of both anionic and cationic species of metals; the elimination of anionic species is achieved via electrostatic interaction [87], ion exchange or hydrogen bonding [48,178,179], whereas the removal of the cationic species is achieved via coordination with the amino groups [85].

Erol and Uzun synthesized PEI modified p(HEMA-GMA) cryogel via co-polymerization with methacryloyl benzotriazole to prepare Cu-MIP cryogel [99]. PEI ligand attracted the Cu^{2+} ions, but the process was strongly depended on pH of the solution because of precipitation of Cu^{2+} ions as hydroxides at the alkaline environment and the adverse effects of acidic environment on the coordinate covalent interaction [99]. Tatykhanova with co-authors discussed in more details the mechanisms of the metals removal by synthesized amphoteric cryogels based on acrylic acid and allylamine [97]. Acrylic acid and methacrylic acid monomers have carboxyl functional groups, while allylamine has amine groups. The pK_a of the carboxyl group of acrylic acid and methacrylic acid is about 4.26 and 4.88, respectively, while $-NH_2$ group is 5.44. At pH values higher than the pK_a, carboxyl groups are ionized, so these monomers can attract cationic metal species through electrostatic interactions. Also, oxygen atoms of carboxyl groups can donate paired electrons to cations and form complexes. Possible reaction paths of metal ions with carboxylic groups via ion-exchange of H^+ followed by chelation are shown in **Fig. 2.11**.

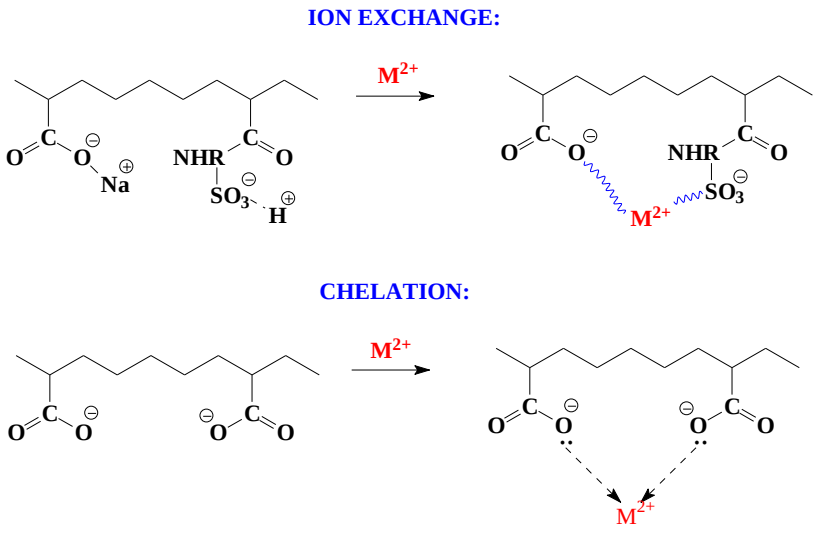

Fig. 2.11. Possible ion-exchange and chelation of metal ions with carboxylic groups [Reprinted with permission from Ref. [149]. Copyright 2020, Elsevier]

Tatykhanova et al. stated that Co^{2+}, Ni^{2+} and Cu^{2+} ions form coordination and ionic bonds with amine and/or carboxylic groups of polymers when water solutions of metals pass through the polymers [97]. Tekin et al. synthesized a p(HEMA) cryogel composite having

p(HEMA-VIM) particles for elimination of bivalent cations (Pb, Cd, Zn and Cu) from water and observed that removal mechanism was covalent bonding. Because of Lewis base character of the nitrogen atoms in the hetero-aromatic ring of VIM monomer, the imidazole group can definitely create coordinated covalent bonds with selected metal ions via N atoms [46].

2.3.3. The effect of pH on adsorption

The pH has critical effect on the removal of heavy metal from the aqueous phase, as some metal ions, for example Cu^{2+}, can be found in the aqueous phase in numerous soluble and insoluble ionic forms. At pH higher than 5, the $Cu(NO_3)_2$ precipitates as insoluble $Cu(OH)_2$ while at pH range between 2 and 5 copper ions are predominant in Cu^{2+} and some $Cu(OH)^+$ ionic forms (**Fig. 2.12**) [103,146].

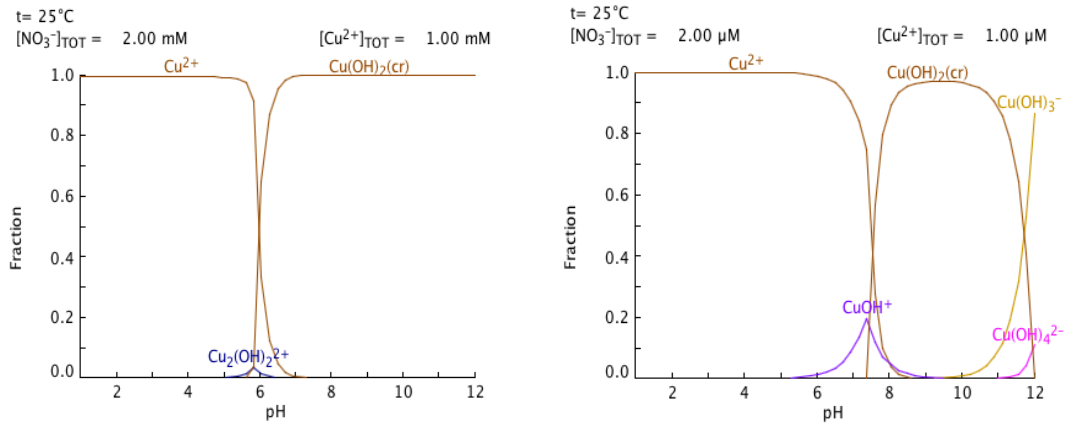

Fig. 2.12. Water phase speciation of $Cu(NO_3)_2$ with Cu^{2+} concentration of 1 mM (left) and 1 um (right). [Reprinted with permission from Ref. [149]. Copyright 2020, Elsevier]

The effect of the pH on the removal of metal ions was presented in **Fig. 2.13** on the example of jeffamine-based cryogels p(Jeff600-GA-DAH). Adsorption of Cu^{2+} ions by the cryogel increased with increasing of the pH. The maximum equilibrium removal capacity for Cu^{2+} ions at pH 5.5 was 118 mg/g. At pH<5.5, Cu^{2+} ions were present as the prevailing species leading to lower adsorption at low pH associated with the competitive adsorption between H^+ and Cu^{2+} ions. As the pH of the solution grew, the number of protons detached from the

functional groups of the polymer influence to the establishment of more metal/cryogel complexes [103]. Owning to the increase of $Cu(OH)_2^{2+}$ species at pH>5.5, removal rate reduced, which demonstrates narrow affinity to the cryogel surface.

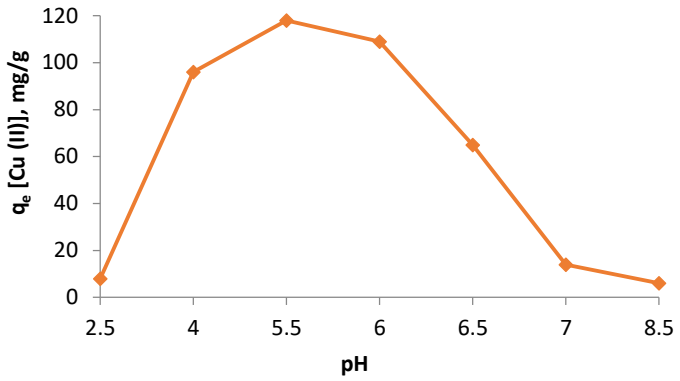

Fig. 2.13. Effect of pH on adsorption of Cu^{2+} by p(Jeff600-GA-DAH) [103]

Tekin et al. examined p(HEMA-VIM)/p(HEMA) cryogels for the adsorption of Pb^{2+}, Cu^{2+}, Zn^{2+} and Cd^{2+} metals at different pH [46]. It was observed that the removal capacity of polymers at pH 3 was in the range of 2-8 mg/g while at pH 4 increased by 5 times. Jalilzadeh et al. studied Cu^{2+} ions adsorption by cryogel at pH range 3-6. The increase of adsorption capacity from 2 to 8 mg/g at pH 6.0 was due to the deprotonation of the functional imidazole ring of MAH, causing enhanced Lewis base character [49]. Deprotonation also reduced the possible repulsive interactions between metal ions and protonated amino groups.

2.3.4. Regeneration and reusability of cryogels

In order to reuse cryogels, two important factors must be observed: reversible adsorption and chemical and / or physical stability of the material. Cryogels must be resistant to typical environmental conditions, chemically and physically stable, and resistant to microbiological degradation during continuous adsorption/desorption cycles. The effectiveness of regeneration and recovery cycles of some cryogels is shown in **Table 2.5**. Several aspects of recovery, such as the choice of an active regeneration solution, its type and concentration, the optimum time and volume of regeneration have not been systematically studied. A right regeneration solution should be inexpensive, relatively non-toxic, and simple in preparation

and storage. The main solutions for recovery are usually acids and/or bases, some of which are listed in **Table 2.5**.

Table 2.5. Efficiency of the regeneration of adsorbents.

Metal	Cryogel	Metal loading (mg/g)	Recovery cycles	Desorption agent	Recovery (%)	Regeneration duration (min)	Ref.
Cu^{2+}	p(Jeff600-GA)	55	3	0.01M HNO_3	56.3	-	[140]
	p(Jeff900-GA)	47	3	0.01M HNO_3	61.5	-	[140]
	p(Jeff2003-GA)	34	3	0.01M HNO_3	69.2	-	[140]
	p(GMA-His)	5.6	5	0.01M HNO_3	97	60	[95]
	p(HEMA-MAH)/MIP-Cu	77.2	5	5 M Na_2(EDTA)	96	180	[49]
	p(HEMA-MAH)/MIP-Cu-Fe_2O_3	182.7	5	5M Na_2(EDTA)	96	180	[49]
	p(HEMA-GMA)-PEI-MIP-Cu	1.21	5	HNO_3	97	-	[99]
Pb^{2+}	p(GMA-His)	6.9	5	HNO_3	97	60	[95]
Zn^{2+}	p(GMA-His)	4.2	5	HNO_3	97	60	[95]
Cd^{2+}	p(GMA-His)	6.4	5	HNO_3	97	60	[95]
	p(HEMA-MAC)	0.006	10	0.1M HNO_3	74.4	120	[94]
	p(HEMA-MAC)/MIP-Cd	0.032	10	0.1M HNO_3	84.1	120	[94]
Ag^{+}	p(HEMA-MAC)MIP-Ag	49.3	1	0.1 M EDTA	72.8	120	[170]

Erdem et al. showed that only three regeneration cycles are possible for p(Jeff600-GA) as it significantly loses its adsorption capacity. They achieved only 56% of the recovery, which is most probably related to precipitation of copper hydroxide on the surface of the material. A more effective regeneration solution would be a solution of hydrochloric acid achieving nearly 100% of metal recovery due to complete protonation of amino groups. Jallilzadeh et al. used Na_2(EDTA) as desorption agent to regenerate Fe-MIP and non-composite cryogels after adsorption of Cu(II) ions. Chemical analysis confirmed that after three adsorption-desorption cycles there were not any iron release and desorption of Cu^{2+} ions was over 96% in all cases [49]. Cimen et al. produced a p(GMA-His) cryogel, which showed rapid adsorption of bivalent Pb, Cd, Zn and Cu ions from water solutions. The p(GMA-His) was regenerated using 0.1 M HNO_3, and after five cycles of adsorption-desorption the regeneration ratio was at the level of 97% for all studied metals that indicate the reusability of studied polymers [95].

2.4. Advantages of cryogels over other adsorbents

A variety of adsorbents based on lignin [180,181], tannin [182,183], chitin [184], zeolite [185–187], clay, by-products of agricultural industry, activated carbons [188,189], carbon nanotubes [190,191] and synthetic polymers [192–194] have been used for elimination of heavy metals from aqueous solutions. The aforementioned adsorbents are typically highly porous, and the adsorption occurs on specific sites on the large surface area within the particles [176,195,196]. Depending on the interaction between the adsorbent and the adsorbate, adsorption is categorized as physical and chemical adsorption. Physical adsorption (physisorption) is a result of the attraction of a substance on the solid surface by van der Waals forces. Physical adsorption occurs as mono- or multi-layer and is reversible. Chemical adsorption (chemisorption) takes place when there is a chemical interaction between functional groups of the materials and adsorbate. This type of adsorption is mono-layered and not reversible adsorption [197]. Another mechanism of removal is the ion-exchange, based on the exchange of ions between the solution phase and the solid matrix. The combination of the above mechanisms may happen to rely on the nature of the adsorbent and adsorbate [198].

For porous materials, the leading property associated with adsorption is the specific surface area, which defines the capacity of the adsorbent. Porous adsorbents such as activated carbons usually have a high surface area, from hundreds to thousands of m^2/g [199,200] while the surface area of cryogels is typically between 5-106 m^2/g [49,99,129,201] similar to natural zeolites and other aluminosilicate materials. However, the absence of a complex porous structure is advantageous when it comes to kinetics due to the lack of restrictions of diffusion in micropores. This might be very crucial for specific applications when rapid adsorption is required. Also, cryogels have open-ended pores which contribute to the fast diffusion in contrast to the closed-end pores of traditional porous materials [52,53,96]. The relatively low surface area can be compensated with a high number of active sites distributed on the cryogel walls and also the adaptability of cryogels as the surface can be easily modified by additional functional groups and ligands, which can expressively contribute to the efficiency and selectivity [41,46,52,55,67,80,95]. Moreover, hydrogels and cryogels have the ability to enlarge their structure due to their high swelling capacity [91,92]. Thus, they can absorb water very fast, resulting in the rapid removal of toxic water spillages or small amounts of poisonous water in soils. The rapid absorption of water improves the

release of toxins as the absorbed water brings them in contact with the surface-active sites [93,124,150,202].

An additional benefit of cryogels is that they can be produced in various sizes and shapes like beads, sheets and columns (**Fig. 2.12**) [203–205]. This flexibility is highly desirable when the material is paced into filtering devices. Also, they can form composites with different materials, such as activated carbons [206–208], zeolites [209] and nanoparticles [49,64,164,170] for obtaining a number of desired properties.

Fig. 2.12. Cryogels prepared in different formats [Reprinted with permission from Ref. [210]. Copyright 2008, Elsevier]

Due to highly macroporous structure with open pores up to hundreds of microns and interconnected flow channels, cryogels in the form of monoliths could be preferred as an adsorbent for the removal of pollutants even at high viscosity and high flow rates. With these structural features, the contaminants could easily be transferred into the polymeric network without any limitations and backpressure [94]. For instance, Plieva et al. designed and prepared macroporous gel monoliths with embedded molecularly imprinted particles packed in the special plastic housings (**Fig. 2.13**) [203]. This plastic housing protects cryogels from mechanical destruction without any loss of adsorption properties and structural changes while unique design on the polymer increases the flow rate of the polluted solutions [203].

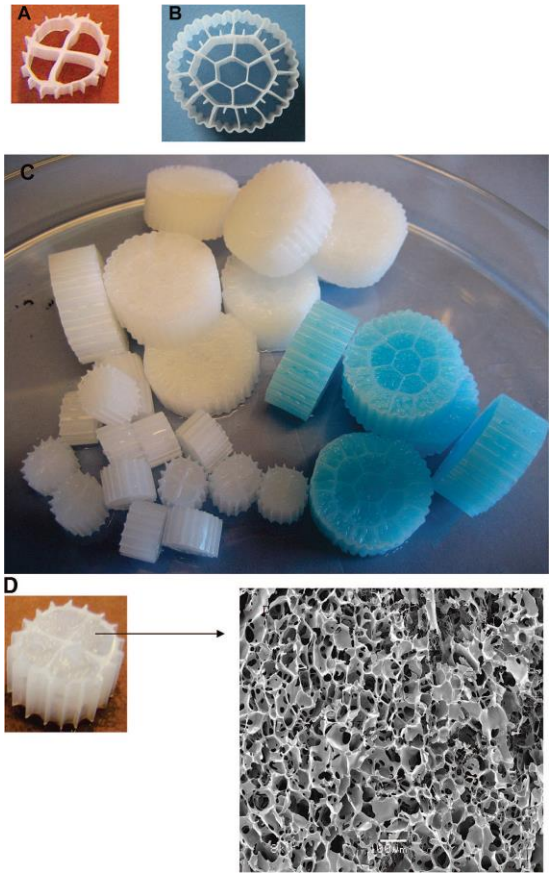

Fig 2.13. The plastic Kaldnes carriers (A) and (B), macroporous gels formed inside the carriers (C) and SEM image of formed macroporous gel (D). [Reprinted with permission from Ref. [211]. Copyright 2008, American Chemical Society]

CHAPTER 3

MATERIALS, SYNTHESIS, AND CHARACTERIZATION

3.1. Materials

For synthesis of cryogels the mentioned monomers and reagents were used: N,N-dimethylacrylamide (DMAAm, 99%), N,N-Methylenebisacrylamide (BisAAm, 99%), allylamine (AA) (98%), methacrylic acid (MAAc) (99%), 2-acrylamido-2-methyl-1-propanesulfonic acid (AMPS), 70 % H_3PO_4, 5M NaOH, ammonium peroxodisulfate (APS, 98%) and N,N,N′,N′-Tetramethyl ethylene diamine (TEMED, ≥99.5%). For the modification and adsorption experiments $HgCl_2$ (≥99.0%), $Hg(NO_3)_2$ (≥99.0%), $Cd(NO_3)_2$ (>98%), $Sr(NO_3)_2$ (≥99.0%), $CsNO_3$ (99.99%), $AgNO_3$ (≥99.0%) and KI (≥99.5%) chemicals were used. All reagents were purchased from Sigma-Algrich (Germany). For the in vivo animal studies, the same metal salts were used, while as a reference material Unithiol (sodium dimercaptopropane sulfonate) (Ellara, Russia) were purchased at a pharmacy. The concentration of the active substance (sodium dimercaptopropane sulfonate) in 1 mL ampule of Unithiol is 50 mg. All solutions for synthesis and experiments were done on ultra-pure water, purified using a Puris MR-RO1600 (Mirae ST, South Korea) reverse osmosis unit.

3.2. Synthesis of cryogels

The AAC and SAC cryogels were synthesized by free-radical polymerisation technique by BisAAm cross-linking in degassed ultra-pure water [47]. The preliminary degassed ultra-pure water was prepared by purging nitrogen gas for 30 min to remove dissolved oxygen. Quantities of the reagents used for AAC and SAC cryogels synthesis are provided in **Table 3.1**. Briefly, MAAc or AMPS for AAC and SAC cryogels, respectively and BisAAm were added to degassed water under vigorous stirring to achieve complete solubilisation followed by alkalinisation by 5M NaOH to neutralise the acid. The other flask contains monomers of DMAAm and AA were dissolved in degassed water under continuous stirring and acidified by adding concentrated H_3PO_4 to convert allylamine into a phosphate salt. Subsequently, after mixing these two separately prepared solutions together and the degassing was carried out for 30 min, TEMED was added dropwise and cooled down to 2-4 °C for 30 minutes under nitrogen atmosphere followed by the addition of 5 wt% of APS

under stirring. Finally, 2 mL of the monomeric mixture was poured into plastic syringes of 1 cm of diameter. The syringes were rapidly sealed to avoid dissolution of oxygen from the air in the solution and to prevent inhibition of radical polymerisation and syringes were immersed in ethanol cooled cryobath having a program-controlled refrigerated bath (Julabo F34, Germany) and kept at -12°C for 24 hours. The obtained monolithic cryogels were thawed out in warm water (23-25°C) and washed firstly with 1 % ethanol and then with 2 L of pure water. For further characterization and experiments, both types of cryogels were freeze-dried on FreeZone 2.5L (Labconco, USA) instrument via lyophilization technique at −53 ◦C and under vacuum (0.4 mbar) for 48 h in order to remove water.

Table 3.1. Mass composition of AAC and SAC cryogels

	AAC	SAC
BisAAm, g	0.2186	0.1395
MAAc, mL	0.4125	-
AMPS, g	-	0.5644
DMAAm, g	0.3445	0.372
AA, mL	0.300	0.200
5M NaOH, mL	1.2	0.42
H_3PO_4, mL	0.1373	0.092
5% APS, mL	0.25	0.25
TEMED, mL	0.0155	0.0155
H_2O, mL	17.3	17.5

3.3 Modification of cryogels by silver nanoparticles

For modification purpose, both types of dry cryogel in the form of monoliths with a mass of 80 mg were placed in a 100 mL solution of $AgNO_3$, containing 140 ppm of Ag for three days by shaking at 100 rpm. The resulting cryogel composites were hereafter called AAC-Ag and SAC-Ag, respectively. The initial and remaining concentrations of silver ions in the solutions were analyzed by AAnalyst 400 (Perkin Elmer, USA) atomic absorption spectrometer. The amount of impregnated silver was calculated using Eq.3.1:

$$q_{eq} = \frac{C_o - C_f}{m} \times V \quad (3.1)$$

where q_{eq} is the amount of adsorbed Ag^+ (mg/g), C_o and C_f are concentrations (mg/L) of silver in the initial and final solutions, respectively, V and m are the volume of solution (L) and mass of the cryogel (g) were taken for experiment. Blank experiments, with the same initial concentration of silver and volume without solids, showed that the Ag^+ losses due to adsorption on tube walls were less than 2%. All modification experiments were carried out in duplicate, and the standard deviation was less than 2%.

3.4 Characterization and analysis techniques

Both types of parent and Ag-modified cryogels were characterized by several morphological and physicochemical techniques and methods before and after metal ions adsorption experiments.

3.4.1 Fourier Transform Infrared (FTIR) spectrometer characterization

The presence of the functional groups in the structure of cryogels before and after adsorption of metal ions the Cary 600 Series (Agilent Technologies, US) FT-IR spectrophotometer equipped with a diamond attenuated total reflection (ATR) accessory was used. The preliminary lyophilized and crushed into fine powder samples were used and infrared spectra were recorded for the sum of 32 scans in the range of 4000–400 cm^{-1} at a resolution of 4 cm^{-1} at room temperature with duplication of measurements.

3.4.2 Microscopic characterization

3.4.2.1 Optical microscopy

The confocal optical microscope CLSM 780 (Carl Zeiss, Germany) was used to obtain colour optical images of liver and kidney structure of rats used in animal studies.

3.4.2.2 SEM/EDS

The structural morphology of polymers was investigated by Scanning Electron Microscope (SEM) at 3-10 kV, equipped with a backscattered electron detector (Zeiss Crossbeam 540, Germany). The spot and mapping elemental composition of materials were analyzed by an Energy-Dispersive X-ray (EDS) spectrometer (INCA X-sight, Oxford Instruments) connected to SEM.

3.4.2.3 TEM/EDS

To determine the size of silver nanoparticles in the modified cryogels, the preliminary crushed into the fine powder samples were suspended in a solution of alcohol and treated with ultra-sonication to avoid the agglomeration of the dissolved particles. A 10 μL drop of the suspension was placed on a 300-mesh carbon-coated copper grid to dry the sample overnight. The sizes and structure of nanoparticles were examined by a high-resolution transmission electron microscope (TEM) (JEM-2100 LaB6 HRTEM, JEOL, Japan) operating at 200 kV. The connected to TEM, an Oxford X-Max 100 Silicon Drift Energy Dispersive X-ray spectrometer was used for elemental analysis of nanoparticles.

3.4.3 X-ray characterization

3.4.3.1 X-Ray Diffraction (XRD)

The X-Ray Diffraction (XRD) technique was used to acquire data on the phase composition of silver nanoparticles before and after iodide adsorption on the surface of cryogel composites. The XRD pattern was identified by X-Ray diffractometer (Rigaku SmartLab, Japan) having HyPix-3000 high energy resolution 2D HPAD detector. The materials were scanned in the range of 5 to 70° with a diffraction angle of 2θ at 40 kV and 40 mA.

3.4.3.2 X-ray photoelectron spectroscopy (XPS)

X-ray photoelectron spectroscopy (XPS) measurements were conducted on a VG-Microtech Mutilab 3000 device equipped with a 9 channeltrons hemispherical electron analyzer and X-ray radiation source with Mg and Al anodes. The binding energies (BE) were calibrated by a C1s core level at 284.8 eV as a reference.

3.4.4 Zeta Potential analysis

Zeta potential of the samples was studied by a batch equilibration method. A mass of 10 mg of polymer was immersed in 10 mL of aqueous solution at initial pH from 2 to 9 values adjusted by adding an appropriate amount 0.1M HCl and 0.1M NaOH keeping the ionic strength constant and equilibrated for 24 h by shaking at room temperature [85]. A Zetasizer Nano (Malvern, UK) was used to determine the zeta potential of cryogels from the electrokinetic data (zeta potential *vs* pH). All analyses were carried out in triplication at room temperature and the average results were presented.

3.4.5 Swelling studies

Cryogels were sliced into 10 mm diameter monoliths and used for determination swelling capacity. The initial weight, w_o (g) of cryogel was measured, and then it was immersed in a 200 mL taped-up glass flask containing ultra-pure water at room temperature. At particular time intervals, the polymer was withdrawn from the water, and its surface was gently wiped to remove excess water and weighed to obtain the weight w at time t. The procedure was repeated until no significant change of weight was distinguished. The swelling degree was calculated by Eq. 3.2:

$$S = \frac{w - w_o}{w_o} \tag{3.2}$$

where S is the degree of swelling.

3.4.6 Metal ions determination techniques

3.4.6.1 Atomic absorption spectroscopy (AAS)

An atomic adsorption spectroscopy (AAS) instrument (AAnalyst 400 AA, Perkin Elmer, USA) operated with 7.5/2.5 mL/min acetylene/oxygen gas mixture was used for determination of metal ions applying suitable lamps. All water solutions were filtered through 0.45 μm hydrophilic syringe filters and acidified by 2% NHO_3. The calibration curve for each metal was performed with a minimum R^2 of 0.997. All measurements on AAS were done in triplicate.

3.4.6.2 Inductively coupled plasma mass spectrometry (ICP-MS)

The iCAP RQ ICP-MS analyser (Thermo Scientific, USA) was used to determine low-concentrations and ultra-low-concentrations of metal ions using argon plasma by detecting isotopic elemental concentrations using a hyperbolic quadrupole mass spectrometer. The sample preparation was the same as for AAS with appropriate dilution.

3.4.6.3 Ultraviolet-visible (UV-Vis) spectroscopy

An UV-Vis spectrophotometer (PhotoLab 6600, Germany) was used to quantitatively determine the iodide concentration of the initial and treated solution. The studied samples, with a volume from 100 μL to 300 μL and were diluted to 3 mL using ultrapure water in quartz cuvettes 10 mm wide

3.4.6.4 Mercury Analyzer

The RA-915M (Lumex, Russia) mercury analyzer was used for determination of the concentrations of mercury ions in water samples before and after adsorption experiments and in the rats' tissues after *in vivo* experiments. Depending on the initial concentration of mercury ions an aliquots of 0.02 to 0.1 mL of was samples from vessels and transferred to with filled by activated carbon quartz boats to measure the samples in pyrolysis furnace device of the RA-915M. The solid samples with known mass were put directly to the sample holder without activated carbon. The mercury detection limit is 0.5 ng/L in both water and solid phases. All adsorption experiments were done in duplicate, and the average results are presented.

3.4.7 Total nitrogen analysis

The total nitrogen of parent and mercury-containing cryogels was determined by DuMaster D-480 (Buchi, Switzerland) analyser according to the Dumas combustion method. Aspartic acid of purity ≥99.5 % (Sigma-Aldrich) was used for calibration of the instrument with an

average total nitrogen content of 9.8±1 %. The experiments were carried out in triplication and the average results presented.

3.4.8 Microwave digestion

In order to determine the Cd^{2+}, Sr^{2+} and Cs^{+} content in the animal tissues after in vivo studies the Multiwave Pro (Anton Paar, Austria) microwave digester was used. The preliminary lyophilized organs such as liver, kidney, stomach, omentum and duodenum were weighed and put into 16HF100 rotor vessels containing 5 mL of HNO_3 and 2.5 mL H_2O_2. The power controlled method of digestion of tissues was used, and experimental conditions are presented in **Table 3.2**. After digestion, the tissue-containing solutions were filtered through paper filters, diluted with ultra-pure water to 25 mL and kept for further studied on AAS instrument for metal amount quantification.

Table 3.2. The conditions of animal tissues digestion

Step	Temperature	Power	Time
Power ramp		600 W	15 min
Power hold		600 W	20 min
Cooling	70 C	0 W	

3.5 Adsorption studies of metal ions from aqueous solutions

3.5.1 Mercury removal studies

3.5.1.1 Adsorption kinetics of mercury

The mercury solutions were prepared by dissolving analytical grade $HgCl_2$ or $Hg(NO_3)_2$ in ultra-pure water. A volume of 100 mL of 100 ppm Hg^{2+} solution without pH adjustment was mixed with 0.08 g of cryogels in plastic tubes under shaking at 120 rpm at room temperature. After certain time intervals, 0.1 mL of sample was taken from the tubes for analysis. The total sampling volume was kept lower than 3% of the initial amount in all experiments. To determine the residual concentration of mercury ions in the solutions, an RA-915 M mercury

analyser (Lumex, Russia) was used. Blanks with the same initial concentration of mercury and volume without solids were measured. The amount of mercury adsorbed onto the polymers was calculated by a mass balance between initial and final solutions, expressed on a cryogel mass basis as Eq. 3.3.

$$q_{eq} = \frac{C_o - C_f}{m} \times V \tag{3.3}$$

where q_{eq} is the amount of metal ion adsorbed (mg/g), C_o and C_f are metal ion concentrations (mg/L) in the initial and final solutions, respectively, V the volume of solution (L) containing the metal ions, and m is the weight of the cryogel (g). Blank experiments showed that the Hg losses due to adsorption on tube walls no more than 3%. All experiments were carried out in duplicate, and the average experimental error was no more than 2%. The released sodium ions during mercury sorption were determined by AAS by use of AAnalyst 400 instrument (Perkin-Elmer, USA). The release of sodium ions from cryogels in the absence of mercury were done by placing 80 mg of dry cryogel in 100 mL of ultra-pure water under shaking at 120 rpm for 14 days. The release of Na^+ ions from both types of cryogels was no more than 1 mg/g.

3.5.1.2 Adsorption equilibrium isotherms of mercury

Equilibrium adsorption isotherms were obtained in the batch mode with the same mercury solutions as was used in kinetics mode by contacting 0.0025 to 0.1 g of cryogel with 100 mL of mercury solution on a Rotamax 120 (Heidolph, Germany) shaker at room temperature until equilibrium was reached. The attainment of equilibrium was monitored by sampling and measuring the residual mercury daily until no concentration change was observed. The pH and conductivity of initial and final solutions were measured with a SevenEasy pH and conductivity meters (Mettler Toledo, USA). The experiments were conducted in duplicate and averaged values with a standard deviation of no more than 3% are reported.

3.5.2 Cadmium, strontium and cesium removal studies

3.5.2.1 Adsorption kinetics of cadmium, strontium and cesium

The metal solutions were prepared by dissolving analytical grade $Cd(NO_3)_2$, $Sr(NO_3)_2$ and $CsNO_3$ in ultra-pure water. A volume of 100 mL of 100 ppm targeted metal solution without and adjusted to pH 4 was mixed with 0.07 g of cryogels in plastic tubes under shaking at 120 rpm at room temperature. At pre-determined time intervals, 0.1 mL of sample was taken from the tubes for analysis. The total sampling volume was kept lower than 3% of the initial volume in all experiments. To determine the residual concentration of metal ions in the solutions iCAP RQ ICP-MS analyser (Thermo Scientific, USA) with appropriate dilution was used. Blanks with the same initial concentration of metal ions and volume without solids were measured. The amount of metal ions adsorbed onto the polymers was calculated by Eq. 3. Blank experiments showed that all metal ions losses due to adsorption on tube walls no more than 2%. All experiments were carried out in duplicate and the average experimental error was no more than 2%. The released sodium ions during metal ions sorption were determined by Dionex ICS 6000 ion-chromatography instrument (Thermo Scientific, USA). The release of sodium ions from cryogels in the absence of metal ions were done by placing 70 mg of dry cryogel in 100 mL of ultra-pure water under shaking at 120 rpm for 30 days. The total release of Na^+ ions from both types of cryogels was no more than 1.3 mg/g.

3.5.2.2 Adsorption equilibrium isotherms of cadmium, strontium and cesium

All adsorption equilibrium isotherms of Cd^{2+}, Sr^{2+} and Cs^+ were carried out in 100 mL solution of the selected metal ion at three different parameters of the initial concentration of metal ions and loading of cryogels. In the first adsorption equilibrium isotherm experiment, the constant concentration metal ion (100 mg/L) under the dosage from 0.0025 to 0.07 g adsorbent was used. The second set of isotherm experiments were conducted by immersing 0.07 g of cryogels into 100 mL solution of metal ions with various initial concentrations from 100 to 1000 mg/L. The last series of experiments were done by adsorption of selected metal ions from 100 mL 1000 mg/L solution varying the mass of polymers from 0.1 to 0.9 g. All experiments were conducted at room temperature. The aliquots of 0.05 to 0.1 mL were collected from adsorption tubes and analyzed by ICP-MS, following the standard procedure of sample preparation. The experiments were done in duplicate, and the average values are presented.

3.5.3 Iodide removal studies

3.5.3.1 Adsorption kinetics of iodide

A volume of 100 mL of 100 ppm iodide solutions were prepared from analytical grade KI without pH adjustment and mixed with 80 mg of cryogels in plastic tubes under shaking at 120 rpm at room temperature. After certain time intervals, aliquots of 50-100 μL were taken from adsorption tubes and diluted to 3 mL to measure the remaining iodide concentration on UV–Vis spectrophotometer (PhotoLab 6600) at the range of 190-500 nm wavelengths with detection of iodide at 225-227 nm. The total sampling volume was no more than 2% of the initial volume in all experiments. The blank tubes with the same amount of KI without materials were also run, and the total adsorption of iodide on tubes walls was less than 1%.

3.5.3.2 Adsorption equilibrium isotherms of iodide

Equilibrium adsorption experiments were conducted by contacting Ag-cryogel composites varying the mass of sorbents from 0.01 to 0.1 g in 100 mL of 100 ppm KI solution by shaking in a Rotamax 120 (Heidolph, Germany) shaker at room temperature until reached the equilibrium. The initial and final concentrations of solutions were analyzed by UV-Vis spectrometer at 190 – 500 nm wavelengths, while pH and conductivity of those solutions were measured by SevenEasy pH and conductivity meters (Mettler Toledo, USA). The experiments were conducted in duplicate and averaged values with standard error no more than 3% are reported. The released sodium ions and adsorbed from KI solution potassium ions were detected by AAnalyst 400 atomic absorption spectroscopy apparatus (Perkin-Elmer, USA).

3.5.3.3 Real seawater studies

The real seawater was provided by a research water plant located at the University of Alicante, Spain. The seawater was collected from Mediterranean Sea of Alicante region, purified by filter paper and spiked with 131 mg of KI (100 ppm of iodide). Equilibrium experiments were conducted under the same conditions as in equilibrium studies with synthetic solutions (see Section 3.4.3.2). The seawater samples after the experiments were diluted and analyzed by using the 850 Professional IC Anion MCS ion chromatography

system (Metrohm AG, Switzerland). The spiked seawater had a pH of 7.42 and initial measured concentrations of anions as follows; 2.544 ppm of F^-, 943.48 ppm Cl^-, 0.042 ppm NO_2^-, 2.541 ppm Br^-, 106.66 ppm NO_3^-, 1468.34 ppm SO_4^{2-} and 98.63 ppm I^-.

3.5.3.4 AgI colloids formation studies

The AgI colloids formation experiments were done by adding dropwise 500 ppm solution of AgNO3 to 500 ppm solution of KI in Ag:I molar ratios from 1:20 to 1:400 under magnetic stirring at 200 rpm. The mixtures were left for 3 days to age and then scanned with UV–Vis spectrophotometer at wavelengths from 190 to 500 nm and analyzed by Zetasizer Nano (Malvern, UK) for determination of sizes and zeta potential of colloids.

3.5.4 Kinetic models

The kinetics of sorption from a solution onto an adsorbent has been explored theoretically to predict the adsorbent-adsorbate interactions. The sorption process obeys pseudo-first-order kinetics when the initial concentration of solute is higher than the adsorbent, while pseudo-second-order kinetics model assumes that the rate of adsorption of solute is proportional to the available sites on the adsorbent. The pseudo-first-order (Eq. 3.4) and pseudo-second-order models (eq. 3.5) were used for evaluation of cations, and anion adsorption at the solid-solution surface by matching the experimental data in linear equation expressed as [212,213]:

$$\ln(q_e - q_t) = \ln q_e - k_1 t \tag{3.4}$$

$$\frac{t}{q_t} = \frac{1}{k_2 q_e^2} + \frac{t}{q_e} \tag{3.5}$$

where q_e and q_t are amounts (mg/g) of metal ion adsorbed on equilibrium point and at specific time t (min), respectively; k_1 (min^{-1}) and k_2 (g mg^{-1} min^{-1}) are the pseudo-first-order and pseudo-second-order constants. The constant $k_1$and q_e^{cal} can be obtained from the slope and intercept of the linear plot of $\ln(q_e^{exp} - q_t)$ versus t. The values of k_2 and q_e^{cal} can be calculated from the linear fit of t/q_t versus t.

3.5.5 Isotherm models

In order to analyze the experimental isotherms Langmuir and Freundlich isotherm models are utilized, both widely used for the description of adsorption of heavy metals on the homogeneous or heterogeneous surfaces, respectively. The linear form of the Langmuir sorption isotherm [213,214] is:

$$\frac{C_e}{q_e} = \frac{1}{q_m K_L} + \frac{C_e}{q_m}, \; R_L = \frac{1}{1+K_L C_0} \tag{3.6}$$

where C_e (mg/L) is the equilibrium concentration of Hg^{2+} ions in solution, q_e and q_m are the equilibrium and maximum adsorption capacities in mg/g, whereas K_L is the Langmuir constant (L/mg). The R_L value is a dimensionless constant of Langmuir model ratifies the adsorption process to be linear ($R_L = 1$), favourable ($0 < R_L < 1$), unfavourable ($R_L > 1$) or irreversible ($R_L = 0$). The linear form of the Freundlich sorption isotherm is [215]:

$$log q_e = log K_F + \frac{1}{n} log C_e \tag{3.7}$$

where C_e (mg/L) and q_e (mg/g) is the concentration and adsorption capacity at the equilibrium and n (dimensionless) and K_F constants (units depend on the 1/n).

3.5.6 Leaching experiments

The evaluation of the retention of metal ions after adsorption and Ag-modification on the solids was performed in leaching experiments under neutral (pH 7.0) conditions. First, the cryogel samples that were used in the metal ions removal experiments were washed with 1 L of ultra-pure water to wash out the residual solution in the structure tightly closed containers were left for 14 days under shaking at 120 rpm at room temperature. The samples were withdrawn from each container and analyzed for leached metal ions. All the leaching experiments were carried out in duplicate and the average values are reported.

3.6 *In vivo* animal studies

3.6.1 Experimental animals

Seven-eight week-old male mongrel rats weighing 210 ± 20 g were purchased and kept in the vivarium at the Kazakh National Medical University (Almaty, Kazakhstan). The rats were placed separately in laboratory animal houses at 22–25 ºC with 50-55% humidity and 12 h light/dark cycle based on the Guidelines of the International Committee on Laboratory Animals. The rats were fed with a standard diet, allowed access to distilled water *ad libitum*.

3.6.2 Oral acute toxicity

All animal experiments were conducted in the laboratory of Experimental and Clinical Pharmacology of the Asfendiyarov Kazakh National Medical University (KazNMU) under the permission of the Local Ethical Committee of KazNMU (reg. №643).

Modeling of acute heavy mercury poisoning was carried out using solutions of $Cd(NO_3)_2$, $CsNO_3$, $Sr(NO_3)_2$, and $HgCl_2$ dissolved in saline. An acute oral study for calculating LD50 was performed according to the Organization for Economic Co-operation and Development (OECD) Guideline 425 ‘‘Up and Down procedure’’ [216]. In this method, animals are dosed once at a time. If the animal has survived, the dose for the next animal is increased; if the animal has died, the dose for the next animal is reduced.

The animals were observed for obvious behavioral, neurological, and toxic effects within 24 hours. The toxicological effect was assessed on the basis of mortality, which was expressed as an average lethal dose (LD_{50}) value. An LD_{50} for rats used in animal experiments is shown in **Table 3.3**.

Table 3.3. An average lethal dose (LD_{50}) of various metal salts for rats

$Cd(NO_3)_2$	LD_{50}	300 mg/kg	oral
$CsNO_3$	LD_{50}	2390 mg/kg	oral
$Sr(NO_3)_2$	LD_{50}	1982 mg/kg	oral
$HgCl_2$	LD_{50}	75 mg/kg	oral

Thirteen experimental groups, in a batch of 10 heads for each dose of metal and for the positive and negative control groups were used. To model acute intoxication with metal (all

metals were used separately), the LD50 dose of metal, recalculated for each animal weight, was introduced to studied animal by an atraumatic intragastric probe.

3.6.3 Treatment of intoxicated animals

The treatment of acutely intoxicated laboratory animals was done by AAC cryogels and unithiol antidote. The introduction of cryogels was done after 60 min of poisoning by the oral route through an atraumatic probe in the form of a suspension at doses of 250 mg/kg in a 15 mL saline solution. For the comparison, the commercial chelating agent – unithiol (was bought in a pharmacy) with a dose of 250 mg/kg body weight was used. Unithiol is a commercial name of 2,3-Dimercapto-1-propane sulfonic acid, the approved antidote for some heavy metal poisoning. The effectiveness of sorbents was estimated by the indicator of 24 h of survival. After 24 h the endured rats were euthanatized, and internal organs (liver, kidney, stomach, omentum, and duodenum were withdrawn for further analysis.

3.6.4 Histopathological examination

The preserved liver and kidneys of the animals from the control and treated by cryogel and unithiol groups were subjected to histological examination. The tissue samples were fixed in 10% neutral formalin and then subjected to paraffin embedding followed by preparation of sections with a thickness of 5 microns. A section of each tissue was stained with hematoxylin and eosin. The study of the slices was carried out in transmitted light using a Zeiss MR Color high-resolution camera of the LSM 780 Confocal scanning microscope (Carl Zeiss, Germany).

3.6.5 Blood biochemistry analysis

For the analysis of blood biochemical parameters, the biomarkers including total serum protein (TP), urea nitrogen (BU), fasting glucose (GLU), serum aspartate aminotransferase (AST), serum alanine aminotransferase (ALT), total bilirubin (TB), direct bilirubin (BD), gamma-glutamyltransferase, alkaline phosphatase (ALP), total cholesterol (TC), high-

density lipoprotein cholesterol, low-density lipoprotein cholesterol were measured on biochemical analyzer Cobas Integra 400 plus (Roche Diagnostics, Switzerland).

CHAPTER 4

SYNTHESIS AND CHARACTERIZATION OF CRYOGELS

4.1. Synthesis optimization and structural formation of cryogels

To better understand the mechanism of polymerization under sub-zero temperatures, an illustration of the cryopolymerization reaction of the non-frozen liquid microphase befalling around the developing ice-crystals on an example of AAC cryogel is shown in **Fig. 4.1.** Firstly, a complex of allylamine with phosphoric acid and neutralization of acrylic acid was formed. Previously allylamine was copolymerized with methacrylic acid under cryo conditions, which characterized by the low yield of gel fraction [97], which was related to the low activity of allylamine radical polymerization process. According to literature to improve the activity of allyl monomer in the radical polymerization process, it is necessary to convert it to a phosphate complex [217,218]. Simultaneously to the radical polymerization of selected monomers and cross-linking of polymeric chains is taking place producing branched macromers and growth of ice-crystals occur expelling all components of the reaction mixture into non-frozen liquid microphase where radical polymerization continues until run out of monomers or termination of polymerization [97]. Upon achievement of the polymerization reaction and solvent thawing melting of 3D structure of microcrystals leads to macro-sized pores formation within the polymeric material.

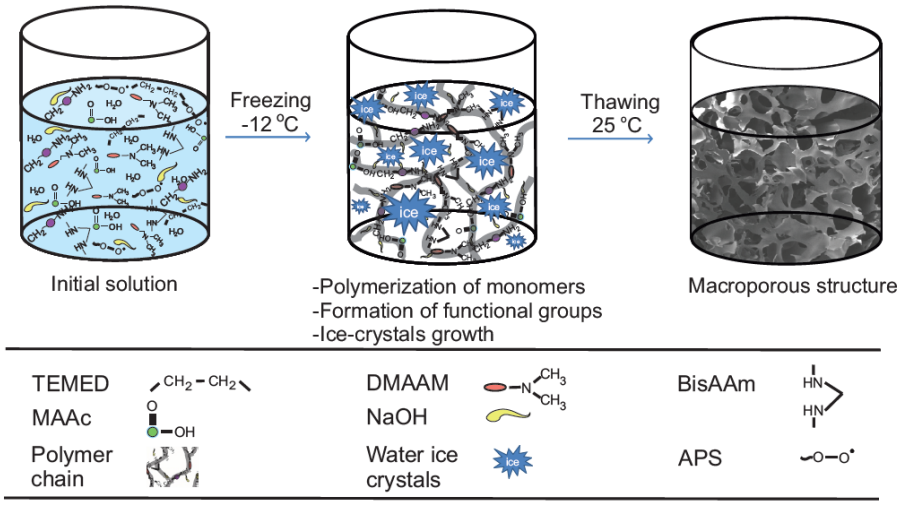

Fig. 4.1. Schematic representation of the formation of cryogels.

During the synthesis of polymers, one of the most important stages is the correct selection of the ratios of monomers, cross-linkers and initiators of the reaction. A crosslinking agent is an essential link in the formation of an elastic polymer matrix; therefore, different monomers/cross-linking agent (BisAAm) mole ratios have been tested. It was found that the optimal ratio of monomers to BisAAm is 10:1. The possible reaction of formation of AAC and SAC cryogels are presented in **Fig. 4.2A** and **4.2B**, respectively.

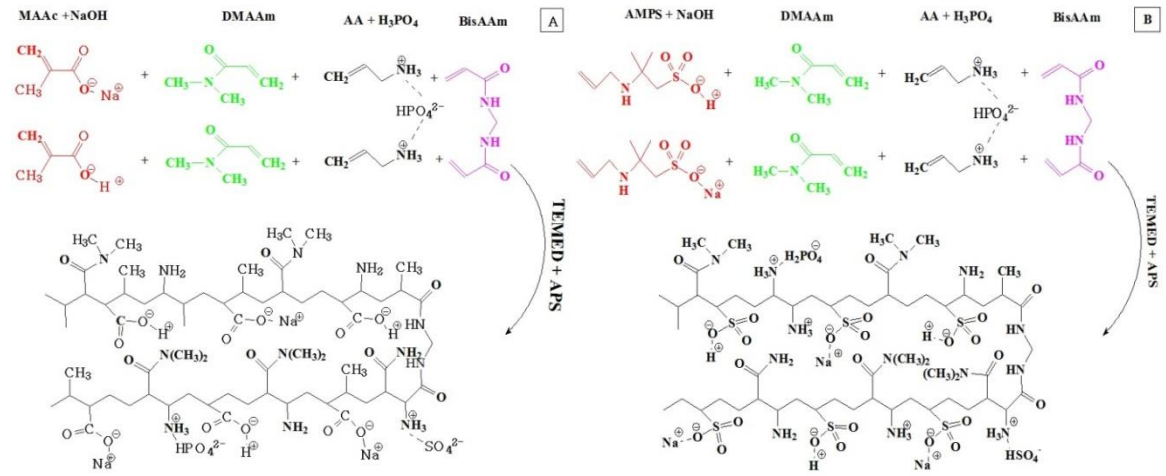

Fig. 4.2. Possible reaction of formation of AAC (A) and SAC (B) cryogels.

4.2. Characterization of cryogels

The presence of various functional groups in the cryogels structure was evaluated by FT-IR analysis which spectra are shown in **Fig 4.3**.

The FT-IR spectra indicate that both cryogels have peaks at approximately 3300 cm^{-1}, which is attributed to the stretching vibration bands of N-H group and 2900 cm^{-1} corresponds to sp^3 hybridized –CH $–CH_2$, $–CH_3$ groups. The peaks at 1621-1610 and 1560-1540 cm^{-1} correspond to the amide(I) and amide(II) groups, respectively [172]. Also, AAC cryogel contains stretching vibrations bands of a dissociated carboxyl group at 1141 cm^{-1} and non-dissociated carboxylic groups at 1390 cm^{-1}, respectively [219]. The presence of sulphur-containing monomer in the structure of SAC cryogel, confirmed by characteristic frequencies of sulfonic acid, sulfoxide, sulphide and C-S functional groups were found at peaks 1452-1401 cm^{-1}, 1186 cm^{-1}, 1035 cm^{-1} and 619 cm^{-1}, respectively [220–222].

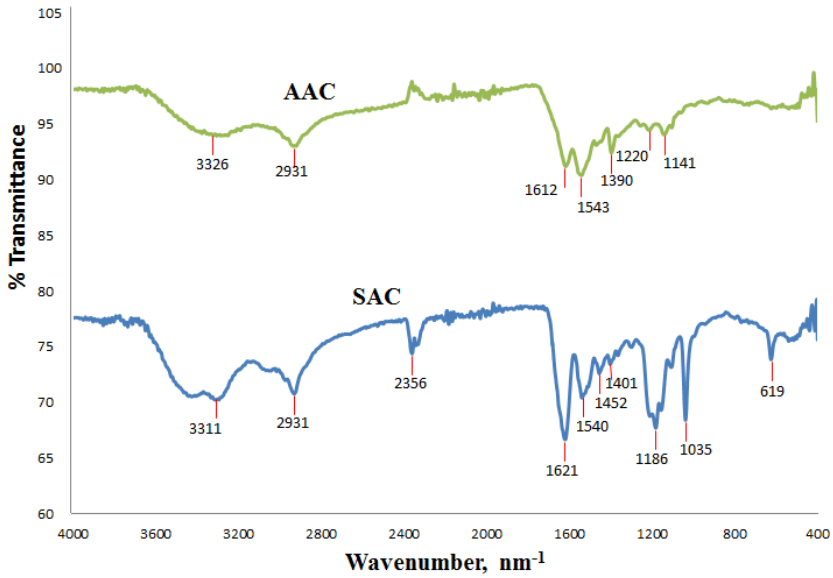

Fig. 4.3. FT-IR spectra of AAC and SAC cryogels.

The zeta potential measurements results are presented in **Fig. 4.4**, which indicate the surface charge of AAC cryogel starting from pH 3.2 is negative due to protonation of carboxyl groups, while SAC cryogel surface is negatively charged for the whole pH range due to existence of sulfonic acid which is a strong acid and dissociates. It can be assumed that amino groups of allylamine are protonated and have intermolecular polyelectrolyte complex with neighbouring sulfonic groups and carboxyl groups. A decrease of negative zeta potential for AAC at pH above 6 is most probably related to the deprotonation of ammonium groups. A positive charge of AAC at pH below 3.2 is attributed to positively charged amino groups of polyallylamine and therefore at pH below 3.2 mostly negatively charged ions will be adsorbed, but adsorption of cations possible via ion-exchange mechanism.

The morphological structure of the cryogels was observed using the SEM. The SEM microphotographs revealed the three-dimensional network associated with super-macroporous and interconnected channels of cryogels with the pore size in the range from 10 to 100 μm (**Fig. 4.5**). The spot elemental analysis confirmed that the mass percentage of carbon, oxygen and nitrogen is approximately the same for AAC and SAC cryogels. An amount of sodium is detected as expected due to the use of NaOH in the synthesis while sulfur is detected in the structure of SAC cryogel due to the AMPS monomer used for the synthesis (**Table 3.1**).

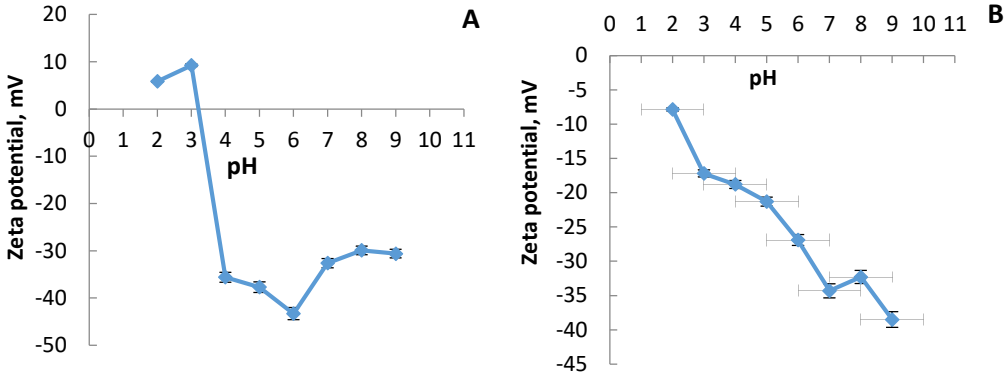

Fig. 4.4. Determination of surface charge of AAC (A) and SAC (B) cryogels at different pH. n=3

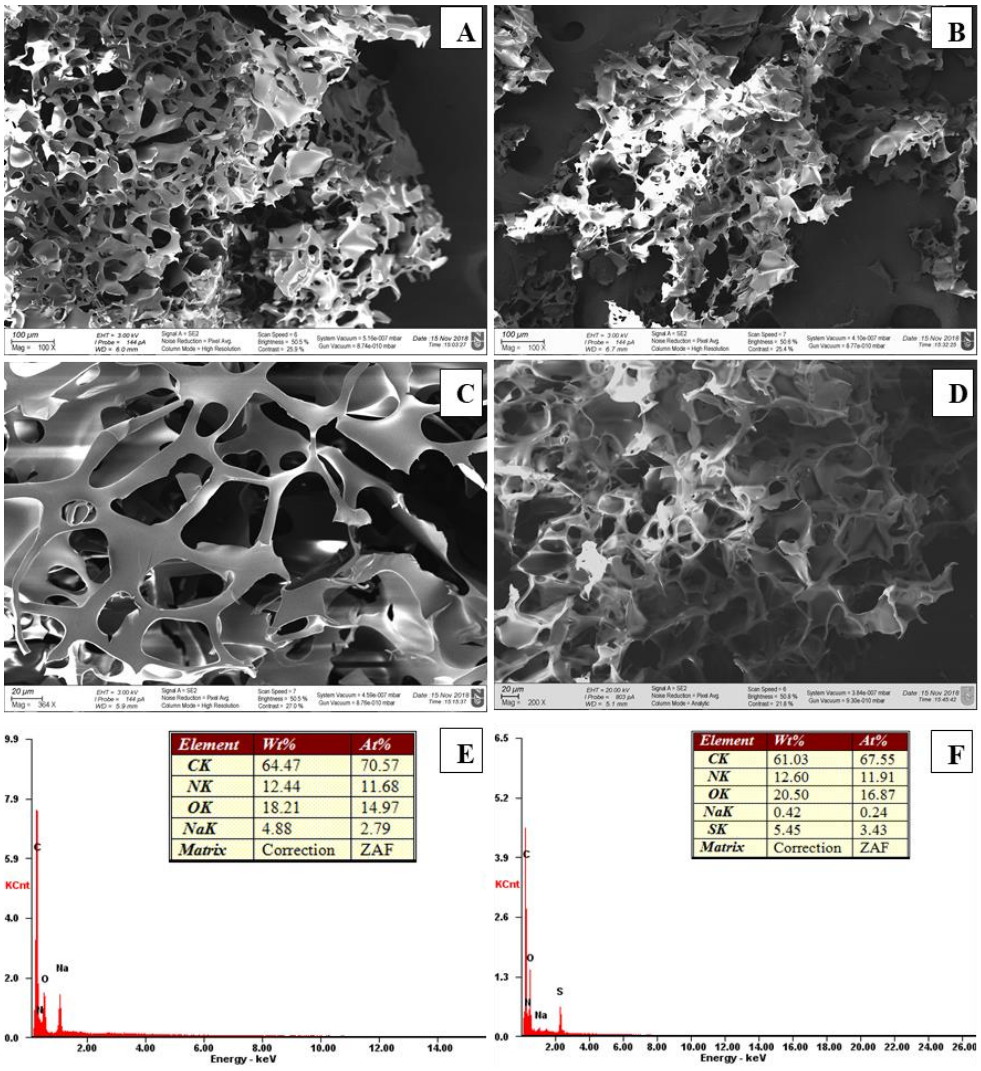

Fig. 4.5. SEM images and elemental composition according to spot EDX analysis of the AAC (A, C, E) and SAC (B, D, F) cryogels.

Finally, swelling results showed that both types of polymers adsorbed water in 1-2 seconds. The swelling degree for AAC cryogel, reached 22.5 gH_2O/g cryogel, while SAC sample indicated a slightly lower degree of swelling at equilibrium 19.5 gH_2O/g cryogel. This fast swelling dynamic is due to the super-macroporous structure of the cryogels.

CHAPTER 5
MERCURY REMOVAL STUDIES

5.1. Introduction

Water pollution with heavy metals, especially Hg^{2+} and its species is a grave worldwide ecological challenge. Although natural sources such as volcanoes, forest fires, geologic deposits of mercury and volatilization from the ocean contribute to the dominant share of mercury emissions comes from human-made sources [223–225]. According to the United Nations Environment Program, 2018 Global Mercury Assessment report [226] the anthropogenic sources emitted in the air more than 2 220 tons of mercury in 2015. The majority of the pollution associated with artisanal and small-scale gold mining accounted for almost 38% of the global total. Stationary combustion of coal-burning occupies about 21% of the assessed global emissions. Other industrial sectors remain non-ferrous metal fabrication (15%), cement industry (11%) and ferrous metal manufacturing (2%). In 2015, artisanal and small-scale gold mining input about 1 220 tons of mercury into the terrain and freshwater environments, while anthropogenic mercury from other sources added 580 tons more to maritime encirclement. The key sectors facilitating these 580 tons are waste treatment (43%), ore mining and processing (40%), and energy (17%) [226].

The removal of mercury from water is a crucial environmental issue due to the adverse effects on both humans and natural ecosystem [227]. Consumption of water contaminated with mercury may affect the neurological and mental functions of the humans, leads to dizziness, irritability, anorexia, hypertension, tachycardia, and memory loss, with less effect on the digestive and renal systems [228–230]. The serious health consequences of consuming mercury poisoned fish and water have been long recognized, especially after the Minamata accident in Japan [231]. As a result, the US EPA established the maximum acceptable concentration of mercury ions as 1 and 10 μg/L in drinking and wastewater, respectively [232,233].

Various mercury removal methods have been applied, including membrane separation and solvent extraction, precipitation, adsorption, ion exchange and bioremediation [234]. Of all these methods, adsorption is an advantageous method in terms of operational simplicity and cost-effectiveness. The variety of materials and the selection of the adsorbent with desirable properties for Hg^{2+} removal is challenging [232]. There are frequent studies on the removal

of Hg^{2+} from aquatic media by use of adsorbents; activated carbons [235], zeolites [200,236], ion-exchange resins [237] and silver-impregnated materials such as alumina, zeolites, graphene [200,219,238] and synthetic polymers [213,239]. **Table 5.1** reviews the used adsorbents and their efficiency for the removal of mercury from water.

Table 5.1 Materials for the removal of Hg^{2+} from the aqueous phase.

Adsorbent type	Initial Hg^{2+} concentration [mg/L]	Initial pH	Hg^{2+} compound	Maximum removal capacity (mg/g)	Reference
SiO_2-carbon nanotubes	40	7.0	$Hg(NO_3)_2$	142	[240]
Au-Al_2O_3	0.4	7.0	$Hg(NO_3)_2$	676	[241]
Ag- Fe_3O_4	1.6	8.0	$Hg(NO_3)_2$	42	[242]
Ion exchange resin TP-214	100	-	$Hg(NO_3)_2$	456	[237]
Chitosan-p(vinyl alcohol) cryogel	374	3.5	$Hg(NO_3)_2$	374	[243]
P. chrysosporium loaded cryogel	100	6.0	$Hg(NO_3)_2$	88	[155]
AAC cryogel	100	3.7	$Hg(NO_3)_2$	742	This
SAC cryogel	100	3.7	$Hg(NO_3)_2$	676	research
AgNP@ mercaptosuccinic acid on alumina	2	5.0	$Hg(O_2CCH_3)_2$	800	[219]
Chitosan-p(vinyl alcohol) cryogel	668	5.5	$Hg(O_2CCH_3)_2$	668	[243]
Chitosan-p(vinyl alcohol) cryogel	2070	5.5	$Hg(O_2CCH_3)_2$	586	[172]
Synthetic sodalite-AgNP	10	2.0	$HgCl_2$	1.3	[236]
Activated carbon	150	6.0	$HgCl_2$	29	[244]
Jute nanofiber	10	6.0	$HgCl_2$	85	[245]
Synthetic zeolite-AgNP	10	2.0	$HgCl_2$	6	[200]
Ag/graphene	100	5.0	$HgCl_2$	281	[238]
Cd/S- polycaprolactam	20	7.0	$HgCl_2$	162	[246]
Single wall carbon nanotubes-thiol groups	30	5.0	$HgCl_2$	131	[247]
Mesoporous silica- ammonium (4-chlro-2-mercaptophenyl) carbamodithioate	2	5.5	$HgCl_2$	164	[248]
Flower-like nanotitanate	50	5.0	$HgCl_2$	454	[249]
Fe_3O_4-SiO_2-thiol groups	50	3.0	$HgCl_2$	90	[250]
Graphene-diatom silica aerogel	100	6.5	$HgCl_2$	500	[225]
Sulfur-modified activated carbon	100	5.0	$HgCl_2$	75	[235]
Chitosan-p(maleic acid) hydrogel	2000	6.0	$HgCl_2$	1044	[213]
Chitosan-p(vinyl alcohol) cryogel	468	5.5	$HgCl_2$	184	[243]
Thiol-grafted p(GMA) polymer	300	7.0	$HgCl_2$	51	[251]
p(EGDMA–VIM)] hydrogel	200	5.0	-	163	[252]
Polyethyleneimine cryogels	100	7.0	$HgCl_2$	1280	[171]
AAC cryogel	100	4.99	$HgCl_2$	263	This
SAC cryogel	100	4.99	$HgCl_2$	240	research

5.2 Chapter Overview

This chapter discusses studies on the removal of mercury ions from nitrate and chloride salts by synthesized cryogels. Studies of kinetics and equilibrium, as well as the use of standard models for determining the adsorption capacity of the polymers, are presented. Also, the chapter describes the proposed mechanism of mercury ions removal. In addition, this chapter also reports on studies on the removal of mercury ions from various aqueous matrices and comparison with commercial adsorbents.

5.3 Adsorption kinetics

Due to its potential risks, effective and fast removal of mercury from aqueous solutions is essential. To evaluate the sorption kinetics of Hg^{2+} on cryogels, batch experiments were conducted and the results are illustrated in **Fig. 5.1**. It is evident that kinetics are fast and in the first two hours, AAC and SAC cryogels are able to remove about 91% and 73% of mercury from $Hg(NO_3)_2$ solution and 64 and 40% from $HgCl_2$ solution, respectively. Both cryogels removed 99 % of mercury ions from the solutions and reached an equilibrium removal within 24h with the exception of SAC for $HgCl_2$ solution, which reached equilibrium within 48h with a removal level of 81.5 %. As is evident, AAC cryogel is superior while removal from $Hg(NO_3)_2$ solution is faster for both cryogels. The potential mechanisms are discussed in section 5.5.

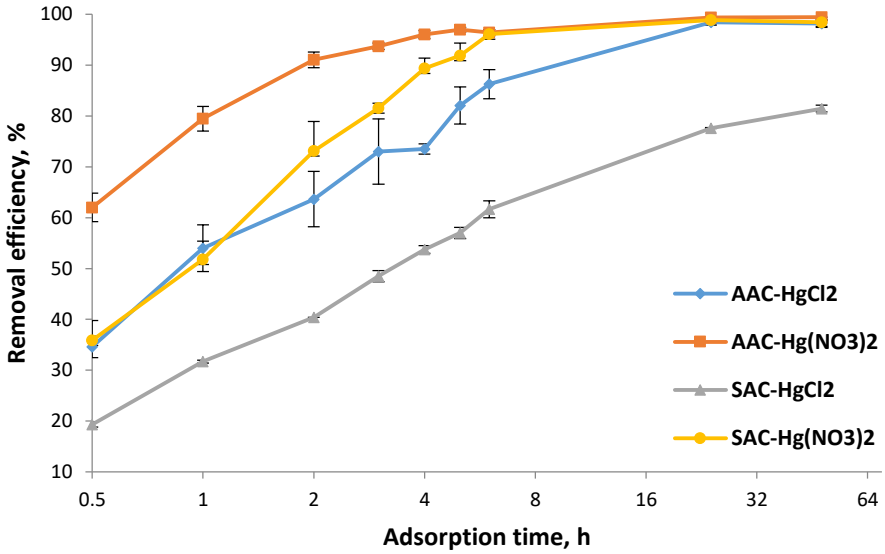

Fig. 5.1. Adsorption kinetics of Hg^{2+} on the AAC and SAC cryogels (80 mg of cryogel in 100 mL of solution).

To further study the mechanism of removal the pseudo-first-order and pseudo-second-order models were used and their linear forms were calculated using Eq. 3.4 and Eq. 3.5, respectively. The modelling results are given in **Table 5.2**.

Table 5.2. Parameters of kinetic models for Hg^{2+} sorption by cryogels.

		Pseudo-first order			Pseudo-second order		
	q_e^{exp} (mg/g)	q_e^{cal} (mg/g)	K_1 (min^{-1})	R^2	q_e^{cal} (mg/g)	K_2 (g mg^{-1} min^{-1})	R^2
AAC-$HgCl_2$	123.3	88.1	0.2704	0.9669	121.9	0.0079	0.9926
SAC-$HgCl_2$	101.9	78.4	0.1958	0.9835	94.3	0.0164	0.9945
AAC-$Hg(NO_3)_2$	122.6	58.8	0.8436	0.9628	126.6	0.0022	0.9996
SAC-$Hg(NO_3)_2$	122.7	95.7	0.5177	0.9937	142.8	0.0080	0.9994

The pseudo-second-order model better fits the experimental capacity data, and the correlation coefficient is higher than the pseudo-first-order.

The presence of mercury on the cryogels surface was proved by semi-quantitative mapping EDX analysis and is shown in **Fig. A1-A4**. The results showed that all samples had adsorbed mercury on the surface of cryogels, and the amount varies from 4.56 to 10.2 % w/w. The EDX mapping analysis images reveal that mercury ions are distributed over the entire surface of the polymers. Also, low nitrogen content in the samples of cryogels after mercury adsorption compared with the initial cryogels (Chapter 4, **Fig. 4.5**) was observed and is discussed in paragraph 5.5. Finally, the cryogels were tested for Hg^{2+} leaching, and the results showed negligible leaching after adsorption, lower than 0.2 % of the Hg^{2+} adsorbed from both $HgCl_2$ and $Hg(NO_3)_2$ solutions under neutral pH after 14 days (**Table A1**). This demonstrates the strong binding of Hg^{2+}on the cryogels surface.

5.4 Adsorption equilibrium

The experimental isotherms are shown in **Fig 5.2.** As is clear, the removal from the $Hg(NO_3)_2$ solution is more efficient, reaching much higher loadings. In the $Hg(NO_3)_2$ solution cryogels show the same efficiency and the shape of the curve is the same while in the $HgCl_2$ solution, AAC is superior, and the isotherms are different. These results are in agreement with the kinetics experiment and also show that the interactions $Hg(NO_3)_2$ solution are similar in both cryogels in contrast to $HgCl_2$ solution were the interactions seem markedly different.

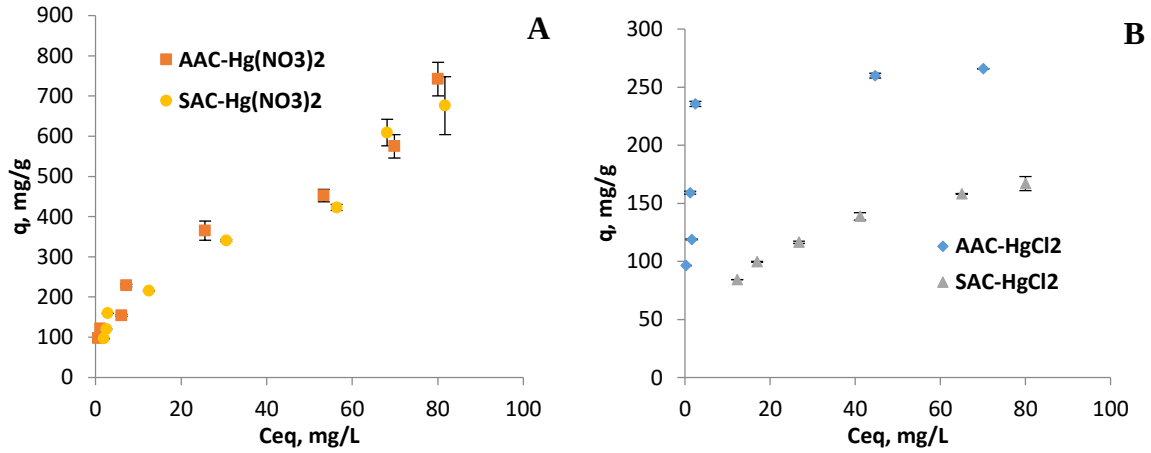

Fig. 5.2. Isotherms of Hg^{2+} removal by cryogels.

In order to analyze the experimental isotherms Langmuir and Freundlich isotherm models are utilized, both widely used for the description of adsorption of heavy metals on the homogeneous or heterogeneous surfaces, respectively. The linear forms of the Langmuir and Freundlich sorption isotherms are presented in Eq. 3.6 and 3.7, respectively.

The correlation coefficient of the Langmuir isotherm model was better than that of the Freundlich isotherm model for both cryogels in $HgCl_2$ solution, and the derived maximum capacities are close to the experimental ones (**Table 5.3**). Despite the fact that the correlation coefficient of the Freundlich model (0.97-0.98) is higher than for the Langmuir model (0.90-

0.93) for samples in $Hg(NO_3)_2$ solution, the capacities derived from Langmuir model are very close to experimental values. The excellent fit of the Langmuir model indicates a monolayer adsorption of Hg^{2+} ions on the surface of cryogels.

Table 5.3. Parameters of isotherm models for Hg^{2+} sorption by cryogels.

		Langmuir model			Freundlich model		
	q_{max}^{exp} (mg/g)	q_m (mg/g)	K_L (L/mg)	R^2	n	K_F	R^2
AAC-$HgCl_2$	262.2	263.2	0.8261	0.9992	0.1758	131.6	0.7501
SAC-$HgCl_2$	174.0	212.8	0.0484	0.9948	0.3787	33.3	0.9966
AAC-$Hg(NO_3)_2$	626.5	666.7	0.6667	0.9312	0.4338	83.6	0.9713
SAC-$Hg(NO_3)_2$	622.5	666.7	0.0568	0.9073	0.4464	78.4	0.9837

Adsorption capacities of both cryogels in $Hg(NO_3)_2$ solution are very high, up to 626 and 622 mg/g by AAC and SAC cryogels, respectively, and comparable to other cryogels found in the literature. Privar et al. synthesized polyethyleneimine cryogels with different crosslinking agents for adsorption of Hg^{2+} and Cu^{2+} ions from water solutions. The maximum adsorption capacity was observed for cryogel crosslinked by diglycidyl ethers and reached 1280 mg/g of Hg^{2+} [171]. Wang et al. used chitosan-p(vinyl alcohol) cryogel for adsorption of mercury ions from different salts [243]. In this study was observed that at pH 5.5 of $HgCl_2$, pH 5.5 of $Hg(CH_3COO)_2$ and at pH 3.5 of $Hg(NO_3)_2$ solutions cryogel samples reached maximum adsorption capacity 184, 668 and 374 mg/g, respectively [243]. Ge and Hua synthesized chitosan-poly(maleic acid) hydrogel crosslinking by glutaraldehyde for the removal of various heavy metals from aqueous media. For Hg^{2+} ions the maximum capacity was valued as 1044 mg/g at pH 6.0 [213]. In another study, Ge with co-authors changed maleic acid to itaconic acid and examined polymers capability to removal Hg^{2+} and Pb^{2+} ions. The results of the experiments revealed that sorption uptake of mercury ions was found to be 870 mg/g [253]. Li et al. modified chitosan-polyacrylamide polymer by SiO_2@Fe_3O_4 nanoparticles and used parent polymer and synthesized composite for removal of Cu^{2+}, Pb^{2+}

and Hg^{2+} ions. The parent polymer showed maximum adsorption capacity at 88.5 mg/g while modification by iron nanoparticles resulted in an improved of 264 mg/g [254].

5.5 Mechanisms of removal

The functional groups of cryogels can act as ion-exchangers and also form chemical bonds rendering the removal mechanism of mercury complex [171]. Before discussing what is happening on the surface, it is essential to understand the aqueous chemistry of mercury, i.e. its speciation. For this purpose, Medusa software was used to study the speciation in $HgCl_2$ and $Hg(NO_3)_2$ solutions at concentrations of 100 ppm (**Fig. 5.3**) and 50 ppm Hg^{2+} (**Fig. A5**). The initial pH and conductivity of the solutions are shown in **Table A2**. The speciation is very different and in acidic conditions while in $HgCl_2$ solution the predominant species is neutral soluble $HgCl_2$ while in $Hg(NO_3)_2$ solution considerable portion of mercury is in the ionic forms of Hg^{2+} and $HgOH^+$. This was confirmed by the conductivity of the solutions 13.08 µS/cm for $HgCl_2$ solution and 244 µS/cm for $Hg(NO_3)_2$ solution.

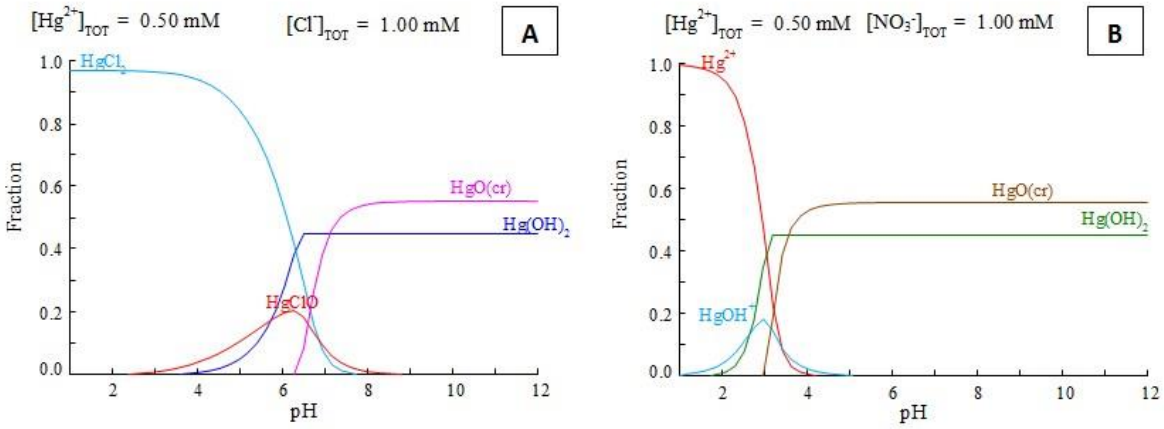

Fig. 5.3. Speciation of 100 ppm Hg^{2+} chloride (A) and nitrate (B) solutions (Diagram created by Medusa software).

The pH of solutions for SAC did not change much compared to the pH of the solution with AAC, which increases to almost neutral (**Table A2**). It should be noted that although precipitation of HgO is possible, according to Medusa, but it was not observed. One reason is that Medusa shows only systems in equilibrium and the formation of some species may take time. Also, in the course of the experiment and as mercury is removed speciation

changes again and precipitation either occurs in higher pH or the portion of mercury precipitated becomes lower (**Fig. A5**).

One of the proposed removal mechanisms is the ion exchange process between H^+ and/or Na^+ in the cryogel phase with mercury ions from the solution phase followed by complexation of mercury ions with functional groups. The conductance and pH data provide some evidence of the interactions between mercury and the cryogels surface (**Table A5**). The conductance of $HgCl_2$ solution after adsorption of mercury was considerably increased by almost 10 fold, due to the simultaneous release of Na^+ and Cl^- ions after $HgCl_2$ interacts with the cryogels functional groups. The removal of mercury from solution by AAC resulted in an increase of pH. On the contrary, the pH in SAC experiment remains acidic, which an indication that H^+ is released, and as expected, it led to the increase of the solution's conductivity. This phenomenon occurs due to the substitution of hydronium from the ionic shell of the sulfonic acid groups the adsorption of mercury ions as it shown in reaction below (5.1):

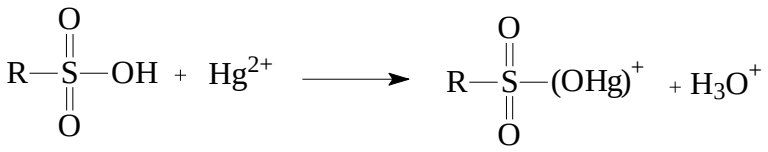

(5.1)

As expected, the adsorption of $Hg(NO_3)_2$ solution by AAC shows that, in comparison to $HgCl_2$ solution, while pH evolution is the same, the conductivity decreased by a factor of 2, due to binding of Hg^{2+}. This is an indication that there is a net decrease of ions in the solution; indeed, while the removal of neutral $HgCl_2$ species from the solution can not have any substantial effect on the conductance, the removal of ionic species of Hg^{2+} and $HgOH^+$ should lead to a decrease of conductance. Based on these observations, the ion exchange process between H^+ and/or Na^+ with mercury is possible and in a good agreement with pH and conductivity. Conductance change depends on both the charge and the ion mobility and while ion exchange is a stoichiometric process the exchange of different ions, particularly H^+, will lead to considerable changes in conductance; for instance, H^+ mobility is almost 7 times this of Na^+ [255]. However, pH and conductance data while useful they cannot provide a solid proof that ion exchange is a predominant mechanism. To study the removal mechanism, the released Na^+ from the cryogels during the interaction with mercury was

considered. The Hg^{2+}/Na^{+} molar ratio is shown in **Fig. 5.4** and depends on the mass of the cryogel/solution volume ratio. For many AAC experimental data, the molar ratio of Hg^{2+}/Na^{+} ratio is close to 0.5, which is the stoichiometric ratio expected when ion exchange takes place. In the case of SAC cryogel, the Hg^{2+}/Na^{+} ratio is much higher, which means that the released amount of Na^{+} is small. This happens due to the low initial concentration of sodium ions in the SAC cryogel but probably also because of the sulfonic acid's H^{+}, which can be exchanged for Hg^{2+}.

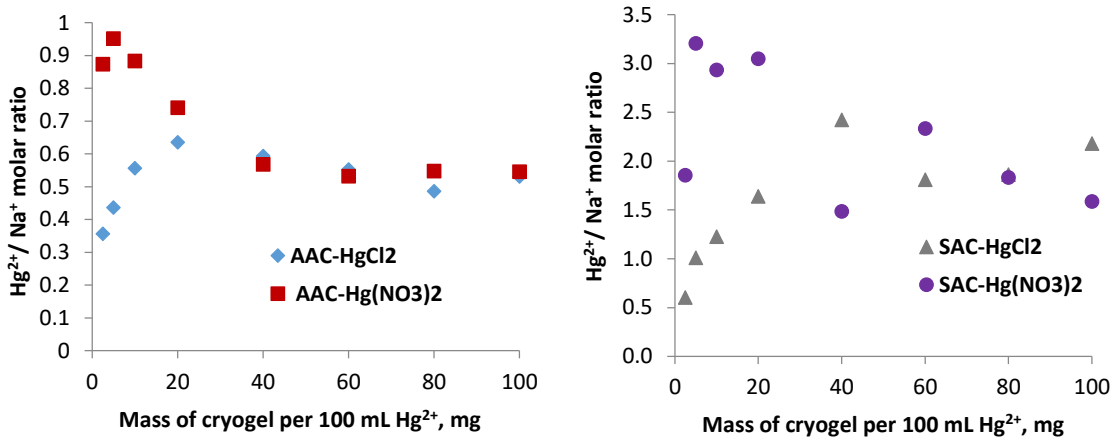

Fig. 5.4. Molar ratio of removed Hg^{2+} and released Na^{+} during adsorption.

The results show that the ion-exchange mechanism is involved in both cryogels, albeit the kinetics and equilibrium strongly depend on the mercury solution phase speciation and the chemistry of the cryogels surface. The availability of the various functional groups in the structure of the cryogel most probably, ion exchange is followed by complexation of Hg^{2+} with functional groups [171]. To investigate this FT-IR spectra of Hg-loaded cryogels was recorded (**Fig. 5.5**). The FT-IR frequencies of amide(I) and amide(II) groups at 1612 and 1543 cm^{-1} in AAC samples are shifted from 2 to 7 cm^{-1} to lower frequencies with decreasing of peaks intensity in comparison to the parent cryogel. This phenomenon indicates deprotonation or metal-bounding on carbonyl groups [256,257]. A similar pattern of amide peaks shifting is observed in the sample SAC after binding of Hg^{2+} ions. Also, the peak of sulfonic acid at 1186 cm^{-1} at parent SAC sample is shifted to 1182 and 1178 cm^{-1} in the samples SAC-$Hg(NO_3)_2$ and SAC-$HgCl_2$, respectively.

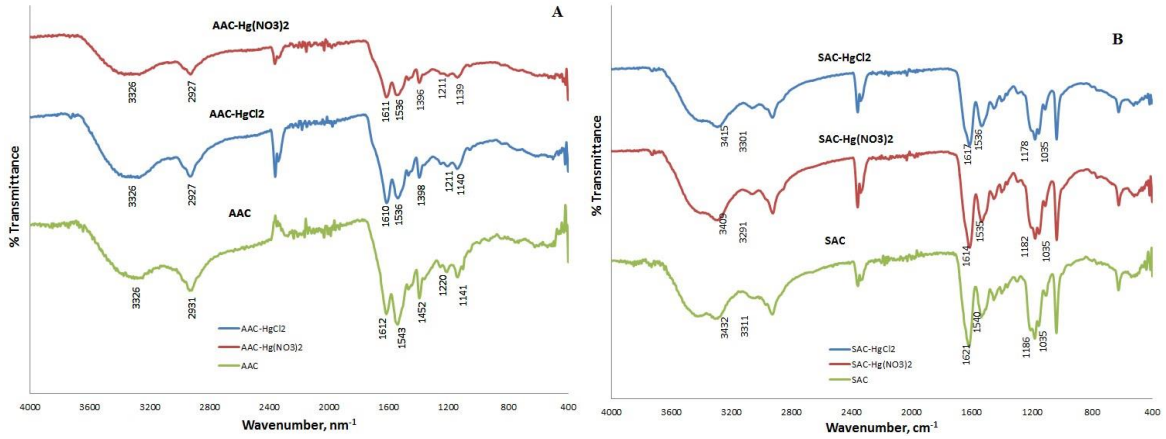

Fig. 5.5. FT-IR patterns of cryogels before and after Hg^{2+} adsorption: A) AAC, B) SAC.

EDX analysis shows that the nitrogen content decreased from 12% in the parent cryogels to about 1% after the interaction with mercury (Fig. S3). However, measurement of the total nitrogen content by Dumas combustion method (**Table A3**) shows that there are no significant changes in nitrogen content. Thus, the shallow nitrogen content observed by EDX after the interaction with mercury can be assigned to the coverage of the surface by mercury, which apparently is masking the nitrogen content. This is an indication of some kind of interaction between mercury and nitrogen occurs.

Based on the observed results the possible complexation reactions on the surface of AAC and SAC cryogels between Hg^{2+} and the carboxylic, amide and sulfonic acid groups can be summarized as follows in reactions (5.2), (5.3), (5.4) and (5.5) [213,239,258,259]:

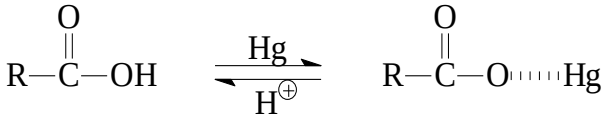

(5.2)

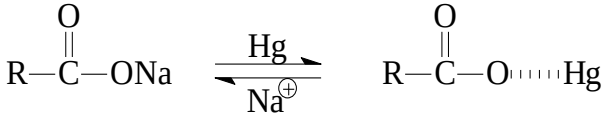

(5.3)

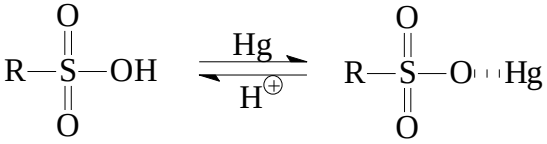

(5.4)

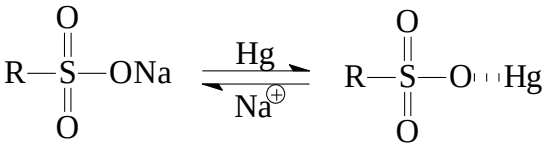

(5.5)

Wang et al observed the same phenomena, after interaction of chitosan-p(vinyl alcohol) cryogel with Cu^{2+} and Hg^{2+} ions where it was suggested that -$NHCOCH_3$ and -NH_2 were involved in metal ions chelation [243]. Based on the presented removal mechanism hypothesis, the structure of the cryogels after the adsorption of Hg^{2+} is shown in **Fig. 5.6**.

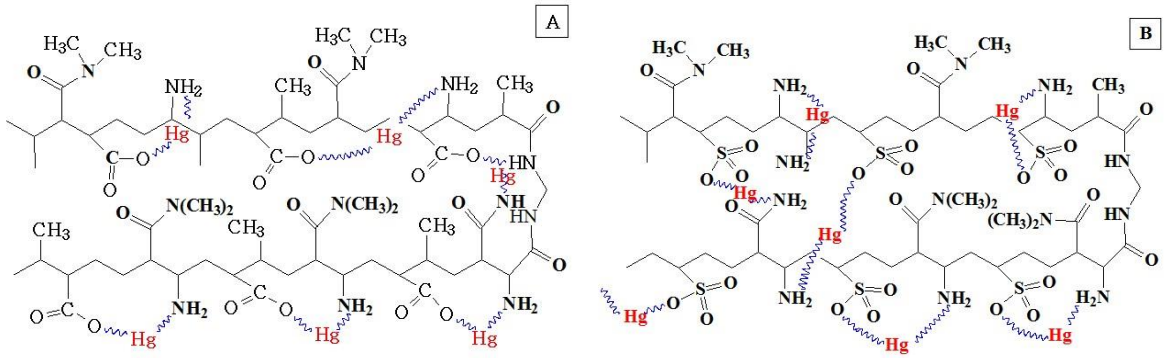

Fig. 5.6. Proposed complexation of Hg^{2+} ions with functional groups of AAC (A) and SAC (B) cryogels.

5.6 Mercury removal from different water matrices

The results of the elimination of mercury ions from various water matrices by different commercial adsorbents and synthesized cryogels are presented in **Table 5.4**. The first 10 min of adsorption both AAC and SAC cryogels showed 20-30% removal of Hg^{2+} ions from UP water, while the rest of materials removed less than 2%. In the tap and river water, the cryogels also showed better removal rate after 10 min of interaction; however, in seawater, the adsorption of mercury ions by all materials was less than 6%. After 24h of adsorption of mercury in ultra-pure water, the AAC cryogel showed the more than 90% removal, the SAC cryogel removed about 70%, while rest of commercial adsorbents eliminated no more than 33%. In tap and seawater, where the concentrations of co-existing cations are higher comparing with ultra-pure water (see **Table A4**), the adsorption capacities decreased for all materials; however, AAC sample still was able to remove ~77% and 87% of mercury ions

from tap and river water, respectively. The best adsorption efficiency of all used commercial sorbents was demonstrated by activated carbon, which reached 47% and 35% of the mercury removal from tap and river water, respectively. The natural seawater was the most complex matrix for the elimination of mercury due to the large concentrations of cations and anions. Thereby, only activated carbon was able to remove about 45% of mercury ions, while the other materials adsorbed only 10-20% of initial values.

Table 5.4. Residual concentrations of mercury ions in various water matrices after interaction with adsorbents at different time points.

	time, min	10	60	240	1440
UP water	Activated carbon	9.83±0.13	9.23±0.17	9.14±0.25	7.09±0.59
	Ion-exchange resin	10.26±0.40	9.73±0.04	9.18±0.14	6.75±0.15
	Zeolite	9.82±0.08	9.66±0.40	9.12±0.13	7.81±0.07
	AAC	8.15±0.40	5.62±0.91	3.46±0.66	0.90±0.36
	SAC	6.93±0.60	4.00±0.19	1.49±0.28	0.31±0.14
	control	10.37±0.18	10.05±0.11	9.88±0.01	9.78±0.03
tap	Activated carbon	9.48±0.72	8.78±0.10	8.12±0.34	5.28±0.17
	Ion-exchange resin	9.81±1.03	9.08±0.13	9.06±0.22	8.99±0.08
	Zeolite	9.08±0.08	8.78±0.22	8.57±0.10	8.34±0.19
	AAC	8.63±0.32	6.66±0.33	5.75±1.55	2.35±1.94
	SAC	8.36±0.36	7.50±0.36	6.84±0.58	5.62±0.30
	control	9.53±0.33	9.30±0.00	9.13±0.05	9.00±0.03
river	Activated carbon	9.23±0.19	8.80±0.04	8.32±0.11	6.48±0.44
	Ion-exchange resin	9.32±0.12	8.86±0.64	8.08±0.37	7.02±0.43
	Zeolite	8.86±0.10	8.11±0.12	7.74±0.16	7.45±0.18
	AAC	7.87±0.34	5.78±0.37	3.85±0.40	1.30±1.19
	SAC	9.02±0.42	8.01±0.44	4.11±0.95	3.27±0.39
	control	9.68±0.11	9.54±0.67	9.14±0.11	9.20±0.20
seawater	Activated carbon	9.23±0.23	9.14±0.06	8.60±0.12	5.46±0.19
	Ion-exchange resin	9.55±0.04	9.56±0.04	9.41±0.06	9.14±0.03
	Zeolite	9.34±0.07	9.54±0.08	9.22±0.08	9.11±0.05
	AAC	9.40±0.05	9.44±0.04	9.22±0.13	8.41±0.30
	SAC	9.41±0.05	9.48±0.05	8.87±0.06	7.86±0.10
	control	9.89±0.79	9.55±0.04	9.50±0.01	9.31±0.08

The behaviour of adsorbents could be described by evaluating the speciation of mercury ions in various water matrices. The speciation of Hg ions was performed by Medusa software using the real concentrations of main cations and anions in investigated water (**Fig. 5.7 and Fig. A6**). In all water matrices except seawater, the primary forms of mercury were $HgCl_2$, $Hg(OH)_2$ and HgClOH at pH 5-8, while in seawater the predominant species were $HgCl_4^{2-}$, $HgCl_3^-$, $HgCl_2$ at the pH of used solution. Knowing that all materials used, except for activated carbon, are cation-exchangers, and from this, it becomes clear why only activated carbon was able to adsorb some mercury ions from seawater. The results in the **Table A4** also confirm the proposed mechanism of adsorption by AAC and SAC cryogel. The concentrations of Na^+ ions after 24 h in both cryogels and zeolites were increased in ultra-pure, tap and river water with increase of pH of the final solutions. The ion-exchange resin removed mercury ions by ion exchange with H^+, which gave the decrease of pH to the acidic range. Finally, in AAC and SAC cryogels an increase of PO_4^{2-} concentrations was observed in tap, river and seawater, probably a result if anion exchange. Also, K^+, Mg^{2+} and Ca^{2+} removed by all materials except activated carbon, which indicates ion-exchange mechanism.

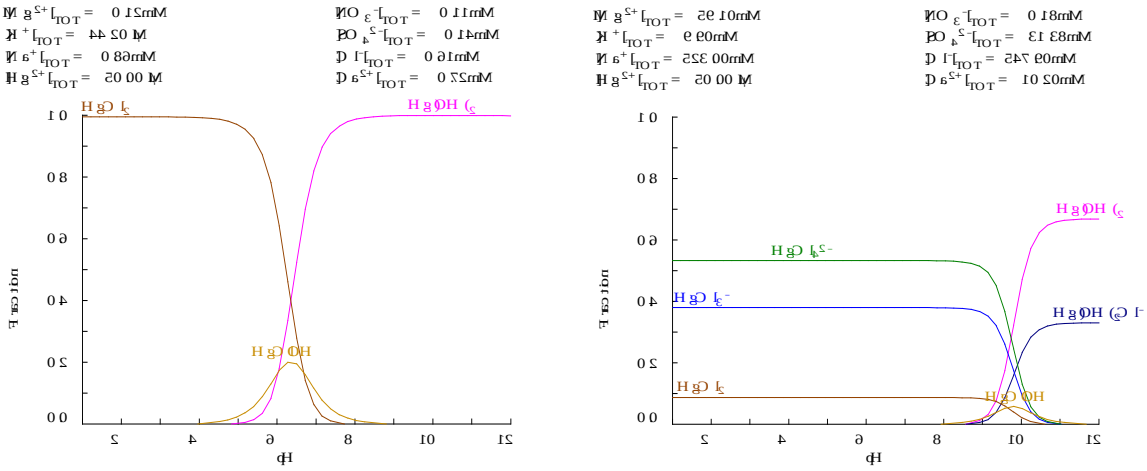

Fig. 5.7. Speciation of 10 ppm Hg in river (left) and sea water (right) matrices (Diagram created by Medusa software).

5.7 Summary

Two novel cryogels were studied towards Hg^{2+} removal from $Hg(NO_3)_2$ and $HgCl_2$ solutions. The results illustrated rapid kinetics of adsorption and high capacities with AAC cryogel being superior over SAC cryogel. The removal of Hg^{2+} is higher in $Hg(NO_3)_2$ solution due

to the ionic species, which are diffusing and interacting faster and more efficiently with the cryogels functional groups. The AAC and SAC samples showed maximum removal capacity around 260 mg/g from $HgCl_2$ salt solution and up to 620 mg/g from $Hg(NO_3)_2$ solution. The Hg^{2+} removal mechanism is ion exchange followed by complexation reactions. The results of adsorption of mercury ions from different real water matrixes show that cryogels removed mercury much faster than commercial adsorbents such as activated carbon, strong acid resin and zeolite Y except for seawater where activated carbon is superior.

CHAPTER 6
CADMIUM REMOVAL STUDIES

6.1 Introduction

Heavy metal pollution of the environment can cause harm to people and living organisms. One of such toxic pollutants is cadmium (Cd), which is commonly used in battery, plastics and coatings production [260]. Once in the human body, Cd is strongly associated with metallothioneins. Cd stands out as a strong poison with a natural half-life of more than 20 years. As the main organ for the accumulation of toxic substances, the kidney is a reliable main target tissue that exhibits early signs of toxic entry [260]. Chronic manifestations of elevated cadmium levels can lead to liver damage, bone degeneration, blood damage, and renal dysfunction. The acceptable limit for cadmium in drinking water prescribed by the US Environmental Protection Agency is 0.005 mg/L. [18].

Removal of toxic heavy metal ions from wastewater is essential, along with other metal ions which have been the focus of treatment studies by various materials and technique [20,260–263]. Several methods have already been considered to recover metal ions from wastewater including chemical precipitation [264], chemical coagulation/flocculation [265], membrane filtration [266], ion-exchange processes [267], bioremediation [268] and adsorption [269]. Typical adsorbents such as activated carbons, natural zeolites and clays are of interest, but often the materials have low adsorption capacity or to be treated chemically to produce desirable adsorption properties [185,186,236,270]. Therefore, a simple synthesis route of materials with high adsorption is beneficial for practical applications.

An ideal sorbent intended for the elimination of heavy metal ions shall meet specific requirements such as I) the chemical structure must have either chelating sites or ion-exchange groups, II) it must contain a hydrophilic and three-dimensional (3D) network structure to maintain the water flow for a long time, III) it must be cost-effective, and IV) it should be practically manufactured [271].

The polymeric materials such as cryogels and hydrogels ideally fit for abovementioned parameters. Cryogels are hydrophilic sponge-like materials with developed macroporous polymeric matrices produced at sub-zero temperatures [149]. To increase the chelating ability to eliminate heavy metal ions, various functional groups, such as carboxyl (-COOH),

hydroxyl (-OH), amine (-NH_2) and / or thiol (-SH), can be successfully grafted using proper modifications. Further remarkable advantages include the fast adsorption kinetics, high sorption capacities and reusability.

6.2 Chapter Overview

This chapter describes the results of the adsorption of cadmium ions by two types of cryogels. The sorption behaviour of cryogels depending on pH is described in detail; the effects of sorption depending on the contact time and the time to reach the equilibrium are shown. Also, the results of experiments of various ratios of cryogel:metal loading, the effect of the concentration of heavy metal ions on the adsorption capacity of cryogels are presented. Using multiple analysis methods, potential mechanisms for the adsorption of cadmium ions were determined. This chapter also presents the result of testing cryogels and commercial sorbents (ion exchange resin and zeolite) for the removal of cadmium ions from various aqueous matrices.

6.3 Adsorption kinetics

The effective and fast removal of highly toxic metal ions is the main parameters of adsorbents. To evaluate the sorption kinetic of Cd^{2+} ions on cryogels, batch experiments at pH 4 and 5.5 were conducted. Still, as soon as kinetic curves behaviour was similar, the results of adsorption at pH 5.5 are given and illustrated in **Fig. 6.1**. The difference in pH did not play a significant role in the rate and adsorption capability of cryogels for cadmium ions since the initial pH of solutions was higher than the isoelectric point of cryogels. It is evident from the kinetic graph that in the first hour AAC cryogel was able to remove more than 50 % from metal ions solution while SAC removed only about 32.5 %. The Cd^{2+} ions removal experiments showed that AAC sample removed almost 98 %, while SAC cryogel reached the maximum removal at 60 % during the first 24 h of adsorption.

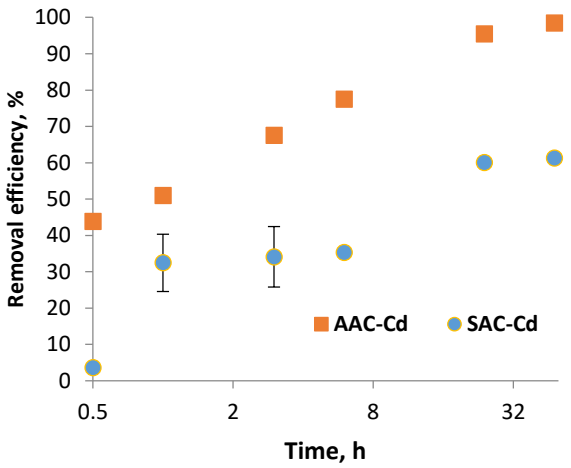

Fig. 6.1. Adsorption kinetics of Cd^{2+}ions on the AAC and SAC cryogels (70 mg of cryogel in 100 mL of solution) at pH 5.5.

In order to estimate the kinetics of adsorption, the pseudo-first-order and pseudo-second-order models were used in linear forms as it shown in Eq. (3.4) and (3.5) in Chapter 3. The results of kinetic models are given in **Table 6.1**.

Table 6.1. Parameters of kinetic models for metal ions sorption by cryogels.

			Pseudo-first order			Pseudo-second order		
	q_e^{exp} (mg/g)	ct (mg/g)	q_e^{cal} (mg/g)	K_1 (min^{-1})	R^2	q_e^{cal} (mg/g)	K_2 (g mg^{-1} min^{-1})	R^2
AAC-Cd	140.7	137.9	84.24	0.1622	0.9769	144.93	0.0084	0.9996
SAC-Cd	87.5	64.2	54.73	0.0821	0.9160	98.04	0.0453	0.9801

The obtained results reveal that the linear correlation coefficients (R^2) of the pseudo-second-order model are close to 1 (0.98-0.99) for adsorbed Cd^{2+} ions for both AAC and SAC cryogel. Additionally, the calculated equilibrium adsorption values q_e^{cal} of pseudo-second-order kinetics better fits the experimental capacity records with the maximum difference of 3 and 11% for AAC and SAC cryogel, respectively.

The appearance of adsorbed Cd^{2+} metal ions on the cryogels surface was evidenced by point EDS analysis and is presented in **Fig. 6.2**. Even though the EDS technique is semi-quantitative, the results fit well with the experimental results (**Table 6.1**) and overall picture of elemental analysis confirms that AAC cryogel has higher adsorption capability compare

with SAC sample. The conducted EDS mapping analysis images reveal that adsorbed metal ions are evenly distributed over the entire surface of the polymers (**Fig. B1, B2**). Also, during the EDS analysis was detected that after the elimination of heavy metal ions by AAC cryogel the presence of nitrogen was not detected, while in parent polymer the N content reaches 12.65 % (**Fig. 6.2C**). This occurrence could be described by the involvement of amino groups in the complexation reaction of metal ions and hiding by larger heavy metal ions. Also, after the interaction with cadmium, the EDS technique did not detect any trace of Na ions, which also indicates the ion-exchange nature of the removal.

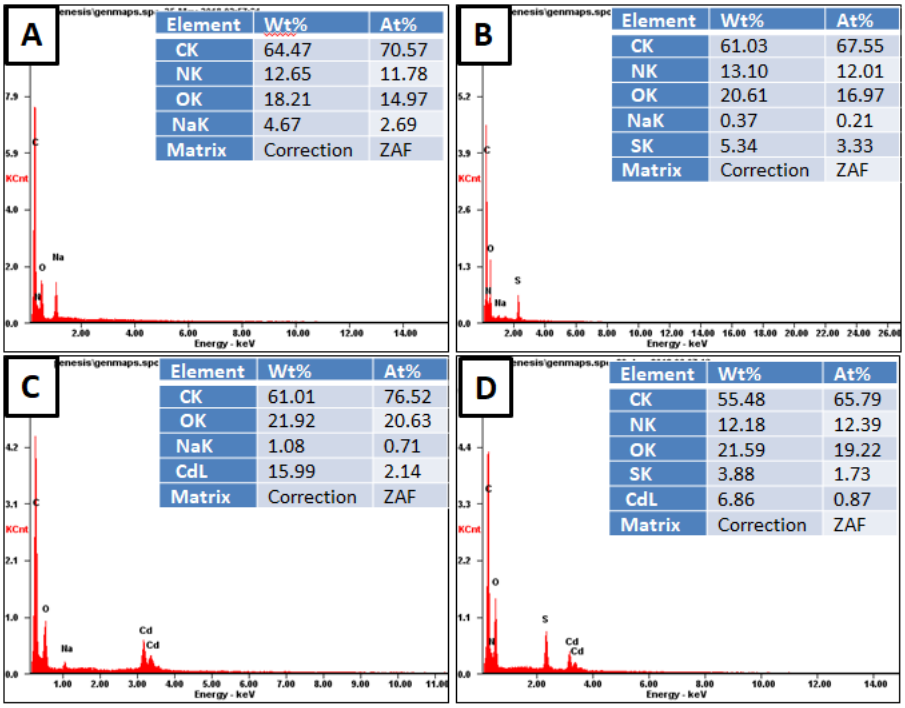

Fig. 6.2. Elemental composition of the cryogels before and after interaction with metal ions according to spot EDX analysis A) AAC, B) SAC, C) AAC-Cd and d) SAC-Cd.

6.4 Effect of pH on metal ions adsorption

The pH is one of the most influential characteristics affecting the adsorption of metal ions. In alkaline environments, at higher pH, metal ions possible react with hydroxide ions to produce insoluble complexes, making removal of metals difficult. At this reason, all the pH measurements were done at pH 5.5 and lower. As it was predicted from the zeta potential measurements (**Fig. 4.4, Chapter 4**) it was found that the adsorption of metal ions on cryogels depends on pH values. At the pH 1.0, the Cd^{2+} ions adsorption by both cryogels

was insufficiently high, about 21 mg/g removal capacity (**Fig. 6.3**). The low removal efficiency at highly acidic media could be attributed to ionic repulsion cationic metal ions with the positively charged functional groups of cryogels [272]. With the rise of the pH to 3.0, conversely, the adsorption capability increased almost 5-7 times for Cd^{2+} ion removal by the SAC and AAC cryogels comparing with values at pH 1.0. This rapid growth in adsorption could be endorsed to changes in the surface charges of both polymers, which perfectly correlate with results presented at Fig 4.4. Removal of the Cd^{2+} increased gradually with an increase of the initial pH from 3.0 to 5.0 and pointed the maximum adsorption capacity of Cd^{2+} ions as 182.8 mg/g by AAC and 101.1 mg/g of SAC. At higher pH values, redundant hydroxyl ions may provoke strong electrostatic interactions of the metal ions with the negatively charged functional groups of cryogels, which causes immediate improvements in adsorption capacity.

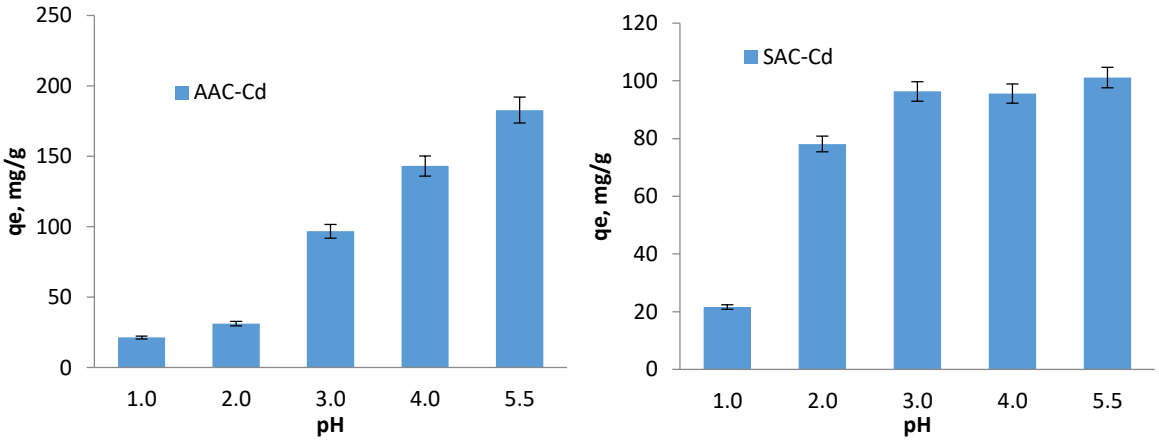

Fig. 6.3. Equilibrium loading of Cd^{2+} ions by AAC (A) and SAC (B) cryogels at different pH values.

6.5 Effect of metal ions initial concentration and cryogels loading for adsorption isotherms

Three equilibrium adsorption isotherms for Cd^{2+} removal by AAC and SAC cryogels are presented in **Fig 6.4(A,B)**. The manipulations with varying the mass of samples and different initial concentrations of metal ions were done to evaluate the adsorption behaviour of polymers in case of various loading of cryogels and initial low/high concentrations of ions. In the first adsorption equilibrium isotherm experiment (exp#1) the constant concentration metal ion (100 mg/L) under the dosage from 0.0025 to 0.07 g adsorbent was used. The

second set of isotherm experiments (exp#2) were conducted by immersing 0.07 g of cryogels into 100 mL solution of metal ions with various initial concentrations from 100 to 1000 mg/L. The last series of experiments (exp#3) were done by adsorption of selected metal ions from 100 mL 1000 mg/L solution varying the mass of polymers from 0.1 to 0.9 g. As is clear from the graphs, the removal capacity increases with the increase of initial concentration of metal ions in the solution. The results show that binding capacities of AAC cryogel were reached the maximum 248.6 mg/g for Cd^{2+} whereas SAC polymer reached 131.9 mg/g. However, the average adsorption capacity reached by AAC cryogel is around 200 mg/g and around 120 mg/g for SAC cryogel. These results fully correspond to the kinetic studies outcomes and reveal that, nor high/low concentration nor various loading do not significantly play a role in the Cd^{2+} adsorption behaviour by cryogels.

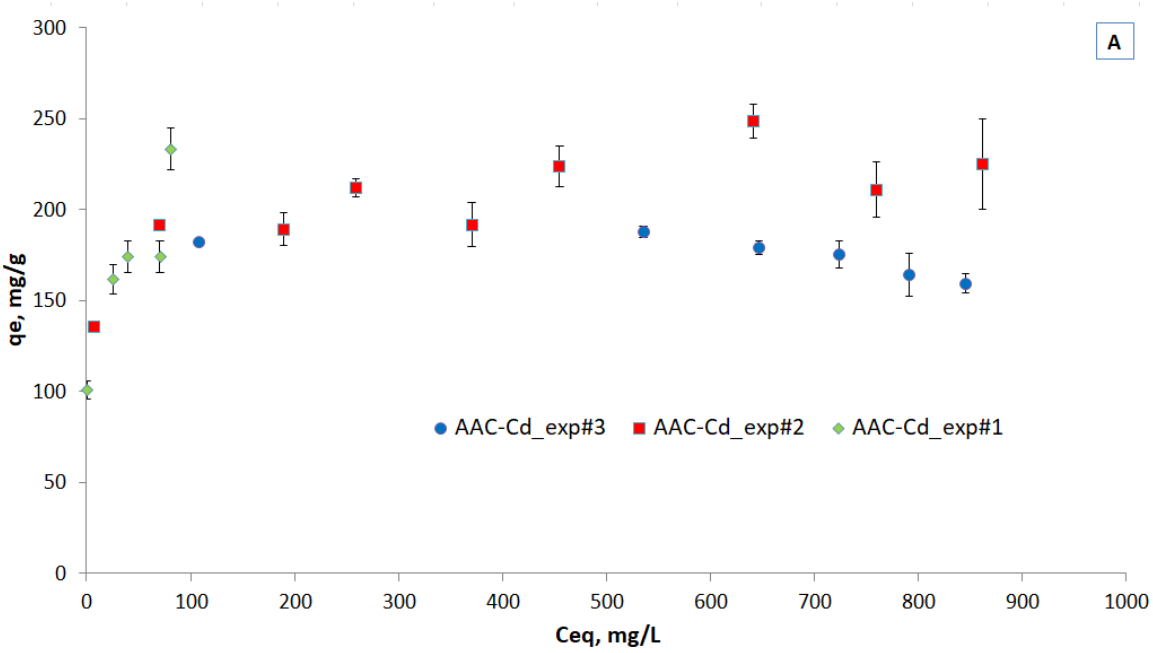

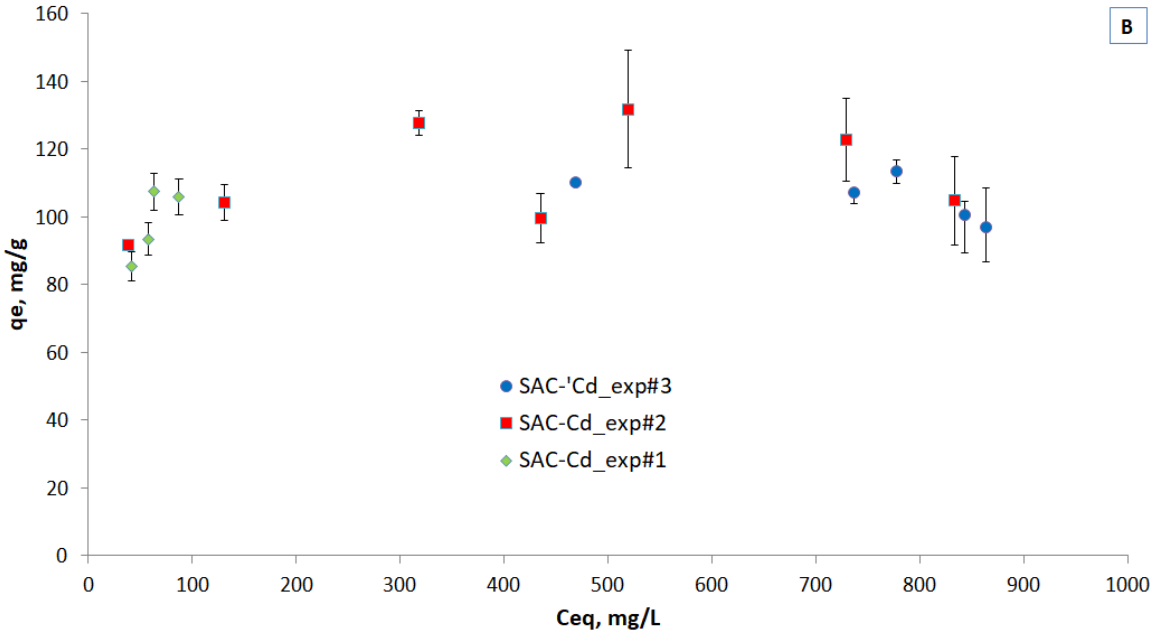

Fig. 6.4. Isotherms of metal ions removal by cryogels A) AAC, B) SAC.

In order of investigation of fitting the experimental isotherms values (experiment #2) to widely use classical models, the Langmuir and Freundlich isotherm models were used for the determination of adsorption of heavy metals on the surface of the materials. The choice of experiment #2 data was made as this is the procedure followed by the vast majority of papers for the derivation of adsorption isotherms in the adsorption literature.

Table 6.2. Parameters of isotherm models for metal ions sorption by cryogels.

		Langmuir model				Freundlich model		
	q_{max}^{exp} (mg/g)	q_m (mg/g)	K_L (L/mg)	R^2	R_L	n	K_F	R^2
AAC-Cd	248.6	263.1	0.0218	0.9269	0.9978	0.105	113.4	0.8171
SAC-Cd	131.9	113.6	0.2829	0.9662	0.9725	0.1212	59.37	0.8726

From the results of used models (**Table 6.2**) was found that the correlation coefficient (R^2) of the Langmuir isotherm model was higher than of the Freundlich isotherm model for both cryogels and the obtained maximum capacities are close to the experimental ones. Also the values of R_L in the range 0–1 confirm the favourable uptake of the metal ions by both polymers.

Adsorption capacities of both AAC and SAC cryogels toward Cd^{2+} are very high and comparable to other 3D polymers found in the literature. Godiya et al fabricated carboxymethyl cellulose/polyacrylamide composite hydrogel for removal Cd^{2+}, Pb^{2+} and Cu^{2+} ions from aqueous solutions. The maximum removal capacity of Cd^{2+} was observed as 256.4 mg/g at pH 5.5 and initial metal concentration 100 ppm [271]. Elgueta et al used the same monomer as was used for SAC cryogel, AMPS co-polymerized with HEMA and used for adsorption of various metal ions, including Cd^{2+}, at concentration from 100 to 1000 ppm and different pH [273]. In this study was observed that at pH 5.0 samples reached maximum adsorption capacity valued 226 mg/g. **Table 6.3** summarizes the 3D polymeric adsorbents used for the removal of Cd^{2+} from water and their efficiency.

Table 6.3. Polymeric materials for the removal of targeted metal ions from the aqueous media.

Metal ion	Adsorbent type	Initial Cd^{2+} concentration [mg/L]	Initial pH	Metal compound	Maximum removal capacity (mg/g)	Reference
Cd^{2+}	GO-PEI hydrogel	100	7.0	$CdCl_2$	175	[274]
	p(AM-AMPS) hydrogel	1000	5.0	$Cd(NO_3)_2$	510.8	[262]
	p(AMPS-VP) hydrogel	200	6.21	$Cd(CH_3CO_2)_2$	70.3	[263]
	p(HEMA-AMPS) hydrogel	1000	5.0	$Cd(NO_3)_2$	226	[273]
	CMC-PAM hydrogel	100	5.5	$Cd(NO_3)_2$	256.4	[271]
	NIPA-BISS hydrogel	300	6.0	$Cd(NO_3)_2$	130	[275]
	NaAlg-g-poly(AMPS-AA-AM) hydrogel	500	7.0	$Cd(NO_3)_2$	456.6	[276]
	p(AMPS-DVE-3) hydrogel	560	5.0	$Cd(NO_3)_2$	134.4	[247]
	Jute/PAA hydrogel	400	6.0	$Cd(NO_3)_2$	401.7	[277]
	AAC cryogel	100	6.0	$Cd(NO_3)_2$	248.6	This research
	SAC cryogel	100	6.0	$Cd(NO_3)_2$	131.9	

6.6 Mechanisms of removal

The functional groups of cryogels can act as ion-exchangers and also chemical reactions rendering the removal mechanism of metal ion complex. One of the proposed removal mechanisms is the ion exchange process between H^+ and/or Na^+ and conjugated phosphate groups in the cryogel structure with metal ions from the solution phase followed by complexation of metal ions with functional groups.

The easiest way to prove this statement is to measure the released Na^+ ions after the interaction of cations with cryogels. The Cd^{2+}/Na^+ molar ratio is shown in **Fig. 6.5** and depends on the mass of the cryogel/solution volume ratio. At lower weight of AAC cryogel the molar ratio of Cd^{2+}/Na^+ the higher 0.5, which is the stoichiometric ratio expected when ion exchange takes place. Thus, could be suggested that not only Na^+ was involved in removal process but also other functional groups also played a role. In the case of SAC cryogel, the Cd^{2+}/Na^+ ratio is much higher which means that the released amount of Na^+ is small. This happens due to the low initial concentration of sodium ions in the SAC cryogel and probably also because of the sulfonic acid's H^+, which might be exchanged for cations.

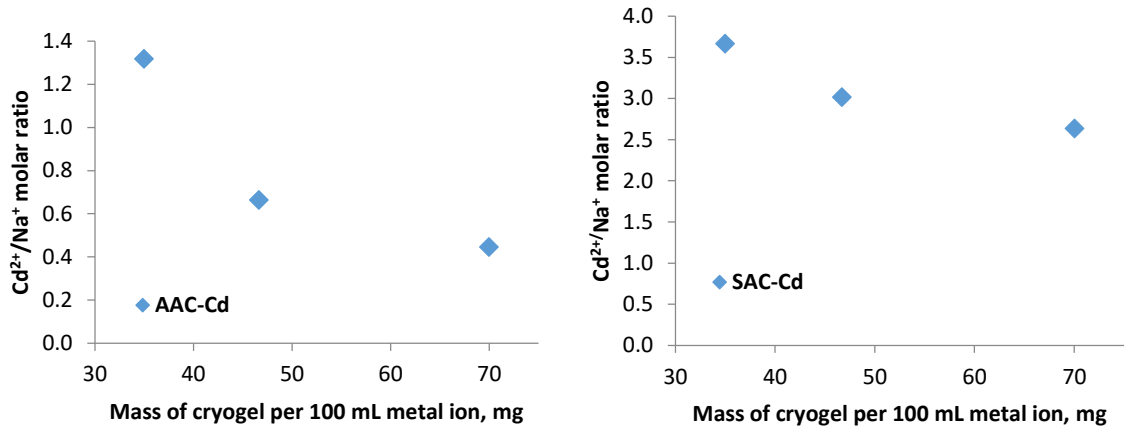

Fig. 6.5. Molar ratio of removed Cd^{2+} ions *vs* released Na^+ during adsorption.

For more in-depth investigation of adsorption mechanism and study the cryogel-metal interaction the XPS characterization were conducted before and after the adsorption of the metal ions for the both cryogels (**Fig. 6.6 (A,B)**). In the AAC cryogel before the adsorption of cations, the three peaks of sodium ions Na 1S peak at ~ 1071.4, Na Auger peak ~ 497.1 and Na 2S peak at ~ 65.1 eV were observed. After the interaction with Cd^{2+} ions the sodium peaks disappeared with the advent of corresponding to metal ions peaks of Cd $3d_{5/2}$ and Cd $3d_{3/2}$ at 405.6 and 412.3 eV indicating the ion-exchange mechanism of sodium ions to selected cations. The C 1S peaks of AAC cryogel at 284.6, 286.8 and 288.2 eV correspond to C-C, C-O and C=O chemical states of carbon [278]. After the interaction of both cryogels with studied cations, the binding energy of C-O and C=O are shifted for 0.7-1.2 eV to higher positions due to the binding of positively charged metal ions. The N 1s core levels are

centered at 399.9 and 401.6 eV, which can be assigned to the non-protonated and protonated amine/amide groups [279]. Moreover, in the structure of parent AAC the small peak of HPO_4^{2-}/PO_4^{3-} is found at the 133.2 eV while after the interaction with metal ions this peak disappeared. This finding also corresponds to the exchange probability of phosphate to Cd^{2+} ions on the surface of polymers. As soon as the most components of SAC are the same to AAC the main difference in presence of sulfonic acid groups in the structure of SAC cryogel. **Fig. 6.6(B)** shows spectrum of SAC cryogel before and after metal ions removal. The S 2p core level spectrum is deconvoluted into two major peaks centered at 167.5 and 169.0 eV which are assigned to 2 $p_{3/2}$ and 2 $p_{1/2}$. These high oxidized states of sulfur are corresponding to sulfonic acid group ($-SO^{3-}$) [280]. After interaction of metal ions the sulfonic acid group peaks shifted for 0.5-0.7 eV to higher region which suggests the formation of coordination bonds of sulfonic acid residues with cations.

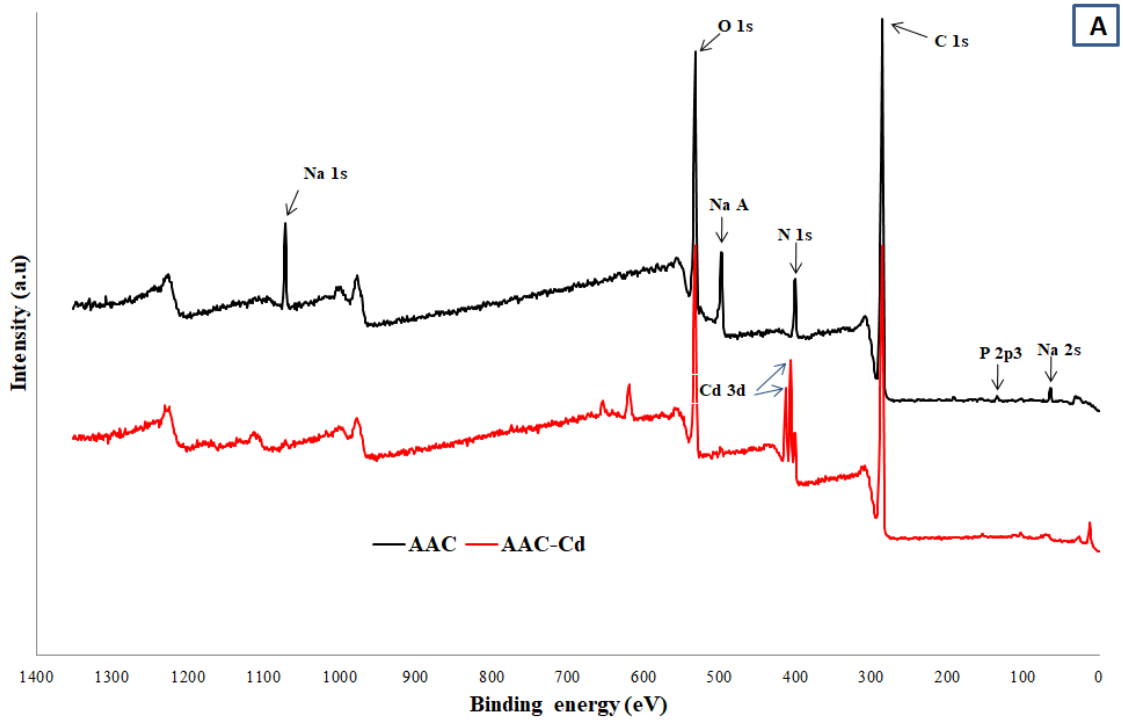

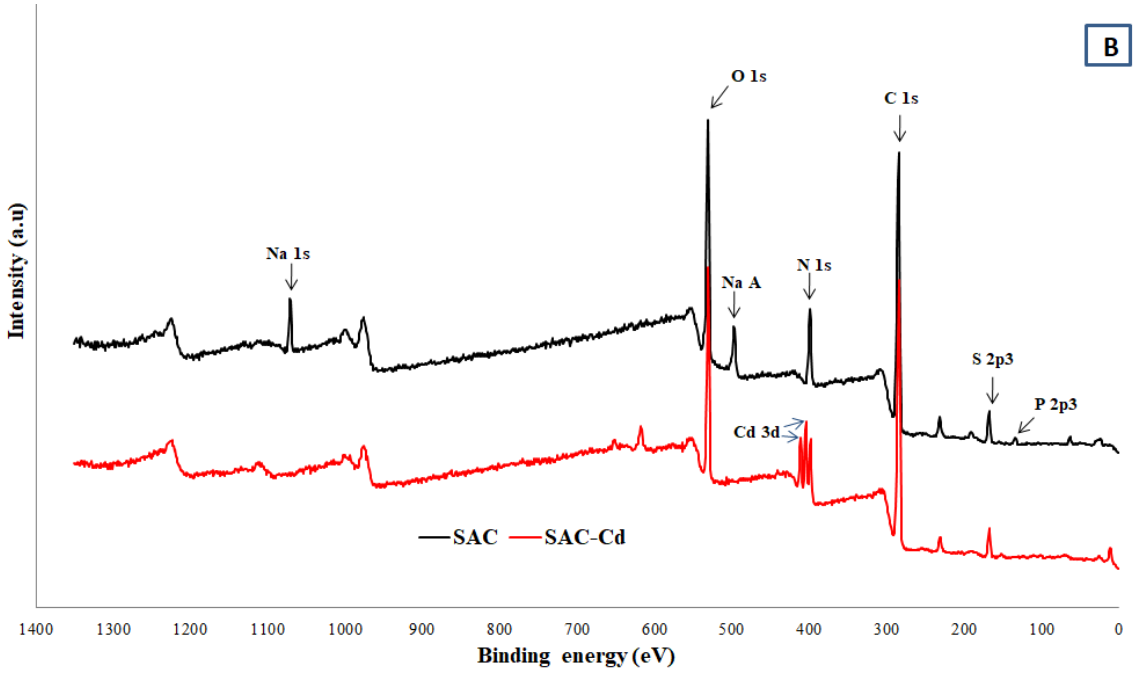

Fig. 6.6. XPS patterns of cryogels before and after metal ions removal a) AAC b) SAC cryogels

Thus, these findings indicate not only ion-exchange mechanism of adsorption but also the involvement of the carboxylic and sulfonic groups in the chelation process, which resulted in the high adsorption capacity of the synthesized cryogels.

The proposed mechanisms of metal ions removal on an example of bivalent ions are presented on **Fig. 6.7(A)** for AAC and **Fig. 6.7(B)** for SAC cryogels.

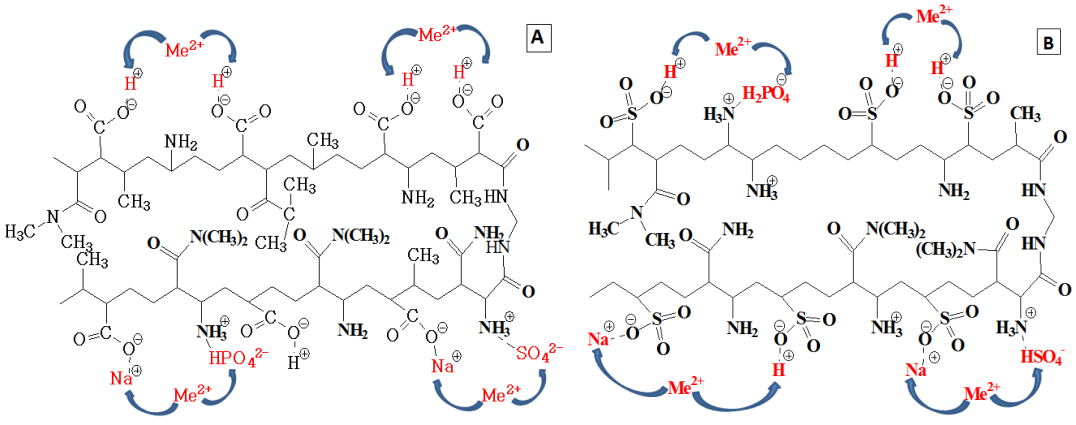

Fig. 6.7. Proposed complexation of bivalent metal ions with functional groups of AAC (A) and SAC (B) cryogels.

6.7 Leaching experiments

Synthesized and used for adsorption AAC and SAC cryogels showed negligible leaching of Cd^{2+} ions, it was less than 1% of total adsorbed metal ions under neutral pH after 30 days (**Table 6.4**).

Table 6.4. Leaching experiment of metal ions from AAC and SAC cryogels at pH 6.5*.

Adsorbent	Total adsorbed metal ions [mg]	Leached metal ion after 30 d [mg]	Leached metal ion after 30 d [%]
AAC-Cd	10.1	0.0007	0.007
SAC-Cd	5.97	0.0353	0.61

*The experimental conditions: 0.07 g of material in 100 mL of 100 mg/L metal ions solution

6.8 Summary

Two types of macroporous cryogels were studied towards Cd^{2+} removal from cadmium nitrate solutions. The results demonstrate a high sorption capacity and fast kinetics of cadmium sorption by both cryogels. The obtained binding capacities of AAC cryogel were reached the maximum 248.6 mg/g, whereas SAC polymer reached 131.9 mg/g. The cation removal mechanism was studied by XPS technique and it was found that ion exchange followed by complexation reactions is the main mechanism of cations removal.

CHAPTER 7
STRONTIUM AND CESIUM REMOVAL STUDIES

7.1 Introduction

With increasing energy consumption, the development of alternative energy sources is becoming increasingly popular. However, despite several advantages of nuclear power, unsafety use of nuclear energy poses many dangers to people and the environment, including the leakage of radioactive waste from tanks and the uncontrolled release of enormous amounts of radionuclides caused by nuclear accidents, such as those in Chernobyl and Fukushima [19]. Among the harmful radionuclides leaked from nuclear power plants accidents, radioactive cesium (^{137}Cs) and strontium (^{90}Sr) have the most substantial toxic effects of emitting beta-particles and gamma rays. Both of radioactive Cs and Sr radioisotopes have half-life around 30 years, therefore, it is imperative to remove cesium from the environment and wastewater for sustainable environmental preservation [20]. Moreover, due to chemical similarity of ^{137}Cs and ^{90}Sr to potassium and calcium, respectively, the released isotopes after a nuclear accident can be easily incorporated into terrestrial and aquatic organisms.

Removal of radioactive elements and most toxic heavy metal ions from wastewater is essential, along with other metal ions which have been the focus of removal studies by various materials and technique [20,260–263]. Several methods have already been considered to recover metal ions from wastewater including chemical precipitation [264], chemical coagulation/flocculation [265], membrane filtration [266], ion-exchange processes [267], bioremediation [268] and adsorption [269]. Typical adsorbents such as activated carbons, natural zeolites and clays are of interest but often the materials have low adsorption capacity or to be treated chemically to produce desirable adsorption properties [185,186,236,270]. Therefore, a simple synthesis route of materials with high adsorption is clearly profitable for practical applications.

7.2 Chapter Overview

In this chapter the results of the removal of strontium and cesium ions by two types of cryogels are presented. The effect of pH on the adsorption, the kinetic studies and isotherm

experiments results are thoroughly investigated and are shown in this chapter. Also, the results of investigations of various ratios of cryogel:metal loading, the effect of the concentration of metal ions on the adsorption capacity of cryogels are presented. Using multiple analysis methods, potential mechanisms for the adsorption of strontium and cesium ions were determined. This chapter also presents the result of testing cryogels and commercial sorbents (ion exchange resin and zeolite) for the removal of strontium and cesium ions from various aqueous matrices.

7.3 Adsorption kinetics

The main parameters that adsorbents should have are the high sorption capacity and fast removal rates towards targeted pollutants. The sorption kinetic experiments of Sr^{2+} and Cs^{+} ions on cryogels were conducted in batch mode at pH 4 and 5 but due to the similarity of the adsorption behavior, the results of adsorption at pH 5 are given and illustrated in **Fig. 7.1**. Because at pH 4 and higher both cryogels serve as cation-exchangers, the difference in pH did not play a significant role in the rate and adsorption capability of cryogels.

It is evident from kinetics graphs that AAC sample is faster in the removal of both cations in first 8 hour, while the SAC sample need time to start adsorbing metal ions. In the first hour AAC cryogel can remove about 42 and 45 % from Sr^{2+} and Cs^{+} solution while SAC removed only about 14 and 21%, respectively. After the 24 h of contact with strontium-containing solution, both cryogels reached the equilibrium at removal values 86% for AAC and 48% for SAC samples. In case of Cs^{+} ions, both AAC and SAC cryogels also reached the equilibrium in 24h with maximum removal 58 and 63%, respectively.

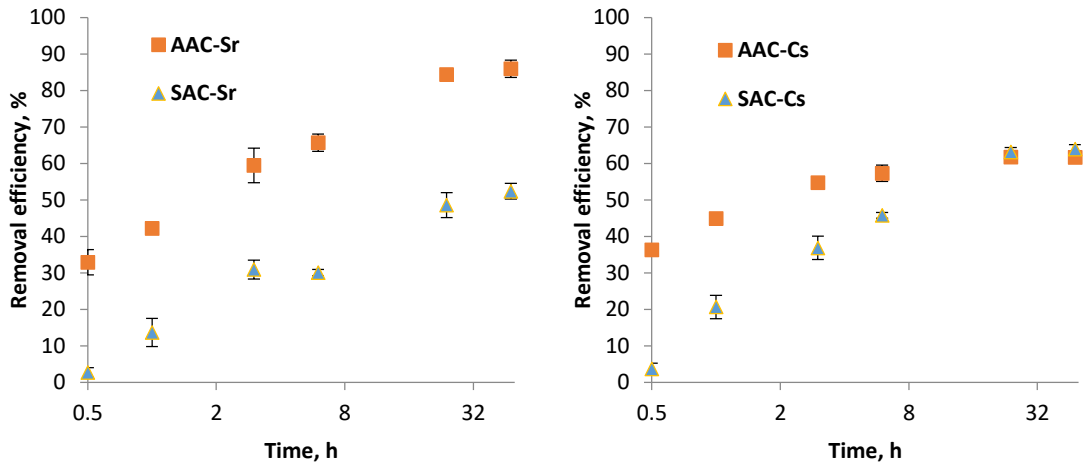

Fig. 7.1. Adsorption kinetics of Sr^{2+} and Cs^{+} ions on the AAC and SAC cryogels (70 mg of cryogel in 100 mL of solution) at pH 5.

The Eq. 3.4 and 3.5 (Chapter 3) of the Lagergren pseudo-first-order and pseudo-second-order models were used to determine the adsorption nature of polymers using the experimental data. The calculated parameters for kinetic models are shown in **Table 7.1**.

Table 7.1. Parameters of kinetic models for metal ions sorption by cryogels.

			Pseudo-first order			Pseudo-second order		
	q_e^{exp} (mg/g)	ct (mg/g)	q_e^{cal} (mg/g)	K_1 (min^{-1})	R^2	q_e^{cal} (mg/g)	K_2 (g mg^{-1} min^{-1})	R^2
AAC-Sr	122.7	134.8	80.65	0.1544	0.9199	128.21	0.0102	0.9995
AAC-Cs	88.1	114.5	36.05	0.2468	0.8897	87.72	0.0045	0.9999
SAC-Sr	74.8	47.3	55.32	0.0606	0.9459	84.47	0.0644	0.9796
SAC-Cs	91.4	72.2	83.49	0.1902	0.9299	100.00	0.0431	0.9818

The obtained results reveal that the linear correlation coefficients (R^2) of pseudo-second order model for AAC cryogel are very close to 1 for both adsorbed metal ions, while for SAC cryogels the R^2 results are a bit lower (~0.98) but still higher than R^2 of pseudo-first order model. Additionally, the calculated equilibrium adsorption values q_e^{cal} of pseudo-second order kinetics better fits the experimental capacity data with the maximum difference of 12% for SAC-Sr sample. It is known that if the adsorption system follows a pseudo-

second order kinetics, then the rate limiting step may be chemical adsorption involving valence forces through sharing or exchange of electrons between the adsorbent and sorbate.

The presence of adsorbed Sr^{2+} and Cs^{+} metal ions on the cryogels surface was verified by point EDS analysis and is presented in **Fig. 7.2**. The overall picture of elemental analysis confirms that AAC cryogel has higher adsorption capability compare with SAC sample. The conducted EDS mapping analysis images reveal that all adsorbed metal ions are evenly distributed over the entire surface of the polymers (**Fig. C1-C4**). Also, during the EDS analysis was observed that after the adsorption of heavy metal ions by AAC cryogel the presence of nitrogen was not detected, while in parent polymer the N content reaches 12.65 % (Chapter 4, **Fig. 4.5**). This phenomenon could be described by involvement of aminogroups in complexation reaction of metal ions and hiding by larger heavy metal ions.

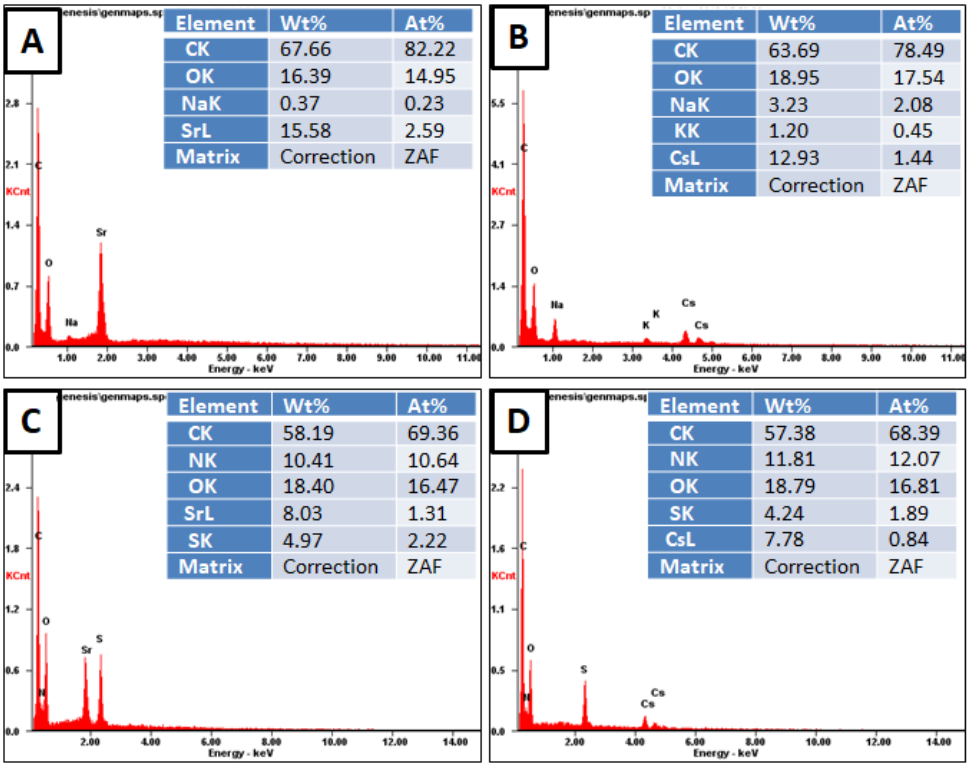

Fig. 7.2. Elemental composition of the cryogels after interaction with metal ions according to spot EDX analysis A) AAC-Sr, B) AAC-Cs, C) SAC-Sr, D) SAC-Cs.

7.4 Effect of pH on metal ions adsorption

The pH of the solutions after the dissolution of 100 ppm Sr^{2+} and Cs^{+} ions of nitrate salt were around 5.5. To avoid the precipitation of studied metal ions the pH of the solution at values 5.5 and lower were chosen for experiments. In alkaline environments, at higher pH values metal ions possible react with hydroxide ions to produce insoluble complexes. As it was seen from Cd^{2+} removal studies the adsorption decreases with decrease of pH. The same phenomenon was observed for strontium and cesium ions. At a highly acidic pH value of 1.0, the adsorption capability of AAC and SAC samples for Sr^{2+} and Cs^{+} was around 44-47 mg/g and 33 mg/g, respectively (**Fig. 7.3**). As the pH increased to 3.0, however, the removal efficiency doubled for Sr^{2+} and Cs^{+} ions and an increase with increase of the pH and showed the highest removal capacity of Sr^{2+} and Cs^{+} ions as 123.7 and 139.4 by AAC and 87.5 and 135.9 mg/g of SAC, respectively. At higher pH values, excessive hydroxyl ions may cause a strong electrostatic attraction with the metal ions for the negatively charged adsorption sites, which causes sudden increases in adsorption capacity.

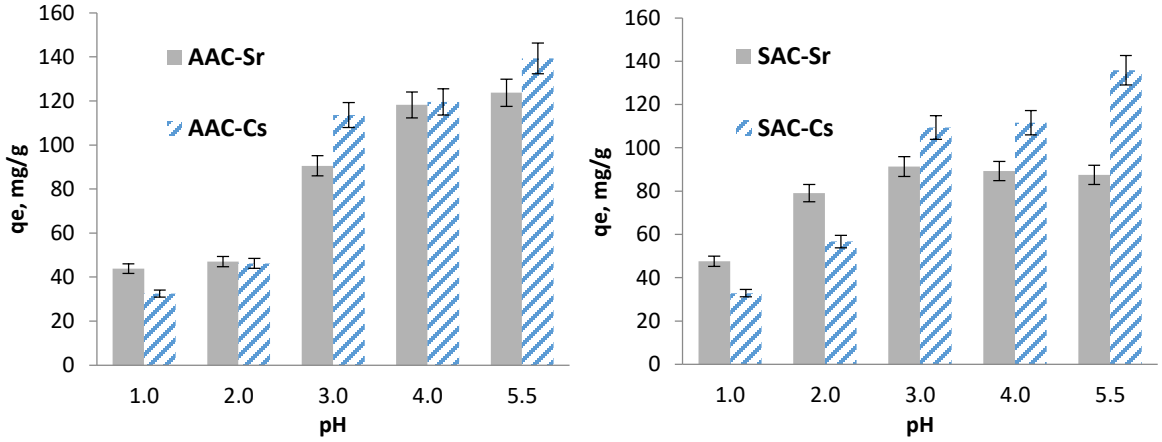

Fig. 7.3. Equilibrium loading of metal ions by AAC (A) and SAC (B) cryogels at different pH values.

7.5 Effect of metal ions initial concentration and cryogels loading for adsorption isotherms

To evaluate the adsorption behavior of polymers in case of various loading of cryogels and initial low/high concentrations of Sr^{2+} and Cs^{+} ions three equilibrium adsorption isotherms were done and presented in **Fig 7.4(A-D)**. In the first set of experiments (exp#1) the various dosage from 0.0025 to 0.07 g of polymers were immersed into the constant concentration

metal ion (100 mg/L). The second batch of isotherm experiments (exp#2) was conducted by putting 0.07 g of cryogels into 100 mL solution of metal ions with various initial concentrations from 100 to 1000 mg/L. The last series of experiments (exp#3) were done by removing of selected metal ions from 100 mL 1000 mg/L solution varying the mass of polymers from 0.1 to 0.9 g. As is clear from the graphs the removal capacity increases with increase of initial concentration of metal ions in the solution. The results show that the maximum adsorption capacities of AAC cryogel were 361.6 mg/g of Cs^{+} and 209.3 mg/g for Sr^{2+}. In contrast, SAC polymer also was best for Cs^{2+} with maximum capacity of 258.7 mg/g, while Sr^{2+} adsorption reached 210.5 mg/g.

In adsorption literature the derivation of isotherms is made by varying the aqueous phase concentration by keeping adsorbent mass to solution volume constant. Interestingly, there are no studies comparing the standard method with alternatives, for instance by varying the weight to volume ratio under constant aqueous phase concentration. Obviously, if only adsorption takes place the process must result in a single isotherm, however in many systems a combination of mechanisms exist and such a comparison of methods becomes interesting. For instance, is well known that the isotherms of ion exchange systems depend on total normality, a phenomenon called concentration-valence effect [159]. Taking into account that the removal mechanism of metals on cryogels is complex, being a combination of adsorption, complexation and ion exchange, all reversible processes, is not the differences between the isotherms derived by using different experimental procedures for Sr^{2+} and Cs^{+} are not surprising. The mechanisms of potential removal are discussed in more details in section 7.6.

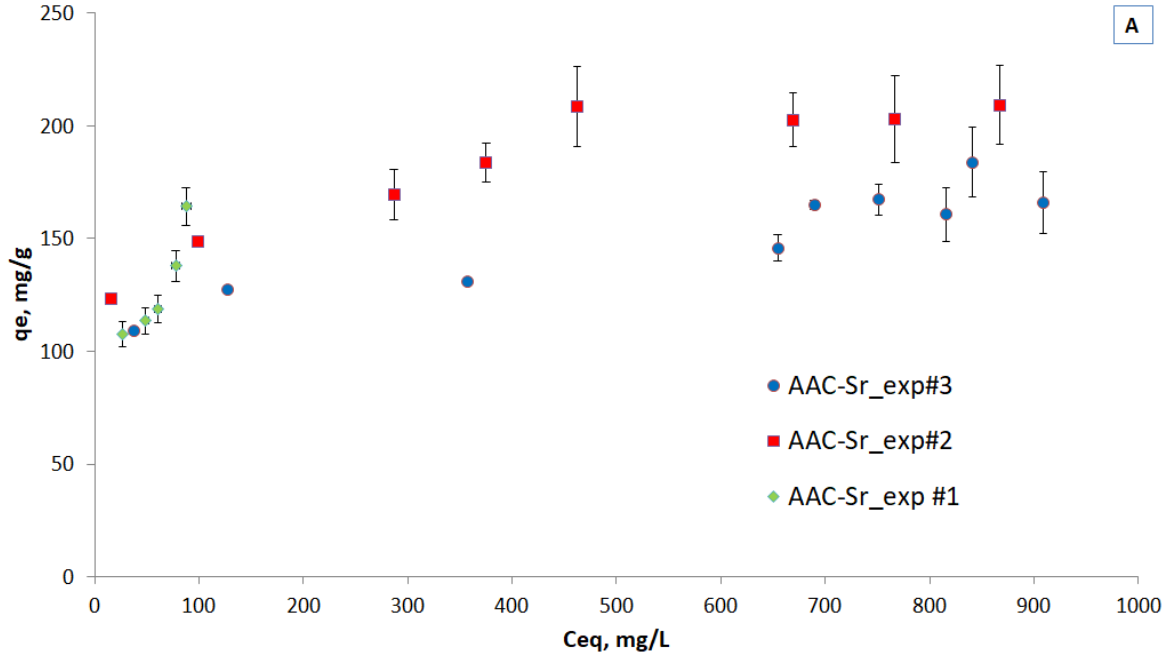
A
250
200
150
100
50
0
qe, mg/g
0
100
200
300
400
500
600
700
800
900
1000
Ceq, mg/L
AAC-Sr_exp#3
AAC-Sr_exp#2
AAC-Sr_exp #1

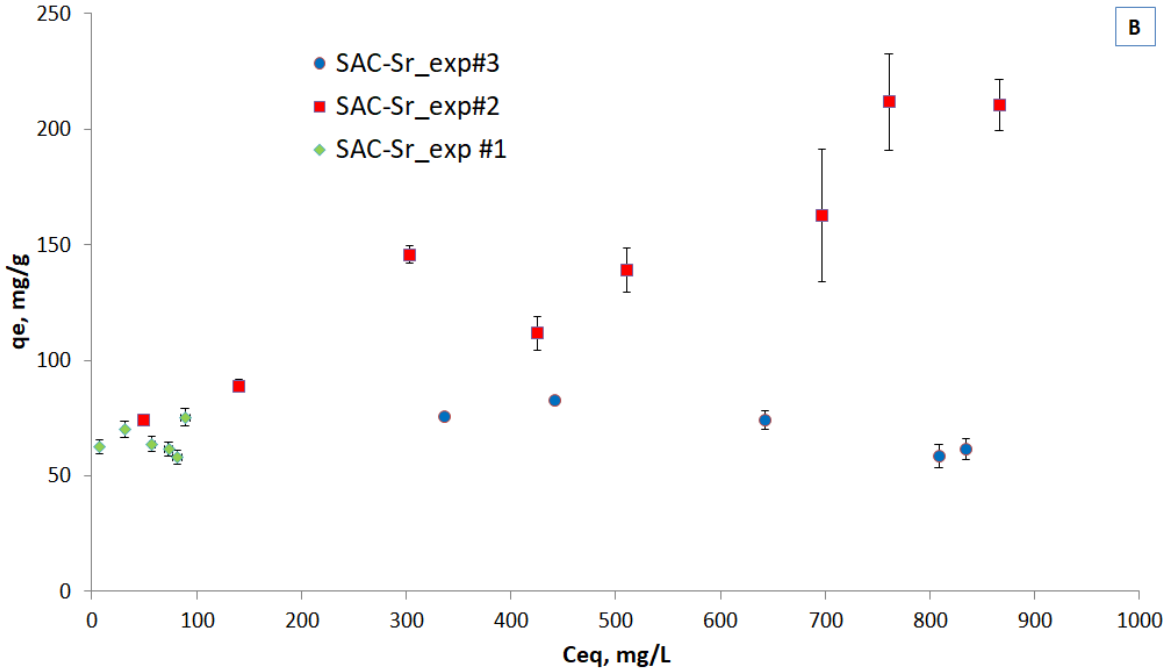
B
250
200
150
100
50
0
qe, mg/g
0
100
200
300
400
500
600
700
800
900
1000
Ceq, mg/L
SAC-Sr_exp#3
SAC-Sr_exp#2
SAC-Sr_exp #1

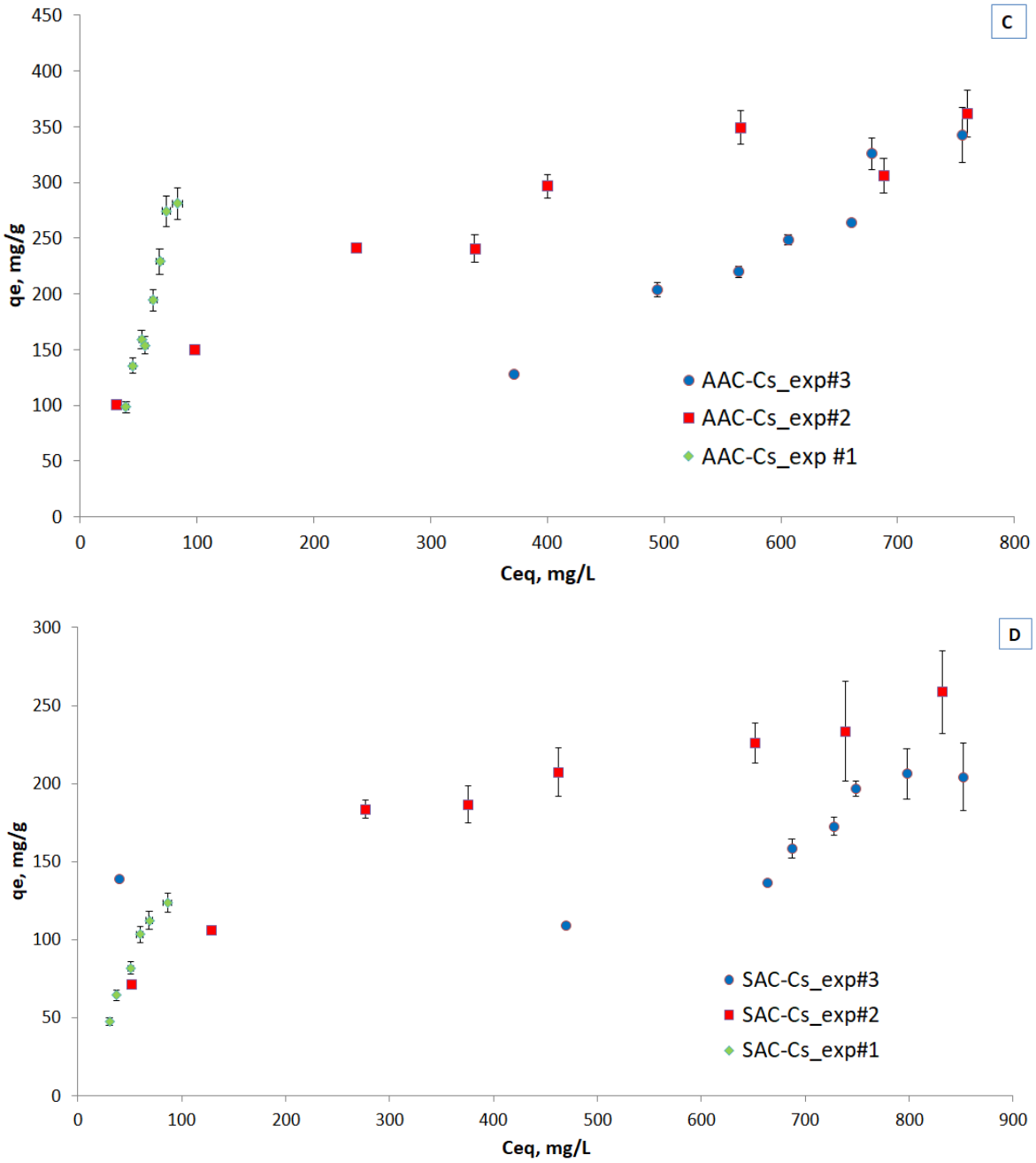

Fig. 7.4. Isotherms of metal ions removal by cryogels.

In order of investigation of fitting the experimental isotherms values (experiment #2) to widely use classical models, the Langmuir and Freundlich isotherm models were used for the determination of adsorption of heavy metals on the surface of the materials. The choice of experiment #2 data was made as this is the procedure followed by the vast majority of papers for the derivation of adsorption isotherms in the adsorption literature.

The Langmuir sorption isotherm assumes the monolayer adsorption of particles onto the homogeneous surfaces while Freundlich sorption isotherm corresponds to multilayer adsorption on energetically heterogeneous surface.

Table 7.2. Parameters of isotherm models for metal ions sorption by cryogels.

		Langmuir model				Freundlich model		
	q_{max}^{exp} (mg/g)	q_m (mg/g)	K_L (L/mg)	R^2	R_L	n	K_F	R^2
AAC-Sr	209.3	217.4	0.2393	0.9944	0.9976	0.1373	82.45	0.9484
AAC-Cs	361.6	400.0	0.0067	0.9566	0.9993	0.3976	25.62	0.9707
SAC-Sr	210.5	242.9	0.0052	0.9359	0.9994	0.3563	16.74	0.8425
SAC-Cs	258.7	312.5	0.0046	0.9851	0.9995	0.4584	12.05	0.9769

From the results of used models (**Table 7.2**) was found that the correlation coefficient (R^2) of the Langmuir isotherm model was higher than of the Freundlich isotherm model for both cryogels in Sr^{2+} solutions and the obtained maximum capacities are close to the experimental ones. In the case of Cs^+ ions, R^2 for both models are close to 1, assuming that the adsorbate is attracted to various types of functional groups on the surface of the material due to the monovalence of cesium ions.

The literature search of other 3D materials used to remove Sr^{2+} and Cs^+ shows that adsorption capacities of AAC and SAC are much higher than many polymers. Garg et al synthesized a series of poly-N-vinyl imidazole based hydrogels by adding four different cross-linkers for the removal of Sr^{2+} ions [281]. The authors reveal that p(N-Vim-*cl*-DVB) hydrogel showed the best adsorption results with maximum capacity 247.4 mg/g at pH 7.0. In another study, Choe and co-authors fabricated alginate/humic acid/Fe-aminoclay hydrogel for targeted removal of Sr^{2+} ions at different conditions of pH, temperature and competing cations. The result of the study showed that in single-metal solution the synthesized hydrogel able to remove up to 45.6 mg/g of Sr^{2+} ions, while from multi-component model solution only 8.2 mg/g [282]. In case of Cs^+ removal, a lot of studies were done by use of Prussian blue modified polymers and clays. Zhao et al reported the production PAMPS/PAAm hydrogel modified by $[Fe(CN)_6]$ and examined polymers composite's capability to removal Cs^+ from 1000 ppm CsCl solution at pH 7.0 [283]. The result showed the high uptake of cesium ions by coupling effect of Cs^I with the framework of Prussian blue

crystals and reached the maximum capacity 420 mg/g of composite. In the studies of Bratskaya et al, macroporous Co^{2+}-chelated carboxyalkylchitosan cryogels were fabricated and modified with potassium ferrocyanide for selective capture of cesium ions. The results of the experiments showed that CEC/Co(II)[$Fe(CN)_6$] cryogel able to adsorb up to 132 mg/g of Cs^+ from 264 ppm solution at pH 3.0 [284]. **Table 7.3** summarizes the 3D polymeric adsorbents used for the removal of Sr^{2+} and Cs^+ from water and their efficiency.

Table 7.3. Polymeric materials for the removal of targeted metal ions from the aqueous media.

Metal ion	Adsorbent type	Initial metal concentration [mg/L]	Initial pH	Metal compound	Maximum removal capacity (mg/g)	Reference
Sr^{2+}	alginate/humic acid/Fe-aminoclay hydrogel	100	7.0	$Sr(NO_3)_2$	45.6	[282]
	p(N-Vim-*cl*-DVB) hydrogel	1000	7.0	$SrBr_2$	247.4	[281]
	Ag_2O-Sodium niobate nanofiber	50-1000	5.0-11.0	$SrCl_2$	312	[19]
	PSA hydrogel membrane	200	6.0	$SrCl_2$	60.7	[285]
	AAC cryogel	100	6.0	$Sr(NO_3)_2$	209.3	This work
	SAC cryogel	100	6.0	$Sr(NO_3)_2$	210.5	
Cs^+	CEC/Co(II)[$Fe(CN)_6$] cryogel	264	3.0	CsCl	132	[284]
	AMP-PVA-SA hydrogel	100	7.0	CsCl	71.3	[286]
	Fe(III)-SA hydrogel	7.7	10.0	CsCl	24.0	[287]
	KCoHCF-PVA-SA hydrogel	150	2-11	$CsNO_3$	15.0	[288]
	Bentonite-chitosan beads	200	8.5	CsCl	57.1	[289]
	NIPAAm/IA hydrogel	800	8.0	CsCl	120.0	[290]
	CuFC-Fe_3O_4-PVA hydrogel	500	7.0	$CsNO_3$	17.4	[261]
	[Fe(CN)6]-PAMPS/PAAm hydrogel	1000	7.0	CsCl	420	[283]
	AAC cryogel	100	6.0	$CsNO_3$	361.6	This work
	SAC cryogel	100	6.0	$CsNO_3$	258.7	

7.6 Mechanisms of removal

The investigated by FT-IR some functional groups of cryogels can act as ion-exchangers and chelation agents toward cationic metals. The proposed in the previous chapters' mechanisms of removal of cations from aqueous solution may also be applied for Sr^{2+} and Cs^+ ions removal. The released from cryogels mass of Na^+ were measured and Me/Na^+ molar ratio is shown in **Fig. 7.5**. Ideally, if the ion-exchange of Sr^{2+} goes only with Na^+, the molar ratio of

this process should be 2:1, while with Cs^+ it should be 1:1. However, at lower mass of AAC cryogel the molar ratio of Sr^{2+}/Na^+ is higher 0.5, which could be suggested that not only Na^+ was involved in removal process but also other functional groups played a role. In the AAC-Cs sample, the released mass of sodium ions is close to adsorbed cesium, which probably could be suggested and main mechanism of removal. In the case of SAC cryogel, the both Me/Na^+ ratio is much higher which means that the released amount of Na^+ is small. This happens due to the low initial concentration of sodium ions in the SAC cryogel (see Chapter 4, Fig. 4.5) and probably also because of the sulfonic acid's H^+, which might be exchanged for cations.

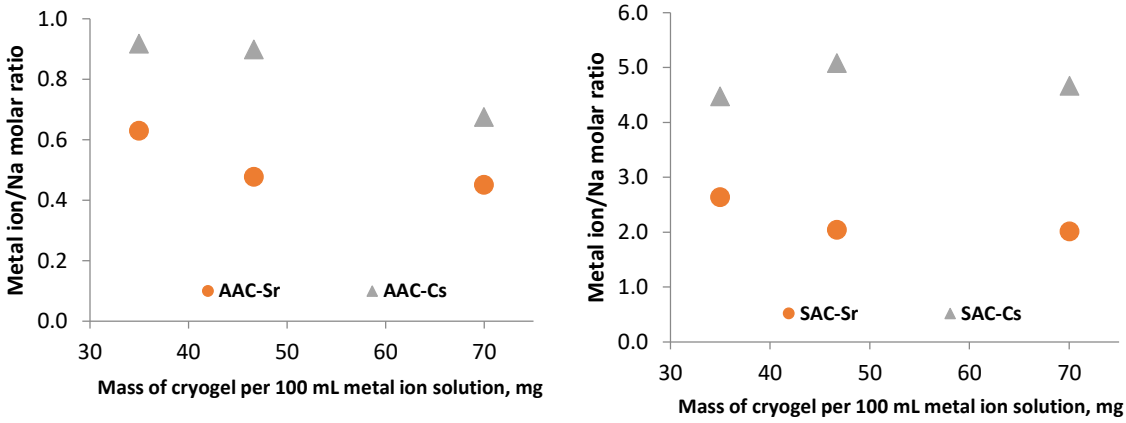

Fig. 7.5. Molar ratio of removed metal ions *vs* released Na^+ during adsorption.

The results of XPS characterization of cryogels before and after adsorption of the metal ions (**Fig. 7.6 (A,B)**) show that peaks of sodium ions Na 1S (~ 1071.4 eV) and Na Auger peak (~ 497.1 eV) of parent AAC and SAC cryogels disappeared with the advent of corresponding to metal ions peaks of strontium at 135.1 eV and cesium peaks at 725.1 and 738.1 eV, indicating the ion-exchange mechanism of sodium ions to selected cations. After the interaction of both cryogels with studied cations, the binding energy of C-O (286.8 eV) and C=O (288.2 eV) are shifted for 0.7-1.2 eV to higher positions due to the binding of positively charged metal ions [278]. As soon as the most components of SAC are the same to AAC the main difference in presence of sulfonic acid groups in the structure of SAC cryogel. **Fig. 7.6(B)** shows spectrum of SAC cryogel before and after metal ions removal. The S 2p core level spectrum is deconvoluted into two major peaks centered at 167.5 and 169.0 eV which are assigned to 2 $p_{3/2}$ and 2 $p_{1/2}$. These high oxidized states of sulfur are corresponding to

sulfonic acid group (-SO^{3-}) [280]. After interaction of metal ions the sulfonic acid group peaks shifted for 0.5-0.7 eV to higher region which suggests the formation of coordination bonds of sulfonic acid residues with cations.

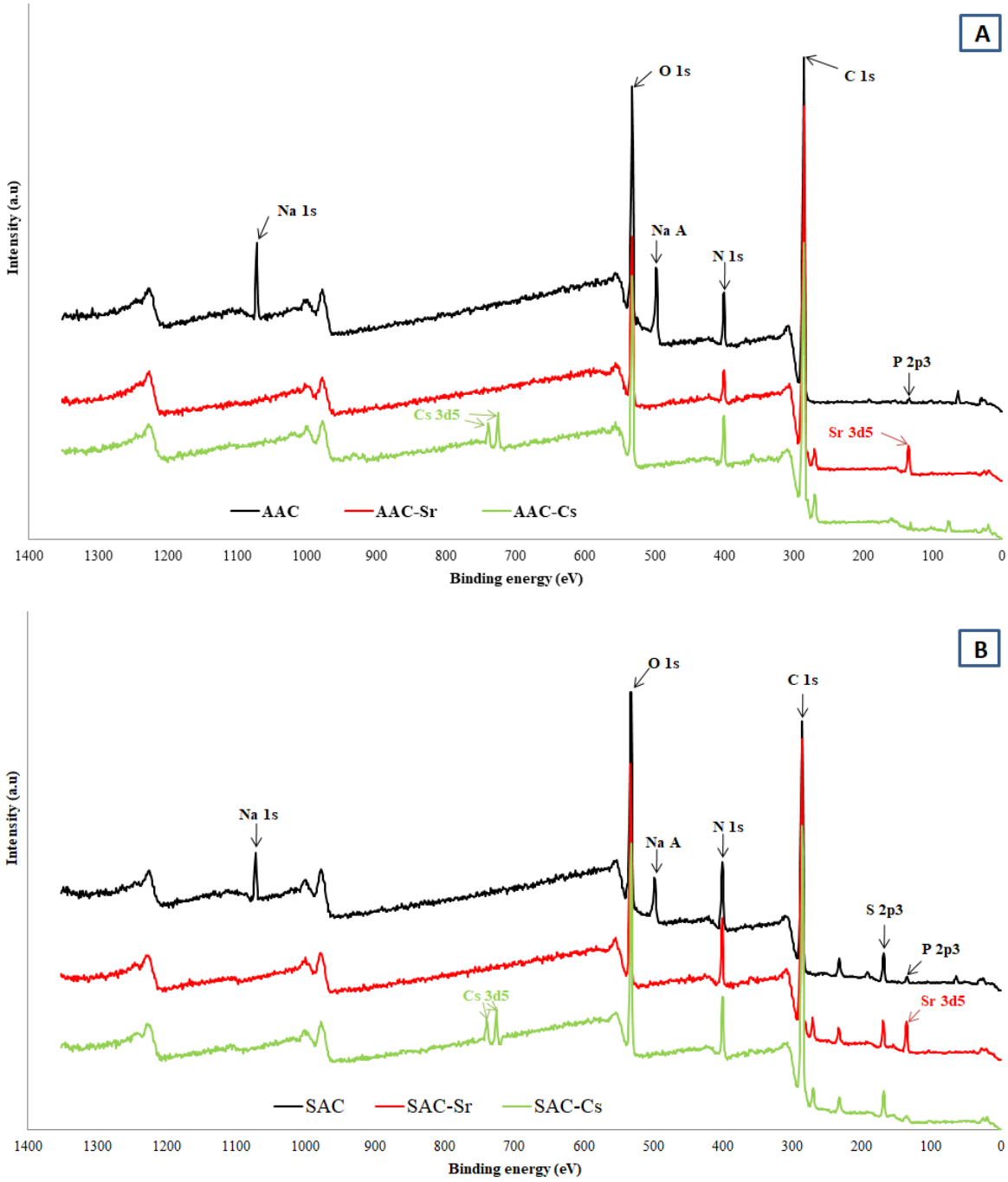

Fig. 7.6. XPS patterns of cryogels before and after metal ions removal a) AAC b) SAC cryogels

Thus, these findings indicate not only ion-exchange mechanism of adsorption but also the involvement of the carboxylic and sulfonic groups in the chelation process, which resulted in the high adsorption capacity of the synthesized cryogels.

7.7 Leaching experiments

Synthesized and used for adsorption AAC and SAC cryogels showed negligible leaching of Sr^{2+} metal ions, it were, less than 1% of total adsorbed metal ions under neutral pH after 30 days (**Table 7.4**). In case of Cs^{+} ions, leaching reached 2.3 and 1.84 % for AAC and SAC, respectively. Presumably, this phenomenon is associated with monovalence of cesium and a weak binding with functional groups of cryogels.

Table 7.4. Leaching experiment of metal ions from AAC and SAC cryogels at pH 6.5*.

Adsorbent type	Total adsorbed metal ions [mg]	Leached metal ion after 30 d [mg]	Leached metal ion after 30 d [%]
AAC-Sr	8.89	0.0656	0.74
AAC-Cs	6.88	0.1585	2.30
SAC-Sr	4.45	0.0418	0.94
SAC-Cs	5.73	0.1054	1.84

*The experimental conditions: 0.07 g of material in 100 mL of 100 mg/L metal ions solution

7.8 Summary

Two types of macroporous cryogels were studied towards Sr^{2+} and Cs^{+} removal from aqueous solutions. The results demonstrated fast removal kinetics and high capacities with AAC cryogel being superior over SAC cryogel. The results show that binding capacities of AAC cryogel were reached 361.6 mg/g of Cs^{+} and 209.3 mg/g of Sr^{2+} whereas SAC polymer also was best for Cs^{+} with maximum capacity of 258.7 mg/g, while Sr^{2+} adsorption reached 210.5 mg/g. The cation removal mechanism was studied by XPS technique and it was found that ion exchange followed by complexation reactions is the main mechanism of cations removal.

CHAPTER 8
IODIDE REMOVAL STUDIES

8.1 Introduction

Iodine is an essential micronutrient required for the operation of the human body's neurological activity and thyroid glands. Depending on the pH and redox conditions of water, iodine exists in iodide (I^-), triiodide (I^{3-}) and iodate (IO^{3-}) forms. Iodine, widely distributed in seawater in the form of iodide, does not pose any possible risk to humans and the environment [291,292]. It is commonly used as a source of iodine products used to treat potable water [293]. Nevertheless, iodide can shape organic species under the oxidative conditions used in water treatment plants, which may subsequently affect people's health issues [294]. Organic sources of iodine, however, are not as harmful as the iodine radionuclides used in uranium fission, as are radioactive nuclear weapons tests and accidental nuclear power plant by-products. [295]. Another cause of radioactive iodide wastes is the therapeutic use of ^{131}I in thyroid cancer care [296]. The radioactive isotopes of iodine ^{129}I and ^{131}I can dissolve in aqueous media and vaporize to air causing environmental hazards [297], and due to extended half-life time (15.7 million years of ^{129}I), it can reason long-standing antagonistic effects on the human metabolic processes [293,298].

The iodide elimination methods, specifically its radioactive forms from water, have paid attention globally, particularly after the accidents in Chernobyl, Ukraine in 1986 and in Fukushima, Japan in 2011, where 1.76×10^{18} Bq and 1.5×10^{17} Bq of ^{131}I, respectively, were discharged to the environment. For fast and efficient iodide removal, new methods are required because current techniques such as anion-exchange have relatively little selectivity and secondary anions are wasted on water. Alternatively, the use of silver nanoparticles (NPs), which selectively react with iodide anions to form insoluble silver iodide (AgI) may improve the situation. It is, however, impracticable to apply directly to iodine a pure Ag NPs or other silver compounds. First of all, the capacity and complexation rates of the elimination mostly rely on the specific surface area of AgNPs [299], and secondly, as a result of the chemistry of AgI in water, it formulae small crystal-like agglomerates and colloids, which are problematic to separate from the aqueous phase [294]. A beneficial procedure to get over these disadvantages is to use silver-modified composites to remove I^- via surface reaction. The summarized in **Table 8.1,** numerous kinds of porous and non-porous materials doped

with AgNPs and its oxides were produced for targeted adsorption of iodide from aqueous solutions. It should be noted that in most studies, the stated removal capacity is a sum of the iodide eliminated by surface reaction and physical adsorption. In these studies, the formed AgI was qualitatively verified by surface characterization techniques like XRD and SEM/EDS, but the surface reaction mechanisms and the possible discharge of Ag ions and subsequent formation of AgI colloidal particles has not been scrupulously investigated. So, a more comprehensive qualitative and quantitative analysis of the mechanism of elimination and quantification of adsorbed iodide and released silver ions is necessary.

Table 8.1. Ag-modified composites for iodide removal from water

Ag-composite	Ag loading (w/w%)	C_o mg/L	q_{max} mg/g	Reference
Ag-activated carbon	1.05	450	38.1	[300]
AgCl-calcium alginate	10.9	0-700	133	[301]
MIL-101(Cr)-SO_3Ag	3.6	920	244	[302]
Ag_2O-Ag/TiO_2	5.8	1150	208	[303]
AgII&MIL101	2	500	43.2	[297]
Ag_2O-Ag_2O_3-ZIF-8	20	600	232	[304]
Ag_2O-$Mg(OH)_2$	32.3	200	368.6	[305]
Ag°-silica aerogel	35.5	17000	88	[306]
Ag-carbon aerogel	10	1.27	0.25	[294]
AgCl-SPAC	34.3	1	160	[307]
Ag_2O-titanate nanolamina	-	500	428	[295]
Ag_2O-sodium niobate nanofibers	-	50-1000	54.5	[308]
Ag°-D201 resin	6.8	300	300	[309]

C_o - initial iodide concentration, mg/L
q_{max} - Adsorption capacity (mg/g)

8.2 Chapter Overview

In this chapter, the results of the modification of cryogels by silver nanoparticles, their characterization by several techniques are described. The formation of Ag^0 and Ag_2O nanoparticles on the surface of the cryogels were investigated in details by XDR, EDS and TEM. The kinetic studies and isotherm experiments were thoroughly investigated and are shown in this chapter. Also, potential release of silver nanoparticles from the cryogels and formation of colloid particles are presented. Using several analytical methods, potential mechanisms of iodide removal were determined. This chapter also presents the result of testing Ag-modified cryogels for the removal of iodide from real seawater. The chapter was written from the results of the thesis author's published paper [3].

8.3 Synthesis and modification of cryogels

The results of modification reveal that the AAC and SAC were able to bind up to 159 mg/g and 98 mg/g of silver ions, respectively. The calculated from the EDS data silver loading values were 137.2 and 89.3 mg/g for AAC-Ag and SAC-Ag, which is also confirmed by EDS mapping of a large region (100-200 μm) of the Ag-polymers (**Fig. D1, D2** and **Table D1**). In **Fig. 8.1 t**he suggested mechanism of interaction of Ag^+ with cryogels' surface is presented. The preliminary experiments and also reports elsewhere [92,295,310] showed that existing on the functional groups of cryogels H^+ and Na^+ ions are able to ion-exchange with Ag^+ ions.

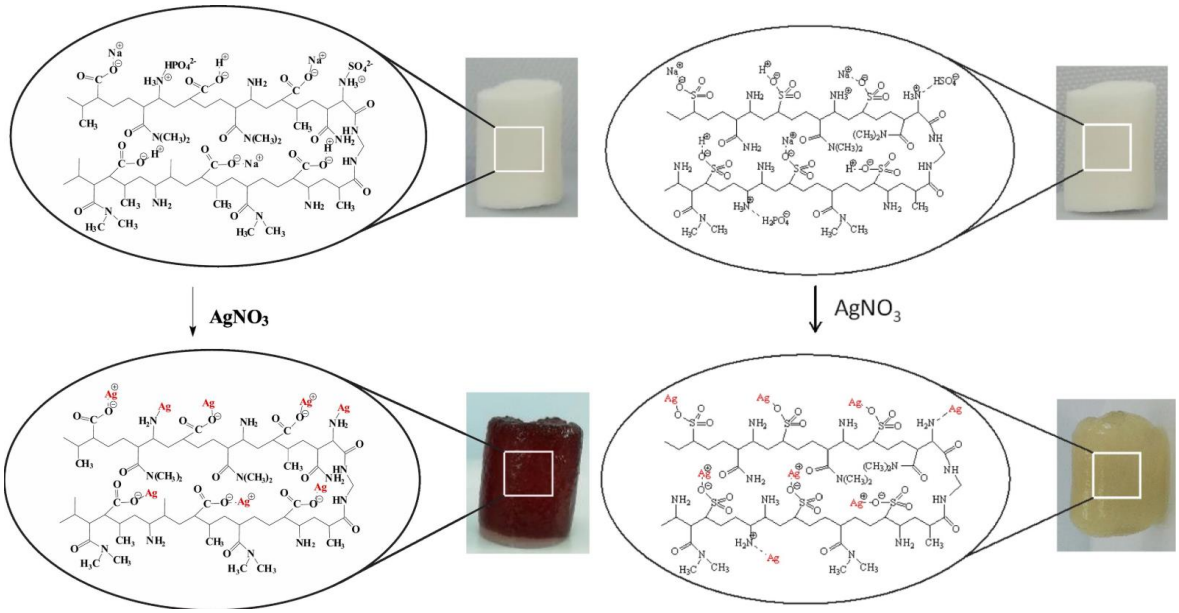

Fig. 8.1. Graphical presentation and photos of AAC (left) and SAC (right) cryogels modification

The FT-IR spectra of the initial and Ag-modified samples are presented in **Fig. 8.2**. The evaluation of functional groups and their peaks are described in detail in Chapter 4, Section 4.2. After the modification of cryogels by silver, the peaks of amide(I) and amide(II) are shifted to the right side by 10 and 9 cm^{-1} in AAC-Ag and 5 and 4 cm^{-1} in SAC-Ag, respectively. These shifts may be qualified as some structural changes of carbonyl groups

due to deprotonation and/or metal-bounding [97]. Also, peaks of non-dissociated carboxylic groups in AAC cryogel are moved for 15-20 cm^{-1} at AAC-Ag. In SAC cryogel, the sulfur-containing groups were shifted by 4-8 cm^{-1}also after interaction with Ag^{+} ions.

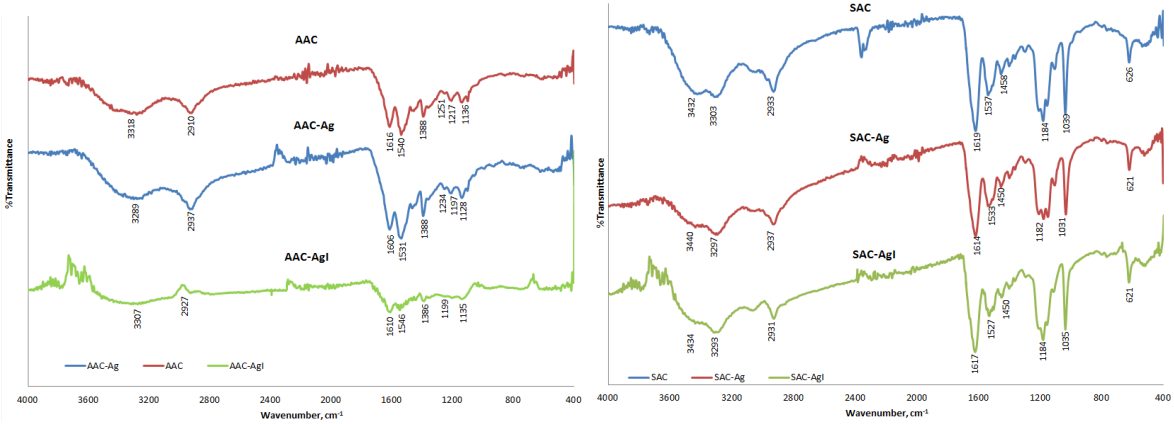

Fig. 8.2. FT-IR spectra of cryogels before and after Ag-modification and iodide adsorption

In **Fig. 8.3** is presented the photos of cryogel composites saturated by silver ions at different time points. AgNPs may have various optical possessions sensed at wavelengths from 400 to 750 nm depending on sizes and shapes of nanoparticles [311–315]. In the reserach of Huang and Hu, citrate-stabilized free Ag° NPs were reduced by various amounts of $NaBH_4$ in the water solutions to validate the statement that colloidal silver nanoparticles of different size and shapes have different colour [315]. The obtained Ag-cryogels were compared by colour with the finding of Huang and Hu. The dark red color of AAC-Ag composite suggests the existence of spherical and rod-shaped silver nanoparticles with an average diameter of 25 nm. The yellow color of SAC-Ag cryogel proposes the development of spherical Ag° NPs with the size of 5 nm [315].

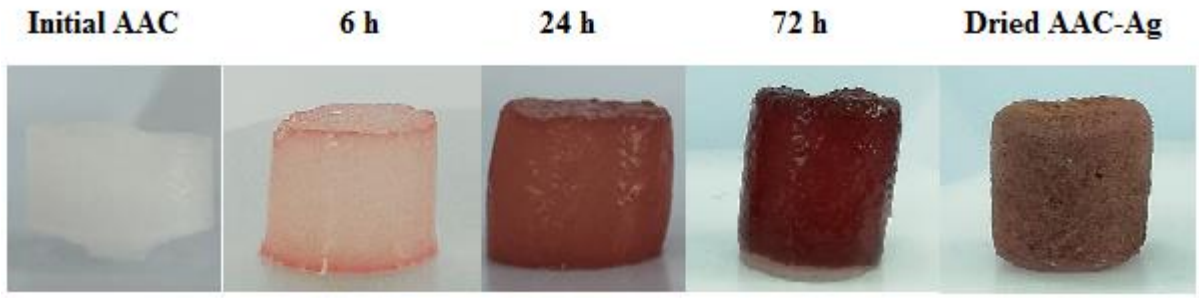

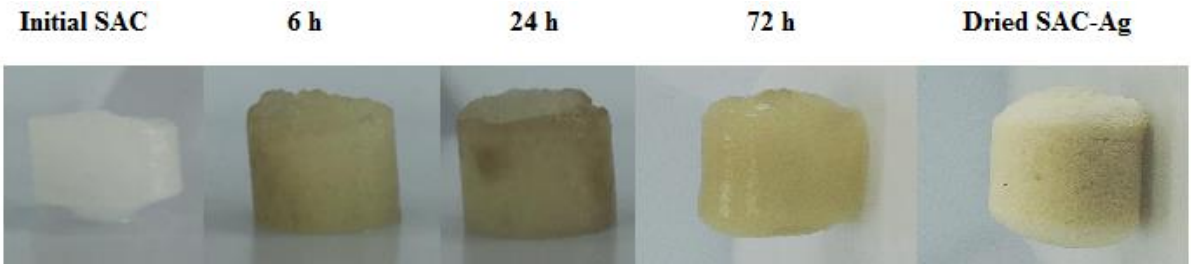

Fig. 8.3. AAC and SAC polymers during the Ag loading at different time points

The TEM technique was used to determine the sizes of silver nanoparticles on the surface of composites. From the microphotographs of TEM (**Fig. 8.4(A,B)**) it was detected, that most of the particles in AAC-Ag are in the range of 20-50 nm while SAC-Ag demonstrates significantly smaller NPs in the range of 3-10 nm. From the TEM pictures, it is clearly seen that Ag NPs are uniformly dispersed on the whole surface of both Ag-cryogel composites with a low degree of agglomeration. The point TEM/EDS investigation is shown in **Fig. 8.4 (C, D)**, revealing the absence of oxygen, which meant that these NPs are Ag°. However, in some TEM/EDS analyses (not shown here) the oxygen content reaches 19% in AAC-Ag and 17% in SAC-Ag and thus Ag_2O NPs coexist on the surface.

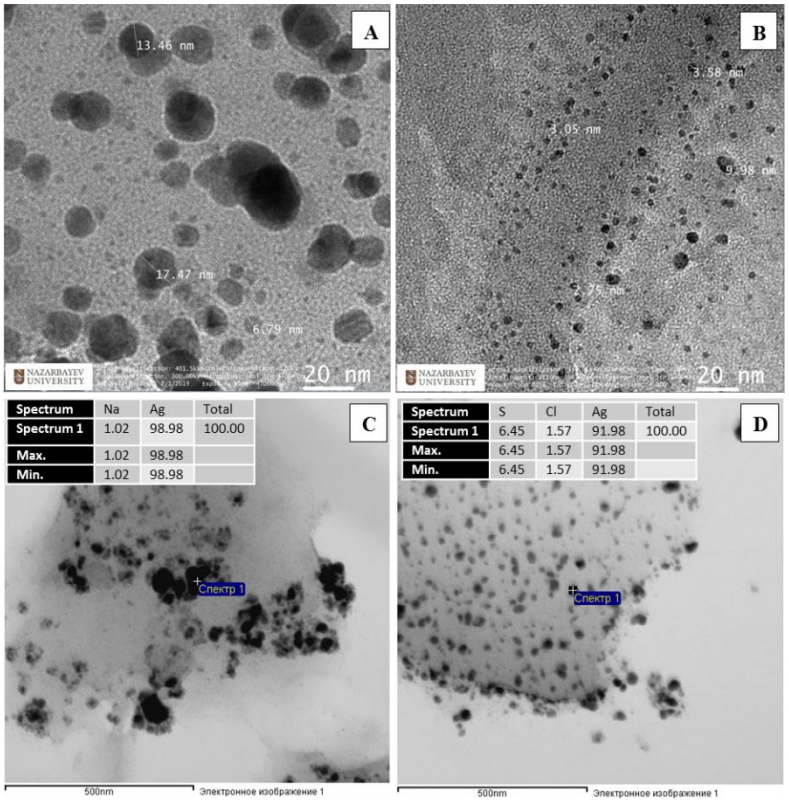

Fig. 8.4. TEM/EDS images and composition of AAC-Ag (A,C) and SAC-Ag (B,D)

XRD investigation validates the presence of silver nanoparticles with characteristic peaks of Ag°NPs at 38.29°, 44.62°, and 77.85° and also peaks of Ag_2O NPs at 32.39° and 65.16° of AAC-Ag cryogel. The SAC-Ag composite has peaks of Ag°NPs at 38.30°, 44.51° and of Ag_2O NPs at 32.50° and 64.85 as shown in **Fig. 8.5**. Afterwards iodide adsorption, numerous characteristic diffraction peaks of AgI at 2θ 23.71°, 39.13°, 46.31° can be detected for both nanocomposites, while the diffraction peaks qualified to Ag° NPs and Ag_2O NPs disappear. These findings demonstrates that the iodide interaction follows according to the reactions with dissolved oxygen [21]:

$$4Ag^{\circ} + O_2 \rightarrow 2Ag_2O(s) \quad (8.1)$$

$$Ag_2O + 2H^+ \rightarrow 2Ag^+ + H_2O \quad (8.2)$$

$$Ag^+ + I^- \rightarrow AgI(s) \quad (8.3)$$

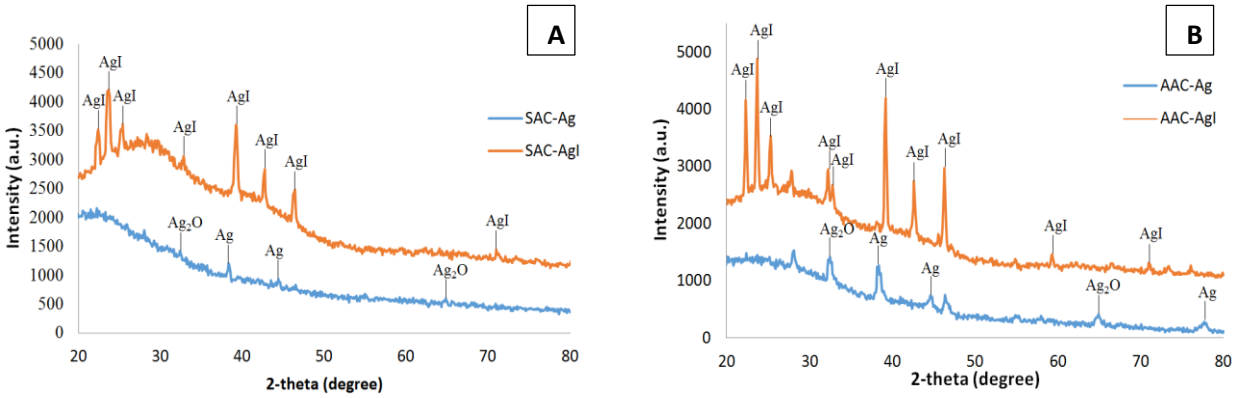

Fig. 8.5. XRD spectrum of AAC-Ag (A) and SAC-Ag (B) nanocomposites before and after iodide removal

The presence of Ag°NPs suggests the *in situ* reduction of silver. The reduction reaction without use of added reducing agent is associated to high oxidative properties of silver ions owing to standard redox potential of +0.75V [316]. Earlier such occurrence of self-reduction upon adequate heating or presence of light was described for chitosan-$[AuCl_4]$ based

cryogels [87,317]. Redox potential amino group is similar to ammonia, which is approximately -0.27 V [318]. Thus, the reduction of Ag^{+} to Ag^{o} could be explained by redox potential of amino group [319]. Lastly, from the SEM-EDS investigation is obvious that after the contact with Ag^{+} the structure of cryogels is still undamaged with uniform distribution of silver (**Fig. D1, D2**). After interaction with iodide the surface of cryogels was covered by iodide ions forming the AgI with congruent yellow colour.

8.4 Adsorption kinetics

In **Fig. 8.6** the iodide adsorption kinetics is shown. Despite the fact that only small mass (80 mg) of cryogels was used for experiments, the iodide adsorption was very fast. In the first 0.5 h AAC-Ag and SAC-Ag nanocomposites were able to remove up to 35% of I^{-}, while the equilibrium was reached in 30 h with the maximum removal of 93% for AAC-Ag cryogel and 77% for SAC-Ag sample. Non-modified AAC and SAC cryogels did not adsorb iodide which can be attributed to the hindrance of protonated amino group with counter ion hydro or dihydrophosphate ($RCH_2\text{-}NH_3^{+}H_2PO_4^{-}$).

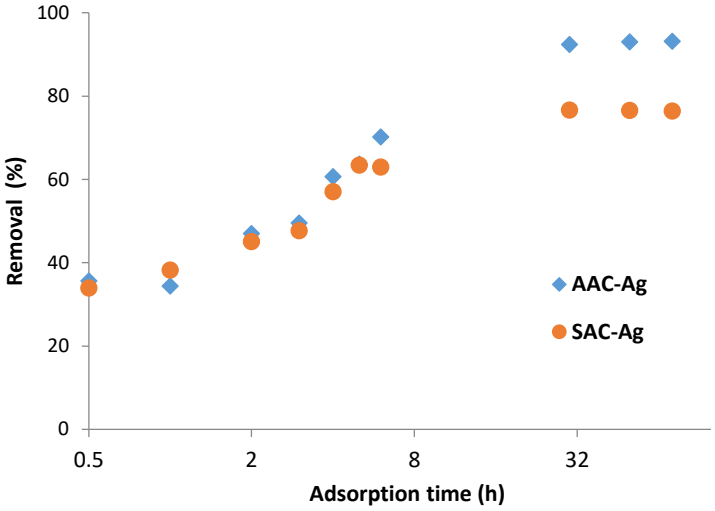

Fig. 8.6. Removal kinetics of iodide from water (80 mg of Ag-cryogel in 100 mL of solution)

The fitting of the experimental data (**Fig. 8.7**) on the pseudo-first and pseudo-second-order models was calculated and the obtained parameters are presented in **Table 8.2**. The R^2 is close for both models but the calculated solid phase loadings (q_e^{cal}) obtained by the pseudo-

second-order model are closer to experimental ones (q_e^{exp}). Hence, it could be determined that the pseudo-second-order model describes better the iodide removal kinetics for both Ag-cryogel nanocomposites demonstrating a chemical sorption process [212], which is in agreement with other results of iodide removal by use of silver-impregnated zeolitic imidazolate framework composite [304].

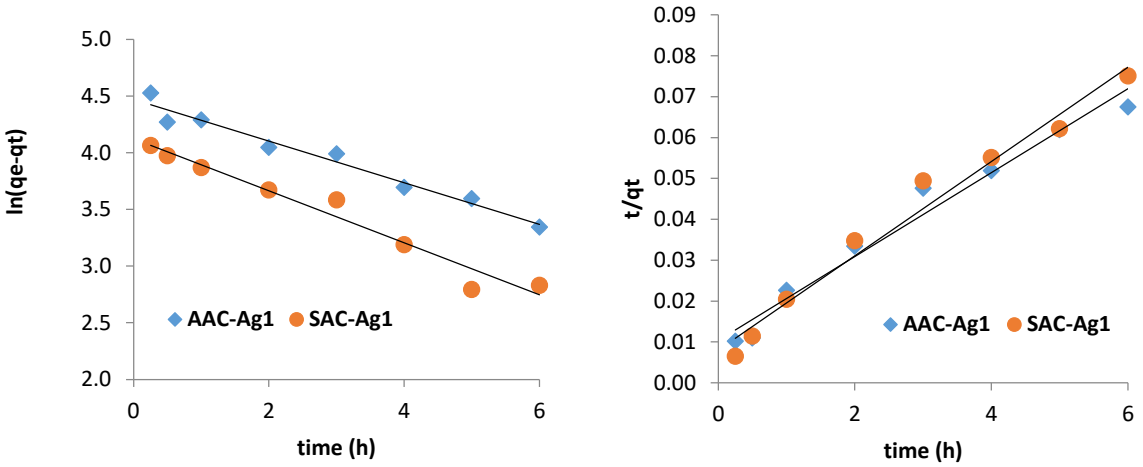

Fig. 8.7. The pseudo-first-order (left) and pseudo-second-order (right) model plots for the adsorption of iodide on the AAC-Ag and SAC-Ag cryogels

Table 8.2. Parameters of kinetic models for iodide sorption by cryogels

	Pseudo-first order			
	q_e^{exp} (mg/g)	q_e^{cal} (mg/g)	K_1 (min^{-1})	R^2
AAC-AgI	117.2	87.3	0.1834	0.9686
SAC-AgI	96.8	61.6	0.2293	0.9834
	Pseudo-second order			
	q_e^{exp} (mg/g)	q_e^{cal} (mg/g)	K_2 (g mg^{-1} min^{-1})	R^2
AAC-AgI	117.2	97.1	0.0103	0.9713
SAC-AgI	96.8	86.9	0.008	0.9765

After removal of I^- the color of both Ag-nanocomposites turns to yellow (Fig. 8A,C), due to the formation of AgI [305]. The existence of AgI on the surface of cryogels was investigated by SEM which demonstrates the surface coated with the precipitate, while EDS technique detected the iodide-distributed surface of the cryogels (**Fig. 8.8 B,D** and **Figs. D3 and D4**). Moreover, the formed AgI particles can be observed in the high resolution TEM photograph (**Fig. 8.9**). As expected, the size of nanoparticles after uptake of I is slightly bigger than the initial NPs (**Fig. 8.4**), which is consistent with the previous findings of Yang

et al. [320] and Mu et al. [308]. TEM shows dark areas which are probably agglomerated silver and AgI NPs.

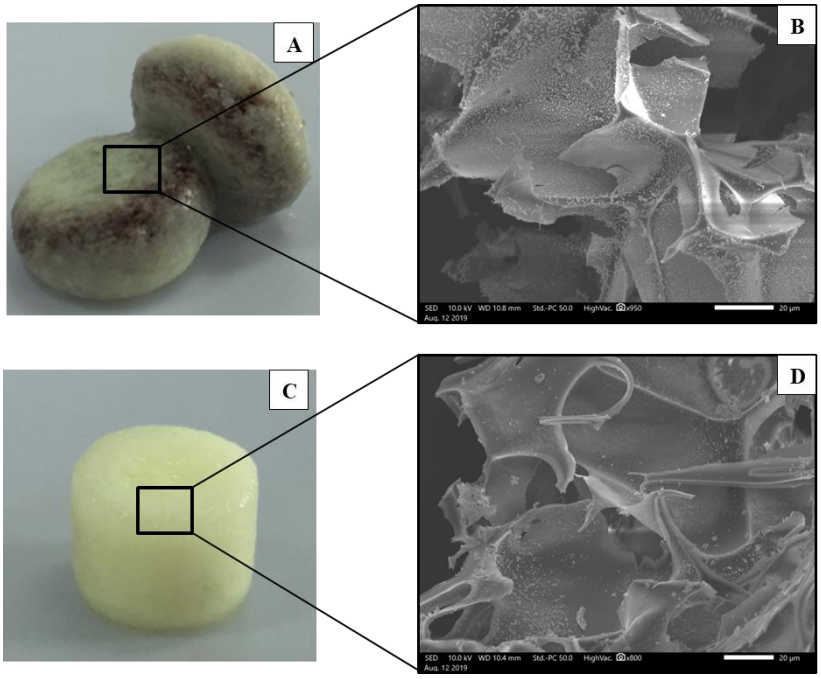

Fig 8.8. Photographs and SEM images of AAC-Ag (A,B) and SAC-Ag (C,D) after iodide adsorption

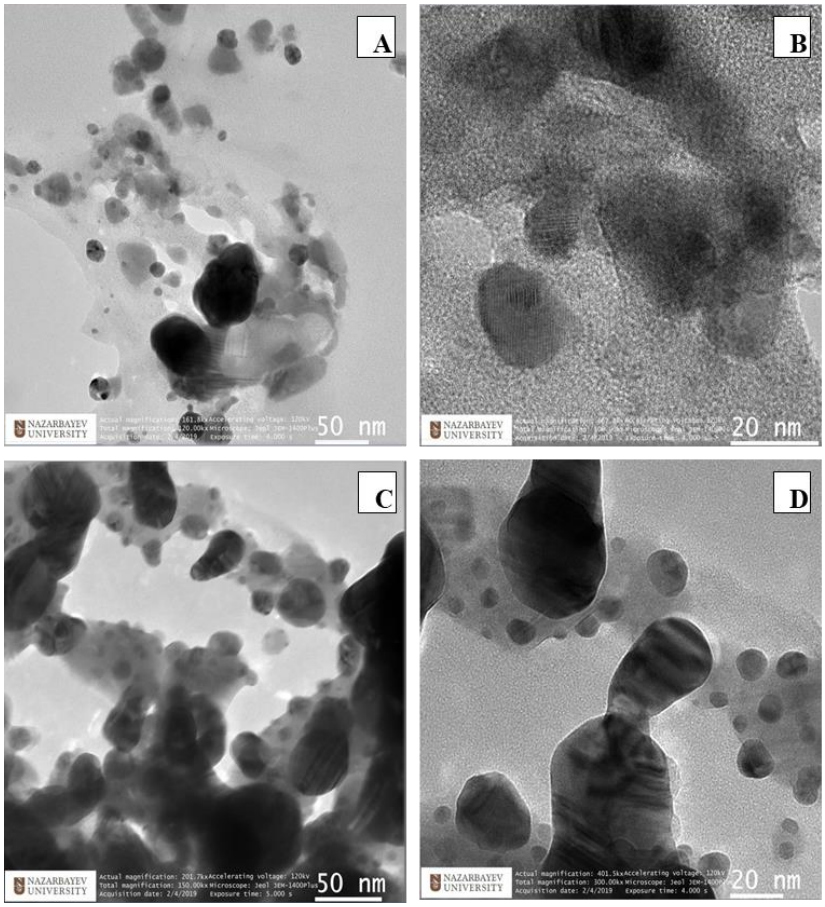

Fig. 8.9. TEM of AAC-AgI (A,B) and SAC-AgI (C,D)

8.5 Equilibrium adsorption isotherms

The sigmoidal shape of the equilibrium isotherms results are presented in **Fig. 8.10**. The AAC-Ag reached the maximum iodide adsorption of 326 mg/g, while SAC-Ag has about 247 mg/g. The reached capacities are of the utmost reported in the literature comparable to advanced materials such as Ag-modified titanate nanoalumina and D201 resin (**Table 8.1**). As is known, the iodide removal efficiency by Ag-modified materials is mainly controlled by the Ag content. But, as the literature review show this is not always true due to several contributing phenomena such as adsorption and colloids formation.

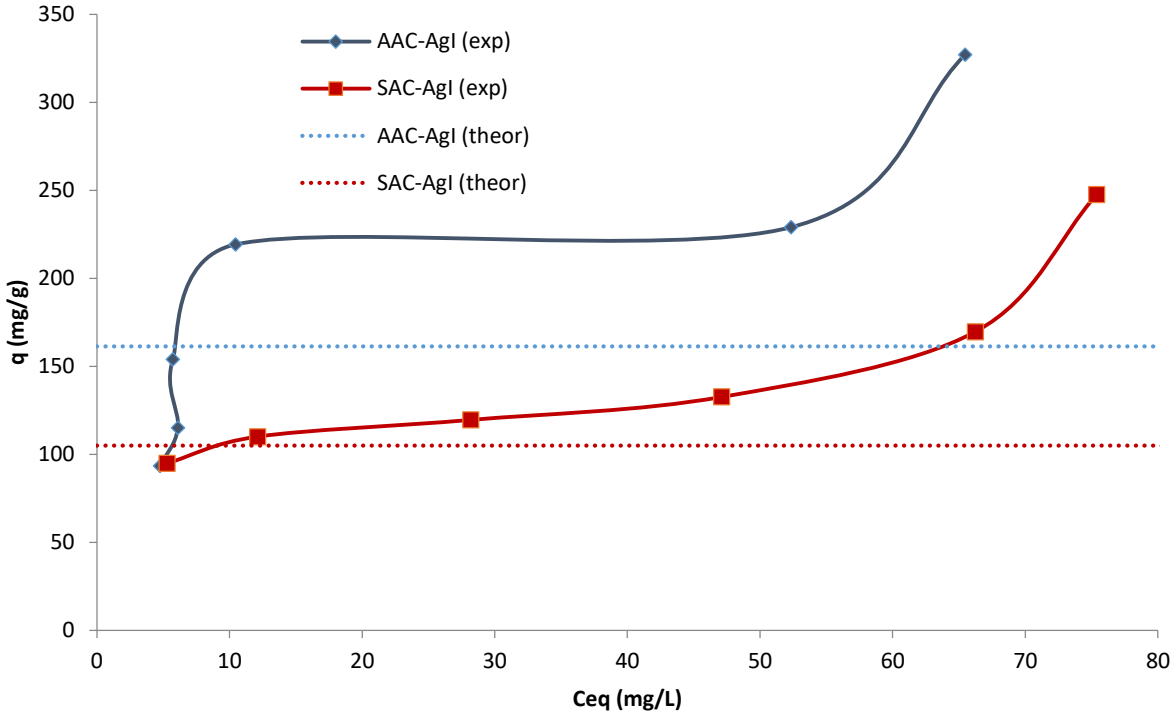

Fig. 8.10. Isotherms of iodide removal by cryogels

Based on the silver content of the Ag-modified cryogels (161.4 mg/g and 105 mg/g for AAC-Ag and SAC-Ag), the theoretical iodide loadings should be no more than Ag content, which is considerably lower than the measured iodide equilibrium loadings (**Fig. 8.10**). The involvement of physisorption is excluded as the non-modified cryogels did not show any affinity towards I^-. Also, the discrepancy between the theoretical and actual iodide loading is increasing by decreasing the mass of cryogel to solution volume ratio. On the other hand, the EDS mapping of a large area (50-100 μm) of the sorbents displayed that Ag and I are uniformly distributed on the cryogels surface with Ag:I molar ratios close to 1 (**Fig. D3, D4**). The silver and iodide content measured by EDS are in excellent agreement with the expected silver (measured by AAS) and iodide (based on the Ag amount) content of the iodide-loaded cryogels (**Table D1**).

Such discrepancies were also observed by Mao et al [297] for the removal of iodide by Ag@MIL-101 composite. The authors presented the following mechanism:

$$Ag@MIL\text{-}101 + 2I^- \rightarrow MIL\text{-}101 + AgI_2 \quad (8.4)$$

$$2AgI_2 \leftrightarrow AgI + AgI_3 \quad (8.5)$$

$$AgI_3 + 2I^- \leftrightarrow AgI + 2I^- + I_2 \quad (8.6)$$

$$AgI + I_2 \rightarrow AgI_3 \quad (8.7)$$

According to these reactions, first Ag^+ is released from the composite and reacts with I^- to yield AgI with simultaneous oxidation of I^- to I_2. Subsequently, the generated I_2 can be adsorbed by the nearby AgI nanoparticles released form the surface of material to form AgI_3, or be adsorbed by complex ions (AgI_{2n-1}) to create more stable complex ions (AgI_{2n+1}). However, no data verified the existence of I_2 except the large adsorption capacity and thus their explanation is incomplete. The same discrepancy between experimental and theoretical iodide loading were observed in the study of Zhao et al [302]. They synthesized MIL-101(Cr)-SO_3H metal-organic framework sample modified by Ag^+ with maximum loading of silver 35.8 mg/g. After interaction with NaI the parent MIL-101(Cr)-SO_3H iodide loading was 94.1 mg/g and this of Ag-modified sample 244.2 mg/g. The difference of almost 150 mg/g between the materials was not explained by the authors although they mentioned some release of silver from the material without any further analysis.

To better understand these observations, the release of Ag^+ and Na^+ from the cryogels and the removal of K^+ from the solutions were studied and the results are presented in **Fig. 8.11**. As it can be seen, although there is no trend there is some Ag^+ release from the cryogels and its concentration in the solution is between 1.3-8 ppm, similar to the concentration of the released Na^+ which is between 2.6-7.8 ppm. Taking into account that leaching experiments in pure water showed negligible release of silver from the Ag-modified cryogels (0.05-0.54%) the release of Ag^+ and possibly Na^+ can be attributed to ion exchange with H^+ and K^+ from the solution. Definitely, as is shown in **Fig. 8.11** the K^+ concentration in the solution is between 5.8-24.5 ppm, lower than its initial concentration of 31.7 ppm. The slow release of Ag^+ in an iodide-rich solution can lead to the formation of colloidal AgI that have lower $Ag:I$ molar ratio than 1 as the theory predicts [321,322]. As it was experimentally confirmed by measurements in the model solutions AgI colloids are formed and detected by UV-Vis (**Fig. 8.13**) but the bounded iodide cannot be measured by UV-Vis or ion chromatography and this explains the discrepancy observed in the equilibrium results. More discussion on this is conducted in paragraph 8.7.

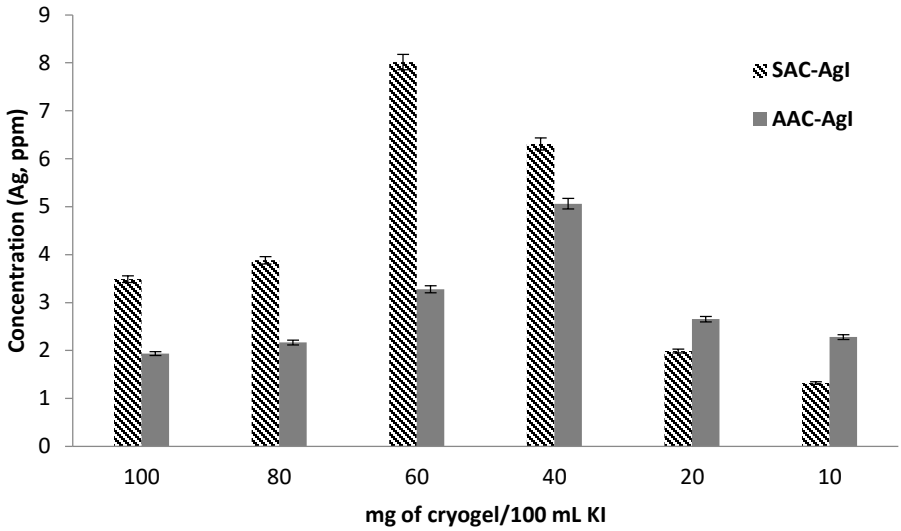
Concentration (Ag, ppm)
9
8
7
6
5
4
3
2
1
0
SAC-AgI
AAC-AgI
100
80
60
40
20
10
mg of cryogel/100 mL KI

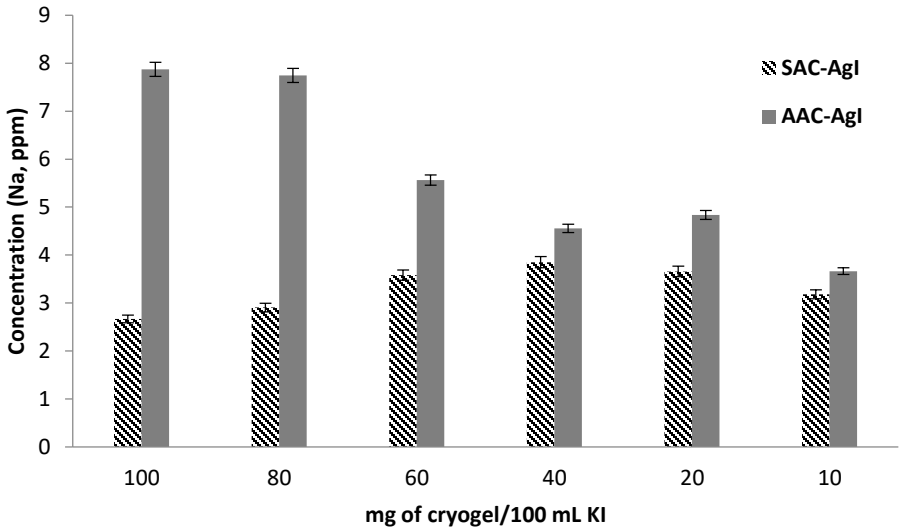
Concentration (Na, ppm)
9
8
7
6
5
4
3
2
1
0
SAC-AgI
AAC-AgI
100
80
60
40
20
10
mg of cryogel/100 mL KI

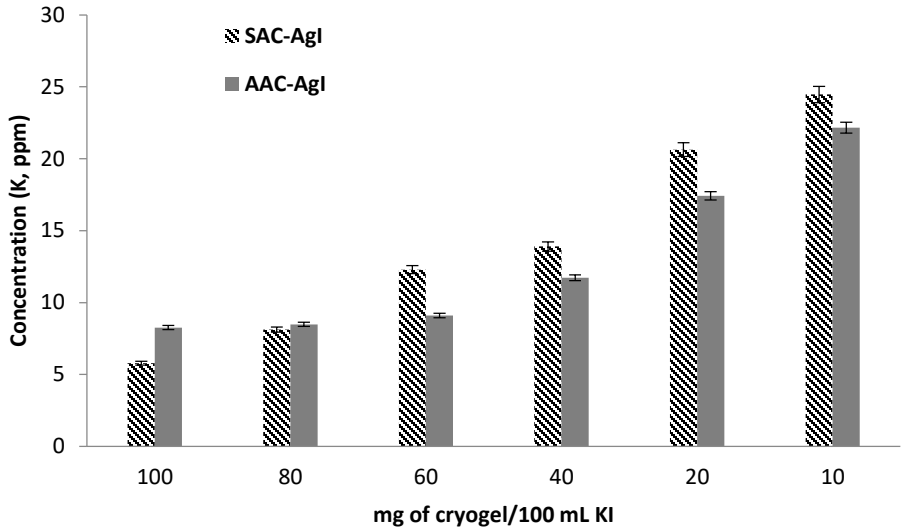

Fig. 8.11. Release of Ag^+ and Na^+ from the cryogels and K^+ remaining in the solution under different cryogel/solution volume ratio.

After interaction with Ag-modified cryogels the pH and conductivity of the solutions changed (**Table D2**). The conductivity of solution falls from 104.4 μS/cm to 29.35- 88.65 μS/cm for AAC-Ag experiments and to 13.3-96.9 μS/cm for SAC-Ag experiments depending on the mass of cryogels, mostly owing to the removal of iodide from the solutions. The pH of solutions containing AAC-AgI cryogels increase from 5.56 to 6.11-7.11 possibly due to the exchange of H^+ from the solution for Na^+ from the cryogels and the dissolution reaction of Ag_2O to Ag^+ (equation 8.2). Quite the opposite, the pH of the solutions having SAC-AgI remains slightly acidic around the initial pH of 5.59 which is possibly due to the H^+ discharge from the sulfonic acid groups.

8.6 Real seawater studies – competitive removal of iodide

The results revealed that the concentration of all anions except Br^- and I^- remain constant (**Fig. 8.12**). However, the initial concentration of bromide was very low and did not significantly inhibit the adsorption of iodide on Ag-cryogels. The AAC-Ag and SAC-Ag nanocomposites were able to adsorb almost 20-100% and 5.3-98.3% of iodide, respectively. The results of iodide removal from real seawater and synthetic solution are very close with the exception of low cryogel/mass ratio (10-20 mg) probably due to the more extended period needed for equilibrium in seawater. It could be concluded that both Ag-cryogels could

be used as efficient, highly selective adsorbents in the treatment of iodide contaminated natural seawater.

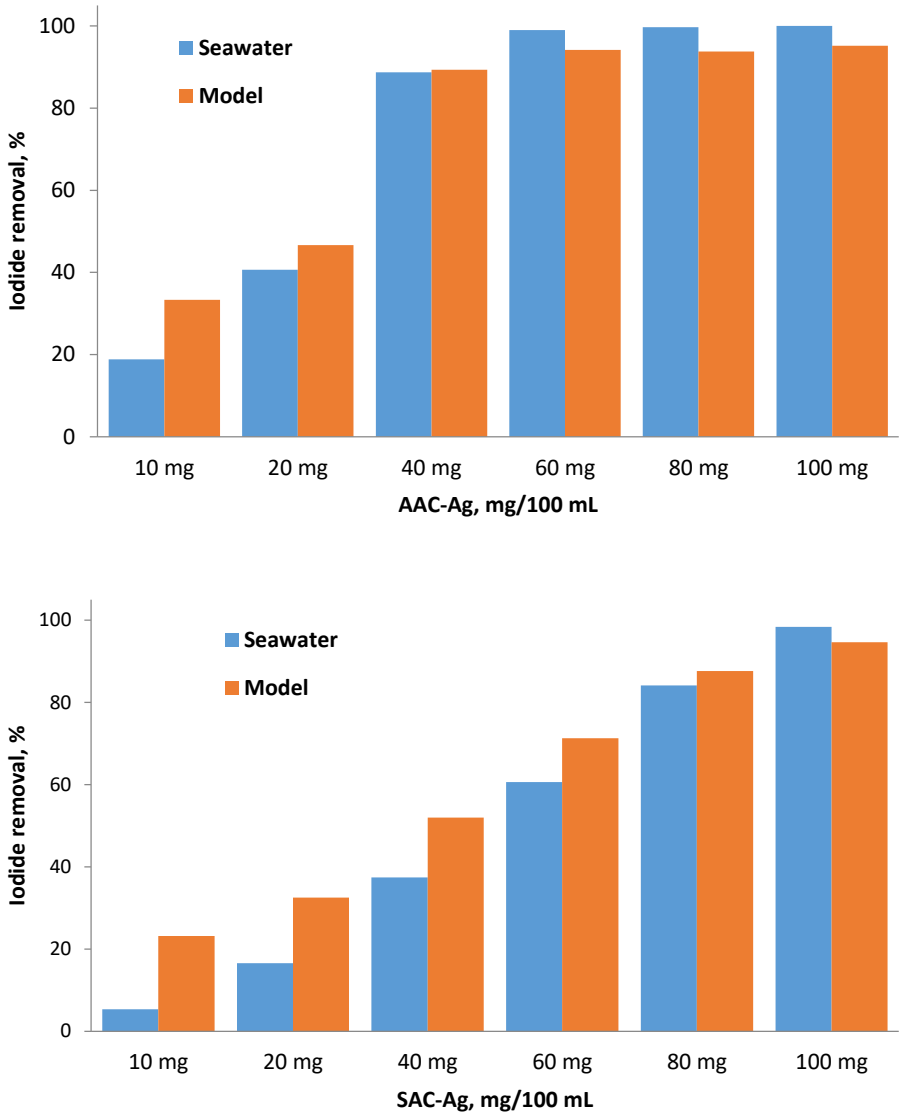

Fig. 8.12. Iodide removal (%) from seawater and synthetic solution under different cryogel/solution volume ratio.

8.7 AgI colloids formation studies

In the early works of the Verwey and Oberbeek [321,323] the theory of formation and stability of lyophobic colloids were described in detail. An electric double layer is formed around the AgI particles with different charges depending on the relative concentrations I^- and Ag^+ in the solution. If silver nitrate is added to a solution of excess of potassium iodide

the formed AgI particles first attract negatively charged iodide anions (**Fig. 8.13**) to form potential-forming layer. To this layer the positively charged potassium (K^+) and negatively charged iodide (I^-) ions join to form the ion diffusion layer of counter ions.

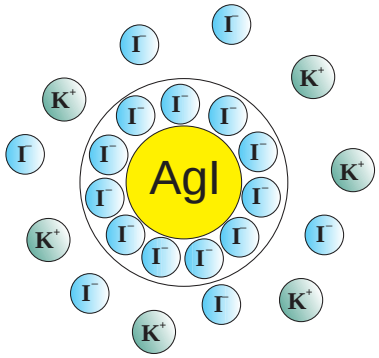

Fig. 8.13. Formation of AgI colloids in excess of iodide

To further investigate the formation of colloids 500 ppm of $AgNO_3$ solution was added dropwise to 500 ppm KI solution resulting in solution Ag:I ratios from 1:20 to 1:400. The solutions were measured by UV-Vis spectrophotometer and the peak at 424-431 nm was detected and attributed to AgI colloids [324]. The same peak was found in the iodide equilibrium solutions after interaction with the Ag-cryogels (**Fig.8.14**).

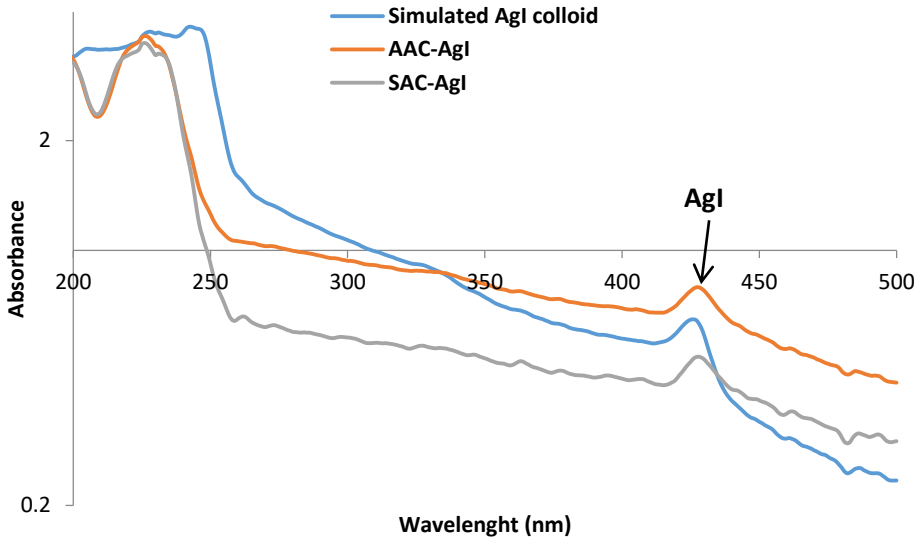

Fig. 8.14. UV-Vis plot determination of AgI formation

The results of zeta potential measurements and size of colloid solutions presented in **Table 8.3** and confirm the formation of negatively charged particles of colloidal particles.

With increasing of Ag:I ratio the zeta potential of the solutions decreases and the size of colloidal AgI increases. The zeta potential of AgI colloidal solution decreased from -65.2 mV at the ratio 1:20 of Ag:I to -50.3 mV at 1:400 ratio, in general agreement with the findings of other studies [325]. The sizes of colloid particles linearly rise from 193.9 to 317 nm when the ratio of Ag:I grows from 20 to 400. This phenomenon is observed with very dilute electrolytic solutions in which the colloidal particle size can reach 1000 nm due to an increase in the diffusion layer of the particle [321]. For comparison, the zeta potential of solutions contained 10 mg of AAC-AgI and SAC-AgI samples were -45.1 and -50.9 mV and the average size of the formed colloids 171.4 and 175.7 nm, respectively. Taking into account that colloids formation is a dynamic process and depends on many factors the results are satisfactory and confirm the creation of colloids. This offers a reasonable explanation of the discrepancies between theoretical and actual iodide loading values as the colloids exhibit Ag:I ratios lower than 1.

Table 8.3. The results of zeta potential and size measurements of AgI colloid solutions

Ag:I molar ratio	Zeta potential (mV)	Average size (nm)
1:20	-65.2 ± 1.0	193±10
1:40	-61.8 ± 2.6	217±9
1:80	-67.1±2.1	212±12
1:80	-66.6±3.2	265±16
1:160	-51.8±2.1	275±14
1:200	-51.2±0.8	264±11
1:240	-52.4±1.9	291±7
1:380	-56.1±2.0	297±14
1:320	-52.4±1.2	307±11
1:360	-52.7±3.1	294±5
1:400	-50.3±2.6	317±21
KI	-0.11±0.03	0

8.8 Summary

In this chapter, two novel Ag^o/Ag_2O nanocomposite cryogels were synthesized, characterized and used for the removal of iodide from modelled and natural waters. The silver loading of AAC and SAC cryogels was 159 and 98 mg/g, respectively. The results revealed the reduction Ag^+ ions by amide groups of cryogels by forming Ag^o nanoparticles with further partial agglomeration and oxidation result in the formation of Ag_2O

nanoparticles. This hypothesis is supported by the colours of the cryogels, XRD, SEM-EDS and TEM-EDS analysis. In the KI solutions Ag^{o} is oxidized to Ag_2O and then dissolution follows to form Ag^{+} which reacts with I^{-} to form insoluble AgI on the surface of the Ag-cryogels. Ion exchange also takes place between Ag^{+} and Na^{+} from the cryogels and K^{+} and H^{+} from the solution. The removal of I^{-} is fast and follows the pseudo-second-order model. Lastly, a small release of Ag^{+} during I^{-} elimination ensued in the establishment of negatively charged AgI colloids in the solution. The Ag:I molar rations of these colloids is considerably lower than 1 resulting in higher than theoretically expected removal of I^{-} by considering the formation of AgI bulk precipitate. The formation of colloids in the solution provides a satisfactory explanation for other similar discrepancies between observed and theoretically expected I^{-} removals in the literature.

CHAPTER 9
IN VIVO ANIMAL STUDIES

1. Introduction

In the environment, heavy metals are omnipresent in different forms and compositions. Humans and animals are mainly intoxicated by the ingestion of contaminated food, polluted water, during the anthropogenic and natural-source activities. However, in addition to chronic heavy metal poisoning, there are several cases of acute intoxication with metals such as cadmium, mercury, strontium, and cesium, which are suicidal or due to accidental poisoning [326–330]. Human exposure to cadmium and mercury can lead to systemic injury of many organs such as kidneys, lungs, liver, reproductive system, and bones [326,331,332]. Various antidotes and chelating agents are prescribed rely upon the quantity of the dose of poison and the severity of the patient's condition.

During the last decades, a numeral of new chelating antidotes have been developed and tried in animal trials showing high efficiency compared to classic chelators. Dimercaptosuccinic acid (DMSA) and dimercaptopropane sulfonate (DMPS) chelating agents are examples of antidote for numerous metal poisonings treatments approved by US FDA [333]. A basic standard in chelation therapy is that metal (Lewis acid) and chelator (Lewis base) should have high similarity, where soft metals (e.g., Pd^{2+}, Ag^{+}, Hg2+, Cu^{2+}, Cd^{2+}, Pt^{2+}, Pb^{2+}) should be chelated by materials with soft ligands (e.g., DMSA and DMPS), while hard metals (e.g., Cr^{3+}, Fe^{3+}, Be^{2+}, Al^{3+}) with chelators with hard ligands [334]. Intermediate metals (e.g., Fe^{2+}, Co^{2+}, Ni^{2+}, Zn^{2+}) can be chelated by both hard and soft bases. A huge amount of chemical complexes was considered as antidotes in experiments on acute cadmium and mercury poisoning in animals [327,333,335]. Generally, metal and antidote injections are given parenterally or orally. Enteral administration of DMSA effectually decreases gastral absorption and toxicity of extremely poisonous oral doses of cadmium, while intraperitoneal administration of DMSA only slightly protected against Cd toxicity. Oral administration of DMSA efficiently reduced intestinal uptake and toxicity of highly toxic oral doses of cadmium, while intraperitoneal injection of DMSA only marginally protected against Cd toxicity. Nevertheless, these agents interfere with vital metal ions like Ca^{2+}, Cu^{2+}, Zn^{2+}, K^{+}, Na^{+} results in abnormal physiologic function [336]. Besides, heavy metals are redistributed

by these agents to potentiate toxicity at intracellular sites of the liver and kidney [332]. To overcome these disadvantages, the investigation and study of new treatment methods and materials are essential. This research aimed to evaluate the antidotal effect of cryogels and Unithiol toward elimination LD_{50} dose of cadmium, cesium, strontium, and mercury from rats. To the best of our knowledge, it is a first time when cryogels were tested as an oral sorbents for heavy metal detoxification *in vivo*, while the Unithiol, the commercial name of DMSA compound was approved by US FDA as effective antidote for cadmium and mercury treatment [326,327]. Despite the fact, that therapeutic pharmacokinetics of cryogels and Unithiol are different in nature, it was decided to compare synthesized cryogel with best efficient commercial antidote. To test the success of treatment, histopathological evaluation of liver and kidney, biochemical parameters of blood and presence of metal ions in various animal tissues were done.

9.2 Chapter Overview

In this chapter, the results of the use of AAC cryogel as oral sorbents for treatment of experimental animal poisoned by LD50 dose of $Cd(NO_3)_2$, $CsNO_3$, $Sr(NO_3)_2$ and $HgCl_2$ in water phase. For the comparison of efficiency of cryogels, the Unithiol was used in the same dose as cryogel. After the animals were withdrawn from the experiment, the internal tissues were removed for histological and chemical analyzes, while blood samples were collected and used to determine the levels of biochemical markers.

9.3 Survival and clinical observations of intoxicated animals

After 2h of metal poisoning, the some rats in the untreated groups moved slowly, showed emphatic noise sensitivity, and frequent convulsions. **Table 9.1** represents the data of the experimental groups depending on the doses of metals received, methods of detoxification, and the percentage of survival in the group. Mortality of animals in the groups poisoned by cadmium and mercury occurred within 2-4 hours after administration of the toxins, while animals from groups with strontium and cesium died within 4-7 hours. Most fatal cases in rats treated with cryogel and unithiol occurred 15-18 hours after metal intoxication.

Table 9.1. Survival rate of rats in the experimental groups depending on metal dose and treatment method

Group	Subgroup	Metal dose and/or antidote	Survival rate, %
Group I	NC	control	100
Group II	Cd-PC	$LD_{50}Cd(NO_3)_2$	40
	Sr-PC	$LD_{50}Sr(NO_3)_2$	50
	Cs-PC	$LD_{50}CsNO_3$	50
	Hg-PC	$LD_{50}HgCl_2$	40
Group III	Cd-AAC	$LD_{50}Cd(NO_3)_2$ + AAC cryogel	90
	Sr-AAC	$LD_{50}Sr(NO_3)_2$ + AAC cryogel	100
	Cs-AAC	$LD_{50}CsNO_3$ + AAC cryogel	90
	Hg-AAC	$LD_{50}HgCl_2$ + AAC cryogel	80
Group IV	Cd-DMSA	$LD_{50}Cd(NO_3)_2$ + unithiol	70
	Sr-DMSA	$LD_{50}Sr(NO_3)_2$ + unithiol	80
	Cs-DMSA	$LD_{50}CsNO_3$ + unithiol	80
	Hg-DMSA	$LD_{50}HgCl_2$ + unithiol	60

9.4 Histopathological studies of liver and kidney

Histopathological analysis of the liver of the control group of animals demonstrates the typical structure of the organ, a distinct cortex with centralized nuclei, glomeruli, and preserved tubules (**Fig. 9.1A**).

During a morphological study of the histological parameters of the liver of animals poisoned with cadmium and strontium (**Fig. 9.1 B,D**), it was found that the introduction of metals in a dose of LD_{50} leads to a significant expansion of sinusoidal capillaries and central veins. The introduction of a more massive dose of toxicant causes a change in the architectonics of the hepatic lobules, a violation of the traditional orientation of hepatocyte beams. Morphological study of the liver in experimental animals receiving intragastric administration of mercury and cesium revealed pronounced hydropic and fatty degeneration of hepatocytes with focal necrosis, and profuse hemorrhage in sinusoidal capillaries (**Fig. 9.1 J, L**). Histological examination of the liver of animals of the Cd-AAC group (**Fig. 9.1 E**) shows a slight hemorrhage in the sinusoid capillaries and damage to hepatocyte cells, while the sample Cd-DMSA (**Fig. 9.1 F**) showed an almost intact liver structure with a slight

hemorrhage in the intercellular space. However, when studying liver samples after the intoxication of animals with strontium followed by the introduction of antidotes, a directly opposite picture is observed. The liver of the sample Sr-AAC looks intact without visible damage, while the liver of the Sr-DMSA animal group is severely damaged with marked increases in sinusoidal capillaries and dystrophic changes in cells. In the case of cesium treatment, the liver samples of Cs-AAC and Cs-DMSA (**Fig. 9.1 M and 9.1N**, respectively) look slightly damaged with a slight hemorrhage and deformation of some hepatocytes. An extremely high degree of liver damage is observed in sample Hg-DMSA (**Fig. 9.1 R**), which is characterized by acute venous hyperemia of the liver, hemorrhage, necrosis of hepatocytes in the central zone of the hepatic lobule, while the sample Hg-AAC (**Fig. 9.1 P**) exhibits less damage with slight hemorrhage.

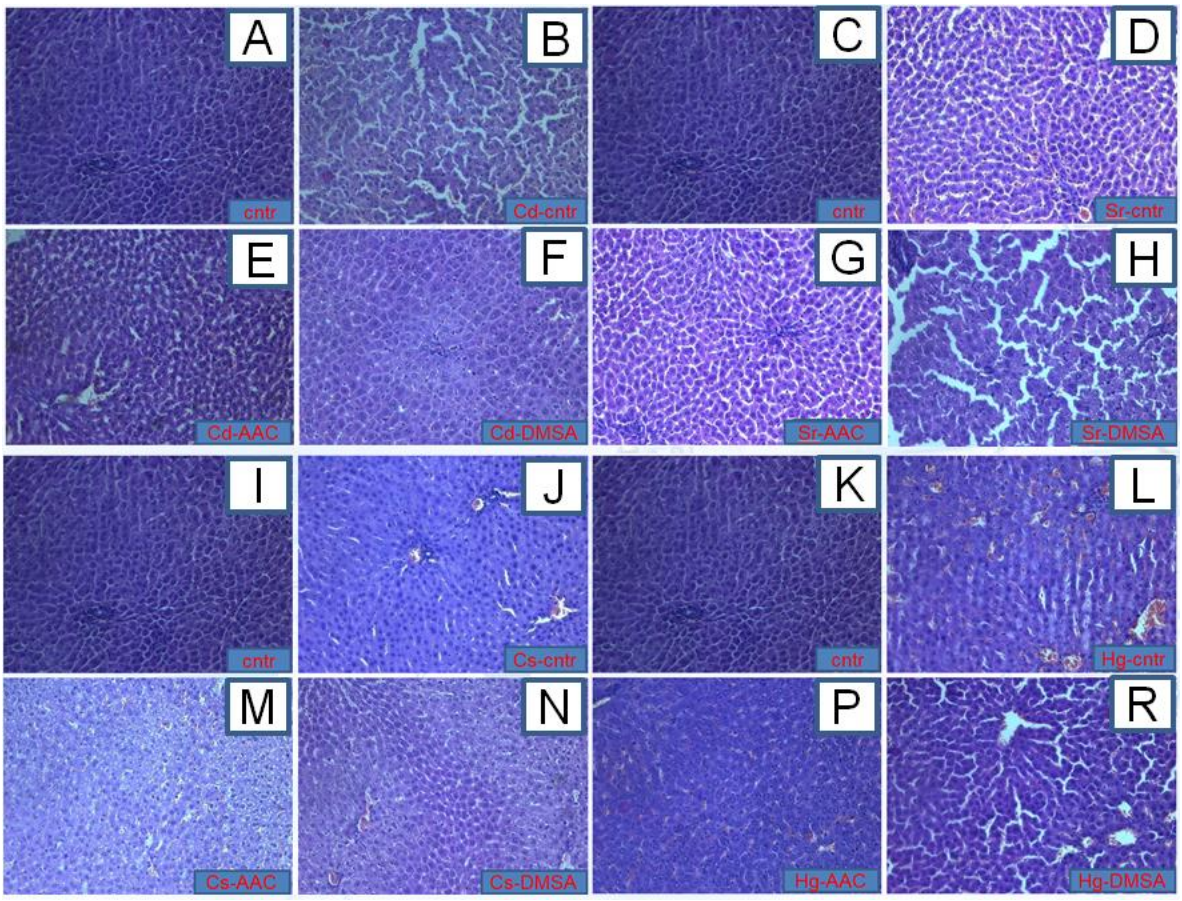

Fig. 9.1. The histopathological images of livers of all groups of experimental animals

The histopathological investigations of kidneys of healthy, poisoned and treated animals are presented in **Fig. 9.2 (A-R)**. In healthy animals (Group I), the capsule, cortical and brain layers are microscopically distinguishable. Numerous glomeruli of nephrons with a spherical shape with a slightly uneven surface are clearly visible in the cortical layer. The glomeruli are enclosed in capsules, the lumen of which is sickle-shaped or surround the glomerulus in the form of a ring. The cavity of the capsule is free of contents. The space between the glomeruli is represented by a homogeneously colored fabric with numerous rounded sections of convoluted tubules and vessels of the cortical substance. The tubule epithelium adheres strictly to the surface of the basement membrane, represented by a continuous unicellular layer of endothelial cells. The nuclei of these cells are rounded, regular in shape with a smooth surface. They are located in the center of a homogeneous cytoplasm. The lumen of the tubules is gaping, free of content. The brain substance is represented by homogeneously colored parenchyma with a parallel tubular apparatus.

In Group II animals poisoned with metals, significant changes in the structure of the histological picture are observed both in the cortical substance. It is noteworthy that in the lumens of the capsules of most glomeruli, there are amorphous deposits and red blood cells (**Fig. 9.2 B,D,J,L**). In the tubules of all levels, significant dystrophic changes in the epithelium are noted, which are manifested in the swelling and separation of epithelial cells from the basement membranes and from each other, the loss of a significant number of basophilia nuclei, karyolysis, and desquamation of epithelial cells. Gleams of tubules were significantly expanded. In interstitium, pronounced edema, lymphocytic and neutrophilic infiltration was observed and had a focal character. The cortical vasculature looks diluted and filled with blood.

In animals treated with cryogel (Group III), on the histological sections, the lumen of individual capsules contains amorphous inclusions (**Fig. 9.1 E,G,M,P**). The tubular apparatus contains signs of dystrophic changes, however, these changes are much less pronounced than in untreated Group II. In contrast to the control group, in which tubular obstruction by amorphous masses is observed throughout the thickness of the section, in this group, these changes are focal in nature and are localized mainly in the zone of transition of cortical substance to the brain. The degree of desquamation of the epithelium and pathological changes in the nuclei is also significantly less pronounced than in control. In animals treated with Unithiol (Group IV), the lumen of individual capsules on histological

sections contains amorphous inclusions and showed a moderate degree of congestion in renal blood vessels and atrophy of some glomeruli. The signs of dystrophic changes in the tubular apparatus are significantly less than in the control group but slightly higher than in the cryogel-treated group.

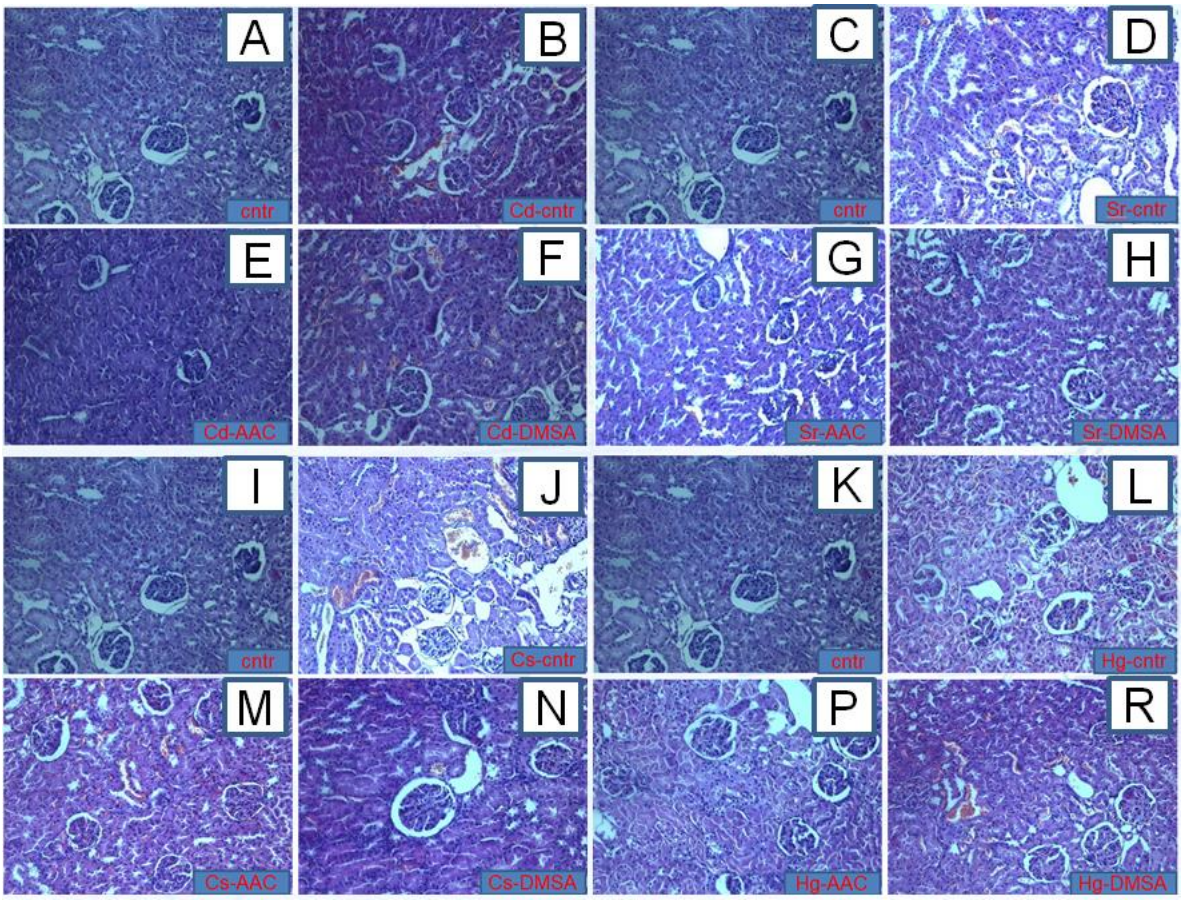

Fig. 9.2. The histopathological images of kidneys of all groups of experimental animals

9.5 Effects of poisoning and treatment on biochemical markers

Blood biochemical parameters are essential in determining damage to the liver and kidneys. The levels of biochemical blood markers of the intact, metal-poisoned, and treated groups are presented in **Table 9.2**. After the metals were introduced into the animal organism, the enzymatic activity of AST, ALT, GGT, alkaline phosphatase in the blood serum tended to increase, however, in the group of cryogel-treated animals these parameters returned to normal, except for alkaline phosphatase. In the results of Group IV, it was found that the ALT levels were within normal limits, AST was higher than that of the intact and the group treated with cryogels, but lower than the metal-poisoned group.

Table 9.2. Effect of metal on blood biochemical markers in experimental animals

	TP, g/L	Urea, mmol/L	Glu, mmol/L	ALT, U/L	AST, U/L	TBil, μM/L	GGT, U/L	ALP, U/L	TC, μM/L
NC	60.35±2.3	4.19±0.2	11.9±1.0	53.5±8.4	91.8±9.5	0.9±0.28	0.81±0.27	115.5±23.3	1.02±0.20
Cd-PC	55.875±2.1	5.71±0.6	18.0±3.8	139.5±10.3	130.4±33.5	0.79±0.26	2.33±1.5	181.8±80.6	0.81±0.52
Sr-PC	64.8±3.8	7.8±2.9	14.7±1.3	137.2±9.5	143.8±14.4	1.05±0.07	2.65±1.34	207.5±64.3	2.06±0.73
Cs-PC	63.15±3.0	6.3±1.6	11.1±1.5	131.4±4.0	130.5±25.7	1.16±0.35	1.4±0.71	204.5±47.4	0.59±0.05
Hg-PC	59.9±3.8	4.1±0.5	13.7±1.4	194.2±9.5	153.3±14.4	1.15±0.21	4.55±5.02	152.5±17.7	1.05±0.08
Cd-AAC	60.8±3.8	7.0±1.2	11.8±0.6	27.3±8.5	71.4±9.5	0.75±0.07	1.2±0.28	219.5±36.1	1.14±0.21
Sr-AAC	62.9±8.8	10.4±5.0	10.9±1.9	43.3±1.9	85.2±7.0	0.95±0.21	0.8±0.0	199±25.5	1.17±0.49
Cs-AAC	62±8.6	6.2±1.3	10.2±2.0	29.8±12.8	93.5±8.3	1.35±0.21	0.56±0.77	178±101.8	0.77±0.48
Hg-AAC	57.2±2.7	6.1±0.1	11.1±2.8	39.55±6.6	88.7±14.8	0.95±0.35	0.45±0.21	200.5±16.3	1.05±0.25
Cd-DMSA	59.45±3.0	6.4±1.8	12.0±2.4	33.8±12.0	126±42.3	1.15±0.49	0.5±0.57	129.5±3.5	0.68±0.35
Sr-DMSA	70.9±3.7	5.4±0.6	23.2±2.4	28.5±6.1	102.3±23.4	1.35±0.07	3.7±4.67	348.5±57.3	2.25±0.19
Cs-DMSA	55.3±4.5	22.7±9.1	14.0±0.1	41.6±17.9	133.6±33.4	0.95±0.35	3.05±3.75	358.5±44.5	1.03±0.58
Hg-DMSA	64.1±3.4	6.8±0.4	15.3±5.9	37.9±7.9	102.8±3.9	1.3±0.14	0.75±0.92	181±46.7	1.13±0.09

TP - total protein, Glu - glucose, ALT - alanine aminotransferase, AST -aspartate aminotransferase, TBil – total billirubin, GGT -gamma-glutamyltransferase, ALP - alkaline phosphatase, TC - total cholesterol

9.6 Evaluation of the existence of metal ions in animal tissues

The results of the evaluation of metal ions presented in various tissues, such as liver, kidney, stomach, omentum, and duodenum of poisoned and treated animals are presented in **Table 9.3**. No metals were detected in the control group. From the **Table 9.3**, it follows that in cadmium-poisoned animals, the maximum concentrations of metal ions was observed in the stomach and intestine, 8.998 and 6.812 g per g of dried organ. When studying the effectiveness of cryogel on the sorption of cadmium ions in infected animals, it was revealed that after 24 hours of contact, the amount of cadmium in the stomach was ten times less, and in the duodenum almost 34 times. Also, a noticeable decrease in the concentration of cadmium in other investigated organs is 2-24 times compared with the data of group Cd-PC. In the case of unithiol-received animals, it was found that DMSA effectively eliminates cadmium ions, the concentration of which is three times lower in the stomach and 2 times lower in the duodenum compared to cryogel-treated animals. When studying the effectiveness of cryogel and unithiol against strontium, it was found that both antidotes have similar metal-binding activity, which can reduce the metal ions in tissues by 3-5 times. During the determining the cesium content in the poisoned and treated animals, it was found that all groups of animals showed high concentrations of cesium ions due to the use of a

large amount of cesium nitrate, which corresponds to an LD_{50} dose. Despite the introduction of antidotes, the levels of cesium in all groups of the studied organs were consistently high, except for the stomach, in which cryogel and unithiol reduced the cesium concentration by half compared to the Cs-PC group. In a group of animals poisoned with mercury was found that high concentrations of mercury are observed in all studied tissues. Comparing the effectiveness of cryogel and Unithiol, it can be seen that after the treatment with Unithiol, the concentrations of mercury in all tissues was very low, while the cryogel was able to decrease the mercury values by an average of 1.5 times compared with the Hg-PC group.

Table 9.3. Concentration of metal ions in the various tissues of experimental animals

	Liver, mg/g	Kidney, mg/g	Stomach, mg/g	Omentum, mg/g	Duodenum, mg/g
Cd-PC	0.234	0.146	8.998	2.498	6.812
Cd-AAC	0.105	0.035	0.899	0.104	0.202
Cd-DMSA	0.079	0.045	0.313	0.092	0.111
Sr-PC	0.025	0.065	0.298	0.123	0.150
Sr-AAC	0.022	0.038	0.103	0.032	0.037
Sr-DMSA	0.013	0.024	0.086	0.037	0.038
Cs-PC	10.52	9.79	16.27	13.59	10.63
Cs-AAC	14.38	13.15	8.18	9.81	10.16
Cs-DMSA	13.07	14.56	8.82	6.78	14.08
Hg-PC	0.247	0.613	3.035	0.493	0.664
Hg-AAC	0.130	0.564	2.126	0.112	0.420
Hg-DMSA	0.014	0.030	0.207	0.046	0.040

9.7 Summary

Studies have shown that heavy metal intoxication leads to increased changes in liver and kidney function, disrupting the regulatory function of liver and kidney enzymes. With intragastric administration of cryogels after 1 hour of poisoning with LD_{50} doses of metals, it was revealed that after 24 hours of experiments, the survival of experimental animals' increases. A histopathological study of the kidneys and liver markedly improves the condition of tissues with less deformed structure. In the study of biochemical blood markers of experimental animals revealed improvements in indicators treated with cryogels and

Unithiol compared with the poisoned group. A study of the presence of metals in animal organs revealed a decrease in the concentration of metal ions after treatment with cryogel in the organs of rats. Preliminary studies of the use of cryogels as antidotes in acute heavy metal poisoning show that these sorbents have potential in the treatment of acute intoxication and require a more detailed study.

CHAPTER 10

CONCLUSIONS AND FUTURE WORK

10.1 Conclusions

Two novel macroporous cryogels were synthesized by free-radical co-polymerization of acrylate-based precursors with allylamine under sub-zero temperature conditions by optimizing the ratios of monomers, cross-linkers and initiators of the reaction. Surface analysis by use of SEM showed that both types of cryogels have a three-dimensional network associated with super-macroporous and interconnected channels with pore sizes in the range from 10 to 100 μm. AAC and SAC cryogels, containing key monomer methacrylic acid and 2-acrylamido-2-methyl-1-propansulfonic acid, respectively were analyzed by use of FTIR, which identified carboxylic, amide(II), amide(III) and amino groups. The main difference between AAC and SAC was observed as well, being the sulfur-containing functional groups in the structure of the later.

The studies of Hg^{2+} removal from $Hg(NO_3)_2$ and $HgCl_2$ solutions demonstrated that the removal is very fast and the loading capacity very high with AAC cryogel being superior over SAC cryogel. The AAC and SAC samples showed maximum removal capacity around 260 and 174 mg/g from $HgCl_2$ salt solution and up to 626 and 622 mg/g from $Hg(NO_3)_2$ solution, respectively. The mercury removal from $Hg(NO_3)_2$ was more effective, both in terms of equilibrium and kinetics, due to the speciation in the aqueous phase allowing the existence of free Hg^{2+} ions in contrast to $HgCl_2$ where neutral complexes dominate the aqueous phase. The Hg^{2+} removal mechanism was studied in detail and is possibly a combination of ion exchange and complexation reactions. The results of mercury removal from different real water matrixes showed that cryogels removed mercury much faster than commercial adsorbents such as activated carbon, strong acid resin and zeolite Y except for seawater where activated carbon is superior. Again, this is a result of speciation as under the presence of Cl^- mercury forms stable neutral complexes favoring adsorption rather than ion exchange and complexation. The removal experiments of Cd^{2+}, Sr^{2+} and Cs^+ showed fast kinetics and high loading capacities as well. The results show that removal capacities of AAC cryogel were reached the maximum in such order: 361.6 mg/g of Cs^+, 248.6 mg/g for Cd^{2+} and 209.3 mg/g for Sr^{2+} whereas SAC polymer also was best for Cs^+ with maximum

capacity of 258.7 mg/g, while Sr^{2+} and Cd^{2+} adsorption reached 210.5 and 131.9 mg/g, respectively. The dominant removal mechanism was found to be similar to mercury involving ion exchange followed by complexation reactions.

The synthesis of two novel Ag^0/Ag_2O nanocomposite cryogels was successfully done. The nanocomposites were used for targeted removal of iodide from model solutions and real seawater. The results showed that AAC and SAC nanocomposites reached 159 and 98 mg/g iodide loading, respectively. It was found that amide groups of cryogels were able to reduce Ag^+ to form Ag^o nanoparticles while agglomeration and oxidation result in the formation of Ag_2O nanoparticles, verified by XRD and TEM. The release of small amounts of Ag^+ during I^- removal resulted in the formation of negatively charged AgI colloids in the solution. The formation of colloids in the solution was verified by independent experiments and it provides a satisfactory explanation of some discrepancies between observed and theoretically expected I^- loadings in our work as well as in the literature. Finally, the seawater experiments showed that both Ag-cryogel nanocomposites were able to remove almost 100 % of iodide from 100 ppm natural water.

The AAC cryogel, due to its superior efficiency towards metals removal, was used for treatment of LD_{50} poisoned experimental animals and compared with commercial antidote Unithiol. It was found that intragastric administration of cryogels after 1 hour of poisoning with LD_{50} doses of metals decreases the mortality rate of examined rats. A histopathological study of the kidneys and liver and also biochemical blood markers of rats revealed improvements in indicators treated with cryogels and Unithiol compared with the poisoned group. A study of the presence of $Cd^{2+,}$ Hg^{2+}, Sr^{2+} and Cs^+ metal ions in animal tissues revealed a decrease in the concentration of metal ions after treatment with cryogel in the organs of rats. Preliminary studies of the use of cryogels as antidotes in acute metals poisoning show that these sorbents have potential in the treatment of acute intoxication and require a more detailed study.

10.2 Future work

The amount and quality of the experimental results enable to suggest future research directions on cryogel-based adsorbents. Future research directions can be summarized as follows:

- Testing the efficiency of cryogels toward examined and other metal ions in flow-through experiments, by varying the flow rate, the size of monoliths and the concentrations of metal ions.
- Modification of cryogels by different metallic nanoparticles, functional groups and materials such as carbons for targeted removal of inorganic and organic substances such as arsenic, chromium, fluoride and phosphorous.
- Scale-up the synthesis of cryogel monoliths by retaining removal efficiency, mechanical strength and elasticity.
- Study of cryogels under variable aqueous chemistry such as in the presence of competing cations and complexing anions extended to a systematic study under real conditions by use of real contaminated water.
- A more detailed study on the biocompatibility and effectiveness of cryogels for detoxification of animals poisoned with metals and other substances and investigation of the elimination mechanisms in biological media and living organisms.

REFERENCES

[1] Baimenov A, Berillo DA, Poulopoulos SG, Inglezakis VJ. A review of cryogels synthesis, characterization and applications on the removal of heavy metals from

aqueous solutions. Adv Colloid Interface Sci 2020;276. https://doi.org/10.1016/j.cis.2019.102088.

[2] Baimenov AZ, Berillo DA, Moustakas K, Inglezakis VJ. Efficient removal of mercury (II) from water by use of cryogels and comparison to commercial adsorbents under environmentally relevant conditions. J Hazard Mater 2020;399:123056. https://doi.org/https://doi.org/10.1016/j.jhazmat.2020.123056.

[3] Baimenov AZ, Berillo DA, Inglezakis VJ. Cryogel-based Ag°/Ag2O nanocomposites for iodide removal from water. J Mol Liq 2019:112134. https://doi.org/10.1016/j.molliq.2019.112134.

[4] Vodela JK, Renden JA, Lenz SD, McElhenney WH, Kemppainen BW. Drinking water contaminants (arsenic, cadmium, lead, benzene, and trichloroethylene). 1. Interaction of contaminants with nutritional status on general performance and immune function in broiler chickens. vol. 76. 1997. https://doi.org/10.1093/ps/76.11.1474.

[5] Öztürk M, Özözen G, Minareci O, Minareci E. Determination of Heavy Metals in Fish, Water and Sediments of Avsar Dam Lake in Turkey. Iran J Environ Heal Sci Eng 2009;6:73–80.

[6] Holder AA. Inorganic pharmaceuticals. Annu Reports Sect "A" (Inorganic Chem 2012;108:350–68. https://doi.org/10.1039/C2IC90009B.

[7] He L, Wang X, Zhao C, Zhu D, Du W. Inhibition of human amylin fibril formation by insulin-mimetic vanadium complexes. vol. 6. 2014. https://doi.org/10.1039/c4mt00021h.

[8] Storr T, Thompson KH, Orvig C. Design of targeting ligands in medicinal inorganic chemistry. Chem Soc Rev 2006;35:534–44. https://doi.org/10.1039/B514859F.

[9] Evans M, Elinder C-G. Chronic renal failure from lead: myth or evidence-based fact? Kidney Int 2011;79:272–9. https://doi.org/10.1038/ki.2010.394.

[10] Kammerer M, Mastain O, Le Dréan-Quenech'du S, Pouliquen H, Larhantec M. Liver and kidney concentrations of vanadium in oiled seabirds after the Erika wreck. Sci Total Environ 2004;333:295–301. https://doi.org/10.1016/j.scitotenv.2004.05.014.

[11] Kim NH, Hyun YY, Lee K-B, Chang Y, Rhu S, Oh K-H, et al. Environmental Heavy Metal Exposure and Chronic Kidney Disease in the General Population. J Korean Med Sci 2015;30:272–7. https://doi.org/10.3346/jkms.2015.30.3.272.

[12] Kirsch-Volders M, Lison D. Re: Hengstler,J.G., Bolm-Auorff,U., Faldum,A., Janssen,K., Reifenrath,M., Gotte,W., Jung,D., Mayer-Popken,O., Fuchs,J., Gebhard,S., Bienfait,H.G., Schlink,K., Dietrich,C., Faust,D., Epe,B. and Oesch,F. Occupational exposure to heavy metals: DNA damage ind. Carcinogenesis 2003;24:1853–4. https://doi.org/10.1093/carcin/bgg165.

[13] Facchini DM, Yuen VG, Battell ML, McNeill JH, Grynpas MD. The effects of vanadium treatment on bone in diabetic and non-diabetic rats. Bone 2006;38:368–77. https://doi.org/https://doi.org/10.1016/j.bone.2005.08.015.

[14] Hyun Soo K, Yeo Jin K, Young Rok S. An Overview of Carcinogenic Heavy Metal:

Molecular Toxicity Mechanism and Prevention. J Cancer Prev 2015;20:232–40.

[15] Clarkson TW. Metal toxicity in the central nervous system. Environ Health Perspect 1987;75:59–64.

[16] Solenkova N V, Newman JD, Berger JS, Thurston G, Hochman JS, Lamas GA. Metal Pollutants and Cardiovascular Disease: Mechanisms and Consequences of Exposure. Am Heart J 2014;168:812–22. https://doi.org/10.1016/j.ahj.2014.07.007.

[17] Lamas GA, Navas-Acien A, Mark DB, Lee KL. Heavy Metals, Cardiovascular Disease, and the Unexpected Benefits of Edetate Disodium Chelation Therapy. J Am Coll Cardiol 2016;67:2411–8. https://doi.org/10.1016/j.jacc.2016.02.066.

[18] Agency USEP, editor. National Primary Drinking Water Regulations 2009:7.

[19] Mu W, Yu Q, Li X, Wei H, Jian Y. Niobate nanofibers for simultaneous adsorptive removal of radioactive strontium and iodine from aqueous solution. J Alloys Compd 2017;693:550–7. https://doi.org/10.1016/j.jallcom.2016.09.200.

[20] Moore JJ, Raine TP, Jenkins A, Livens FR, Law KA, Morris K, et al. Decontamination of caesium and strontium from stainless steel surfaces using hydrogels. React Funct Polym 2019;142:7–14. https://doi.org/10.1016/j.reactfunctpolym.2019.04.004.

[21] Tauanov Z, Inglezakis VJ. Removal of iodide from water using silver nanoparticles-impregnated synthetic zeolites. Sci Total Environ 2019;682:259–70. https://doi.org/10.1016/j.scitotenv.2019.05.106.

[22] Fu F, Wang Q. Removal of heavy metal ions from wastewaters: A review. J Environ Manage 2011;92:407–18. https://doi.org/10.1016/j.jenvman.2010.11.011.

[23] O'Connell DW, Birkinshaw C, O'Dwyer TF. Heavy metal adsorbents prepared from the modification of cellulose: A review. Bioresour Technol 2008;99:6709–24. https://doi.org/https://doi.org/10.1016/j.biortech.2008.01.036.

[24] Li K, Li H, Xiao T, Zhang G, Long J, Luo D, et al. Removal of thallium from wastewater by a combination of persulfate oxidation and iron coagulation. Process Saf Environ Prot 2018;119:340–9. https://doi.org/10.1016/j.psep.2018.08.018.

[25] Oncel MS, Muhcu A, Demirbas E, Kobya M. A comparative study of chemical precipitation and electrocoagulation for treatment of coal acid drainage wastewater. J Environ Chem Eng 2013;1:989–95. https://doi.org/10.1016/j.jece.2013.08.008.

[26] Fu F, Xie L, Tang B, Wang Q, Jiang S. Application of a novel strategy—Advanced Fenton-chemical precipitation to the treatment of strong stability chelated heavy metal containing wastewater. Chem Eng J 2012;189–190:283–7. https://doi.org/10.1016/j.cej.2012.02.073.

[27] Alhasawi A., Auger C., Appanna V.P., Chahma M., V.D. A. Zinc toxicity and ATP production in Pseudomonas fluorescens. J Appl Microbiol 2014;117:65–73. https://doi.org/doi:10.1111/jam.12497.

[28] Prince C. Roger. Bioremediation: An Overview of How Microbiological Processes can be Applied to the Cleanup of Organic and Inorganic Environmental Pollutants.

Encycl. Environ. Microbiol., 2003. https://doi.org/10.1002/0471263397.env168.

[29] Feng D, Aldrich C. Adsorption of heavy metals by biomaterials derived from the marine alga Ecklonia maxima. Hydrometallurgy n.d.;73:1–10. https://doi.org/10.1016/S0304-386X(03)00138-5.

[30] Wan W, Bannerman AD, Yang L, Mak H. Poly(Vinyl Alcohol) Cryogels for Biomedical Applications. In: Okay O, editor. Polym. Cryogels Macroporous Gels with Remarkable Prop., Cham: Springer International Publishing; 2014, p. 283–321. https://doi.org/10.1007/978-3-319-05846-7_8.

[31] Timofejeva A, D'Este M, Loca D. Calcium phosphate/polyvinyl alcohol composite hydrogels: A review on the freeze-thawing synthesis approach and applications in regenerative medicine. Eur Polym J 2017;95:547–65. https://doi.org/10.1016/j.eurpolymj.2017.08.048.

[32] Chu KC, Rutt BK. Polyvinyl alcohol cryogel: An ideal phantom material for MR studies of arterial flow and elasticity. Magn Reson Med 1997;37:314–9. https://doi.org/10.1002/mrm.1910370230.

[33] Dainiak MB, Galaev IY, Kumar A, Plieva FM, Mattiasson B. Chromatography of Living Cells Using Supermacroporous Hydrogels, Cryogels. In: Kumar A, Galaev IY, Mattiasson B, editors. Cell Sep. Fundam. Anal. Prep. Methods, Berlin, Heidelberg: Springer Berlin Heidelberg; 2007, p. 101–27. https://doi.org/10.1007/10_2006_044.

[34] Qian L, Zhang H. Controlled freezing and freeze drying: a versatile route for porous and micro-/nano-structured materials. J Chem Technol Biotechnol 2011;86:172–84. https://doi.org/10.1002/jctb.2495.

[35] Baker MI, Walsh SP, Schwartz Z, Boyan BD. A review of polyvinyl alcohol and its uses in cartilage and orthopedic applications. J Biomed Mater Res Part B Appl Biomater 2012;100B:1451–7. https://doi.org/10.1002/jbm.b.32694.

[36] Altunina LK, Fufaeva MS, Filatov DA, Svarovskaya LI, Rozhdestvenskii EA, Gan-Erdene T. Effect of cryogel on soil properties. Eurasian Soil Sci 2014;47:425–31. https://doi.org/10.1134/S1064229314010025.

[37] Hixon KR, Lu T, Sell SA. A comprehensive review of cryogels and their roles in tissue engineering applications. Acta Biomater 2017;62:29–41. https://doi.org/10.1016/j.actbio.2017.08.033.

[38] Lozinsky VI. Polymeric cryogels as a new family of macroporous and supermacroporous materials for biotechnological purposes. Russ Chem Bull 2008;57:1015–32. https://doi.org/10.1007/s11172-008-0131-7.

[39] Lozinsky VI, Damshkaln LG, Kurochkin IN, Kurochkin II. Cryostructuring of polymeric systems. 36. Poly(vinyl alcohol) cryogels prepared from solutions of the polymer in water/low-molecular alcohol mixtures. Eur Polym J 2014;53:189–205. https://doi.org/10.1016/j.eurpolymj.2014.01.020.

[40] Okay O, Lozinsky VI. Synthesis and Structure–Property Relationships of Cryogels. In: Okay O, editor. Polym. Cryogels Macroporous Gels with Remarkable Prop., Cham: Springer International Publishing; 2014, p. 103–57. https://doi.org/10.1007/978-3-319-05846-7_3.

[41] Gun'ko VM, Savina IN, Mikhalovsky S V. Cryogels: morphological, structural and adsorption characterisation. Adv Colloid Interface Sci 2013;187–188:1–46. https://doi.org/10.1016/j.cis.2012.11.001.

[42] Berillo Dmitriy, Elowsson Linda, Harald K. Oxidized Dextran as Crosslinker for Chitosan Cryogel Scaffolds and Formation of Polyelectrolyte Complexes between Chitosan and Gelatin. Macromol Biosci 2012;12:1090–9. https://doi.org/doi:10.1002/mabi.201200023.

[43] Lozinsky V. Cryogels on the basis of natural and synthetic polymers: preparation, properties and application. Russ Chem Rev 2002;71:489–511. https://doi.org/1070/RC2002v071n06ABEH000720.

[44] Kumar Ashok, Mishra Ruchi, Reinwald Yvonne, Sumrita B. Cryogels: Freezing unveiled by thawing. Mater Today 2010;13:42–4. https://doi.org/10.1016/S1369-7021(10)70202-9.

[45] Lozinsky VI, Galaev IY, Plieva FM, Savina IN, Jungvid H, Mattiasson B. Polymeric cryogels as promising materials of biotechnological interest. Trends Biotechnol 2003;21:445–51. https://doi.org/10.1016/j.tibtech.2003.08.002.

[46] Tekin K, Uzun L, Şahin ÇA, Bektaş S, Denizli A. Preparation and characterization of composite cryogels containing imidazole group and use in heavy metal removal. React Funct Polym 2011;71:985–93. https://doi.org/10.1016/j.reactfunctpolym.2011.06.005.

[47] Abdurrahmanoglu S, Can V, Okay O. Design of high-toughness polyacrylamide hydrogels by hydrophobic modification. Polymer (Guildf) 2009;50:5449–55. https://doi.org/10.1016/j.polymer.2009.09.042.

[48] Su E, Okay O. Polyampholyte hydrogels formed via electrostatic and hydrophobic interactions. Eur Polym J 2017;88:191–204. https://doi.org/10.1016/j.eurpolymj.2017.01.029.

[49] Jalilzadeh M, Şenel S. Removal of Cu(II) ions from water by ion-imprinted magnetic and non-magnetic cryogels: A comparison of their selective Cu(II) removal performances. J Water Process Eng 2016;13:143–52. https://doi.org/10.1016/j.jwpe.2016.08.010.

[50] Kurozumi M, Yano Y, Kiyoyama S, Kumar A, Shiomori K. Adsorption Properties of Arsenic(V) by Polyacrylamide Cryogel Containing Iron Hydroxide Oxide Particles Prepared by *in situ* Method. Resour Process 2015;62:17–23. https://doi.org/10.4144/rpsj.62.17.

[51] Baimenov A, Berillo D, Abylgazina L, Poulopoulos SG, Inglezakis VJ. Novel Amphoteric Cryogels for Cd2+ Ions Removal from Aqueous Solutions. Key Eng. Mater., vol. 775, Trans Tech Publ; 2018, p. 376–82.

[52] Alkan H. Poly(hydroxyethyl methacrylate)-co-N-methacryloyl-(L)-histidine methyl ester Based Cryogel for the Removal of Fe3+ from Human Plasma effected with Beta Thalassemia. Hacettepe J Biol Chem 2015;43:179–85. https://doi.org/10.15671/HJBC.20154314240.

[53] Choudhury S, Connolly D, White B. Supermacroporous polyHIPE and cryogel

monolithic materials as stationary phases in separation science: a review. Anal Methods 2015;7:6967–82. https://doi.org/10.1039/C5AY01193K.

[54] Essawy HA, Ibrahim HS. Synthesis and characterization of poly(vinylpyrrolidone-co-methylacrylate) hydrogel for removal and recovery of heavy metal ions from wastewater. React Funct Polym 2004;61:421–32. https://doi.org/10.1016/j.reactfunctpolym.2004.08.003.

[55] Kutlusoy T, Oktay B, Apohan NK, Süleymanoğlu M, Kuruca SE. Chitosan-co-Hyaluronic acid porous cryogels and their application in tissue engineering. Int J Biol Macromol 2017;103:366–78. https://doi.org/10.1016/j.ijbiomac.2017.05.067.

[56] Alexandratos SD. New polymer-supported ion-complexing agents: Design, preparation and metal ion affinities of immobilized ligands. J Hazard Mater 2007;139:467–70. https://doi.org/https://doi.org/10.1016/j.jhazmat.2006.02.042.

[57] Milakin KA, Acharya U, Hodan J, Trchová M, Stejskal J, Bober P. Effect of 1,3-phenylenediamine concentration on the properties of poly(aniline-co-1,3-phenylenediamine) cryogels. Mater Lett 2018;229:68–70. https://doi.org/10.1016/j.matlet.2018.06.080.

[58] Zaborina OE, Gasanov RG, Peregudov AS, Lozinsky VI. Cryostructuring of polymeric systems. 38. The causes of the covalently-crosslinked cryogels formation upon the homopolymerization of N,N-dimethylacrylamide in moderately-frozen aqueous media. Eur Polym J 2014;61:226–39. https://doi.org/10.1016/j.eurpolymj.2014.10.006.

[59] Caykara T, Küçüktepe S, Turan E. Thermosensitive Poly[(2-(diethylamino)ethyl methacrylate)-co-(N,N-dimethylacrylamide)] Cryogels Prepared by a Two-Step Polymerization Method. Macromol Mater Eng 2006;291:1278–86. https://doi.org/doi:10.1002/mame.200600232.

[60] Lozinsky VI, Golovina TO, Gusev DG. Study of cryostructuration of polymer systems:: XIII. Some characteristic features of the behaviour of macromolecular thiols in frozen aqueous solutions. Polymer (Guildf) 2000;41:35–47. https://doi.org/10.1016/S0032-3861(99)00136-6.

[61] Lozinsky VI, Vainerman ES, Titova EF, Belavtseva EM, Rogozhin S V. Study of cryostructurization of polymer systems. Colloid Polym Sci 1984;262:769–74. https://doi.org/10.1007/BF01451705.

[62] Lozinsky VI, Vainerman ES, Ivanova SA, Titova EF, Shtil'man MI, Belavtseva EM, et al. Study of cryostructurization of polymer systems. VI. The influence of the process temperature on the dynamics of formation and structure of cross-linked polyacrylamide cryogels. Acta Polym 1986;37:142–6. https://doi.org/10.1002/actp.1986.010370303.

[63] Onnby L, Giorgi C, Plieva FM, Mattiasson B. Removal of Heavy Metals from Water Effluents Using Supermacroporous Metal Chelating Cryogels. Biotechnol Prog 2010;26:1295–302. https://doi.org/10.1002/btpr.422.

[64] Önnby L, Svensson C, Mbundi L, Busquets R, Cundy A, Kirsebom H. γ-Al2O3-based nanocomposite adsorbents for arsenic(V) removal: Assessing performance, toxicity

and particle leakage. Sci Total Environ 2014;473–474:207–14. https://doi.org/10.1016/j.scitotenv.2013.12.020.

[65] Wang X, Gil Min B. Cadmium sorption properties of poly(vinyl alcohol)/hydroxyapatite cryogels: I. kinetic and isotherm studies. Fibers Polym 2007;43:99–104. https://doi.org/10.1007/s10971-007-1548-4.

[66] Elbarbary AM, Ghobashy MM. Phosphorylation of chitosan/HEMA interpenetrating polymer network prepared by γ-radiation for metal ions removal from aqueous solutions. Carbohydr Polym 2017;162:16–27. https://doi.org/10.1016/j.carbpol.2017.01.013.

[67] Önnby L, Harald K, Nges IA. Cryogel-supported titanate nanotubes for waste treatment: Impact on methane production and bio-fertilizer quality. J Biotechnol 2015;207:58–66. https://doi.org/10.1016/j.jbiotec.2015.05.014.

[68] Wang L-Y, Wang M-J. Removal of Heavy Metal Ions by Poly(vinyl alcohol) and Carboxymethyl Cellulose Composite Hydrogels Prepared by a Freeze–Thaw Method. ACS Sustain Chem Eng 2016;4:2830–7. https://doi.org/10.1021/acssuschemeng.6b00336.

[69] Bakhshpour M, Idil N, Perçin I, Denizli A. Biomedical applications of polymeric cryogels. Appl Sci 2019;9. https://doi.org/10.3390/app9030553.

[70] Carvalho BMA, Da Silva SL, Da Silva LHM, Minim VPR, Da Silva MCH, Carvalho LM, et al. Cryogel poly(acrylamide): Synthesis, structure and applications. Sep Purif Rev 2014;43:241–62. https://doi.org/10.1080/15422119.2013.795902.

[71] Henderson TMA, Ladewig K, Haylock DN, McLean KM, O'Connor AJ. Cryogels for biomedical applications. J Mater Chem B 2013;1:2682–95. https://doi.org/10.1039/c3tb20280a.

[72] Plieva FM, Kirsebom H, Mattiasson B. Preparation of macroporous cryostructurated gel monoliths, their characterization and main applications. J Sep Sci 2011;34:2164–72. https://doi.org/10.1002/jssc.201100199.

[73] Radhouani H, Bicho D, Gonçalves C, Maia FR, Reis RL, Oliveira JM. Kefiran cryogels as potential scaffolds for drug delivery and tissue engineering applications. Mater Today Commun 2019:100554. https://doi.org/10.1016/j.mtcomm.2019.100554.

[74] Rac V, Lević S, Balanč B, Graells BO, Bijelić G. PVA Cryogel as model hydrogel for iontophoretic transdermal drug delivery investigations. Comparison with PAA/PVA and PAA/PVP interpenetrating networks. Colloids Surfaces B Biointerfaces 2019;180:441–8. https://doi.org/10.1016/j.colsurfb.2019.05.017.

[75] Zhao S, Wang D, Zhu S, Liu X, Zhang H. 3D cryogel composites as adsorbent for isolation of protein and small molecules. Talanta 2019;191:229–34. https://doi.org/10.1016/j.talanta.2018.08.068.

[76] Dobritoiu R, Patachia S. A study of dyes sorption on biobased cryogels. Appl Surf Sci 2013;285:56–64. https://doi.org/10.1016/j.apsusc.2013.07.164.

[77] Li Z, Yang L, Cao H, Chang Y, Tang K, Cao Z, et al. Carbon materials derived from

chitosan/cellulose cryogel-supported zeolite imidazole frameworks for potential supercapacitor application. Carbohydr Polym 2017;175:223–30. https://doi.org/10.1016/j.carbpol.2017.07.089.

[78] Khalid B, Meng Q, Li J, Cao B. Nitrogen rich graphene-cross-linked melamine formaldehyde carbon cryogels for supercapacitors. Electrochim Acta 2014;142:101–7. https://doi.org/10.1016/j.electacta.2014.07.102.

[79] Sahiner N, Demirci S. The use of graphene oxide-embedded superporous poly(2-hydroxyethylmethacrylate) cryogels for p(aniline) conductive polymer synthesis and their use in sensor applications. Mater Des 2017;120:47–55. https://doi.org/10.1016/j.matdes.2017.02.004.

[80] Esen C, Şenay R, Feyzioğlu Demir E, Akgöl S. Poly(hydroxyethyl methacrylate-co-methacryloylglutamic acid) nanospheres for adsorption of Cd2+ ions from aqueous solutions. vol. 16. 2014. https://doi.org/10.1007/s11051-014-2255-z.

[81] Chen J, Zhao C, Huang H, Wang M, Ge X. Highly crosslinked poly(ethyleneglycol dimethacrylate)-based microspheres via solvothermal precipitation polymerization in alcohol–water system. Polymer (Guildf) 2016;83:214–22. https://doi.org/10.1016/j.polymer.2015.12.028.

[82] Pisarev OA, Polyakova I V. Molecularly imprinted polymers based on methacrylic acid and ethyleneglycol dimethacrylate for l-lysine recognition. React Funct Polym 2018;130:98–110. https://doi.org/https://doi.org/10.1016/j.reactfunctpolym.2018.06.002.

[83] Berillo DA, Caplin JL, Cundy AB, Savina IN. A cryogel-based bioreactor for water treatment applications. Water Res 2019.

[84] Zaushitsyna O, Berillo D, Kirsebom H, Mattiasson B. Cryostructured and crosslinked viable cells forming monoliths suitable for bioreactor applications. Top Catal 2014;57:339–48.

[85] Akilbekova D, Shaimerdenova M, Adilov S, Berillo D. Biocompatible scaffolds based on natural polymers for regenerative medicine. Int J Biol Macromol 2018;114:324–33.

[86] Chen Z, Xu L, Liang Y, Wang J, Zhao M, Li Y. Polyethylene glycol diacrylate-based supermacroporous monolithic cryogel as high-performance liquid chromatography stationary phase for protein and polymeric nanoparticle separation. J Chromatogr A 2008;1182:128–31. https://doi.org/10.1016/j.chroma.2007.12.084.

[87] Berillo D, Mattiasson B, Kirsebom H. Cryogelation of Chitosan Using Noble-Metal Ions: In Situ Formation of Nanoparticles. Biomacromolecules 2014;15:2246–55. https://doi.org/10.1021/bm5003834.

[88] Kavoshchian M, Üzek R, Uyanık SA, Şenel S, Denizli A. HSA immobilized novel polymeric matrix as an alternative sorbent in hemoperfusion columns for bilirubin removal. React Funct Polym 2015;96:25–31. https://doi.org/10.1016/j.reactfunctpolym.2015.09.004.

[89] Li Y, Wu Y, Xu Q, Gao Y, Cao G, Meng Z, et al. Facile and controllable synthesis of polystyrene/palladium nanoparticle@ polypyrrole nanocomposite particles. Polym

Chem 2013;4:4655–62.

[90] Önnby L, Pakade V, Mattiasson B, Kirsebom H. Polymer composite adsorbents using particles of molecularly imprinted polymers or aluminium oxide nanoparticles for treatment of arsenic contaminated waters. Water Res 2012;46:4111–20. https://doi.org/10.1016/j.watres.2012.05.028.

[91] Sahiner N, Seven F. Energy and environmental usage of super porous poly(2-acrylamido-2-methyl-1-propan sulfonic acid) cryogel support. RSC Adv 2014;4:23886–97. https://doi.org/10.1039/C4RA01386G.

[92] Loo S-L, Fane AG, Lim T-T, Krantz WB, Liang Y-N, Liu X, et al. Superabsorbent Cryogels Decorated with Silver Nanoparticles as a Novel Water Technology for Point-of-Use Disinfection. Environ Sci Technol 2013;47:9363–71. https://doi.org/10.1021/es401219s.

[93] Rehman S ur, Siddiq M, Al-Lohedan H, Aktas N, Sahiner M, Demirci S, et al. Fast removal of high quantities of toxic arsenate via cationic p(APTMACl) microgels. J Environ Manage 2016;166:217–26. https://doi.org/10.1016/j.jenvman.2015.10.026.

[94] Tabaklı B, Topçu AA, Döker S, Uzun L. Particle-Assisted Ion-Imprinted Cryogels for Selective CdII Ion Removal. Ind Eng Chem Res 2015;54:1816–23. https://doi.org/10.1021/ie504312e.

[95] Çimen D, Türkmen D, Denizli A. Poly-L-Histidine Attached Poly(glycidyl methacrylate) Cryogels for Heavy Metal Removal. J Macromol Sci Part A 2015;52:724–31. https://doi.org/10.1080/10601325.2015.1063868.

[96] Ozmen MM, Okay O. Superfast responsive ionic hydrogels with controllable pore size. Polymer (Guildf) 2005;46:8119–27. https://doi.org/10.1016/j.polymer.2005.06.102.

[97] Tatykhanova G, Sadakbayeva Zh, Berillo D, Galaev I, Abdullin Kh, Adilov Zh, et al. Metal Complexes of Amphoteric Cryogels Based on Allylamine and Methacrylic Acid. Macromol Symp 2012;317–318:18–27. https://doi.org/10.1002/masy.201100065.

[98] Kudaibergenov S, Adilov Z, Berillo D, Tatykhanova G, Sadakbaeva Z. Novel macroporous amphoteric gels: Preparation and characterization 2012;6:346–53. https://doi.org/10.3144/expresspolymlett.2012.38.

[99] Erol K, Uzun L. Two-step polymerization approach for synthesis of macroporous surface ion-imprinted cryogels. J Macromol Sci Part A Pure Appl Chem 2017;54:867–75. https://doi.org/10.1080/10601325.2017.1342519.

[100] Sahiner N, Demirci S, Sahiner M, Yilmaz S, Al-Lohedan H. The use of superporous p(3-acrylamidopropyl)trimethyl ammonium chloride cryogels for removal of toxic arsenate anions. J Environ Manage 2015;152:66–74. https://doi.org/10.1016/j.jenvman.2015.01.023.

[101] Srinivas P, Rao KN, Sethuram B, Rao TN. Polymerization of Acrylonitrile Initiated by Ce4+ Msopropyl Alcohol Redox System in the Presence and Absence of Ag+: A Kinetic Study. J Macromol Sci 1982;18:261–70.

[102] Wang C, Sun Y. Double sequential modifications of composite cryogel beds for enhanced ion-exchange capacity of protein. J Chromatogr A 2013;1307:73–9. https://doi.org/10.1016/j.chroma.2013.07.066.

[103] Erdem A, Ngwabebhoh FA, Çetintaş S, Bingöl D, Yildiz U. Fabrication and characterization of novel macroporous Jeffamine/diamino hexane cryogels for enhanced Cu(II) metal uptake: Optimization, isotherms, kinetics and thermodynamic studies. Chem Eng Res Des 2017;117:122–38. https://doi.org/10.1016/j.cherd.2016.10.010.

[104] Dragan ES, Humelnicu D, Dinu MV, Olariu RI. Kinetics, equilibrium modeling, and thermodynamics on removal of Cr(VI) ions from aqueous solution using novel composites with strong base anion exchanger microspheres embedded into chitosan/poly(vinyl amine) cryogels. Chem Eng J 2017;330:675–91. https://doi.org/10.1016/j.cej.2017.08.004.

[105] Kanno T, Uyama H. Unique Ivy-Like Morphology Composed of Poly(lactic acid) and Bacterial Cellulose Cryogel. ACS Omega 2018;3:631–5. https://doi.org/10.1021/acsomega.7b01968.

[106] Lozinsky V, Kolosova O, Michurov D, Dubovik A, Vasil'ev V, Grinberg V. Cryostructuring of Polymeric Systems. 49. Unexpected "Kosmotropic-Like" Impact of Organic Chaotropes on Freeze–Thaw-Induced Gelation of PVA in DMSO. Gels 2018;4:81.

[107] Zhai M, Ma F, Li J, Wan B, Yu N. Preparation and properties of cryogel based on poly(hydroxypropyl methacrylate). J Biomater Sci Polym Ed 2018;29:1–44. https://doi.org/10.1080/09205063.2018.1464263.

[108] Zhang X-Z, Chu C-C. Thermosensitive PNIPAAm cryogel with superfast and stable oscillatory properties. Chem Commun 2003:1446–7. https://doi.org/10.1039/B301423A.

[109] Orakdogen N, Kizilay MY, Okay O. Suppression of inhomogeneities in hydrogels formed by free-radical crosslinking copolymerization. Polymer (Guildf) 2005;46:11407–15. https://doi.org/10.1016/j.polymer.2005.09.082.

[110] Lozinsky VI, Morozova SA, Vainerman ES, Titova EF, Shtil'Man MI, Belavtseva EM, et al. Study of cryostructurization of polymer systems. VIII. Characteristic features of the formation of crosslinked poly(acryl amide) cryogels under different thermal conditions. Acta Polym 1989;40:8–15. https://doi.org/10.1002/actp.1989.010400103.

[111] Topuz F, Okay O. Macroporous hydrogel beads of high toughness and superfast responsivity. React Funct Polym 2009;69:273–80. https://doi.org/10.1016/j.reactfunctpolym.2009.01.009.

[112] Zhao Q, Sun J, Ling Q, Zhou Q. Synthesis of Macroporous Thermosensitive Hydrogels: A Novel Method of Controlling Pore Size. Langmuir 2009;25:3249–54. https://doi.org/10.1021/la8038939.

[113] Kumakura M, Kaetsu I. Polymeric microspheres by radiation copolymerization of acrolein and various monomers at low temperatures. Colloid Polym Sci

1984;262:450–4. https://doi.org/10.1007/BF01412039.

[114] Reichelt S, Abe C, Hainich S, Knolle W, Decker U, Prager A, et al. Electron-beam derived polymeric cryogels. Soft Matter 2013;9:2484–92. https://doi.org/10.1039/C2SM27517A.

[115] Berillo D, Mattiasson B, Galaev IY, Kirsebom H. Formation of macroporous self-assembled hydrogels through cryogelation of Fmoc-Phe-Phe. J Colloid Interface Sci 2012;368:226–30. https://doi.org/10.1016/j.jcis.2011.11.006.

[116] Kirsebom H, Elowsson L, Berillo D, Cozzi S, Inci I, Piskin E, et al. Enzyme-Catalyzed Crosslinking in a Partly Frozen State: A New Way to Produce Supermacroporous Protein Structures. Macromol Biosci 2013;13:67–76.

[117] Kramareva N V, Stakheev AY, Tkachenko OP, Klementiev K V, Grünert W, Finashina ED, et al. Heterogenized palladium chitosan complexes as potential catalysts in oxidation reactions: study of the structure. J Mol Catal A Chem 2004;209:97–106.

[118] Lozinsky VI. Cryostructuring of Polymeric Systems. 50.(†) Cryogels and Cryotropic Gel-Formation: Terms and Definitions. Gels (Basel, Switzerland) 2018;4:77. https://doi.org/10.3390/gels4030077.

[119] Lozinsky VI. Cryogels on the basis of natural and synthetic polymers: preparation, properties and application. Russ Chem Rev 2002;71:489–511. https://doi.org/10.1070/rc2002v071n06abeh000720.

[120] Zhang H, Zhang F, Wu J. Physically crosslinked hydrogels from polysaccharides prepared by freeze–thaw technique. React Funct Polym 2013;73:923–8. https://doi.org/10.1016/j.reactfunctpolym.2012.12.014.

[121] Oshchepkova M V, Oshchepkov AS, Zaborina OE, Fedorova OA, Fedorov Y V, Lozinsky VI. Fluorescent cryogels based on copolymers of N,N-dimethylacrylamide and allyl derivatives of 1,8-naphthalimide. Polym Sci Ser B 2015;57:631–7. https://doi.org/10.1134/S1560090415060159.

[122] Andac M, Plieva FM, Denizli A, Galaev IY, Mattiasson B. Poly(hydroxyethyl methacrylate)-Based Macroporous Hydrogels with Disulfide Cross-Linker. Macromol Chem Phys 2008;209:577–84. https://doi.org/10.1002/macp.200700467.

[123] Bereli N, Ertürk G, Denizli A. Histidine Containing Macroporous Affinity Cryogels for Immunoglobulin G Purification. Sep Sci Technol 2012;47:1813–20. https://doi.org/10.1080/01496395.2012.662258.

[124] Srivastava A, Jain E, Kumar A. The physical characterization of supermacroporous poly(N-isopropylacrylamide) cryogel: Mechanical strength and swelling/de-swelling kinetics. Mater Sci Eng A 2007;464:93–100. https://doi.org/10.1016/j.msea.2007.03.057.

[125] Savina IN, English CJ, Whitby RLD, Zheng Y, Leistner A, Mikhalovsky S V, et al. High efficiency removal of dissolved As(III) using iron nanoparticle-embedded macroporous polymer composites. J Hazard Mater 2011;192:1002–8. https://doi.org/10.1016/j.jhazmat.2011.06.003.

[126] Zhu Q, Li Z. Hydrogel-supported nanosized hydrous manganese dioxide: Synthesis, characterization, and adsorption behavior study for Pb2+, Cu2+, Cd2+ and Ni2+ removal from water. Chem Eng J 2015;281:69–80. https://doi.org/10.1016/j.cej.2015.06.068.

[127] Lofrano G, Carotenuto M, Libralato G, Domingos RF, Markus A, Dini L, et al. Polymer functionalized nanocomposites for metals removal from water and wastewater: An overview. Water Res 2016;92:22–37. https://doi.org/10.1016/j.watres.2016.01.033.

[128] Onorevoli B, da Silva Maciel GP, Machado ME, Corbelini V, Caramão EB, Jacques RA. Characterization of feedstock and biochar from energetic tobacco seed waste pyrolysis and potential application of biochar as an adsorbent. J Environ Chem Eng 2018;6:1279–87. https://doi.org/10.1016/j.jece.2018.01.039.

[129] Kim MY, Lee TG. Removal of Pb(II) ions from aqueous solutions using functionalized cryogels. Chemosphere 2019;217:423–9. https://doi.org/10.1016/j.chemosphere.2018.10.021.

[130] Yeşilova E, Osman B, Kara A, Özer ET. Molecularly imprinted particle embedded composite cryogel for selective tetracycline adsorption. Sep Purif Technol 2018;200:155–63. https://doi.org/10.1016/j.seppur.2018.02.002.

[131] Köse K, Erol K, Ÿzgür E, Uzun L, Denizli A. PolyAdenine cryogels for fast and effective RNA purification. Colloids Surfaces B Biointerfaces 2016;146:678–86. https://doi.org/10.1016/j.colsurfb.2016.07.003.

[132] Baydemir G, Türkołlu EA, Andaç M, Perçin I, Denizli A. Composite cryogels for lysozyme purification. Biotechnol Appl Biochem 2015;62:200–7. https://doi.org/10.1002/bab.1259.

[133] Perçin I, Idil N, Denizli A. Molecularly imprinted poly(N-isopropylacrylamide) thermosensitive based cryogel for immunoglobulin G purification. Process Biochem 2019;80:181–9. https://doi.org/10.1016/j.procbio.2019.02.001.

[134] Chen Y, Ru J, Geng B, Wang H, Tong C, Du C, et al. Charge-functionalized and mechanically durable composite cryogels from Q-NFC and CS for highly selective removal of anionic dyes. Carbohydr Polym 2017;174:841–8. https://doi.org/10.1016/j.carbpol.2017.07.024.

[135] Perçin I, Khalaf R, Brand B, Morbidelli M, Gezici O. Strong cation-exchange chromatography of proteins on a sulfoalkylated monolithic cryogel. J Chromatogr A 2015;1386:13–21. https://doi.org/10.1016/j.chroma.2015.01.075.

[136] Erol K. Polychelated cryogels: hemoglobin adsorption from human blood. Artif Cells, Nanomedicine Biotechnol 2017;45:31–8. https://doi.org/10.1080/21691401.2016.1215326.

[137] Zheng Y, Gun'ko VM, Howell CA, Sandeman SR, Phillips GJ, Kozynchenko OP, et al. Composites with Macroporous Poly(vinyl alcohol) Cryogels with Attached Activated Carbon Microparticles with Controlled Accessibility of a Surface. ACS Appl Mater Interfaces 2012;4:5936–44. https://doi.org/10.1021/am301577c.

[138] Jain E, Kumar A. Designing Supermacroporous Cryogels Based on Polyacrylonitrile

and a Polyacrylamide–Chitosan Semi-interpenetrating Network. J Biomater Sci Polym Ed 2009;20:877–902. https://doi.org/10.1163/156856209X444321.

[139] Spiller KL, Laurencin SJ, Charlton D, Maher SA, Lowman AM. Superporous hydrogels for cartilage repair: Evaluation of the morphological and mechanical properties. Acta Biomater 2008;4:17—25. https://doi.org/10.1016/j.actbio.2007.09.001.

[140] Erdem A, Ngwabebhoh FA, Yildiz U. Novel macroporous cryogels with enhanced adsorption capability for the removal of Cu(II) ions from aqueous phase: Modelling, kinetics and recovery studies. J Environ Chem Eng 2017;5:1269–80. https://doi.org/10.1016/j.jece.2017.02.011.

[141] Yue Y, Mayes RT, Gill G, Kuo L-J, Wood J, Binder A, et al. Macroporous monoliths for trace metal extraction from seawater. RSC Adv 2015;5:50005–10. https://doi.org/10.1039/C5RA02131F.

[142] Mohamed RR, Elella MHA, Sabaa MW. Cytotoxicity and metal ions removal using antibacterial biodegradable hydrogels based on N-quaternized chitosan/poly(acrylic acid). Int J Biol Macromol 2017;98:302–13. https://doi.org/https://doi.org/10.1016/j.ijbiomac.2017.01.107.

[143] Andrabi SM, Tiwari J, Singh S, Sarkar J, Verma N, Kumar A. Supermacroporous hybrid polymeric cryogels for efficient removal of metallic contaminants and microbes from water. Int J Polym Mater Polym Biomater 2016;65:636–45. https://doi.org/10.1080/00914037.2016.1157795.

[144] Li Q, Chen S, Zhuang L, Xu X, Li H. Preparation of a sulfonated activated carbon fiber catalyst with γ-irradiation-induced grafting method. J Mater Res 2012;27:3083–9. https://doi.org/10.1557/jmr.2012.360.

[145] Zheng F-C, Chen Q-W, Hu L, Yan N, Kong X-K. Synthesis of sulfonic acid-functionalized Fe3O4@C nanoparticles as magnetically recyclable solid acid catalysts for acetalization reaction. Dalt Trans 2014;43:1220–7. https://doi.org/10.1039/C3DT52098F.

[146] Minović TZ, Gulicovski JJ, Stoiljković MM, Jokić BM, Živković LS, Matović BZ, et al. Surface characterization of mesoporous carbon cryogel and its application in arsenic (III) adsorption from aqueous solutions. Microporous Mesoporous Mater 2015;201:271–6. https://doi.org/10.1016/j.micromeso.2014.09.031.

[147] Adamson AW, Gast AP. Physical chemistry of surfaces. New York, N.Y: Wiley-Interscience Publication; 1997.

[148] Kudaibergenov SE. Polyampholytes : synthesis, characterization, and application. 1st ed. New York: Springer US; 2002. https://doi.org/10.1007/978-1-4615-0627-0.

[149] Baimenov A, Berillo DA, Poulopoulos SG, Inglezakis VJ. A review of cryogels synthesis, characterization and applications on the removal of heavy metals from aqueous solutions. Adv Colloid Interface Sci 2020;276:102088. https://doi.org/10.1016/j.cis.2019.102088.

[150] Wang X, Kim JH, Min BG. Column study of cadmium adsorption onto poly(vinyl alcohol)/hydroxyapatite composite cryogel. Fibers Polym 2008;9:263–6.

https://doi.org/10.1007/s12221-008-0041-1.

[151] Aşır S, Uzun L, Türkmen D, Say R, Denizli A. Ion-selective Imprinted Superporous Monolith for Cadmium Removal from Human Plasma. Sep Sci Technol 2005;40:3167–85. https://doi.org/10.1080/01496390500385376.

[152] Hennink WE, van Nostrum CF. Novel crosslinking methods to design hydrogels. Adv Drug Deliv Rev 2012;64:223–36. https://doi.org/10.1016/j.addr.2012.09.009.

[153] Lozinsky VI, Vainerman ES, Rogozhin S V. Study of cryostructurization of polymer systems. Colloid Polym Sci 1982;260:776–80. https://doi.org/10.1007/BF01452068.

[154] Han M-E, Kang BJ, Kim S-H, Kim HD, Hwang NS. Gelatin-based extracellular matrix cryogels for cartilage tissue engineering. J Ind Eng Chem 2017;45:421–9. https://doi.org/10.1016/j.jiec.2016.10.011.

[155] Cetin K, Türkmen D, Qureshi T, Saglam N, Denizli A. Phanerochaete Chrysosporium Loaded Cryogel Column for Biosorption of Mercury (II) Ions from Aqueous Solutions. Hacettepe J Biol Chem 2016;44:77–86. https://doi.org/10.15671/HJBC.20164417568.

[156] Goher ME, Hassan AM, Abdel-Moniem IA, Fahmy AH, Abdo MH, El-sayed SM. Removal of aluminum, iron and manganese ions from industrial wastes using granular activated carbon and Amberlite IR-120H. Egypt J Aquat Res 2015;41:155–64. https://doi.org/https://doi.org/10.1016/j.ejar.2015.04.002.

[157] Bosso ST, Enzweiler J. Evaluation of heavy metal removal from aqueous solution onto scolecite. Water Res 2002;36:4795–800. https://doi.org/10.1016/S0043-1354(02)00208-7.

[158] Alvarez-Ayuso E, García-Sánchez A, Querol X. Purification of metal electroplating waste waters using zeolites. Water Res 2003;37:4855—4862. https://doi.org/10.1016/j.watres.2003.08.009.

[159] Inglezakis VJ, Loizidou MD, Grigoropoulou HP. Equilibrium and kinetic ion exchange studies of Pb2+, Cr3+, Fe3+ and Cu2+ on natural clinoptilolite. Water Res 2002;36:2784–92. https://doi.org/10.1016/S0043-1354(01)00504-8.

[160] Wang S, Peng Y. Natural zeolites as effective adsorbents in water and wastewater treatment. Chem Eng J 2010;156:11–24. https://doi.org/10.1016/j.cej.2009.10.029.

[161] Sprynskyy M, Buszewski B, Terzyk AP, Namieśnik J. Study of the selection mechanism of heavy metal (Pb2+, Cu2+, Ni2+, and Cd2+) adsorption on clinoptilolite. J Colloid Interface Sci 2006;304:21–8. https://doi.org/10.1016/j.jcis.2006.07.068.

[162] Burakov AE, Galunin E V, Burakova I V, Kucherova AE, Agarwal S, Tkachev AG, et al. Adsorption of heavy metals on conventional and nanostructured materials for wastewater treatment purposes: A review. Ecotoxicol Environ Saf 2018;148:702–12. https://doi.org/10.1016/j.ecoenv.2017.11.034.

[163] Silva RMP, Manso JPH, Rodrigues JRC, Lagoa RJL. A comparative study of alginate beads and an ion-exchange resin for the removal of heavy metals from a metal plating effluent. J Environ Sci Heal Part A 2008;43:1311–7.

https://doi.org/10.1080/10934520802177953.

[164] Shu Y, Huang R, Wei X, Liu L, Jia Z. Pb(II) Removal Using TiO2-Embedded Monolith Composite Cryogel as an Alternative Wastewater Treatment Method. Water, Air, Soil Pollut 2017;228:375. https://doi.org/10.1007/s11270-017-3559-2.

[165] Kocaoba S. Comparison of Amberlite IR 120 and dolomite's performances for removal of heavy metals. J Hazard Mater 2007;147:488–96. https://doi.org/10.1016/j.jhazmat.2007.01.037.

[166] Rengaraj S, Yeon K-H, Kang S-Y, Lee J-U, Kim K-W, Moon S-H. Studies on adsorptive removal of Co(II), Cr(III) and Ni(II) by IRN77 cation-exchange resin. J Hazard Mater 2002;92:185–98. https://doi.org/10.1016/S0304-3894(02)00018-3.

[167] Pestov A V, Privar YO, Mekhaev A V, Fedorets AN, Ezhikova MA, Kodess MI, et al. A new approach to the green synthesis of imidazole-containing polymer ligands and cryogels. Eur Polym J 2019;115:356–63. https://doi.org/10.1016/j.eurpolymj.2019.03.049.

[168] Suresh Kumar P, Önnby L, Kirsebom H. Arsenite adsorption on cryogels embedded with iron-aluminium double hydrous oxides: Possible polishing step for smelting wastewater? J Hazard Mater 2013;250–251:469–76. https://doi.org/10.1016/j.jhazmat.2013.02.022.

[169] Suresh Kumar P, Flores RQ, Sjöstedt C, Önnby L. Arsenic adsorption by iron–aluminium hydroxide coated onto macroporous supports: Insights from X-ray absorption spectroscopy and comparison with granular ferric hydroxides. J Hazard Mater 2016;302:166–74. https://doi.org/10.1016/j.jhazmat.2015.09.065.

[170] Şarkaya K, Bakhshpour M, Denizli A. Ag+ ions imprinted cryogels for selective removal of silver ions from aqueous solutions. Sep Sci Technol 2018. https://doi.org/10.1080/01496395.2018.1556300.

[171] Privar Y, Malakhova I, Pestov A, Fedorets A, Azarova Y, Schwarz S, et al. Polyethyleneimine cryogels for metal ions sorption. Chem Eng J 2018;334:1392–8. https://doi.org/10.1016/j.cej.2017.11.097.

[172] Wang X, Deng W, Xie Y, Wang C. Selective removal of mercury ions using a chitosan–poly(vinyl alcohol) hydrogel adsorbent with three-dimensional network structure. Chem Eng J 2013;228:232–42. https://doi.org/10.1016/j.cej.2013.04.104.

[173] Lloyd-Jones PJ, Rangel-Mendez JR, Streat M. Mercury Sorption from Aqueous Solution by Chelating Ion Exchange Resins, Activated Carbon and a Biosorbent. Process Saf Environ Prot 2004;82:301–11. https://doi.org/10.1205/095758204323162328.

[174] Zhu L, Zhang L, Tang Y. Synthesis of Montmorillonite/Poly(acrylic acid-co-2-acrylamido-2-methyl-1-propane sulfonic acid) Superabsorbent Composite and the Study of its Adsorption. Bull Korean Chem Soc 2012;33. https://doi.org/10.5012/bkcs.2012.33.5.1669.

[175] Inglezakis VJ, Poulopoulos SG. 4 - Adsorption and Ion Exchange. In: Inglezakis VJ, Poulopoulos SG, editors. Adsorpt. Ion Exch. Catal., Amsterdam: Elsevier; 2006, p. 243–353. https://doi.org/10.1016/B978-044452783-7/50004-5.

[176] Aguayo-Villarreal IA, Bonilla-Petriciolet A, Muñiz-Valencia R. Preparation of activated carbons from pecan nutshell and their application in the antagonistic adsorption of heavy metal ions. J Mol Liq 2017;230:686–95. https://doi.org/10.1016/j.molliq.2017.01.039.

[177] Khan M, Lo IMC. A holistic review of hydrogel applications in the adsorptive removal of aqueous pollutants: Recent progress, challenges, and perspectives. Water Res 2016;106:259–71. https://doi.org/10.1016/j.watres.2016.10.008.

[178] Türkmen D, Bereli N, Derazshamshir A, Perçin I, Shaikh H, Yılmaz F. Megaporous poly(hydroxy ethylmethacrylate) based poly(glycidylmethacrylate-N-methacryloly-(l)-tryptophan) embedded composite cryogel. Colloids Surfaces B Biointerfaces 2015;130:61–8. https://doi.org/10.1016/j.colsurfb.2015.04.004.

[179] Tamahkar E, Bakhshpour M, Andaç M, Denizli A. Ion imprinted cryogels for selective removal of Ni(II) ions from aqueous solutions. Sep Purif Technol 2017;179:36–44. https://doi.org/10.1016/j.seppur.2016.12.048.

[180] Chen H, Qu X, Liu N, Wang S, Chen X, Liu S. Study of the adsorption process of heavy metals cations on Kraft lignin. Chem Eng Res Des 2018;139:248–58. https://doi.org/10.1016/j.cherd.2018.09.028.

[181] Šćiban MB, Klašnja MT, Antov MG. Study of the biosorption of different heavy metal ions onto Kraft lignin. Ecol Eng 2011;37:2092–5. https://doi.org/10.1016/j.ecoleng.2011.08.006.

[182] Bacelo HAM, Santos SCR, Botelho CMS. Tannin-based biosorbents for environmental applications – A review. Chem Eng J 2016;303:575–87. https://doi.org/10.1016/j.cej.2016.06.044.

[183] Xu Q, Wang Y, Jin L, Wang Y, Qin M. Adsorption of Cu (II), Pb (II) and Cr (VI) from aqueous solutions using black wattle tannin-immobilized nanocellulose. J Hazard Mater 2017;339:91–9. https://doi.org/10.1016/j.jhazmat.2017.06.005.

[184] Saravanan D, Gomathi T, Sudha PN. Sorption studies on heavy metal removal using chitin/bentonite biocomposite. Int J Biol Macromol 2013;53:67–71. https://doi.org/10.1016/j.ijbiomac.2012.11.005.

[185] Hong M, Yu L, Wang Y, Zhang J, Chen Z, Dong L, et al. Heavy metal adsorption with zeolites: The role of hierarchical pore architecture. Chem Eng J 2019;359:363–72. https://doi.org/10.1016/j.cej.2018.11.087.

[186] Inglezakis VJ, Fyrillas MM, Stylianou MA. Two-phase homogeneous diffusion model for the fixed bed sorption of heavy metals on natural zeolites. Microporous Mesoporous Mater 2018;266:164–76. https://doi.org/10.1016/j.micromeso.2018.02.045.

[187] Visa M. Synthesis and characterization of new zeolite materials obtained from fly ash for heavy metals removal in advanced wastewater treatment. Powder Technol 2016;294:338–47. https://doi.org/10.1016/j.powtec.2016.02.019.

[188] Marciniak M, Goscianska J, Frankowski M, Pietrzak R. Optimal synthesis of oxidized mesoporous carbons for the adsorption of heavy metal ions. J Mol Liq 2019;276:630–7. https://doi.org/10.1016/j.molliq.2018.12.042.

[189] Yang X, Wan Y, Zheng Y, He F, Yu Z, Huang J, et al. Surface functional groups of carbon-based adsorbents and their roles in the removal of heavy metals from aqueous solutions: A critical review. Chem Eng J 2019;366:608–21. https://doi.org/10.1016/j.cej.2019.02.119.

[190] Zhan W, Gao L, Fu X, Siyal SH, Sui G, Yang X. Green synthesis of amino-functionalized carbon nanotube-graphene hybrid aerogels for high performance heavy metal ions removal. Appl Surf Sci 2019;467–468:1122–33. https://doi.org/10.1016/j.apsusc.2018.10.248.

[191] Ranjan B, Pillai S, Permaul K, Singh S. Simultaneous removal of heavy metals and cyanate in a wastewater sample using immobilized cyanate hydratase on magnetic-multiwall carbon nanotubes. J Hazard Mater 2019;363:73–80. https://doi.org/10.1016/j.jhazmat.2018.07.116.

[192] Shah LA, Khan M, Javed R, Sayed M, Khan MS, Khan A, et al. Superabsorbent polymer hydrogels with good thermal and mechanical properties for removal of selected heavy metal ions. J Clean Prod 2018;201:78–87. https://doi.org/10.1016/j.jclepro.2018.08.035.

[193] Demirbilek C, Dinç CÖ. Synthesis of diethylaminoethyl dextran hydrogel and its heavy metal ion adsorption characteristics. Carbohydr Polym 2012;90:1159–67. https://doi.org/10.1016/j.carbpol.2012.06.068.

[194] Siyal AA, Shamsuddin MR, Khan MI, Rabat NE, Zulfiqar M, Man Z, et al. A review on geopolymers as emerging materials for the adsorption of heavy metals and dyes. J Environ Manage 2018;224:327–39. https://doi.org/10.1016/j.jenvman.2018.07.046.

[195] Eeshwarasinghe D, Loganathan P, Vigneswaran S. Simultaneous removal of polycyclic aromatic hydrocarbons and heavy metals from water using granular activated carbon. Chemosphere 2019;223:616–27. https://doi.org/10.1016/j.chemosphere.2019.02.033.

[196] Inglezakis VJ, Loizidou MD. Ion exchange of some heavy metal ions from polar organicsolvents into zeolite. Desalination 2007;211:238–48. https://doi.org/10.1016/j.desal.2006.02.094.

[197] Kecili R, Hussain CM. Chapter 4 - Mechanism of Adsorption on Nanomaterials. In: Hussain CM, editor. Nanomater. Chromatogr., Elsevier; 2018, p. 89–115. https://doi.org/https://doi.org/10.1016/B978-0-12-812792-6.00004-2.

[198] Ma A, Abushaikha A, Allen SJ, McKay G. Ion exchange homogeneous surface diffusion modelling by binary site resin for the removal of nickel ions from wastewater in fixed beds. Chem Eng J 2019;358:1–10. https://doi.org/10.1016/j.cej.2018.09.135.

[199] Satayeva AR, Howell CA, Korobeinyk A V, Jandosov J, Inglezakis VJ, Mansurov ZA, et al. Investigation of rice husk derived activated carbon for removal of nitrate contamination from water. Sci Total Environ 2018;630:1237–45. https://doi.org/10.1016/j.scitotenv.2018.02.329.

[200] Tauanov Z, Tsakiridis PE, Mikhalovsky S V, Inglezakis VJ. Synthetic coal fly ash-derived zeolites doped with silver nanoparticles for mercury (II) removal from water.

J Environ Manage 2018;224:164–71. https://doi.org/10.1016/j.jenvman.2018.07.049.

[201] Stylianou M, Inglezakis V, Agapiou A, Itskos G, Jetybayeva A, Loizidou M. A comparative study on phyllosilicate and tectosillicate mineral structural properties. Desalin Water Treat 2018;112:119–46. https://doi.org/10.5004/dwt.2018.21968.

[202] Savina IN, Mattiasson B, Galaev IY. Graft polymerization of acrylic acid onto macroporous polyacrylamide gel (cryogel) initiated by potassium diperiodatocuprate. Polymer (Guildf) 2005;46:9596–603.

[203] Ertürk G, Mattiasson B. Cryogels-versatile tools in bioseparation. J Chromatogr A 2014;1357:24–35. https://doi.org/10.1016/j.chroma.2014.05.055.

[204] Tripathi A, Kumar A. Multi-featured macroporous agarose-alginate cryogel: synthesis and characterization for bioengineering applications. Macromol Biosci 2011;11:22–35. https://doi.org/10.1002/mabi.201000286.

[205] Yun J, Dafoe JT, Peterson E, Xu L, Yao S-J, Daugulis AJ. Rapid freezing cryo-polymerization and microchannel liquid-flow focusing for cryogel beads: Adsorbent preparation and characterization of supermacroporous bead-packed bed. J Chromatogr A 2013;1284:148–54. https://doi.org/10.1016/j.chroma.2013.02.014.

[206] Busquets R, Ivanov AE, Mbundi L, Hörberg S, Kozynchenko OP, Cragg PJ, et al. Carbon-cryogel hierarchical composites as effective and scalable filters for removal of trace organic pollutants from water. J Environ Manage 2016;182:141–8. https://doi.org/10.1016/j.jenvman.2016.07.061.

[207] Ivanov AE, Kozynchenko OP, Mikhalovska LI, Tennison SR, Jungvid H, Gun'ko VM, et al. Activated carbons and carbon-containing poly(vinyl alcohol) cryogels: characterization, protein adsorption and possibility of myoglobin clearance. Phys Chem Chem Phys 2012;14:16267–78. https://doi.org/10.1039/C2CP42869E.

[208] Savina IN, Gun'ko VM, Turov V V, Dainiak M, Phillips GJ, Galaev IY, et al. Porous structure and water state in cross-linked polymer and protein cryo-hydrogels. Soft Matter 2011;7:4276–83. https://doi.org/10.1039/C0SM01304H.

[209] Dinu MV, Cocarta AI, Dragan ES. Synthesis, characterization and drug release properties of 3D chitosan/clinoptilolite biocomposite cryogels. Carbohydr Polym 2016;153:203–11. https://doi.org/10.1016/j.carbpol.2016.07.111.

[210] Plieva FM, Galaev IY, Noppe W, Mattiasson B. Cryogel applications in microbiology. Trends Microbiol 2008;16:543–51. https://doi.org/10.1016/j.tim.2008.08.005.

[211] Plieva FM, Mattiasson B. Macroporous Gel Particles As Novel Sorbent Materials: Rational Design. Ind Eng Chem Res 2008;47:4131–41. https://doi.org/10.1021/ie071406o.

[212] Ho YS, McKay G. Pseudo-second order model for sorption processes. Process Biochem 1999;34:451–65. https://doi.org/10.1016/S0032-9592(98)00112-5.

[213] Ge H, Hua T. Synthesis and characterization of poly(maleic acid)-grafted crosslinked chitosan nanomaterial with high uptake and selectivity for Hg(II) sorption. Carbohydr Polym 2016;153:246–52.

https://doi.org/https://doi.org/10.1016/j.carbpol.2016.07.110.

[214] Langmuir I. THE CONSTITUTION AND FUNDAMENTAL PROPERTIES OF SOLIDS AND LIQUIDS. PART I. SOLIDS. J Am Chem Soc 1916;38:2221–95. https://doi.org/10.1021/ja02268a002.

[215] Hayati B, Maleki A, Najafi F, Gharibi F, McKay G, Gupta VK, et al. Heavy metal adsorption using PAMAM/CNT nanocomposite from aqueous solution in batch and continuous fixed bed systems. Chem Eng J 2018;346:258–70. https://doi.org/10.1016/j.cej.2018.03.172.

[216] Test No. 425: Acute Oral Toxicity: Up-and-Down Procedure. OECD; 2008. https://doi.org/10.1787/9789264071049-en.

[217] Masterova MN, Andreyeva LI, Zubov VP, Polak LS, Kabanov VA. Polymerization of allylamines in the presence of protonic acids. Polym Sci USSR 1976;18:2234–42. https://doi.org/10.1016/0032-3950(76)90096-4.

[218] Kreindel' MY, Andreyeva LI, Kaplan AM, Golubev VB, Masterova MN, Zubov VP, et al. The kinetics and mechanism of the low temperature post-polymerization of allylamine in the presence of phosphoric acid. Polym Sci USSR 1976;18:2553–61. https://doi.org/10.1016/0032-3950(76)90181-7.

[219] Sumesh E, Bootharaju MS, Anshup, Pradeep T. A practical silver nanoparticle-based adsorbent for the removal of Hg2+ from water. J Hazard Mater 2011;189:450–7. https://doi.org/10.1016/j.jhazmat.2011.02.061.

[220] Anto PL, Anto RJ, Varghese HT, Panicker CY, Philip D, Brolo AG. FT-IR, FT-Raman and SERS spectra of anilinium sulfate. J Raman Spectrosc 2009;40:1810–5. https://doi.org/10.1002/jrs.2323.

[221] Rao CNR, Venkataraghavan R. The C=S stretching frequency and the "-N-C=S bands" in the infrared. Spectrochim Acta 1962;18:541–7. https://doi.org/10.1016/S0371-1951(62)80164-7.

[222] Soliman FM, Yang W, Guo H, Shinger MI, Idris AM, Hassan ES. Preparation of Carboxymethyl Cellulose-g-Poly (Acrylic Acid - 2-Acrylamido-2-Methylpropane Sulfonic Acid)/Attapulgite Superabsorbent Composite. Am J Oil Chem Technol 2016;2:11–9. https://doi.org/10.11648/j.ajpst.20160201.12.

[223] Gworek B, Bemowska-Kałabun O, Kijeńska M, Wrzosek-Jakubowska J. Mercury in Marine and Oceanic Waters---a Review. Water, Air, Soil Pollut 2016;227:371. https://doi.org/10.1007/s11270-016-3060-3.

[224] Siva S, Sudharsan S, Sayee Kannan R. Synthesis, characterization and ion-exchange properties of novel hybrid polymer nanocomposites for selective and effective mercury(ii) removal. RSC Adv 2015;5:79665–78. https://doi.org/10.1039/C5RA13004B.

[225] Kabiri S, Tran DNH, Azari S, Losic D. Graphene-Diatom Silica Aerogels for Efficient Removal of Mercury Ions from Water. ACS Appl Mater Interfaces 2015;7:11815–23. https://doi.org/10.1021/acsami.5b01159.

[226] AMAP/UN Environment Expert Group. Technical Background Report to the Global

Mercury Assessment 2018. 2019.

[227] Yu J-G, Yue B-Y, Wu X-W, Liu Q, Jiao F-P, Jiang X-Y, et al. Removal of mercury by adsorption: a review. Environ Sci Pollut Res 2016;23:5056–76. https://doi.org/10.1007/s11356-015-5880-x.

[228] Yorifuji T, Tsuda T, Inoue S, Takao S, Harada M. Long-term exposure to methylmercury and psychiatric symptoms in residents of Minamata, Japan. Environ Int 2011;37:907–13. https://doi.org/10.1016/j.envint.2011.03.008.

[229] Yorifuji T, Tsuda T, Kashima S, Takao S, Harada M. Long-term exposure to methylmercury and its effects on hypertension in Minamata. Environ Res 2010;110:40–6. https://doi.org/10.1016/j.envres.2009.10.011.

[230] Kamensky OL, Horton D, Kingsley DP, Bridges CC. A Case of Accidental Mercury Intoxication. J Emerg Med 2019;56:275–8. https://doi.org/10.1016/j.jemermed.2018.12.039.

[231] Yorifuji T, Takaoka S, Grandjean P. Accelerated functional losses in ageing congenital Minamata disease patients. Neurotoxicol Teratol 2018;69:49–53. https://doi.org/10.1016/J.NTT.2018.08.001.

[232] Lu P, Chen T, Liu H, Li P, Peng S, Yang Y. Green Preparation of Nanoporous Pyrrhotite by Thermal Treatment of Pyrite as an Effective Hg(II) Adsorbent: Performance and Mechanism. Miner 2019;9. https://doi.org/10.3390/min9020074.

[233] Huang S, Ma C, Liao Y, Min C, Du P, Jiang and Y. Removal of Mercury(II) from Aqueous Solutions by Adsorption on Poly(1-amino-5-chloroanthraquinone) Nanofibrils: Equilibrium, Kinetics, and Mechanism Studies,. J Nanomater 2016;2016:11.

[234] Azimi A, Azari A, Rezakazemi M, Ansarpour M. Removal of Heavy Metals from Industrial Wastewaters: A Review. ChemBioEng Rev 2017;4:37–59. https://doi.org/10.1002/cben.201600010.

[235] Saha D, Barakat S, Van Bramer SE, Nelson KA, Hensley DK, Chen J. Noncompetitive and Competitive Adsorption of Heavy Metals in Sulfur-Functionalized Ordered Mesoporous Carbon. ACS Appl Mater Interfaces 2016;8:34132–42. https://doi.org/10.1021/acsami.6b12190.

[236] Tauanov Z, Tsakiridis PE, Shah D, Inglezakis VJ. Synthetic sodalite doped with silver nanoparticles: Characterization and mercury (II) removal from aqueous solutions. J Environ Sci Heal - Part A Toxic/Hazardous Subst Environ Eng 2019. https://doi.org/10.1080/10934529.2019.1611129.

[237] De Clercq J. Removal of mercury from aqueous solutions by adsorption on a new ultra stable mesoporous adsorbent and on a commercial ion exchange resin. Int J Ind Chem 2012;3:1. https://doi.org/10.1186/2228-5547-3-1.

[238] Qu Z, Fang L, Chen D, Xu H, Yan N. Effective and regenerable Ag/graphene adsorbent for Hg(II) removal from aqueous solution. Fuel 2017;203:128–34. https://doi.org/10.1016/j.fuel.2017.04.105.

[239] Wang X, Sun R, Wang C. pH dependence and thermodynamics of Hg(II) adsorption

onto chitosan-poly(vinyl alcohol) hydrogel adsorbent. Colloids Surfaces A Physicochem Eng Asp 2014;441:51–8. https://doi.org/10.1016/j.colsurfa.2013.08.068.

[240] Saleh TA. Isotherm, kinetic, and thermodynamic studies on Hg(II) adsorption from aqueous solution by silica- multiwall carbon nanotubes. Environ Sci Pollut Res Int 2015;22:16721—16731. https://doi.org/10.1007/s11356-015-4866-z.

[241] Lo S-I, Chen P-C, Huang C-C, Chang H-T. Gold Nanoparticle–Aluminum Oxide Adsorbent for Efficient Removal of Mercury Species from Natural Waters. Environ Sci Technol 2012;46:2724–30. https://doi.org/10.1021/es203678v.

[242] Elhouderi ZA, Beesley DP, Nguyen TT, Lai P, Sheehan K, Trudel S, et al. Synthesis, characterization, and application of Fe3O4/Ag magnetic composites for mercury removal from water. Mater Res Express 2016;3:45013. https://doi.org/10.1088/2053-1591/3/4/045013.

[243] Wang X, Yang L, Zhang J, Wang C, Li Q. Preparation and characterization of chitosan–poly(vinyl alcohol)/bentonite nanocomposites for adsorption of Hg(II) ions. Chem Eng J 2014;251:404–12. https://doi.org/10.1016/j.cej.2014.04.089.

[244] Rao MM, Reddy DHKK, Venkateswarlu P, Seshaiah K. Removal of mercury from aqueous solutions using activated carbon prepared from agricultural by-product/waste. J Environ Manage 2009;90:634—643. https://doi.org/10.1016/j.jenvman.2007.12.019.

[245] Baheti V, Padil V, Militky J, Cernik M, Mishra R. Removal of Mercury from Aqueous Environment by Jute Nano fiber. J Fiber Bioeng Informatics 2013;6:175–84. https://doi.org/10.3993/jfbi06201306.

[246] Sereshti H, Gaikani H, Rashidi Nodeh H. The effective removal of mercury ions (Hg2+) from water using cadmium sulfide nanoparticles doped in polycaprolactam nanofibers: kinetic and equilibrium studies. J Iran Chem Soc 2018;15:743–51. https://doi.org/10.1007/s13738-017-1274-y.

[247] Bandaru NM, Reta N, Dalal H, Ellis A V, Shapter J, Voelcker NH. Enhanced adsorption of mercury ions on thiol derivatized single wall carbon nanotubes. J Hazard Mater 2013;261:534—541. https://doi.org/10.1016/j.jhazmat.2013.07.076.

[248] Awual MR, Hasan MM, Eldesoky GE, Khaleque MA, Rahman MM, Naushad M. Facile mercury detection and removal from aqueous media involving ligand impregnated conjugate nanomaterials. Chem Eng J 2016;290:243–51. https://doi.org/10.1016/j.cej.2016.01.038.

[249] Liu W, Zhao X, Wang T, Fu J, Ni J. Selective and irreversible adsorption of mercury(ii) from aqueous solution by a flower-like titanate nanomaterial. J Mater Chem A 2015;3:17676–84. https://doi.org/10.1039/C5TA04521E.

[250] Wang Z, Xu J, Hu Y, Zhao H, Zhou J, Liu Y, et al. Functional nanomaterials: Study on aqueous Hg(II) adsorption by magnetic Fe3O4@SiO2-SH nanoparticles. J Taiwan Inst Chem Eng 2016;60:394–402. https://doi.org/10.1016/j.jtice.2015.10.041.

[251] Kim HH, Lee TG. Removal of mercury ions in a simulated wastewater using functionalized poly(glycidyl methacrylate). J Ind Eng Chem 2017;47:446–50.

https://doi.org/10.1016/j.jiec.2016.12.019.

[252] Kara A, Uzun L, Beşirli N, Denizli A. Poly(ethylene glycol dimethacrylate-n-vinyl imidazole) beads for heavy metal removal. J Hazard Mater 2004;106:93—99. https://doi.org/10.1016/j.jhazmat.2003.08.016.

[253] Ge H, Hua T, Wang J. Preparation and characterization of poly (itaconic acid)-grafted crosslinked chitosan nanoadsorbent for high uptake of Hg2+ and Pb2+. Int J Biol Macromol 2017;95:954–61. https://doi.org/10.1016/j.ijbiomac.2016.10.084.

[254] Li K, Wang Y, Huang M, Yan H, Yang H, Xiao S, et al. Preparation of chitosan-graft-polyacrylamide magnetic composite microspheres for enhanced selective removal of mercury ions from water. J Colloid Interface Sci 2015;455:261–70. https://doi.org/10.1016/j.jcis.2015.05.043.

[255] Atkins P, Paula J De. Atkins' Physical chemistry 8th edition. Chemistry (Easton) 2009:430–68. https://doi.org/10.1021/ed056pA260.1.

[256] Uppal R, Incarvito CD, Lakshmi K V, Valentine AM. Aqueous Spectroscopy and Redox Properties of Carboxylate-Bound Titanium. Inorg Chem 2006;45:1795–804. https://doi.org/10.1021/ic051714j.

[257] Wu N, Fu L, Su M, Aslam M, Wong KC, Dravid VP. Interaction of Fatty Acid Monolayers with Cobalt Nanoparticles. Nano Lett 2004;4:383–6. https://doi.org/10.1021/nl035139x.

[258] Rivas BL, Maureira A. Water-soluble Polyelectrolytes Contaning Sulfonic Acid Groups with Metal Ion Binding Ability by Using the Liquid Phase Polymer Based Retention Technique. Macromol Symp 2008;270:143–52. https://doi.org/10.1002/masy.200851017.

[259] Yavuz E, Senkal BF, Bicak N. Poly(acrylamide) grafts on spherical polyvinyl pyridine resin for removal of mercury from aqueous solutions. React Funct Polym 2005;65:121–5. https://doi.org/10.1016/j.reactfunctpolym.2004.12.006.

[260] Vardhan KH, Kumar PS, Panda RC. A review on heavy metal pollution, toxicity and remedial measures: Current trends and future perspectives. J Mol Liq 2019;290:111197. https://doi.org/10.1016/j.molliq.2019.111197.

[261] Lee I, Park CW, Yoon SS, Yang H-M. Facile synthesis of copper ferrocyanide-embedded magnetic hydrogel beads for the enhanced removal of cesium from water. Chemosphere 2019:776–85. https://doi.org/10.1016/j.chemosphere.2019.02.199.

[262] Atta AM, Ismail HS, Elsaaed AM. Application of anionic acrylamide-based hydrogels in the removal of heavy metals from waste water. J Appl Polym Sci 2012;123:2500–10. https://doi.org/10.1002/app.34798.

[263] Çavuş S, Çakal E. Poly(2-acrylamido-2-methyl-1-propane sulfonic acid-co-1-vinyl-2-pyrrolidone) hydrogel and its use in the removal of Cd(II), Pb(II) and Cu(II). Acta Phys Pol A 2017;132:505–8. https://doi.org/10.12693/APhysPolA.132.505.

[264] Matlock MM, Howerton BS, Atwood DA. Chemical precipitation of heavy metals from acid mine drainage. Water Res 2002;36:4757–64. https://doi.org/10.1016/S0043-1354(02)00149-5.

[265] Charerntanyarak L. Heavy metals removal by chemical coagulation and precipitation. Water Sci Technol 1999;39:135–8. https://doi.org/https://doi.org/10.1016/S0273-1223(99)00304-2.

[266] Sunil K, Karunakaran G, Yadav S, Padaki M, Zadorozhnyy V, Pai RK. Al-Ti2O6 a mixed metal oxide based composite membrane: A unique membrane for removal of heavy metals. Chem Eng J 2018;348:678–84. https://doi.org/10.1016/j.cej.2018.05.017.

[267] Kang S-Y, Lee J-U, Moon S-H, Kim K-W. Competitive adsorption characteristics of Co2+, Ni2+, and Cr3+ by IRN-77 cation exchange resin in synthesized wastewater. Chemosphere 2004;56:141–7. https://doi.org/10.1016/j.chemosphere.2004.02.004.

[268] Sarwar N, Imran M, Shaheen MR, Ishaque W, Kamran MA, Matloob A, et al. Phytoremediation strategies for soils contaminated with heavy metals: Modifications and future perspectives. Chemosphere 2017;171:710–21. https://doi.org/10.1016/j.chemosphere.2016.12.116.

[269] Da'na E. Adsorption of heavy metals on functionalized-mesoporous silica: A review. Microporous Mesoporous Mater 2017;247:145–57. https://doi.org/10.1016/j.micromeso.2017.03.050.

[270] Song K-C, Lee HK, Moon H, Lee KJ. Simultaneous removal of the radiotoxic nuclides Cs137 and I129 from aqueous solution. Sep Purif Technol 1997;12:215–27. https://doi.org/https://doi.org/10.1016/S1383-5866(97)00045-2.

[271] Godiya CB, Cheng X, Li D, Chen Z, Lu X. Carboxymethyl cellulose/polyacrylamide composite hydrogel for cascaded treatment/reuse of heavy metal ions in wastewater. J Hazard Mater 2019;364:28–38. https://doi.org/10.1016/j.jhazmat.2018.09.076.

[272] Zhang Y, Yan L, Xu W, Guo X, Cui L, Gao L, et al. Adsorption of Pb(II) and Hg(II) from aqueous solution using magnetic CoFe2O4-reduced graphene oxide. J Mol Liq 2014;191:177–82. https://doi.org/10.1016/j.molliq.2013.12.015.

[273] Elgueta E, Rivas BL, Mancisidor A, Núñez D, Dahrouch M. Hydrogels derived from 2-hydroxyethyl-methacrylate and 2-acrylamido-2-methyl-1-propanesulfonic acid, with ability to remove metal cations from wastewater. Polym Bull 2019. https://doi.org/10.1007/s00289-019-02697-z.

[274] Arshad F, Selvaraj M, Zain J, Banat F, Haija MA. Polyethylenimine modified graphene oxide hydrogel composite as an efficient adsorbent for heavy metal ions. Sep Purif Technol 2019;209:870–80. https://doi.org/10.1016/j.seppur.2018.06.035.

[275] Karbarz M, Khalil AM, Wolowicz K, Kaniewska K, Romanski J, Stojek Z. Efficient removal of cadmium and lead ions from water by hydrogels modified with cystine. J Environ Chem Eng 2018;6:3962–70. https://doi.org/10.1016/j.jece.2018.05.054.

[276] Mohammad N, Atassi Y, Tally M. Synthesis and swelling behavior of metal-chelating superabsorbent hydrogels based on sodium alginate-g-poly(AMPS-co-AA-co-AM) obtained under microwave irradiation. Polym Bull 2017;74:4453–81. https://doi.org/10.1007/s00289-017-1967-5.

[277] Zhou G, Luo J, Liu C, Chu L, Crittenden J. Efficient heavy metal removal from industrial melting effluent using fixed-bed process based on porous hydrogel

adsorbents. Water Res 2018;131:246–54. https://doi.org/10.1016/j.watres.2017.12.067.

[278] Kim Y, Kim YK, Kim S, Harbottle D, Lee JW. Nanostructured potassium copper hexacyanoferrate-cellulose hydrogel for selective and rapid cesium adsorption. Chem Eng J 2017;313:1042–50. https://doi.org/10.1016/j.cej.2016.10.136.

[279] Das SK, Dickinson C, Lafir F, Brougham DF, Marsili E. Synthesis{,} characterization and catalytic activity of gold nanoparticles biosynthesized with Rhizopus oryzae protein extract. Green Chem 2012;14:1322–34. https://doi.org/10.1039/C2GC16676C.

[280] Nasef MM, Saidi H. Surface studies of radiation grafted sulfonic acid membranes: XPS and SEM analysis. Appl Surf Sci 2006;252:3073–84. https://doi.org/https://doi.org/10.1016/j.apsusc.2005.05.013.

[281] Garg G, Chauhan GS, Ahn J-H. Strontium(II) ion uptake on poly(N-vinyl imidazole)-based hydrogels. J Appl Polym Sci 2012;124:3721–7. https://doi.org/10.1002/app.35369.

[282] Choe SR, Haldorai Y, Jang S-C, Rethinasabapathy M, Lee Y-C, Han Y-K, et al. Fabrication of alginate/humic acid/Fe-aminoclay hydrogel composed of a grafted-network for the efficient removal of strontium ions from aqueous solution. Environ Technol Innov 2018;9:285–93. https://doi.org/10.1016/j.eti.2017.12.008.

[283] Zhao P, Zhang W, Kaneti Y V, Azhar A, Alshehri AA, Yamauchi Y, et al. Confined synthesis of coordination frameworks inside double-network hydrogel for fabricating hydrogel-based water pipes with high adsorption capacity for cesium ions. Bull Chem Soc Jpn 2018;91:1357–63. https://doi.org/10.1246/bcsj.20180083.

[284] Bratskaya S, Privar Y, Slobodyuk A, Shashura D, Marinin D, Mironenko A, et al. Cryogels of carboxyalkylchitosans as a universal platform for the fabrication of composite materials. Carbohydr Polym 2019;209:1–9. https://doi.org/10.1016/j.carbpol.2018.12.094.

[285] Yoon JY, Zhang H, Kim YK, Harbottle D, Lee JW. A high-strength polyvinyl alcohol hydrogel membrane crosslinked by sulfosuccinic acid for strontium removal via filtration. J Environ Chem Eng 2019;7. https://doi.org/10.1016/j.jece.2018.102824.

[286] Chen S, Hu J, Shi J, Wang M, Guo Y, Li M, et al. Composite hydrogel particles encapsulated ammonium molybdophosphate for efficiently cesium selective removal and enrichment from wastewater. J Hazard Mater 2019:694–704. https://doi.org/10.1016/j.jhazmat.2019.03.047.

[287] Cho E, Kim J, Park CW, Lee K-W, Lee TS. Chemically bound Prussian blue in sodium alginate hydrogel for enhanced removal of Cs ions. J Hazard Mater 2018;360:243–9. https://doi.org/10.1016/j.jhazmat.2018.08.031.

[288] Dwivedi C, Pathak SK, Kumar M, Tripathi SC, Bajaj PN. Potassium cobalthexacyanoferrate-gel beads for cesium removal: Kinetics and sorption studies. RSC Adv 2013;3:22102–10. https://doi.org/10.1039/c3ra43463j.

[289] Wang K, Ma H, Pu S, Yan C, Wang M, Yu J, et al. Hybrid porous magnetic bentonite-chitosan beads for selective removal of radioactive cesium in water. J Hazard Mater

2019;362:160–9. https://doi.org/10.1016/j.jhazmat.2018.08.067.

[290] Taşdelen B, Osmanlioglu AE, Kam E. The adsorption behavior of cesium on poly(N-isopropylacrylamide/itaconic acid) copolymeric hydrogels. Polym Bull 2013;70:3041–53. https://doi.org/10.1007/s00289-013-1006-0.

[291] Gong T, Zhang X. Determination of iodide, iodate and organo-iodine in waters with a new total organic iodine measurement approach. Water Res 2013;47:6660–9. https://doi.org/10.1016/j.watres.2013.08.039.

[292] Yu K, Li X, Chen L, Fang J, Chen H, Li Q, et al. Mechanism and efficiency of contaminant reduction by hydrated electron in the sulfite/iodide/UV process. Water Res 2018;129:357–64. https://doi.org/10.1016/j.watres.2017.11.030.

[293] Mao P, Liu Y, Jiao Y, Chen S, Yang Y. Enhanced uptake of iodide on Ag@Cu2O nanoparticles. Chemosphere 2016;164:396–403. https://doi.org/10.1016/j.chemosphere.2016.08.116.

[294] Sánchez-Polo M, Rivera-Utrilla J, Salhi E, von Gunten U. Ag-doped carbon aerogels for removing halide ions in water treatment. Water Res 2007;41:1031–7. https://doi.org/https://doi.org/10.1016/j.watres.2006.07.009.

[295] Bo A, Sarina S, Zheng Z, Yang D, Liu H, Zhu H. Removal of radioactive iodine from water using Ag2O grafted titanate nanolamina as efficient adsorbent. J Hazard Mater 2013;246–247:199–205. https://doi.org/10.1016/j.jhazmat.2012.12.008.

[296] Zhao Y, Zhong L, Yi H. A review on the mechanism of iodide metabolic dysfunction in differentiated thyroid cancer. Mol Cell Endocrinol 2019;479:71–7. https://doi.org/10.1016/j.mce.2018.09.002.

[297] Mao P, Qi B, Liu Y, Zhao L, Jiao Y, Zhang Y, et al. AgII doped MIL-101 and its adsorption of iodine with high speed in solution. J Solid State Chem 2016;237:274–83. https://doi.org/10.1016/j.jssc.2016.02.030.

[298] Kireev S V., Shnyrev SL. Study of molecular iodine, iodate ions, iodide ions, and triiodide ions solutions absorption in the UV and visible light spectral bands. Laser Phys 2015;25:75602. https://doi.org/10.1088/1054-660X/25/7/075602.

[299] Sarina S, Bo A, Liu D, Liu H, Yang D, Zhou C, et al. Separate or Simultaneous Removal of Radioactive Cations and Anions from Water by Layered Sodium Vanadate-Based Sorbents. Chem Mater 2014;26:4788–95. https://doi.org/10.1021/cm501846z.

[300] Hoskins JS, Karanfil T, Serkiz SM. Removal and sequestration of iodide using silver-impregnated activated carbon. Environ Sci Technol 2002;36:784–9. https://doi.org/10.1021/es010972m.

[301] Zhang H, Gao X, Guo T, Li Q, Liu H, Ye X, et al. Adsorption of iodide ions on a calcium alginate–silver chloride composite adsorbent. Colloids Surfaces A Physicochem Eng Asp 2011;386:166–71. https://doi.org/10.1016/j.colsurfa.2011.07.014.

[302] Zhao X, Han X, Li Z, Huang H, Liu D, Zhong C. Enhanced removal of iodide from water induced by a metal-incorporated porous metal–organic framework. Appl Surf

Sci 2015;351:760–4. https://doi.org/10.1016/j.apsusc.2015.05.186.

[303] Liu S, Wang N, Zhang Y, Li Y, Han Z, Na P. Efficient removal of radioactive iodide ions from water by three-dimensional Ag2O–Ag/TiO2 composites under visible light irradiation. J Hazard Mater 2015;284:171–81. https://doi.org/10.1016/j.jhazmat.2014.10.054.

[304] Chen J, Gao Q, Zhang X, Liu Y, Wang P, Jiao Y, et al. Nanometer mixed-valence silver oxide enhancing adsorption of ZIF-8 for removal of iodide in solution. Sci Total Environ 2019;646:634–44. https://doi.org/10.1016/j.scitotenv.2018.07.298.

[305] Chen Y-Y, Yu S-H, Yao Q-Z, Fu S-Q, Zhou G-T. One-step synthesis of Ag2O@Mg(OH)2 nanocomposite as an efficient scavenger for iodine and uranium. J Colloid Interface Sci 2018;510:280–91. https://doi.org/https://doi.org/10.1016/j.jcis.2017.09.073.

[306] Asmussen RM, Matyáš J, Qafoku NP, Kruger AA. Silver-functionalized silica aerogels and their application in the removal of iodine from aqueous environments. J Hazard Mater 2018. https://doi.org/https://doi.org/10.1016/j.jhazmat.2018.04.081.

[307] Ateia M, Erdem CU, Ersan MS, Ceccato M, Karanfil T. Selective removal of bromide and iodide from natural waters using a novel AgCl-SPAC composite at environmentally relevant conditions. Water Res 2019;156:168–78. https://doi.org/10.1016/j.watres.2019.03.028.

[308] Mu W, Li X, Liu G, Yu Q, Xie X, Wei H, et al. Safe disposal of radioactive iodide ions from solutions by Ag2O grafted sodium niobate nanofibers. Dalt Trans 2016;45:753–9. https://doi.org/10.1039/C5DT03458B.

[309] Li J, Wang M, Liu G, Zhang L, He Y, Xing X, et al. Enhanced Iodide Removal from Water by Nano-Silver Modified Anion Exchanger. Ind Eng Chem Res 2018;57:17401–8. https://doi.org/10.1021/acs.iecr.8b04635.

[310] Alonso A, Muñoz-Berbel X, Vigués N, Rodríguez-Rodríguez R, Macanás J, Mas J, et al. Intermatrix synthesis of monometallic and magnetic metal/metal oxide nanoparticles with bactericidal activity on anionic exchange polymers. RSC Adv 2012;2:4596–9. https://doi.org/10.1039/C2RA20216F.

[311] Chhatre A, Solasa P, Sakle S, Thaokar R, Mehra A. Color and surface plasmon effects in nanoparticle systems: Case of silver nanoparticles prepared by microemulsion route. Colloids Surfaces A Physicochem Eng Asp 2012;404:83–92. https://doi.org/10.1016/j.colsurfa.2012.04.016.

[312] Mendis P, de Silva RM, de Silva KMN, Wijenayaka LA, Jayawardana K, Yan M. Nanosilver rainbow: a rapid and facile method to tune different colours of nanosilver through the controlled synthesis of stable spherical silver nanoparticles. RSC Adv 2016;6:48792–9. https://doi.org/10.1039/C6RA08336F.

[313] Fuku K, Hayashi R, Takakura S, Kamegawa T, Mori K, Yamashita H. The Synthesis of Size- and Color-Controlled Silver Nanoparticles by Using Microwave Heating and their Enhanced Catalytic Activity by Localized Surface Plasmon Resonance. Angew Chemie Int Ed 2013;52:7446–50. https://doi.org/10.1002/anie.201301652.

[314] González AL, Noguez C, Beránek J, Barnard AS. Size, Shape, Stability, and Color of

Plasmonic Silver Nanoparticles. J Phys Chem C 2014;118:9128–36. https://doi.org/10.1021/jp5018168.

[315] Huang T, Xu X-HN. Synthesis and characterization of tunable rainbow colored colloidal silver nanoparticles using single-nanoparticle plasmonic microscopy and spectroscopy. J Mater Chem 2010;20:9867–76. https://doi.org/10.1039/C0JM01990A.

[316] Vanysek P. Electrochemical series. CRC Handb. Chem. Phys., 2000.

[317] Boufi S, Vilar MR, Ferraria AM, Botelho do Rego AM. In situ photochemical generation of silver and gold nanoparticles on chitosan. Colloids Surfaces A Physicochem Eng Asp 2013;439:151–8. https://doi.org/10.1016/j.colsurfa.2012.12.036.

[318] Lindley BM, Appel AM, Krogh-Jespersen K, Mayer JM, Miller AJM. Evaluating the Thermodynamics of Electrocatalytic N 2 Reduction in Acetonitrile. ACS Energy Lett 2016;1:698–704. https://doi.org/10.1021/acsenergylett.6b00319.

[319] Jia Z, Sun H, Gu Q. Preparation of Ag nanoparticles with triethanolamine as reducing agent and their antibacterial property. Colloids Surfaces A Physicochem Eng Asp 2013;419:174–9. https://doi.org/10.1016/j.colsurfa.2012.12.003.

[320] Yang D, Liu H, Liu L, Sarina S, Zheng Z, Zhu H. Silver oxide nanocrystals anchored on titanate nanotubes and nanofibers: promising candidates for entrapment of radioactive iodine anions. Nanoscale 2013;5:11011–8. https://doi.org/10.1039/C3NR02412A.

[321] Verwey EJW, Overbeek JTG, van Nes K. Theory of the Stability of Lyophobic Colloids: The Interaction of Sol Particles Having an Electric Double Layer. Elsevier Publishing Company; 1948.

[322] Mladenovic IL, Kegel WK, Bomans P, Frederik PM. Observation of Equilibrium, Nanometer-Sized Clusters of Silver Iodide in Aqueous Solutions. J Phys Chem B 2003;107:5717–22. https://doi.org/10.1021/jp027401g.

[323] Verwey EJW. The Electrical Double Layer and the Stability of Lyophobic Colloids. Chem Rev 1935;16:363–415. https://doi.org/10.1021/cr60055a002.

[324] Kalnina D, Gross KA, Medvids A, Onufrijevs P. Formation of Negatively Charged AgI Colloid Nanoparticles by Condensation. Inter Acad. 2014 - Glob. Res. Educ., vol. 1117, Trans Tech Publications Ltd; 2015, p. 159–63. https://doi.org/10.4028/www.scientific.net/AMR.1117.159.

[325] Crundwell FK. The mechanism of dissolution of minerals in acidic and alkaline solutions: Part V surface charge and zeta potential. Hydrometallurgy 2016;161:174–84. https://doi.org/10.1016/j.hydromet.2016.01.031.

[326] Andersen O. Chelation Treatment During Acute and Chronic Metal Overexposures—Experimental and Clinical Studies. Chelation Ther. Treat. Met. Intox., 2016, p. 85–252. https://doi.org/10.1016/B978-0-12-803072-1.00004-3.

[327] Bernhoft R. Mercury Toxicity and Treatment: A Review of the Literature. J Environ Public Health 2012;2012:460508. https://doi.org/10.1155/2012/460508.

[328] Cohen-Solal M. Strontium overload and toxicity: impact on renal osteodystrophy. Nephrol Dial Transplant 2002;17 Suppl 2:30–4. https://doi.org/10.1093/ndt/17.suppl_2.30.

[329] Lyon AW, Mayhew WJ. Cesium toxicity: a case of self-treatment by alternate therapy gone awry. Ther Drug Monit 2003;25:114–6. https://doi.org/10.1097/00007691-200302000-00018.

[330] Melnikov P, Zanoni L. Clinical Effects of Cesium Intake. Biol Trace Elem Res 2009;135:1–9. https://doi.org/10.1007/s12011-009-8486-7.

[331] Braitberg G. Drugs and Antidotes in Acute Intoxication. Crit. Care Nephrol. Third Ed., 2017, p. 574-588.e3. https://doi.org/10.1016/B978-0-323-44942-7.00098-4.

[332] Rana MN, Tangpong J, Rahman MM. Toxicodynamics of Lead, Cadmium, Mercury and Arsenic- induced kidney toxicity and treatment strategy: A mini review. Toxicol Reports 2018;5:704–13. https://doi.org/10.1016/j.toxrep.2018.05.012.

[333] Domingo JL. Prevention by chelating agents of metal-induced developmental toxicity. Reprod Toxicol 1995;9:105–13. https://doi.org/10.1016/0890-6238(94)00060-3.

[334] Flora SJS, Pachauri V. Chelation in metal intoxication. Int J Environ Res Public Health 2010;7:2745–88. https://doi.org/10.3390/ijerph7072745.

[335] Andersen O. Choice of chelating antidotes for acute cadmium intoxication. Toxicol Environ Chem 1989;23:105–20. https://doi.org/10.1080/02772248909357456.

[336] Aposhian H V, Maiorino RM, Gonzalez-Ramirez D, Zuniga-Charles M, Xu Z, Hurlbut KM, et al. Mobilization of heavy metals by newer, therapeutically useful chelating agents. Toxicology 1995;97:23–38. https://doi.org/10.1016/0300-483x(95)02965-b.

APPENDICIES

A. Appendices for Chapter 5.

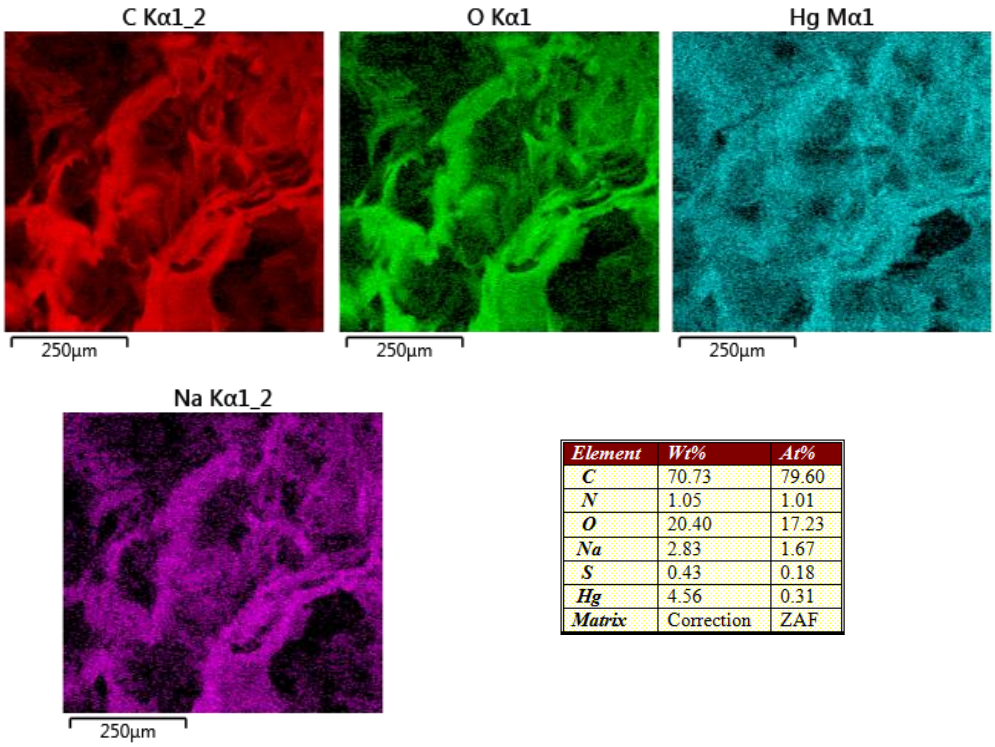

Element	Wt%	At%
C	70.73	79.60
N	1.05	1.01
O	20.40	17.23
Na	2.83	1.67
S	0.43	0.18
Hg	4.56	0.31
Matrix	Correction	ZAF

Fig A1. EDX mapping images and elemental composition of AAC-$HgCl_2$ sample

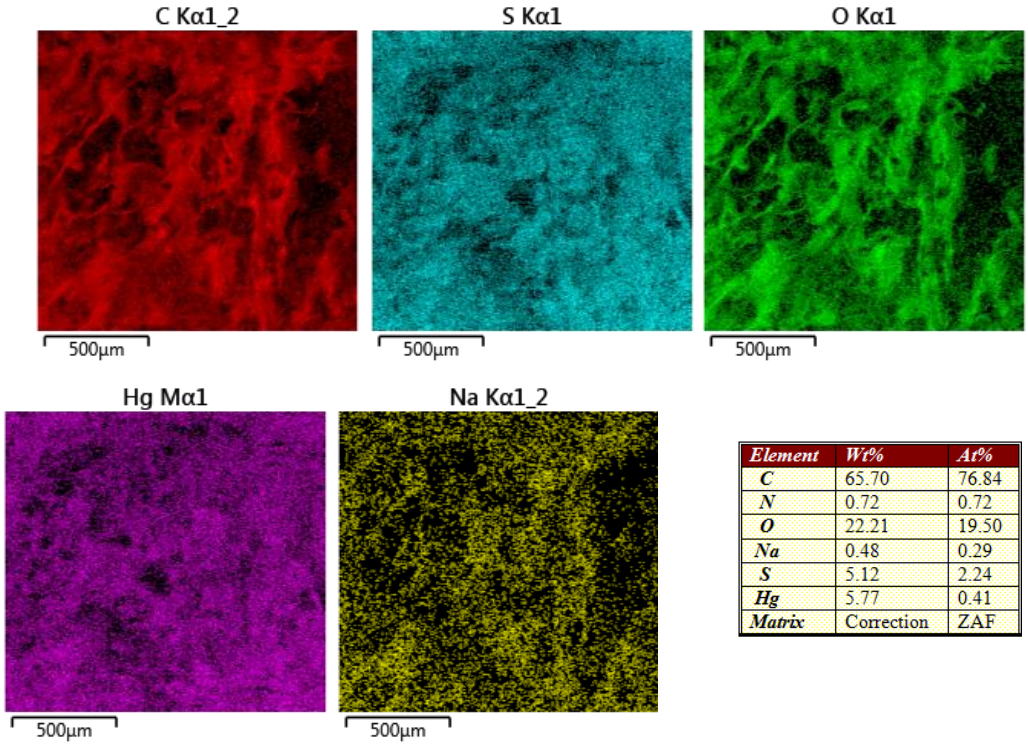

Element	Wt%	At%
C	65.70	76.84
N	0.72	0.72
O	22.21	19.50
Na	0.48	0.29
S	5.12	2.24
Hg	5.77	0.41
Matrix	Correction	ZAF

Fig A2. EDX mapping images and elemental composition of SAC-$HgCl_2$ sample

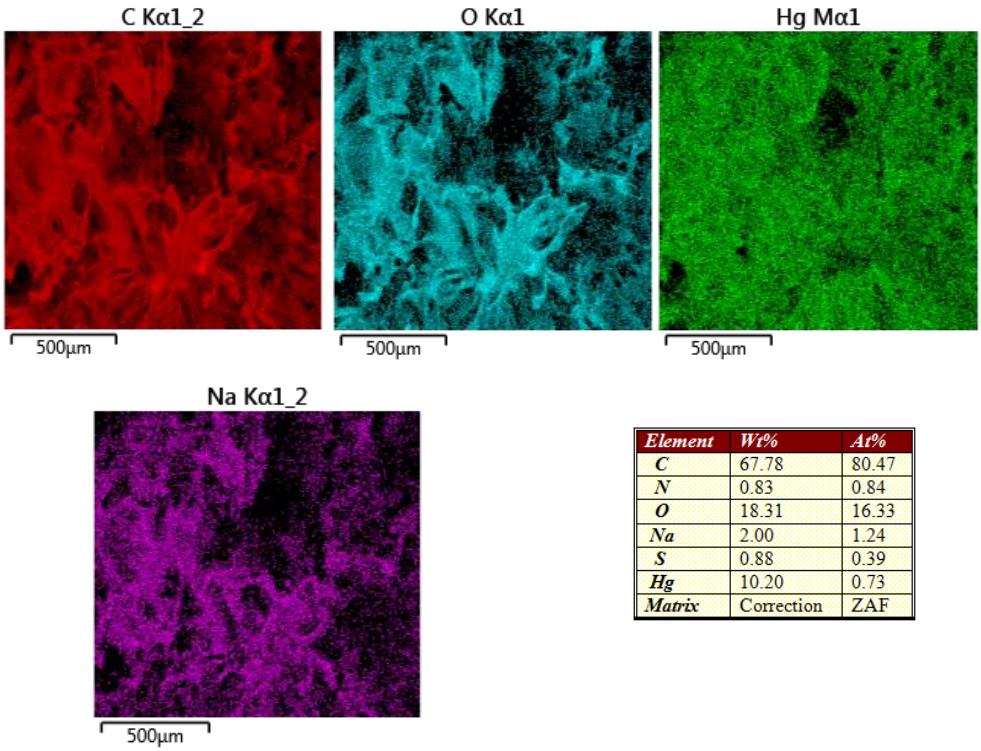

Element	Wt%	At%
C	67.78	80.47
N	0.83	0.84
O	18.31	16.33
Na	2.00	1.24
S	0.88	0.39
Hg	10.20	0.73
Matrix	Correction	ZAF

Fig A3. EDX mapping images and elemental composition of AAC-$Hg(NO_3)_2$ sample

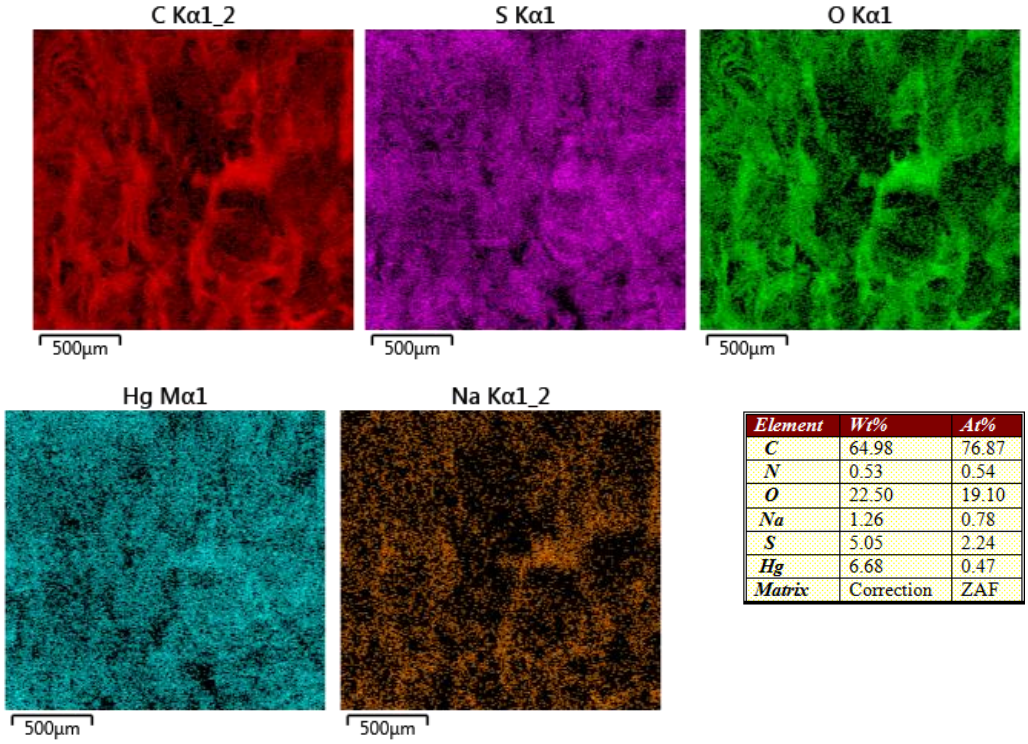

Element	Wt%	At%
C	64.98	76.87
N	0.53	0.54
O	22.50	19.10
Na	1.26	0.78
S	5.05	2.24
Hg	6.68	0.47
Matrix	Correction	ZAF

Fig A4. EDX mapping images and elemental composition of SAC-$Hg(NO_3)_2$ sample

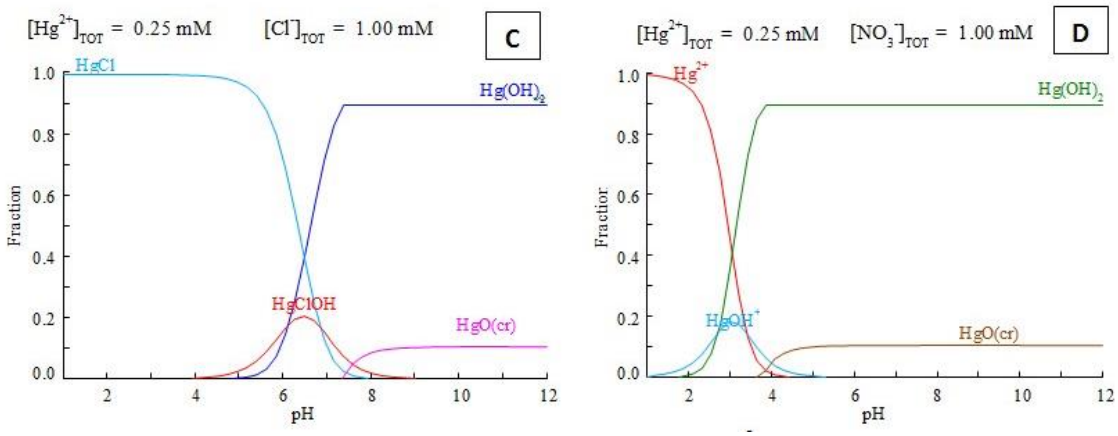

Fig. A5. Speciation of 50 ppm (C, D) Hg^{2+} chloride and nitrate solutions (Diagram created by Medusa software).

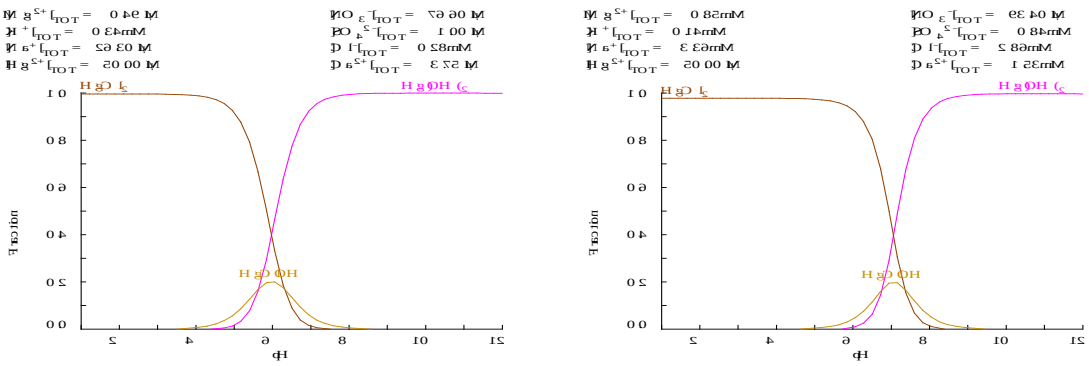

Fig. A6. Speciation of 10 ppm Hg^{2+} in ultra-pure (left) and tap (right) water matrices (Diagram created by Medusa software).

Table A1. Leaching experiment of Hg^{2+} from AAC and SAC cryogels at pH 7*.

Adsorbent type	Total adsorbed Hg [mg]	Leached Hg after 14 d [mg]	Leached Hg after 14 d [%]
AAC-$HgCl_2$	9.96	0.021	0.21
SAC-$HgCl_2$	8.36	0.0015	0.018
AAC-$Hg(NO_3)_2$	9.94	0.008	0.08
SAC-$Hg(NO_3)_2$	9.84	0.02	0.20

*The experimental conditions: 0.08 g of material in 100 mL of 100 mg/L Hg^{2+} solution

Table A2. The pH and conductivity of the mercury solutions before and after sorption (80 mg cryogel in 100 mL solution).

Sample-metal precursor	Initial pH	Final pH	Initial conductivity, μS/cm	Final conductivity, μS/cm
AAC-$HgCl_2$	4.38 ± 0.03	7.16±0.13	13.08 ± 0.53	115.15±0.15
SAC-$HgCl_2$	4.38 ± 0.03	3.99±0.1	13.08 ± 0.53	122.5±2.1
AAC-$Hg(NO_3)_2$	3.39 ± 0.5	7.42±0.18	244 ± 2	112.8±0.9
SAC-$Hg(NO_3)_2$	3.39 ± 0.5	3.77±0.0	244 ± 2	170.45±0.15

Table A3. Total nitrogen content (% w/w) in parent and mercury-treated cryogels.

AAC	9.32±0.43
SAC	8.70±1.90
AAC-$Hg(NO_3)_2$	7.27±0.36
AAC-$HgCl_2$	8.24±1.06
SAC-$Hg(NO_3)_2$	10.13±0.18
SAC-$HgCl_2$	11.32±0.73

Table A4. The pH, electrolytic conductivity and concentrations of cations and anions after 24 h removal of mercury ions in different water matrices.

		Na, ppm	K, ppm	Mg, ppm	Ca, ppm	CI, ppm	SO4, ppm	PO4, ppm	pH	EC**, uS/cm
UP water	Activated carbon	6.61	57.97	0.09	12.41	43.87	3.81	0.07	9.34	175.95
	Ion-exchange resin	0.55	29.25	0.02	0.32	22.93	0.33	0.04	4.66	77.25
	Zeolite	1.63	16.37	0.01	0.23	13.12	0.51	n.a.*	5.04	46.25
	AAC	12.12	7.98	0.04	0.39	7.73	n.a.	n.a.	7.78	96.10
	SAC	4.98	7.13	0.05	0.47	6.95	0.53	n.a.	6.80	72.25
	control	0.61	13.47	0.01	0.16	10.01	0.10	n.a.	5.06	98.20
tap	Activated carbon	80.59	6.06	23.52	53.65	100.81	86.04	n.a.	8.09	894.00
	Ion-exchange resin	31.49	1.59	6.17	17.45	102.96	82.52	n.a.	2.49	1618.00
	Zeolite	145.62	2.45	11.79	22.36	104.17	82.63	n.a.	8.08	1031.50
	AAC	154.43	3.08	3.57	9.90	106.90	85.09	14.55	8.32	935.50
	SAC	128.71	3.14	11.23	31.09	106.91	89.25	55.01	8.06	995.50
	control	77.29	5.45	20.55	61.27	101.51	80.79	n.a.	8.02	875.00

river	Activated carbon	20.89	2.80	4.99	26.92	22.27	19.55	0.83	8.26	335.00
	Ion-exchange resin	6.12	2.15	1.02	10.06	23.31	15.40	n.a.	3.10	399.50
	Zeolite	60.72	0.30	0.16	1.30	21.43	14.25	0.07	7.67	357.50
	AAC	53.35	0.54	0.46	5.20	22.00	15.02	17.01	8.44	355.50
	SAC	62.26	1.45	0.53	6.17	23.47	19.37	58.38	8.11	435.50
	control	19.68	1.72	2.98	29.01	21.43	13.63	n.a.	6.95	285.00
seawater	Activated carbon	11250.63	333.18	1309.56	369.19	18526.32	2493.97	7.51	7.96	42.05
	Ion-exchange resin	10885.58	322.74	1203.07	322.71	18281.98	2451.75	n.a.	2.12	45.95
	Zeolite	11302.83	321.00	1290.32	365.63	18846.18	2525.92	6.73	7.83	44.40
	AAC	11367.18	325.95	1256.80	378.17	18906.10	2561.40	12.31	7.71	45.05
	SAC	11046.52	326.39	1271.15	380.73	18702.95	2520.04	26.81	7.81	45.40
	control	12031.77	386.27	1436.59	412.21	19425.47	3012.78	n.a.	7.99	46.10

*n.a. – not availbale, below detection limit

** - electrolytic conductivity of solutions

B. Appendices for Chapter 6.

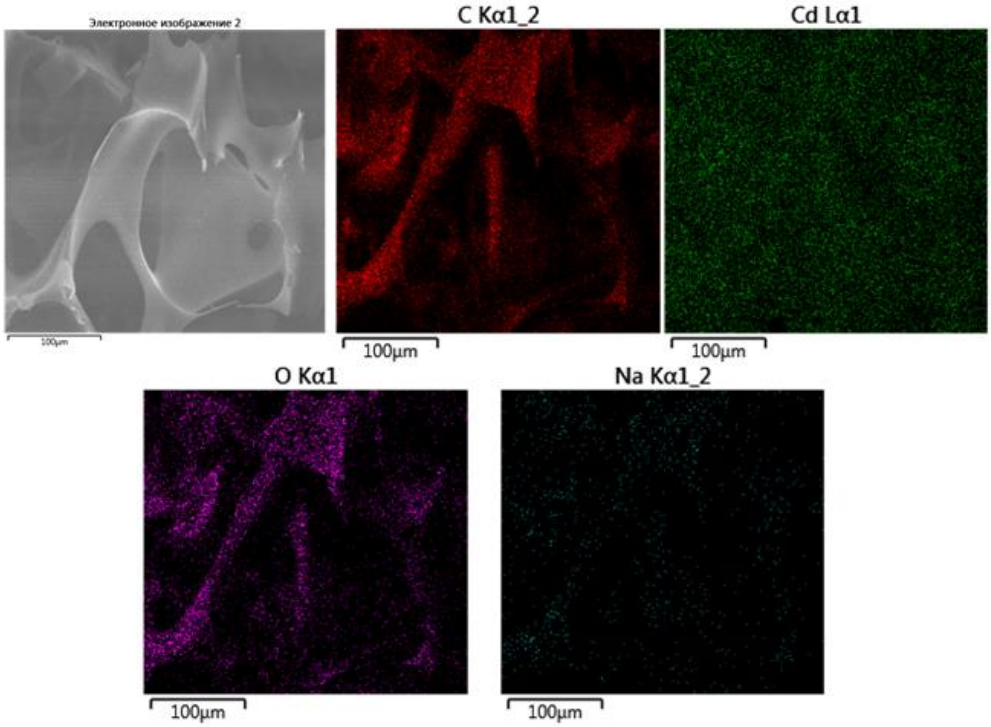

Fig B1. EDX mapping images of AAC-Cd sample

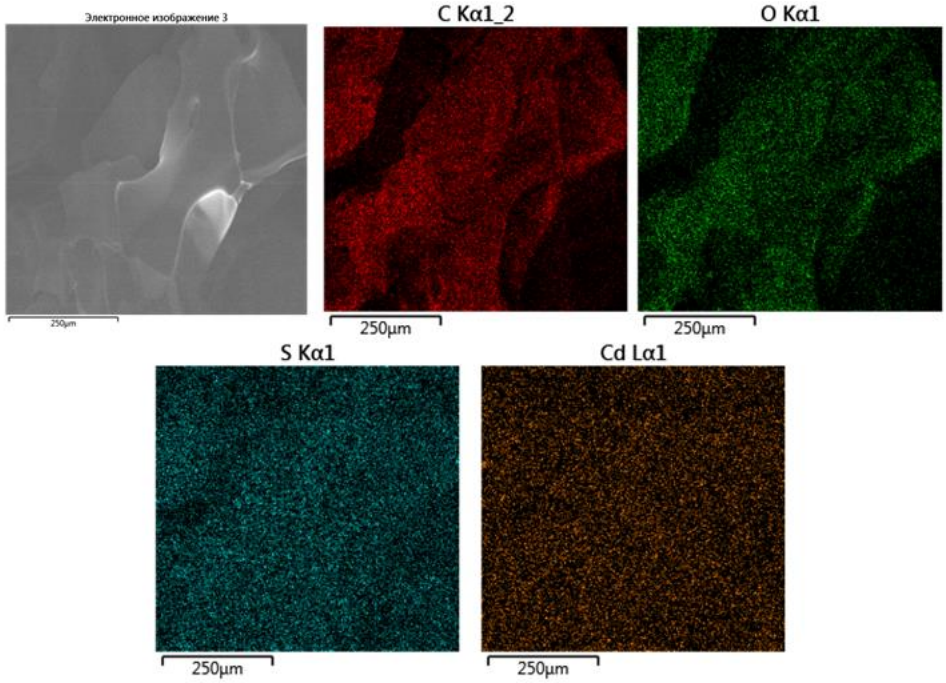

Fig B2. EDX mapping images of SAC-Cd sample

C. Appendices for Chapter 7.

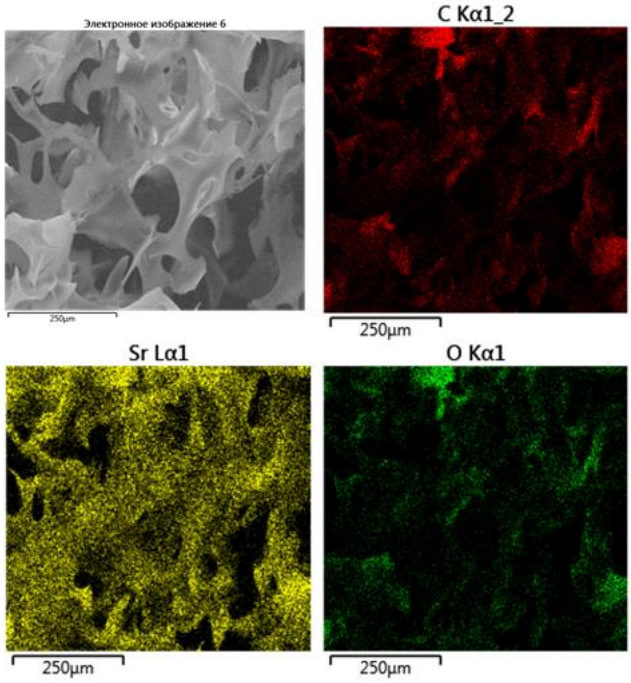

Fig C1. EDX mapping images of AAC-Sr sample

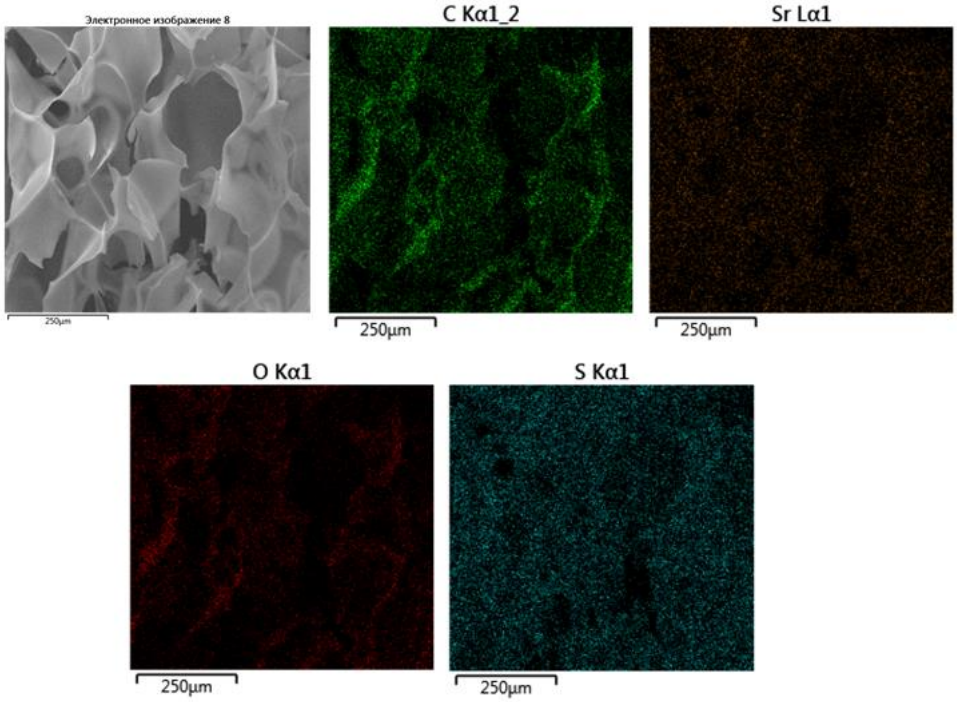

Fig C2. EDX mapping images of SAC-Sr sample

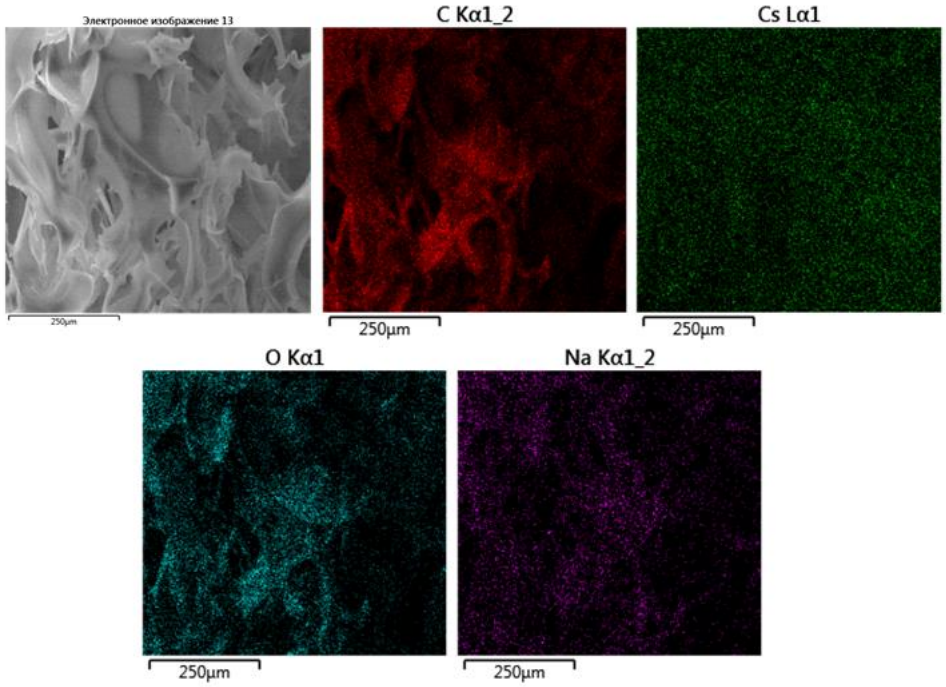

Fig C3. EDX mapping images of AAC-Cs sample

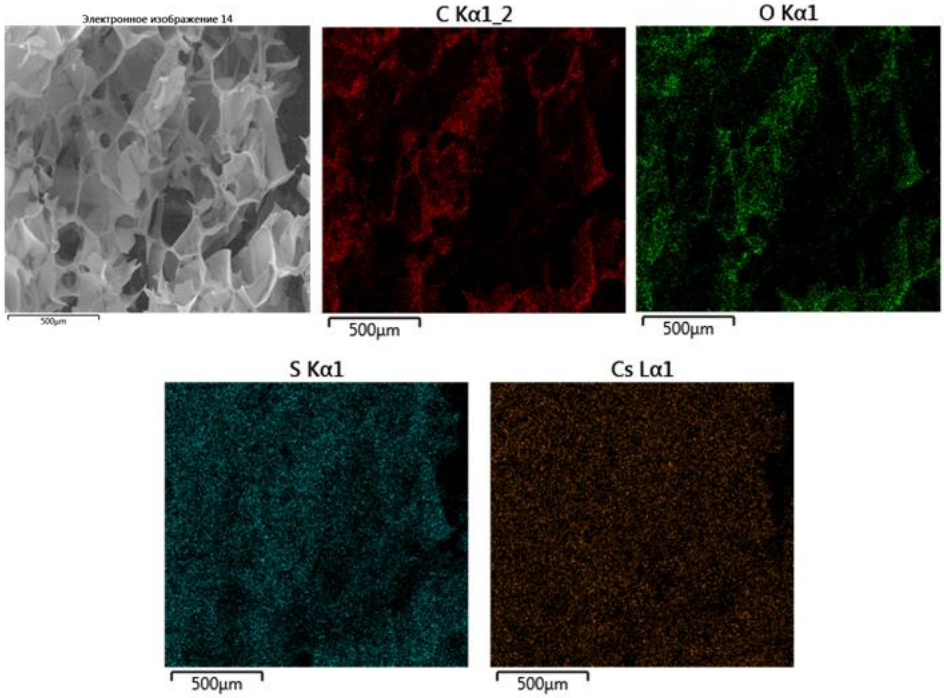

Fig C4. EDX mapping images of SAC-Cs sample

D. Appendices for Chapter 8.

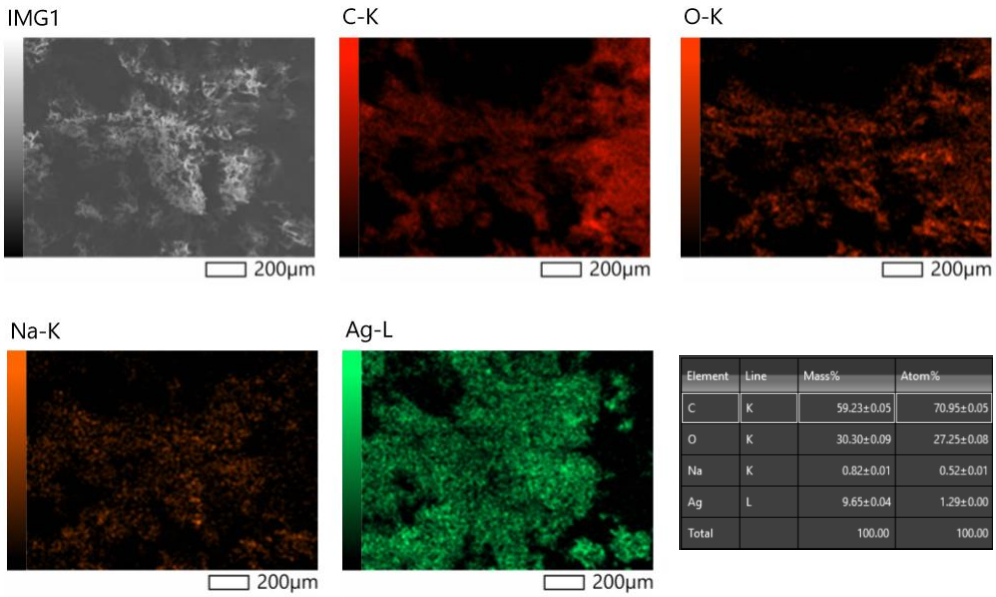

Element	Line	Mass%	Atom%
C	K	59.23±0.05	70.95±0.05
O	K	30.30±0.09	27.25±0.08
Na	K	0.82±0.01	0.52±0.01
Ag	L	9.65±0.04	1.29±0.00
Total		100.00	100.00

Fig D1. EDS mapping images of AAC-Ag sample

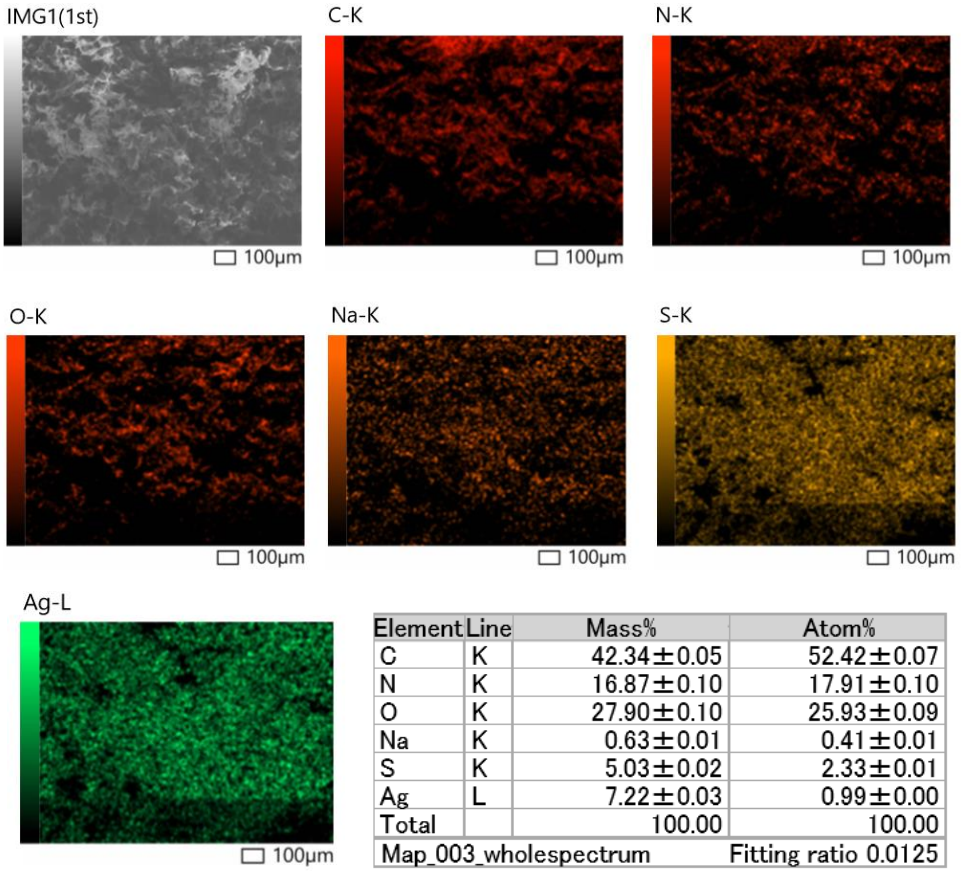

Element	Line	Mass%	Atom%
C	K	42.34±0.05	52.42±0.07
N	K	16.87±0.10	17.91±0.10
O	K	27.90±0.10	25.93±0.09
Na	K	0.63±0.01	0.41±0.01
S	K	5.03±0.02	2.33±0.01
Ag	L	7.22±0.03	0.99±0.00
Total		100.00	100.00
Map_003_wholespectrum			Fitting ratio 0.0125

Fig D2. EDS mapping images of SAC-Ag sample

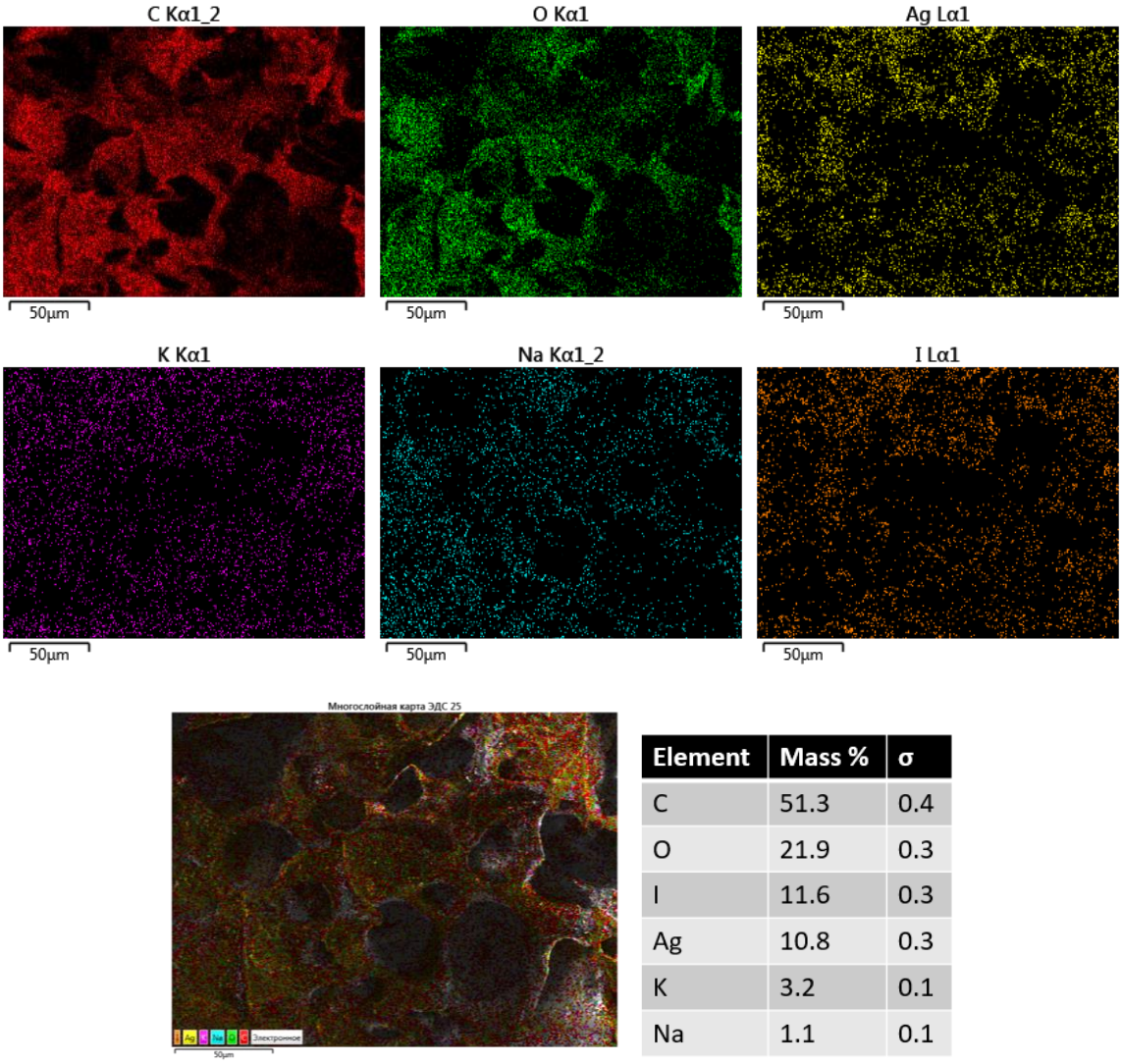

Element	Mass %	σ
C	51.3	0.4
O	21.9	0.3
I	11.6	0.3
Ag	10.8	0.3
K	3.2	0.1
Na	1.1	0.1

Fig D3. EDS mapping images of AAC-AgI sample

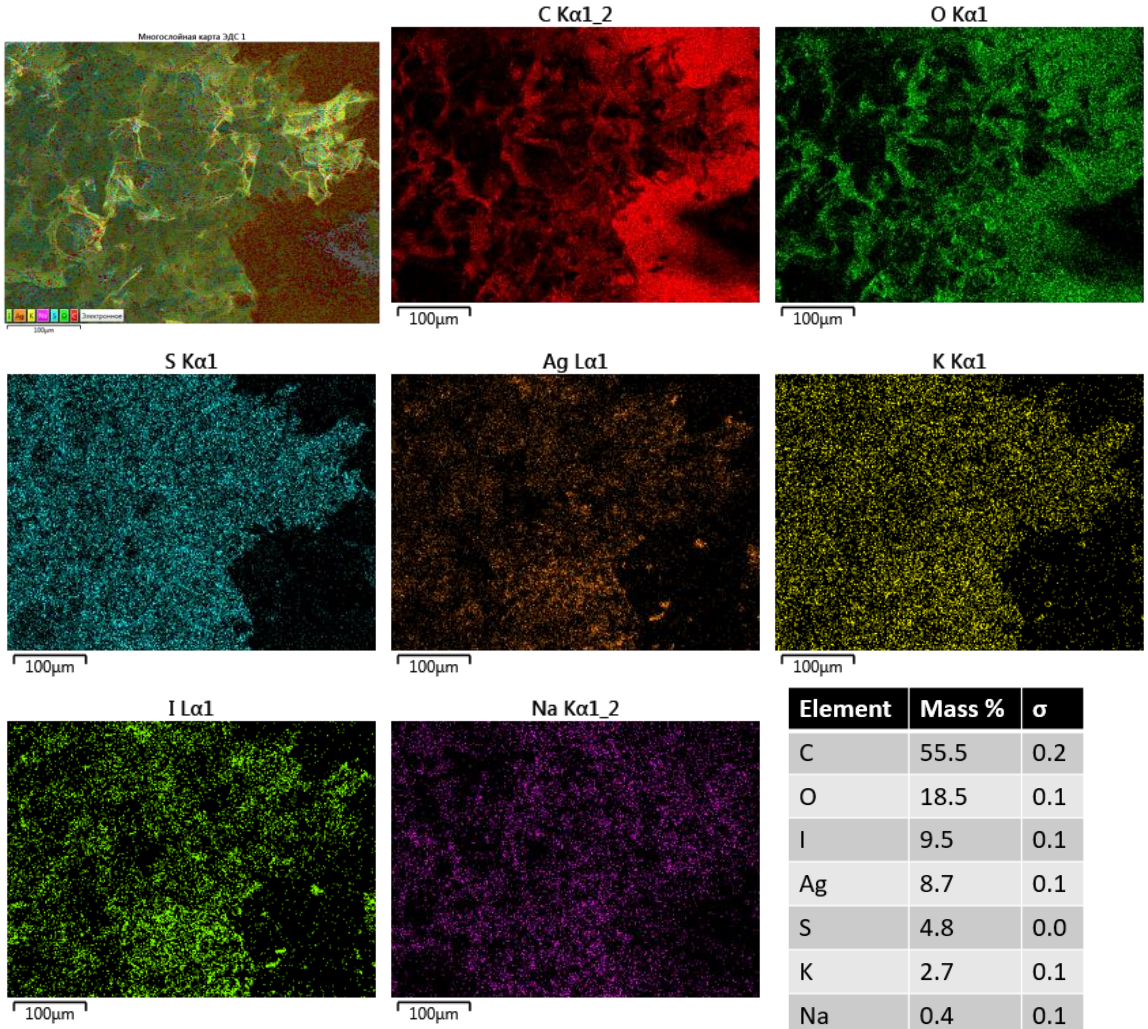

Element	Mass %	σ
C	55.5	0.2
O	18.5	0.1
I	9.5	0.1
Ag	8.7	0.1
S	4.8	0.0
K	2.7	0.1
Na	0.4	0.1

Fig S4. EDS mapping images of SAC-AgI sample

Table D1. Silver and iodide content in Ag-modified and iodide-loaded cryogels (wt %).

	Ag-modified		**Iodide-loaded**			
	Ag		**Ag**		**I**	
Cryogel	EDS	Expected	EDS	Expected	EDS	Expected
AAC	9.65	13.72	10.80	11.82	11.60	13.9
SAC	7.22	8.93	8.70	8.08	9.50	9.50

Table D2. Conductivity and pH of solutions after I^- removal by Ag-cryogels

	AAC-AgI		SAC-AgI	
Cryogel, mg /100 mL KI	Conductivity, μS/cm	pH	Conductivity, μS/cm	pH
100	29.35±2.75	7.11±0.27	13.3±0.9	5.255±0.05
80	27.95±0.45	6.67±0.03	22.3±1.9	5.24±0.13
60	26.6±0.6	6.18±0.02	43.0±0.3	5.02±0.09
40	33.7±2	6.53±0.06	65.0±0.5	5.21±0.06
20	76.85±0.45	6.25±0.15	84.2±0.1	5.35±0.12
10	88.65±0.65	6.11±0.03	96.9±0	5.59±0
KI stock	104.4	5.56	104.4	5.56